Julius-Maximilians-
UNIVERSITÄT
WÜRZBURG

UNIVERSITÄT WÜRZBURG
PHYSIKALISCHES INSTITUT
epVI

The Effect of Morphology on the Photocurrent Generation in Organic Solar Cells

Dissertation zur Erlangung des
naturwissenschaftlichen Doktorgrades
der Bayrischen Julius-Maximilians-Universität Würzburg

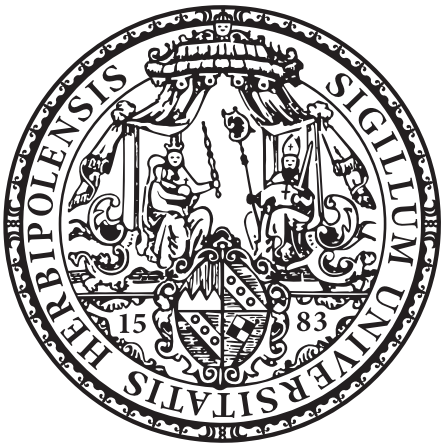

vorgelegt von

Andreas Zusan

aus Rottweil

Würzburg 2014

Eingereicht am: 18. Dezember 2014
bei der Fakultät für Physik und Astronomie

1. Gutachter: Prof. Dr. Carsten Deibel
2. Gutachter: Priv. Doz. Dr. Achim Schöll
der Dissertation.

1. Prüfer: Prof. Dr. Carsten Deibel
2. Prüfer: Priv. Doz. Dr. Achim Schöll
3. Prüfer: Prof. Dr. Giorgio Sangiovanni
im Promotionskolloquium.

Tag des Promotionskolloquiums: 23. Juli 2015

Doktorurkunde ausgehändigt am:

Abstract

Organic solar cells have great potential to become a low-cost and clean alternative to conventional photovoltaic technologies based on the inorganic bulk material silicon. As a highly promising concept in the field of organic photovoltaics, bulk heterojunction (BHJ) solar cells consist of a mixture of an electron donating and an electron withdrawing component. Their degree of intermixing crucially affects the generation of photocurrent. In this work, the effect of an altered blend morphology on polaron pair dissociation, charge carrier transport, and nongeminate recombination is analyzed by the charge extraction techniques time delayed collection field (TDCF) and open circuit corrected transient charge extraction (OTRACE). Different comparative studies cover a broad range of material systems, including polymer and small-molecule donors in combination with different fullerene acceptors.

The field dependence of polaron pair dissociation is analyzed in blends based on the polymer pBTTT-C_{16}, allowing a systematic tuning of the blend morphology by varying the acceptor type and fraction. The effect of both excess photon energy and intercalated phases are minor compared to the influence of excess fullerene, which reduces the field dependence of photogeneration. The study demonstrates that the presence of neat fullerene domains is the major driving force for efficient polaron pair dissociation that is linked to the delocalization of charge carriers. Furthermore, the influence of the processing additive diiodooctane (DIO) is analyzed using the photovoltaic blends PBDTTT-C:$PC_{71}BM$ and PTB7:$PC_{71}BM$. The study reveals a multi-tiered alteration of the blend morphology of PBDTTT-C based blends upon a systematic increase of the amount of DIO. Domains on the hundred nanometers length scale in the DIO-free blend are identified as neat fullerene agglomerates embedded in an intermixed matrix. With the addition of the additive, 0.6 % and 1 % DIO already substantially reduces the size of these domains until reaching the optimum 3 % DIO mixture, where a 7.1 % power conversion efficiency is obtained. It is brought into connection with the formation of interpenetrating polymer and fullerene phases. Similar to PBDTTT-C, the morphology of DIO-free PTB7:$PC_{71}BM$ blends is characterized by large fullerene domains being decreased in size upon the addition of 3 % DIO. OTRACE measurements reveal a reduced Langevin-type, super-second order recombination in both blends. It is demonstrated that the deviation from bimolecular recombination kinetics cannot be fully attributed to the carrier density dependence of the mobility but is rather related to trapping in segregated $PC_{71}BM$ domains. Finally, with regard to small-molecule donors, a higher yield of photogeneration and balanced transport properties are identified as the dominant factors enhancing the efficiency of vacuum deposited MD376:C_{60} relative to its solution processed counterpart MD376:$PC_{61}BM$. The finding is explained by a higher degree of dimerization of the merocyanine dye MD376 and a stronger donor-acceptor interaction at the interface in the case of the vacuum deposited blend.

Kurzdarstellung

Organische Solarzellen sind dank der Möglichkeit einer preisgünstigen und umweltfreundlichen Herstellung eine erfolgversprechende Alternative zu konventionellen Photovoltaiktechnologien, bei denen heutzutage hauptsächlich Silizium zum Einsatz kommt. Ein aussichtsreiches Konzept ist dabei die Heterogemisch (*bulk heterojunction*, BHJ)-Solarzelle. Deren aktive Schicht besteht aus einer Elektron-gebenden und einer Elektron-entziehenden Komponente, wobei die Generierung von Photostrom entscheidend von der Durchmischung beider Materialien abhängt. Dieser Einfluss der Morphologie auf die Trennung von Polaronpaaren, den Transport von freien Ladungsträgern und deren nichtgeminale Rekombination wird durch die Verwendung der Ladungsextraktionsmethoden *time delayed collection field* (TDCF) sowie *open circuit corrected transient charge extraction* (OTRACE) in dieser Arbeit im Detail untersucht. Die vorgestellten Studien umfassen mit Polymeren und kleinen Molekülen als Donatoren sowie verschiedenen Fulleren-Akzeptoren unterschiedlichste Materialsysteme.
Der erste Teil der Arbeit befasst sich mit der feldabhängigen Trennung von Polaronpaaren in Solarzellen, die unter Verwendung des Polymers pBTTT-C_{16} hergestellt werden. Das Materialsystem erlaubt eine systematische Anpassung der Morphologie durch Art und Anteil des Akzeptors. Die Untersuchungen zeigen, dass sowohl Überschussenergie als auch interkalierte Phasen lediglich eine geringe Auswirkung auf die Photogenerierung haben, diese jedoch stark von der Fullerenmenge im Gemisch beeinflusst wird. Das Ergebnis verdeutlicht, dass reine Fullerendomänen die treibende Kraft für eine effiziente Trennung von Polaronpaaren sind, was mit der Delokalisierung von Ladungsträgern verknüpft wird. Im zweiten Teil wird der Einfluss des Additivs Diiodooktan (DIO) auf das Materialsystem PBDTTT-C:$PC_{71}BM$ untersucht. Die Studie zeigt eine mehrstufige Änderung der Morphologie bei einer schrittweisen Erhöhung der verwendeten DIO Menge. Wird das Heterogemisch PBDTTT-C:$PC_{71}BM$ ohne DIO hergestellt, ist dessen Nanostruktur durch große Agglomerate geprägt, die als reine Fullerendomänen identifiziert werden. Bereits die Verwendung von 0.6 % und 1 % DIO führt zu einer deutlichen Verkleinerung dieser Domänen, wobei erst die maximale Effizienz der mit 3 % DIO hergestellten Solarzelle mit der Ausbildung von vernetzten Polymer- und Fullerenphasen in Verbindung gebracht wird. Vergleichbar zu PBDTTT-C weist auch PTB7:$PC_{71}BM$ große Fullerendomänen und deren bessere Dispersion durch die Verwendung von 3 % DIO auf. In beiden Fällen zeigt OTRACE eine reduzierte Langevin-artige Rekombination sowie die Abweichung von einem bimolekularen Verhalten. Da diese erhöhte Rekombinationsordnung nicht mit der Ladungsträgerdichtenabhängigkeit der Mobilität erklärt werden kann, wird sie dem Einfangen von Ladungsträgern in Fullerendomänen zugeordnet. Im letzten Teil wird gezeigt, dass eine ergiebigere Photogenerierung sowie ausgeglichene Transporteigenschaften eine erhöhte Bauteileffizienz von aufgedampften MD376:C_{60} Solarzellen im Vergleich zum flüssigprozessierten Pendant MD376:$PC_{61}BM$ bedingen. Die Beobachtung wird mit einer verbesserten Dimerisation des Merocyanins MD376 und einer stärkeren Donator-Akzeptor-Wechselwirkung an der Grenzfläche erklärt.

Contents

1. Introduction

During the last decades, the total global primary energy consumption per year increased continuously and reached 17 TW in 2011. [1] This demand is covered by about 3 % from nuclear energy, about 17 % from renewable sources, in particular biomass and hydropower, and by alarming 80 % from non-renewable fossil fuels, i.e., coal, oil, and natural gas. [2] Their combustion is inescapably accompanied by the emission of the greenhouse gas carbon dioxide (CO_2). Since the beginning of industrialization, human activities raised the concentration of CO_2 in the atmosphere by almost 50 %. Although, the earth's natural greenhouse effect is precondition for life as we know it today, the steady increase in atmospheric CO_2 causes an enhanced reduction of thermal radiation emittance to space. This anthropogenic greenhouse effect can be related to the increase in the globally averaged temperature by 0.8 K initiating in the last century. [3] Stopping the burn of fossil fuels within the next 50 years—long before available resources will be depleted—and the development of clean energy sources is necessary for minimizing global warming and the correlated climate change. Regarding the solar irradiation of 170,000 TW per year, photovoltaic (PV), i.e., the direct conversion of solar energy to electricity, can be ascribed great potential in the long-term solution of this global energy problem.

The discovery of the silicon (Si) solar cell dates back to 1954 at Bell labs. In the 1990s, the large-scale production of PV devices was initiated by diverse national funding programs. [3] As a result, the uninterrupted progress in technology and manufacturing provoked a steady reduction of module costs reaching a value below €0.50 per Watt peak in 2014. [4] However, the fabrication of mono- or polycrystalline solar cells and thin-film technologies, still using Si as the most popular bulk material, is commonly linked with a high energy and material requisition. During the past 25 years, major progress has been made in the field of photovoltaic devices made from carbon-based, organic semiconductors. [5] This kind of devices is often seen as the third generation of solar energy obviating the major drawbacks of their inorganic counterparts. Organic solar cells offer the possibility of simple roll-to-roll fabrication with low material input, e.g., by thermal deposition at room temperature or by printing from inks, semi-transparent layers of different colors, and flexible substrates (Figure 1.1). [6] By comparison, organic photovoltaic (OPV) is a rather young technology that still requires a considerable need for research in order to be able to compete with common inorganic PV systems. This includes the increase in generated power relative to incurred expenses in first place, but also processing and lifetime issues have to be solved. One of the most successful concepts of OPV devices is the bulk heterojunction (BHJ) architecture reaching current peak efficiencies up to 10 %. [7,8] The active layer of a BHJ solar cells consists of polymers or small molecules as electron donor (D) blended with typically fullerenes as electron acceptor (A). A critical aspect of the BHJ concept is the degree

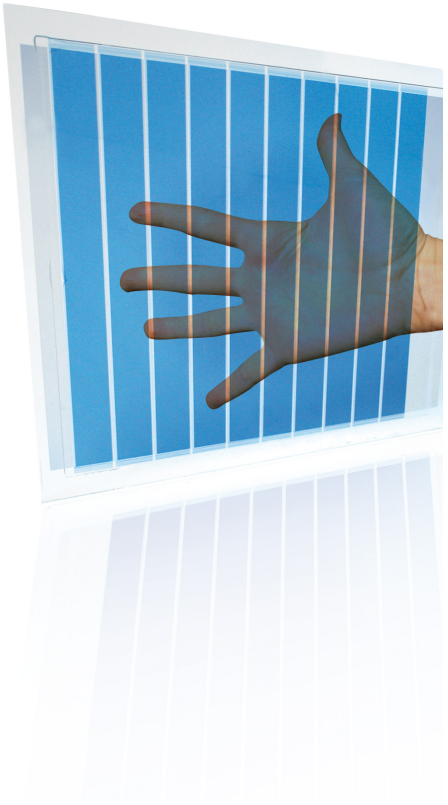

Figure 1.1.: Semi-transparent organic solar cell (image taken by Tim Deussen, Berlin, reproduced with permission from www.heliatek.com).

of the D-A intermixing that is commonly referred to as the active layer morphology. The controlled change of this nanostructure and grasping the impact on the factors driving an efficient photocurrent generation are key aspects for further improving the performance of state-of-the-art BHJ solar cells.

The aim of this work is to contribute to a better understanding of the effect of modified structural properties of the active layer on the essential processes in BHJ solar cells. As such a device is exposed to light, bound electron-hole (e-h) pairs are generated in neat donor or acceptor phases by the absorption of photons. In order to get dissociated, e-h pairs have to reach the D-A interface between neat phases within their lifetime, where one charge carrier can be transferred across the interface. This separation commonly involves an intermediate, interfacial state that has to be overcome to obtain free electrons and holes. Driven by an electric field, free charge carriers then move through the percolating D-A network and are extracted at the electrodes. Since the generation of free electrons and holes as well as their transport towards the electrodes might be affected by strong loss mechanism, these two processes can be seen as the most crucial steps in photocurrent generation. In addition, it is easy to imagine that the degree of D-A intermixing impacts both: Whereas a fine dispersion of the blend constituents increases the interfacial area and thus benefits e-h separation, efficient charge carrier transport requires the presence of pure, interconnected phases. With focus on the trade-off between these two factors, charge carrier extraction measurements are applied in this work. Consisting of an op-

tical pump and an electronic probe, these experiments allow access to both photogeneration and transport in OPV devices under operating conditions.

The thesis is organized as follows. Chapter 2 provides a short historical review on organic photovoltaics and introduces the fundamental steps from photon absorption to charge extraction in a BHJ solar cell. In addition, different concepts of optimizing blend morphology are presented. Chapter 3 addresses the main steps of photocurrent generation, i.e., the formation and transport of free charge carriers, and outlines the main loss mechanisms. The experimental background is described in Chapter 4 including the introduction of the used materials, sample preparation, and the applied measurement techniques. After that, the thesis covers three individual subjects. Chapter 5 analyzes the impact of fullerene loading on the field and excitation energy dependence of photogeneration. Chapter 6 covers a common method to optimize the morphology and efficiency of state-of-the-art BHJ devices that is the use of solvent additives during processing of the active layer. The effect of both a systematically increased additive content as well as the effect of the optimized amount of the additive on device physics are studied in two different material systems. Chapter 7 stands out from the study of polymer:fullerene blends in the two previous chapters and analyzes the differences in photogeneration and transport between vacuum deposited and solution processed small-molecule solar cells.

2. Organic Photovoltaics

The chapter gives a brief overview on the basic properties of organic semiconductors and the origin of their semiconducting behavior. It further outlines the application of organic semiconductors in photovoltaics and emphasizes the concept of so-called bulk heterojunction solar cells. The working principle of BHJ devices is summarized with focus on polymer:fullerene blends mostly used in this work, unless stated otherwise. The chapter then goes on to examine examples for the crucial effect of the active layer morphology on device physics, which is the major aspect of this thesis. In addition, the device characterization by current-voltage measurements is addressed. The chapter is based on the review article by Deibel et al.[6] For a more comprehensive insight, the reader may also consult other review articles, e.g., Dennler et al.[9], Brabec et al.[10,11], or Heeger[5].

2.1. Organic Semiconductors

Semiconductors are generally defined by an electrical conductivity that can be varied over several orders of magnitude. This property is related to the presence of an energy band gap E_g between zero and about 4 eV.[12] Prominent examples of crystalline, inorganic semiconductors are Si or the compound gallium arsenide (GaAs). The term organic is conventionally used for matter that is generally based on carbon (C).[13] The go-ahead for organic semiconductors dates back to the discovery of the conductivity of halogen-doped organic complexes in the 1950s.[14] The observation led to a systematic research on the optical excitation and charge carrier transport of so-called small molecules representing the first important class of organic semiconductors.[15,16] In the late 1970s, the second important class of organic semiconductors, conjugated polymers, was developed,[17] which was honored by the Nobel Price in Chemistry in 2000.

The conductivity of organic semiconductors is based on the tetravalent character of carbon and the quasi-free motion of electrons in a π-conjugated system. The ground state of a free C atom is the $1s^2 2s^2 2p^2$ configuration. In conductive, carbon-based compounds, it is energetically favored that carbon will sp^2 hybridize, i.e., the 2s and the 2p orbitals form three equivalent sp^2 orbitals in a trigonal planar geometry and a fourth p orbital perpendicular to this plane (Figure 2.1a and b). Adjacent C atoms are bound by overlapping two sp^2 orbitals and a p-p overlap, forming localized σ-bonds and a delocalized π-conjugated system, respectively. In carbon-based compounds with alternating single and double bonds, the former builds up a molecular- or polymer-backbone whereas the latter delocalizes along this backbone (Figure 2.1c).[15,18]

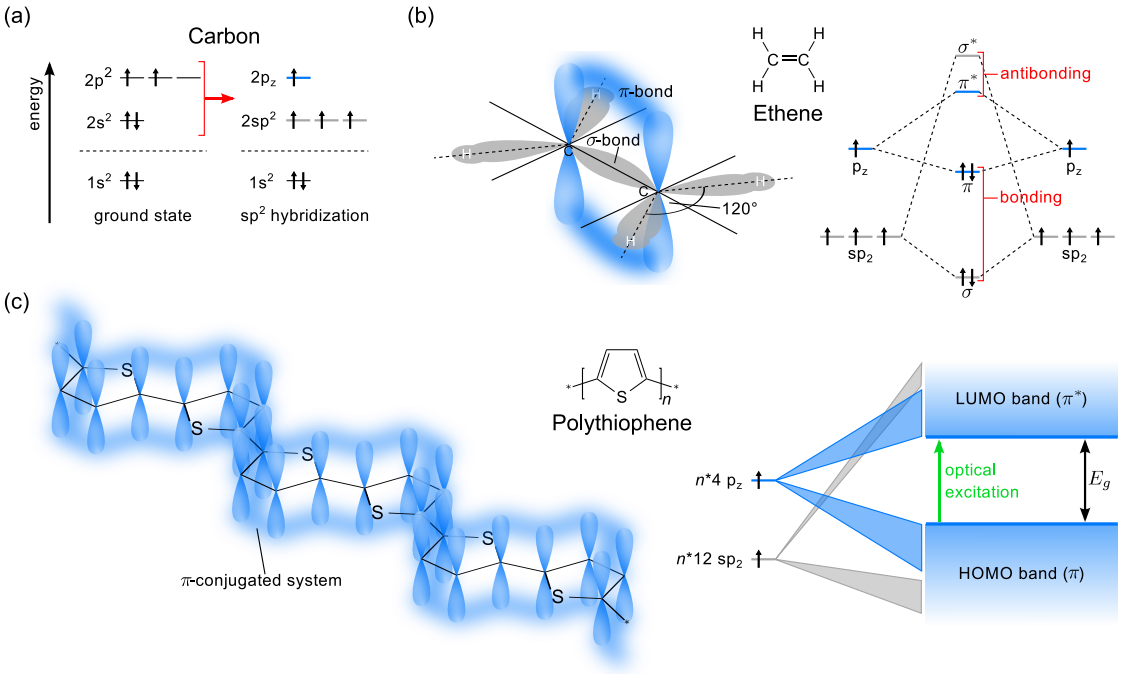

Figure 2.1.: (a) Schematic illustration of the $1s^2 2s^2 2p^2$ electron configuration of the C ground state and the sp^2 hybridization. **(b)** The drawing illustrates ethene (C_2H_4) as the simplest example of a π-conjugated system build up by two sp^2 hybridized C atoms. The three sp^2 orbitals of each C atom form a plane with an angle of 120° to each other, and the remaining 2p orbital is perpendicular to it. The C atoms are bound by overlapping two sp^2 orbitals and a p-p overlap forming σ and π bonds, respectively. The orbitals are split in bonding and antibonding orbitals with a π-π^* transition as the lowest electronic excitation. **(c)** Alternating single and double bonds in carbon-based compounds, e.g., coplanar polythiophene, result in a conjugated system of π-electrons along the polymer backbone. For reasons of simplicity, hydrogen (H) atoms are not shown. The delocalization of p orbitals involves the formation of a HOMO and LUMO energy band separated by the energy gap E_g (modified from Reference 19).

By the overlap of two sp^2 orbitals, occupied bonding orbitals (σ) and unoccupied antibonding orbitals (σ^*) are formed (Figure 2.1b). Due to their localized character, the excitation of a σ-electron to the σ^*-state requires a quite large energy. In contrast, the p-p overlap results in an only small energetic difference between the delocalized π- and π^*-orbitals as the highest occupied molecular orbital (HOMO) and the lowest unoccupied molecular orbital (LUMO), respectively, covering the range of 1 to 3 eV. Thus, an absorption in the visible and near-ultraviolet spectrum is possible. Regarding compounds that involve a multitude of carbon atoms (Figure 2.1c), π electrons delocalize along the whole polymer backbone giving rise to the formation of HOMO and LUMO energy bands. Due to the electron-phonon interaction, which causes an alternating length of single and double bonds (Peierls instability [20]), an energy gap between the HOMO (valence band) and LUMO (conduction band) occurs. The gap opening gives rise to the semiconducting behavior of organic compounds. The magnitude of the HOMO-LUMO gap E_g depends on the degree of conjugation and can be tuned over wide range from the near-infrared (NIR) to the near-ultraviolet spectrum. [15,21]

As outlined above, organic semiconductors can be divided into the two major classes, small molecules and polymers. Polymers consist of a sequence of monomeric units. Their so-called conjugation length is limited by distortions of this sequence, e.g., twists and kinks in the polymer backbone or chemical defects causing an energetic barrier.[22] Regarding both classes of organic semiconductors, weak interactions between adjacent molecules or polymer chains are mainly caused by van der Waals forces. As a consequence, the optical excitation of organic semiconductors results in the formation of an electrically neutral electron-hole pair localized on one molecule or few monomeric units. Its binding energy can be estimated by the Coulomb attraction of two charges at a distance of roughly 1 nm matching the typical size of a molecule or monomer. Using a dielectric constant of $\varepsilon_r = 3.5$, which is characteristic for organic semiconductors, yields a binding energy of about 0.5 eV. This value substantially exceeds the thermal energy at room temperature (RT) of $k_B T = 26$ meV. Excitations in organic compounds therefore lead to the formation of strongly bound so-called Frenkel excitons. In contrast, the dielectric constant of inorganic semiconductors is considerably larger ($\varepsilon_r \geq 10$[23]) yielding rather weakly bound so-called Wannier-Mott excitons.[18]

2.2. Organic Bulk Heterojunction Solar Cells

2.2.1. Brief History

The first application of organic semiconductors for photovoltaic solar energy conversion dates back to the 1970s, when first devices were made of one single active material. The organic layer, e.g., perylene derivatives, was sandwiched between a high work function metal or conducting glass and a low work function metal. Whereas the former acts as ohmic contact, the latter ensures a rectifying electrode due to an interfacial oxide layer. To generate photocurrent, excitons, which form upon the absorption of light, have to be separated into free electrons and holes. Since the temperature under working conditions is not high enough to overcome the substantial binding energy (Section 2.1), the dissociation mainly occurs at the metal-organic barrier.[24] Consequently, the single layer devices suffered from high recombination losses and reached a power conversion efficiency (PCE) of far less than 1 %.[25]

A significant improvement of the photovoltaic efficiency was made by the development of the organic bilayer solar cell in 1986 (Figure 2.2a) reaching a PCE of about 1 %.[26] In this approach, the driving force for the dissociation of singlet excitons is provided by the energy offset between the LUMO of the absorbing donor material and the LUMO of a second, strongly electronegative acceptor material, e.g., both from the class of small molecules. Although the planar heterojunction (PHJ) architecture results in an efficient charge transfer of the electron at the D-A heterointerface, the concept is limited by the short diffusion length d_e of excitons in organic semiconductors. Based on a variety of techniques to determine d_e, it is reasonable to assume a diffusion length in the range of 5 to 10 nm.[27–35] This value is far below the typical active layer thickness of about 100 to 200 nm which is required for an adequate absorption of organic thin

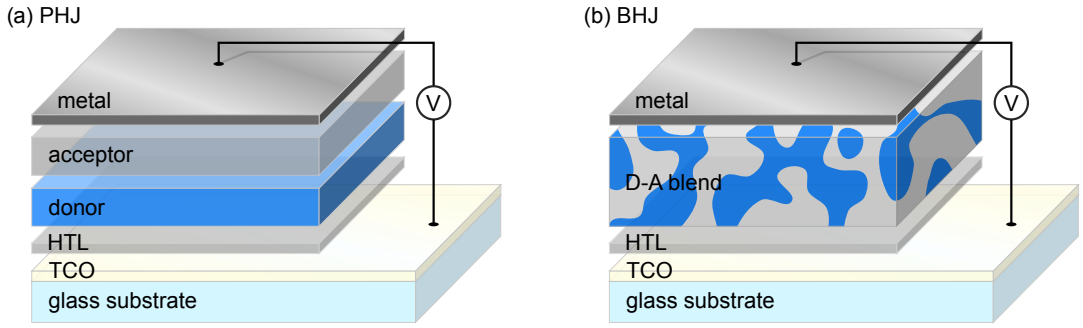

Figure 2.2.: Device architecture of **(a)** an organic PHJ solar cell and **(b)** an organic bulk heterojunction solar cell. The glass substrate is coated with a transparent conductive oxide (TCO), e.g., indium tin oxide (ITO), acting as anode. It is followed by a hole transport layer (HTL) used for planarization of the TCO layer at the same time. The active layer consists of either **(a)** the bilayer of donor and acceptor or **(b)** a D-A blend and is illuminated through the glass substrate. On top, a metallic electrode acts as cathode.

films. As a consequence, only about 10 % of the generated excitons reach the D-A interface within their lifetime and get separated.

The decisive approach to circumvent the tradeoff between the short exciton diffusion length and the required film thickness was introduced in 1995. In a BHJ solar cell (Figure 2.2b), the active layer consists of an interpenetrating D-A blend.[7] Thus, the heterointerface is distributed throughout the whole bulk of the active layer allowing a highly efficient exciton dissociation, while the thickness of the active layer can be still adjusted to the absorption length. The bicontinuous network of the donor and acceptor components is achieved by spin casting of blend solutions or by the coevaporation of the molecular components, allowing the use of a variety of D-A combinations. First BHJ devices were made of blends of the polymer poly(2-methoxy-5-(2-ethylhexyloxy)-1,4-phenylenevinylene) (MEH-PPV) as donor and the fullerene C_{60} as acceptor yielding a PCE of 2.9 %.[7] During the last decades, the power conversion efficiency of solution processed solar cells could be enhanced up to 9.2 % for blends of the low-bandgap copolymer poly[(4,8-bis-(2-ethylhexyloxy)-benzo(1,2-b:4,5-b')dithiophene)-2,6-diyl-alt-(4-(2-ethylhexyl)-3-fluorothieno[3,4-b]thiophene-)-2-carboxylate-2-6-diyl)] (PTB7) and the small molecule [6,6]-phenyl-C_{71}-butyric acid methyl ester ($PC_{71}BM$).[36–40] The current record efficiency of BHJ devices is 10.7 %.[8]

2.2.2. Working Principle

Figure 2.3a schematically shows the fundamental processes of photocurrent generation in a BHJ solar cell. The same processes are depicted in a simplified energy diagram in Figure 2.3b and more detailed in Figure 3.2. The individual steps, starting with the generation of excitons in the donor material which is followed by the electron transfer at the heterointerface, the dissociation of coulombically bound e-h pairs, the transport of free electrons and holes, and their final extraction, will be discussed in the following. In principle, these processes can also result from the absorption and generation of excitons in the acceptor material yielding a hole transfer

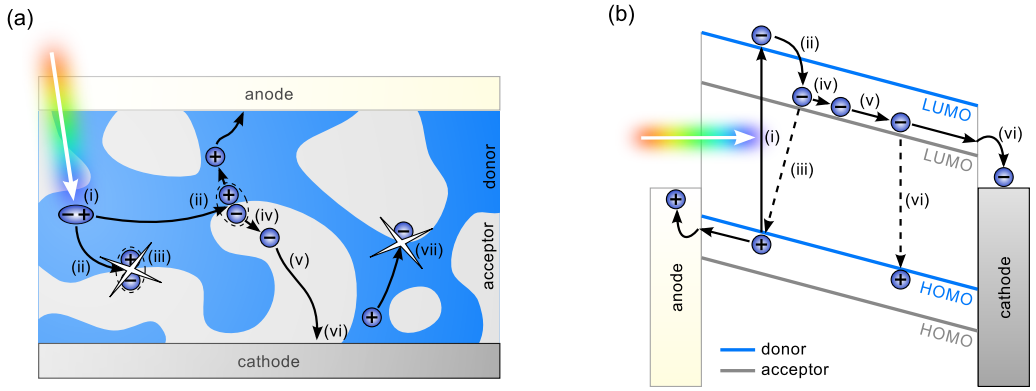

Figure 2.3.: (a) Schematic illustration of the fundamental steps from light absorption to photocurrent in an organic BHJ solar cells. (i) Light absorption and generation of a singlet exciton. (ii) Exciton diffusion to the D-A interface followed by the transfer of the electron to the acceptor. (iii) The coulombically bound e-h pair can either recombine geminately or (iv) get fully separated. (v) Hopping transport of free electrons and holes to the respective electrode. (vi) Charge carrier extraction. (vii) On their way through the D-A network, nongeminate recombination of independently generated electrons and holes can occur. **(b)** The same processes depicted in an energy level diagram. (iii) Geminate and (vii) nongeminate recombination losses are indicated as dashed lines.

to the donor. However, for reasons of simplicity, only the case of an "electron-perspective" is considered throughout this work, unless stated otherwise.

Light absorption and exciton generation: The active layer thickness of polymer:fullerene BHJ solar cells of about 100 to 200 nm results from the very high absorption coefficient of common organic semiconductors. It is typically in a range beyond 10^7 m^{-1} and thus exceeds inorganic counterparts by several orders of magnitude in the respective absorption band.[41] In BHJ solar cells, the absorption mainly takes place in the donor material, i.e., in polymer phases, which typically shows a quite narrow absorption range covering the visible spectral range only. Despite improvements in the extension of the cutoff wavelength from around 650 nm in standard thiophene based polymers, e.g., the workhorse donor material poly(3-hexylthiophene-2,5-diyl) (P3HT), to the 750 nm range in state-of-the-art low-bandgap copolymers,[36,42–44] the large mismatch between the polymer absorption and the solar spectrum (Figure 2.4) is still one of the major drawbacks as compared to inorganic photovoltaics. They typically show an absorption up to the far-infrared (FIR) range. As already mentioned, there is a certain absorption arising from the acceptor material, i.e., fullerene phases,[45,46] establishing the use of fullerene derivatives with a stronger absorption such as $PC_{71}BM$.[47] However, the continuously improved photovoltaic performance of BHJ solar cells has been mainly driven by materials research efforts with focus on the development of novel donor materials. The absorption of light is followed by the excitation of an electron from the HOMO to the LUMO level. Due to specific selection rules, the excitation has a resulting spin of zero. Therefore, a so-called singlet exciton is generated. As outlined above, this Frenkel-type excitation is located on one single molecule or on a segment of the polymer chain and exhibits a substantial binding energy exceeding the thermal energy at RT.

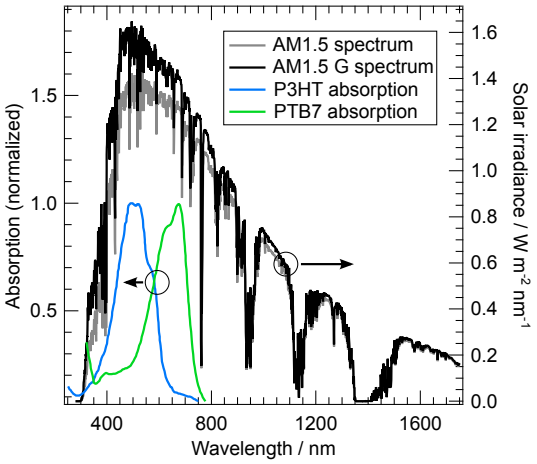

Figure 2.4.: Comparison of the AM1.5 (direct) and AM1.5 G (direct and diffuse reflected) solar irradiance spectra after ASTM G-173 standard (right axis) with the absorption spectra of the polymer P3HT,[48] and the low-bandgap copolymer PTB7 (left axis).[36]

Exciton diffusion and charge transfer (CT): In order to get separated, the exciton has to diffuse towards the D-A interface within its lifetime of around 1 ns,[49–51] corresponding to a diffusion length d_e of about 10 nm. At the heterojunction, excitons get dissociated driven by the offset between the LUMO levels of the donor and the acceptor. However, the initial charge transfer takes place only if energy is gained, i.e., if the energetic offset between the initial and final state is larger than the binding energy of the exciton, E_b^{exc}. It can be assumed that the transfer itself happens on an sub-picosecond timescale.[50,52–55] After charge transfer, the electron and hole reside on adjacent D and A molecules at a small mutual distance. Therefore the charge transfer is not directly tied to the formation of free charge carriers but rather to the formation of a coulombically bound interfacial complex also known as charge transfer complex (CTC) or polaron pair. If the exciton fails to reach the heterojunction within its lifetime, i.e, if the typical size of neat D and A phases exceeds d_e, it usually decays radiatively in form of photoluminescence (PL). As a consequence, the singlet emission of D-A systems provides information about the size of the individual domains. An additional loss mechanism is the transition of the singlet exciton to a triplet state which is known as intersystem crossing (ISC). It must be emphasized that the terms polaron pair and polaron are commonly used in organic photovoltaics to describe bound e-h pairs and free charges, respectively. The terms are based on the general concept of a polaron, which is used in condensed matter physics to describe the interaction of a charge and the correlated distortion of the charge's environment.

Polaron pair dissociation and geminate recombination: Since the binding energy of the interfacial polaron pair, E_b^{pp}, is typically larger than the thermal energy at RT (Section 3.1.2), the separation of the bound electron-hole pair requires the presence of an additional driving force. Although the polaron pair dissociation is one of the most crucial steps in the photocurrent generation of BHJ solar cells, the detailed mechanism explaining the high yield of free charge carrier generation has not yet been clarified in any detail. In this context, several scenarios

were asserted, e.g., a field assisted photogeneration and the dissociation via non-relaxed or fully thermalized charge transfer states (CTS).[56–61] These different concepts will be discussed in Section 3.1. If a polaron pair is not separated, it recombines nonradiatively or radiatively. The latter is connected with a substantially red shifted PL emission.[62–65] The loss process is known as geminate recombination, since the participating electron and hole originate from the common precursor state. As an additional loss channel, the electron can be transferred to a triplet exciton state of the donor, if the energy of the triplet is lower than the CT state.[66] The process is known as electron back transfer (EBT).

Transport and nongeminate recombination: Once free electrons and holes are generated, they have to be transported through the D-A network on their respective phase in order to reach the electrode and to be extracted. Since organic semiconductors commonly consist of randomly arranged molecules or polymer chains, a strong interaction between adjacent sites is missing. Therefore, charge carriers move by hopping in contrast to the band transport in inorganic, crystalline semiconductors. The transport thus has to be seen as a combination of a temperature assisted process and tunneling between localized states with a certain spatial and energetic disorder. It results in a very slow macroscopic charge carrier mobility μ on the order of 10^{-8} $m^2(Vs)^{-1}$ relative to Si with $\mu \approx 0.1$ $m^2(Vs)^{-1}$ [23]. During their transport, free polarons of opposite charge can meet each other and recombine. This process is called nongeminate, since the participating charges do not originate from the same precursor state. Apart from the recombination of free polarons, spatially or energetically trapped charges have to be considered. A detailed description of charge carrier transport and nongeminate recombination processes as well as a review of underlying theoretical models are given in Section 3.2.

Charge carrier extraction: If free charge carriers reach the respective electrode without recombination, they are extracted. Apart from geminate and nongeminate losses, the voltage dependence of the photocurrent is adversely affected by the collection of charge carriers at the contacts. Imbalanced electron and hole mobilities can cause the accumulation of charges at the electrodes and therefore, a space-charge limited current (SCLC) that reduces photovoltaic performance.[67] In addition, the contacts itself crucially affect the functioning of an organic solar cell. In a working device, electrons are extracted at the cathode and holes at the anode. Thus, the extraction of charge carriers at the opposite electrode corresponds to a leakage current that has to be avoided by blocking layers. In the context of charge extraction, S-shaped current-voltage characteristics have to be mentioned. As shown by numerical modeling, the appearance of S-kinks may result from interfacial dipoles[68,69] or a reduced surface recombination velocity describing the extraction rates of electrons and holes.[70,71] However, a multitude of other effects, e.g., interfacial doping or traps, are debated.[72]

2.2.3. Bulk Heterojunction Morphology

The bulk heterojunction concept itself is both a blessing and a curse. Despite the superior performance of BHJ solar cells as compared to their PHJ complement, the degree of D-A intermixing crucially affects every step of photocurrent generation. In this regard, the ideal active layer morphology entails a compromise between fine and coarse grained domains. Large domains of the neat blend constituents and continuous percolation paths favors the spatial separation and transport of free charge carriers, which might be additionally favored by the presence of crystalline regions. In contrast, a strong D-A intermixing hampers charge carrier mobility, but benefits the exciton dissociation yield. Various possibilities have been found in previous research to improve the photovoltaic performance of both polymer and small-molecule based blends by optimizing the blend microstructure.[11,73–75] Starting on the molecular level, the molecular weight of polymers, i.e., the effective conjugation length, is ascribed an impact on intermolecular ordering and the scale of D-A phase separation. Regarding the blend processing, the chosen fabrication technique itself plays an important role, e.g., certain types of small molecules allow both solution processing and vacuum deposition with a clear difference in PCE. In the case of solution processing, the choice of solvent or the use of solvent additives might affect film formation. Finally, the active layer can be post-processed by solvent annealing, slowing-down film drying, or thermal annealing. The success of each concept depends to a large extent on the respective BHJ composite, which is exemplified by four prominent polymer:fullerene compounds below. Furthermore, the understanding of the effect of an altered morphology on device physics is one of the crucial—if not the most important—key aspect for the further improvement of state-of-the-art organic solar cells.

As most prominent example, the PCE of P3HT:[6,6]-phenyl-C_{61}-butyric acid methyl ester ($PC_{61}BM$) solar cells can be enhanced up to typically 3-4 % by thermal annealing after spin-casting,[76] e.g., at around 130 °C for several minutes. The optimum performance of annealed blends with a blend ratio of 1:0.8 to 1:1 is believed to result mainly from an enhanced absorption and better transport properties due to both an improved phase segregation as well as polymer crystallization.[11,77,78] An increase in $PC_{61}BM$ loading beyond 50 % in turn adversely affects the crystallinity of P3HT phases and thus limits the hole mobility.[79,80] Another material for which thermal annealing increases the molecular order is poly(2,5-bis(3-alkylthiophene-2-yl)thieno[3,2-b]thiophene) (pBTTT). Blended with $PC_{61}BM$, intercalated phases are formed upon annealing, i.e., fullerene molecules fill the sites between linear side chains (Figure 5.1b).[81,82] However, in contrast to P3HT:$PC_{61}BM$, the increase in fullerene loading beyond one molecule per pBTTT monomer up to a ratio of 1:4 results in a maximum PCE exceeding the performance of 1:1 pBTTT:$PC_{61}BM$ blends and non-intercalated blends of the bis-adduct bis$PC_{61}BM$. The increased efficiency is ascribed to both an efficient dissociation of excitons within the intercalated phase and an improved spatial separation and transport of charge carriers due to the formation of pure fullerene domains.[81,83,84]

In analogy to the thermal annealing of P3HT:$PC_{61}BM$ blends, the performance of devices based on low-bandgap copolymers is commonly improved by the use of small amounts of sol-

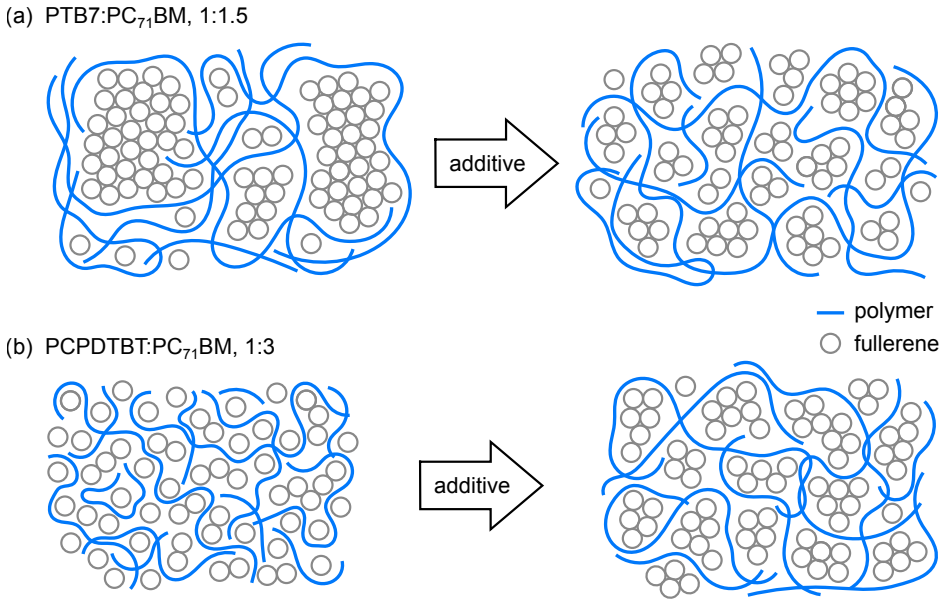

Figure 2.5.: Schematic illustration of the contrary effect of the alkanedithiol processing additives DIO and ODT on the microstructure of **(a)** PTB7:PC_{71}BM and **(b)** PCPDTBT:PC_{71}BM blends (modified from References 85 and 86). In the first case, the solvent additive results in a reduced size of large fullerene domains. In the latter case, the formation of a larger scale phase segregation is reported.

vent additives, e.g., 1,8-octanedithiol (ODT) or 1,8-diiodooctane (DIO).[87] The additive generally acts as a cosolvent, i.e., it is added in small amounts to the blend solution from which the active layers are cast and increases the dissolving power of the fullerene component. Due to the additive's typical low volatility and selective solubility, its use results in an increased mobility of one blend constituent during film formation and thus, a slowed-down precipitation causing a significantly altered D-A intermixing relative to the blend processed without additive. Perhaps the most well-known example of a low-bandgap copolymer processed by the use of DIO is PTB7. Already in the first publication, Liang et al. report on the increase in PCE of PTB7:PC_{71}BM devices from 3.9 % to 7.4 % upon the use of DIO.[36] In subsequent studies, the photovoltaic performance could be raised up to 9.2 %.[37–40] The outperforming efficiency of devices processed by the use of DIO is generally linked with the reduced size of fullerene aggregates resulting in an overall enhanced D-A intermixing (Figure 2.5a) and thus a more efficient polaron pair dissociation (Chapter 6).[85,88–93] Prior to PTB7, a PCE increased from 2.8 % to 5.5 % upon the use of ODT was reported for poly[2,6-(4,4-bis-(2-ethylhexyl)-4H-cyclopenta[2,1-b;3,4-b']-dithiophene)-alt-4,7-(2,1,3-benzothiadiazole)] (PCPDTBT) as the first promising candidate of low-bandgap copolymers.[43,44] Again, the superior efficiency is ascribed to an optimized microstructure of PCPDTBT:PC_{71}BM blends processed with the additive. However, as compared to PTB7, PCPDTBT:PC_{71}BM shows the contrary trend of larger interconnected domains (Figure 2.5b).[86] The altered blend morphology is related to an enhanced generation efficiency and lifetime of mobile charge carriers as well as a three-fold increase in mobility.[94–96] In this regard, a similar effect as caused by the use of ODT is reported for the substitution of the bridging carbon atom in PCPDTBT by Si that yields the polysilole

poly[(4,40-bis(2-thylhexyl)dithieno[3,2-b:20,30-d]silole)-2,6-diyl-alt-(4,7-bis(2-thienyl)-2,1,3-benzothiadiazole)-5,50-diyl] (Si-PCPDTBT).[97,98] The PCE of Si-PCPDTBT:$PC_{71}BM$ solar cells beyond 5 % is achieved without any post-deposition treatment. The fact again manifests the high sensitivity of the blend morphology and the correlated device physics to even smallest changes of the blend constituents on the molecular level.

2.3. Current Voltage Characterization and Photovoltaic Performance

The most important information about the functionality of a solar cell is provided by the voltage dependence of the photocurrent, i.e., the current-voltage (j-V) characteristics. Figure 2.6a shows the j-V characteristics of an organic BHJ solar cell measured in the dark and under illumination. Based on the j-V characteristics, the photovoltaic parameters short circuit current density j_{sc}, open circuit voltage V_{oc} and fill factor (FF) are determined. The FF is defined as the ratio of the product of j_{sc} and V_{oc}, and the maximum power of the device that is provided at the turning point of the power density $j(V) \cdot V$ (Figure 2.6a, green line). Thus, the FF describes the "squareness" of the j-V curve. The photovoltaic parameters yield the power conversion efficiency (PCE) of a photovoltaic device, defined by

$$\mathrm{PCE} = \frac{j_{sc} V_{oc} \mathrm{FF}}{P_L} \quad , \tag{2.1}$$

with the total incident irradiance P_L. The maximum theoretical efficiency for a photovoltaic device of 33 % is given by the Shockley-Queisser limit derived from a detailed balance calculation for inorganic p-n junctions in 1961.[99]

The j-V response of an organic solar cell can approximately be described by the Shockley equation.[99] It was derived for inorganic devices and is given by

$$j(V) = j_0 \left(\exp\left(\frac{q(V - jR_s)}{n_{id} k_B T} \right) - 1 \right) - \frac{V - jR_s}{R_p} - j_{ph} \quad , \tag{2.2}$$

with the ideality factor n_{id} and the photocurrent density j_{ph}. The dark saturation current density j_0 can be related to intrinsic, thermaly activated charge carriers. The series and parallel resistances R_s and R_p account for contact resistance and local shunts, respectively, and provoke a deviation from the exponential behavior of an ideal diode. Figure 2.6b illustrates this divergence in a semilogarithmic representation of the dark j-V characteristics.

The accurate j-V characterization, which is essential for a proper comparison of efficiencies, requires standard reporting conditions (SRC). The SRC for solar cells are given by 25 °C device temperature as well as AM1.5 global (G) reference spectrum and an irradiance of 100 mW cm^{-2} defining P_L.[100] The air mass (AM) coefficient of 1.5 corresponds to the solar irradiance spectrum after passing the atmosphere under a solar zenith angle of $\cos(1/1.5) = 48°$, i.e., for mid-latitudes. The global (G) reference spectrum represents the overall yearly average of both the direct and diffuse solar irradiance. It is important to note that fulfilling SRC is associated with

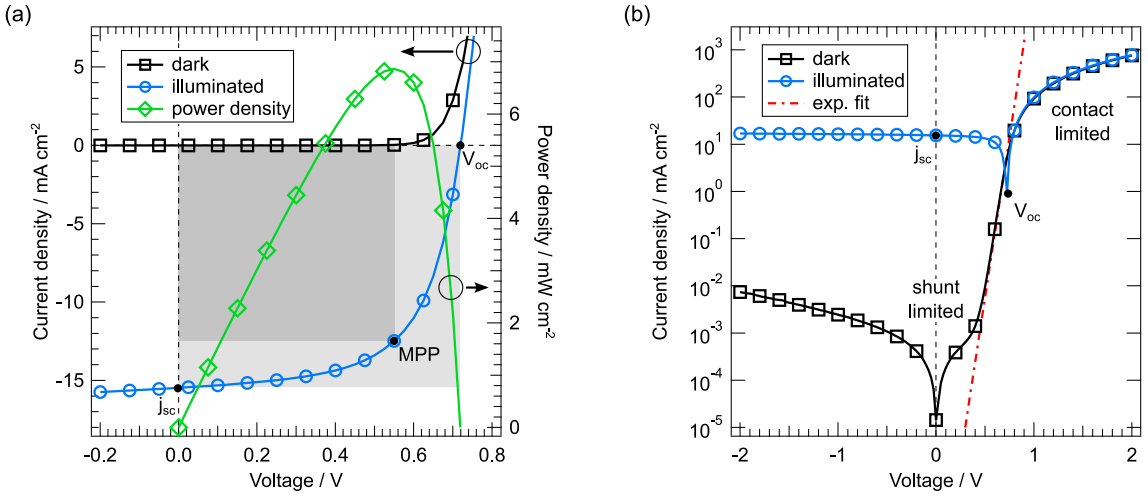

Figure 2.6.: (a) j-V characteristics obtained in the dark and under simulated AM1.5 G conditions (left axis) and power density $j(V) \cdot V$ (right axis) of an organic BHJ solar cell. The photovoltaic parameters j_{sc} and V_{oc} as well as the maximum power point (MPP) are highlighted. The fill factor corresponds to the ratio of $j_{sc} \cdot V_{oc}$ and the maximum power density of the device (shaded areas). **(b)** Dark and illuminated $j(V)$ in semilogarithmic representation illustrating the influence of parallel and series resistance in terms of a deviation from the exponential regime (dash-dotted line).

a calibration procedure of the light source used for simulating sunlight due to the spectral mismatch between reference spectrum and test device. Details concerning the calculation of the spectral correction factor can be found in Reference 100. In case of large variations between the absorption profiles of different test devices, e.g., using P3HT and PTB7 as donor materials (Figure 2.4), this procedure should be repeated for each blend system.

Apart from j-V curves, the spectral response (SR) is an additional, important quantity for characterizing the performance of a solar cell. It is defined by the ratio of j_{sc} and the correlated P_L, both as a function of wavelength. The spectral response is directly correlated to the external quantum efficiency (EQE)

$$\mathrm{EQE}(\lambda) = \frac{hc}{q\lambda}\mathrm{SR}(\lambda) \quad , \tag{2.3}$$

with the Planck constant h, the speed of light c and the elementary charge q. The EQE of a photosensitive device describes the number of photogenerated and extracted charge carriers with respect to the number of incident monochromatic photons. It therefore contains both the absorption of photons as well as all types of losses occurring between exciton generation and the collection of charge carriers at the electrodes. Most commonly, the EQE is measured at short circuit. Additional information regarding the field dependence of free charge carrier formation can be obtained from bias dependent EQE measurements. In contrast to the EQE, the internal quantum efficiency (IQE) measures the ratio between the number of collected charge carriers and the number of absorbed photons of a given energy. Thus, the IQE is always larger than the EQE and describes how efficient photons are converted into extractable charge carriers within the active layer of a solar cell.

3. Main Steps of Photocurrent Generation

The detailed understanding of photocurrent generation in a BHJ solar cell as a sequence of multiple independent steps (Section 2.2.2) is a key aspect in the field of organic photovoltaics. The following chapter addresses this issue and describes the most crucial processes in photon-to-current conversion. More precisely, the first part deals with the formation of charge transfer states at the D-A interface and presents different scenarios for polaron pair dissociation, i.a., addressing the role of non-relaxed and fully thermalized CTS. Furthermore, the field dependence of polaron pair dissociation is highlighted by introducing Braun-Onsager theory. In the second part, the hopping transport of free charge carriers through the D-A interpenetrating network is characterized. This also includes nongeminate recombination of charge carriers on their way to the electrodes, e.g., described by Langevin theory. In analogy to Chapter 2, all processes are described using the example of an electron. The chapter is mostly based on the review articles by Clarke et al. [101] and Deibel et al. [6,102]

3.1. Charge Carrier Photogeneration and Geminate Recombination

3.1.1. Charge Transfer States and Polaron Pair Dissociation

As addressed in Section 2.2.2, the photogeneration in a BHJ solar cell involves a charge transfer taking place at the D-A heterointerface. This CT results in the formation of polaron pairs and requires a further dissociation step in order to obtain free electrons and holes. The separation of polaron pairs is strongly affected by the properties of interfacial charge transfer states, arising from the interaction of the HOMO of the donor and the LUMO of the acceptor. [103] Hence, CT ground and excited states are formed within the energetic gap of the two constituents of the D-A blend (Figure 3.1). The presence of CTS can be evidenced by their weak optical absorption or their radiative relaxation appearing as red shifted PL or electroluminescence (EL). [63–65,104–106]

In addition to the kinetic picture shown in Figure 2.3, the individual steps of photocurrent generation can be understood in an energy state diagram as illustrated in Figure 3.2. After the generation of a singlet exciton S_1, the photoexcitation is transferred to the CTS manifold. This process corresponds to exciton dissociation and polaron pair formation at the interface. Furthermore, the CTS can be populated either by direct optical excitation involving sub-bandgap transitions or by a relaxation from the charge separated state (CSS), i.e., the nongeminate re-

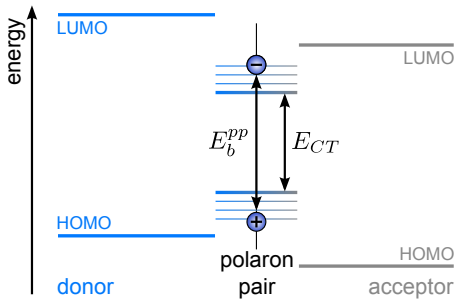

Figure 3.1.: Schematic illustration of the formation of an interfacial CT ground and excited states due to the interaction of the donor HOMO and the acceptor LUMO (modified from Reference 107). The polaron pair binding energy and the energy of the CT ground state are denoted as E_b^{pp} and E_{CT}, respectively.

combination of free charge carriers (Section 3.2). For thermalized polaron pairs occupying the CTS ground level, typical lifetimes of only a few nanoseconds are reported in literature.[108,109] If no transition to the CSS occurs within this time, the polaron pair can decay to the ground state via radiative or nonradiative recombination, or it is transferred to the triplet state T_1 via EBT. The relaxation to the ground state corresponds to the annihilation of opposite polarons at the D-A interface that stem from the same precursor state. As a consequence, this geminate recombination is a 1st order or monomolecular process characterized by a constant lifetime τ. Geminate losses scale linearly with the polaron pair density n_{pp} being proportional to the amount of absorbed photons, i.e., the illumination intensity. The geminate recombination rate R_f is thus given by

$$R_f = \frac{1}{\tau} n_{pp} \quad . \tag{3.1}$$

The formation of polaron pairs is the crucial intermediate step between singlet exciton generation and extraction of free charge carriers. Thus, the properties of the interfacial complex have a strong influence on the efficiency of a BHJ solar cell. Various studies have shown that the maximum value of the open circuit voltage is fundamentally correlated with the energy of the polaron pair.[63,103,110] Furthermore, the fill factor is strongly affected by the field dependence of polaron pair dissociation. Regarding the short circuit current, it was demonstrated that a decrease in j_{sc} is correlated with an increased PL emission arising from polaron pair recombination.[111] On the whole, the generation of free charge carriers via interfacial CTS is of utmost relevance for both V_{oc} as well as the voltage dependent photocurrent.[107]

Although—or rather because—the separation of primary excitations is of major importance for the functioning of an organic solar cell, there is still a dispute about the detailed mechanism of free charge carrier generation.[57,58,60,112,113] As the simplest dissociation pathway, the direct generation of free charge carriers was proposed.[114] In this mechanism, the singlet exciton breaks directly into free polarons without any interaction. From an experimental point of view, this direct pathway cannot be distinguished from the mechanism involving vibrationally and energetically non-relaxed, so-called hot CTS as intermediate step (Figure 3.2, red arrow). In

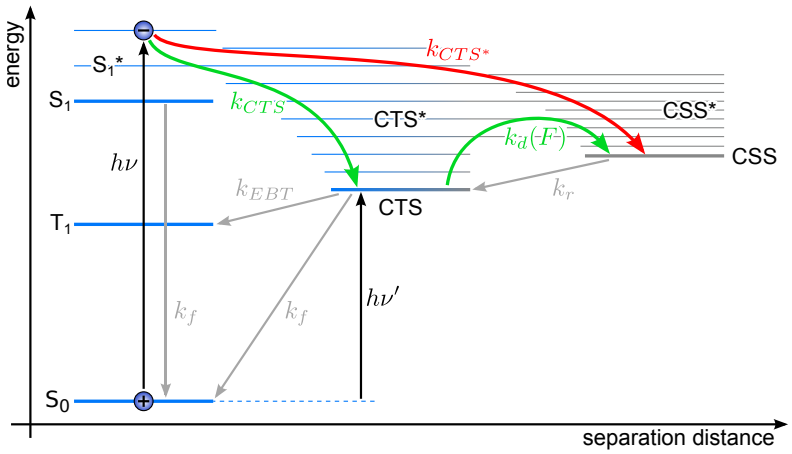

Figure 3.2.: Energy state diagram illustrating the different pathways of free charge carrier photogeneration and the corresponding rate constants (modified from Reference 60 and 101). The donor singlet exciton S_1^* is generated by the absorption of a photon with the energy $h\nu$. The excitation either might be transferred to the CSS via excited CTS* occurring at rate k_{CTS^*}, or vibrationally relax to the lowest energy CTS and subsequently dissociate described by the rate constants k_{CTS} and $k_d(F)$. The latter process is independent of photon energy down to the direct excitation of the CTS manifold with the energy $h\nu'$. Geminate loss mechanisms are given by the recombination of the singlet exciton or the bound polaron pair to the singlet ground state S_0 (k_f) or by electron back transfer to the triplet exciton state T_1 (k_{EBT}). The rate constant k_r describes the formation of a polaron pair as precursor state in a nongeminate recombination process.

this scenario, the separation of an energetically and vibrationally excited polaron pair is much faster than the vibrational relaxation within the CTS manifold.[50,115] Thus, the relaxed CTS will act as trap with an only minor contribution to the overall generation of free charge carriers. In addition, the mechanism suggests a crucial impact of excess energy of the initially formed polaron pair which helps to overcome the Coulomb barrier.[116] This dissociation via hot CT states is accretively questioned in recent publications mainly based on measurements of the IQE revealing a marginal influence of the excitation energy down to the lowest emissive CT level.[57,59,60,117] The observation supports the model of an ultrafast thermal relaxation of the polaron pair to the relaxed CTS that is much faster than the direct separation (Figure 3.2, green arrow). In this scenario, the generation of free charges is exclusively determined by the tradeoff between dissociation and recombination described by the field dependent rate constant $k_d(F)$ and the constant recombination rate k_f, respectively. These processes can be handled in an Braun-Onsager type description, as it will be discussed in the following.

3.1.2. Field Dependence of Polaron Pair Dissociation

The binding energy of a polaron pair, E_b^{pp}, is commonly defined as the potential difference between the two fully separated electrons and holes in their respective D and A material and the thermally relaxed CTS. E_b^{pp} can be estimated using the Coulomb binding energy

$$E_b = \frac{q^2}{4\pi\varepsilon_r\varepsilon_0 a} \quad , \tag{3.2}$$

with the vacuum permittivity ε_0 and the e-h distance a of the thermalized polaron pair. The latter can be estimated by the typical intermolecular distance of about 1 nm between adjacent molecules at the D-A interface. Taking into account a dielectric constant of $\varepsilon_r = 3.5$, Equation 3.2 yields a binding energy of about 400 meV. Furthermore, experimental studies gave evidence for E_b^{pp} of up to 200 meV in MEH-PPV:$PC_{61}BM$ as derived from photoluminescence,[65,105] and about 300 meV in P3HT:$PC_{61}BM$.[66] These values are far beyond $k_B T$ at RT suggesting an only minor probability for an efficient dissociation of polaron pairs into free charge carriers. However, near-unity quantum yields are reported for state-of-the-art BHJ solar cells.[36,118] The observation suggest the presence of an additional driving force, e.g., provided by an applied electric field F. The most commonly applied model to describe the electric field assisted separation of a thermally relaxed polaron pair in BHJ solar cells is the Braun-Onsager model. It goes back to a theory proposed by Onsager describing geminate recombination,[119] based on which Braun founded a macroscopic model characterizing the field dependent photogeneration yield in polymeric D-A systems.[120]

The Onsager theory dates back to 1938 and describes the probability that a coulombically bound pair of opposite ions is separated under the assumption of Brownian motion. In his model, Onsager proposed that the prerequisite for dissociation is that the initially set thermalization length a between the ions exceeds the so-called Onsager radius r_c. The radius is defined by the distance at which the thermal energy equals the Coulomb repulsion yielding

$$r_c = \frac{q^2}{4\pi\varepsilon_r\varepsilon_0 k_B T} \quad . \tag{3.3}$$

In the case $a > r_c$ the ion pair is fully dissociated. On the contrary, if $a \leq r_c$, the probability for separation is given by the escape probability P depending on the applied electric field F (Figure 3.3). The probability for geminate recombination of the ion pair into the ground state is thus given by $1 - P(F)$.

In 1984 Braun adopted the model to describe the dissociation of the lowest CT excited state in low-mobility D-A blends. In contrast to Onsager theory, the CTS was now considered as precursor state with a finite lifetime τ. The kinetics of the CTS dissociation is defined by the rate constants $k_f = 1/\tau$, $k_d(F)$ and k_r describing the geminate recombination of a polaron pair to the ground state, its field dependent dissociation into the CSS, and the possible subsequent formation of a polaron pair, respectively. Figure 3.2 illustrates the rate constants associated with the respective transitions in an energy state diagram. The dissociation probability is given by

$$P(F) = \frac{k_d(F)}{k_d(F) + k_f} \quad . \tag{3.4}$$

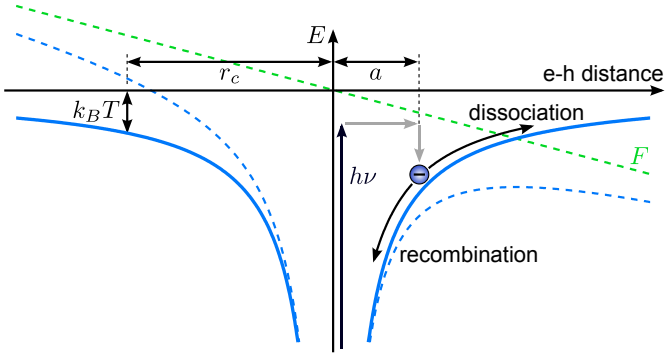

Figure 3.3.: Potential energy of an electron due to Coulomb interaction as a function of the e-h distance (modified from Reference 101). After photoexcitation with the energy $h\nu$, the electron thermalizes at a certain thermalization length a. If a is smaller than the Onsager radius r_c, the polaron pair may either be separated or recombines. Thereby, the presence of an electric field F increases the escape probability $P(F)$ (dashed line).

In contrast to Onsager, the CTS can be recovered from only partially dissociated polarons. Hence, the full dissociation may require several attempts. The field dependent dissociation rate was adopted from Onsager's theory as

$$k_d(F) = \frac{3\gamma}{4\pi a^3} \exp\left(-\frac{E_b}{k_B T}\right)\left(1 + b + \frac{b^2}{3} + \frac{b^3}{18} + \ldots\right) \quad , \tag{3.5}$$

with the factor γ derived from Langevin theory (Equation 3.15), the Coulomb binding energy E_b according to Equation 3.2, and the reduced electric field

$$b = \frac{q^3 F}{8\pi\varepsilon_r\varepsilon_0(k_B T)^2} \quad . \tag{3.6}$$

The series in brackets is the Taylor expansion of the first-order Bessel function. It must be noted that the dissociation probability $P(F)$, i.e., the charge carrier lifetime, is independent of the actual polaron pair density being characteristic for a first-order decay (Equation 3.1).

As already pointed out, E_b^{pp} clearly outstrips the thermal energy at RT. According to Braun-Onsager theory (Equation 3.5), this implies an electric field on the order of 10^7 V m^{-1} for an efficient CTS dissociation. However, such a highly field dependent polaron pair dissociation efficiency is not supported by experimental results for a multitude of material systems. More specifically, optical and electrical techniques demonstrate an almost field independent photocurrent generation and no significant geminate losses for P3HT:PC_{61}BM as well as for PTB7 based devices under working conditions.[92,112,121–123] Additionally, distinct but still moderate geminate losses are reported for poly[[9-(1-octylnonyl)-9H-carbazole-2,7-diyl]-2,5-thiophenediyl-2,1,3-benzothiadiazole-4,7-diyl-2,5-thiophenediyl] (PCDTBT) and PCPDTBT based polymer:fullerene blends.[96,124] Of course, these observations could be related to a direct dissociation or a hot separation pathway (Figure 3.2), however also other explanations can be found in literature. On the one hand, a reduced field dependence might be explained by an interfacial dipolar layer screening Coulomb interactions.[125] On the other hand, Braun-Onsager

theory disregards increased local mobilities as it can be found for both segments of conjugated polymers and fullerene nanocrystals.[126,127] A high local mobility can be correlated with an enhanced delocalization of charge carriers in fullerene domains or along polymer chains.[128,129] The increased separation distance lowers the effective binding energy and leads to a higher dissociation yield. Indeed, a more efficient photogeneration due to the presence of pure fullerene domains was recently claimed using simulations and spectroscopy.[130–133] Although the crucial effect of the phases segregation and the blend morphology on polaron pair dissociation is widely accepted, the detailed understanding of the correlation between both remains incomplete.

3.2. Charge Carrier Transport and Recombination

3.2.1. Hopping Transport and Gaussian Disorder Model

Once free electrons and holes are generated, they are transported to the electrodes in corresponding A and D phases. Thereby, the transport in organic semiconductors is affected by the spatial and energetic disorder of this kind of materials. Typically, the electron wave functions are spatially restricted on a molecular site, on a segment of a polymer chain defined by the conjugation length, or at best on a partially crystalline phase. This localization results in a fast, intramolecular transport within small areas of the bulk, but a rather slow intermolecular hopping transport between only weak interacting sites. The hopping of charge carriers can be understood in terms of a combination of tunneling and a phonon assisted process (Figure 3.4a).[134,135] Accordingly, the transport in organic semiconductors clearly contradicts the quasi free transport of electrons and holes in the respective conduction and valence band of inorganic semiconductors based on a delocalization of the wave function over the whole periodic crystal lattice.

In 1960, Miller and Abrahams proposed the rate ν_{ij} for a hopping between an occupied site i and an unoccupied site j with an energy E_i and E_j.[136] The model is known as variable range hopping (VRH) and originally results from describing the transport in inorganic semiconductors limited by impurities at low temperature. It yields

$$\nu_{ij} = \nu_0 \exp(-\Gamma r_{ij}) \begin{cases} \exp\left(-\frac{E_j - E_i}{k_B T}\right) & , \quad E_j > E_i \quad \text{(uphop)} \\ 1 & , \quad E_j \leq E_i \quad \text{(downhop)} \end{cases} , \tag{3.7}$$

with the maximum hopping rate or so-called attempt-to-escape frequency ν_0, the inverse localization radius Γ that is proportional to the wave function overlap, and the actual distance between the sites r_{ij}. The VRH model therefore explicitly includes the two contributions tunneling and thermal activation by means of the first and the second, Boltzmann-type exponent, respectively. Based on transport processes as described in Equation 3.7, there have been several attempts to determine the charge carrier mobility μ. Correlating the drift velocity of charge carriers and the applied electric field F, μ can be seen as the most important figure of merit describing transport on a macroscopic scale.

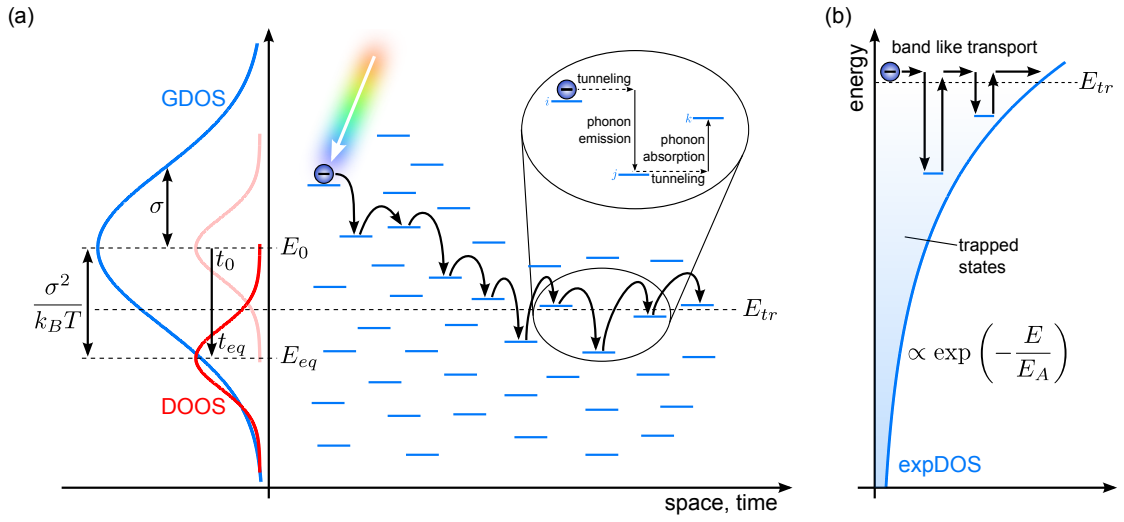

Figure 3.4.: (a) Schematic illustration of the charge carrier hopping in a disordered system. Localized sites are assumed to form a Gaussian distributed DOS with the width 2σ centering at E_0, e.g., representing the LUMO level. After photogeneration, electrons thermalize by hopping to energetically lower sites causing a relaxation of the DOOS to an equilibrium $\sigma^2/(k_B T)$ below the center of the DOS.[137] The hopping between adjacent sites i and j takes place via phonon interaction and tunneling to overcome energy barriers and spatial distance, respectively (modified from Reference 138). **(b)** In the MTR approach, a band-like transport of free charge carriers n_c is assumed above E_{tr}. Immobile charges n_t are trapped in tail states that is approximated by an expDOS characterized by the slope E_A. To participate to the transport, immobile charges have to be thermally activated above E_{tr}.

In the famous Gaussian disorder model (GDM), Bässler directly uses the Miller-Abrahams hopping rate in a Monte Carlo simulation study, yielding the field and temperature dependence of μ according to

$$\mu_{GDM}(T,F) = \mu_0 \exp\left(-\frac{4}{9}\hat{\sigma}^2\right) \exp\left(C\left(\hat{\sigma}^2 - \Sigma^2\right) F^{1/2}\right) \quad , \tag{3.8}$$

with the scaling factor C.[137] The equation was derived for the case of a Gaussian density of states distribution (GDOS)

$$g_G(E) \propto \exp\left(-\frac{(E-E_0)^2}{2\sigma^2}\right) \quad , \tag{3.9}$$

centered around the energy E_0, which is commonly assumed for disordered systems based on absorption measurements. In his model, Bässler used a GDOS to describe both the energetic and spatial distribution of localized states independent from each other. Therefore, $\hat{\sigma} = \sigma/(k_B T)$ and Σ were introduced as energetic and spatial disorder parameters, respectively. Equation 3.8 resembles the experimental observation of a Poole-Frenkel type field dependence according to $\ln\mu \propto F^{1/2}$, whereas the actual slope depends on the interplay between energetic and spatial disorder. In addition, the approach describes a thermally activated transport following $\ln\mu \propto -1/T^2$.[137,139] This proportionality differs from inorganic, crystalline materials that typically show a characteristic temperature dependence of $\mu \propto T^{3/2}$ at low T and $\mu \propto T^{-3/2}$

at high T.[12] It must be noted that the temperature dependence of μ derived for disordered materials varies with the assumed shape of the density of states (DOS). For example, the use of an exponential tail of the DOS results in an only weak temperature dependence $\ln\mu \propto -1/T$. Since the actual shape of the DOS in organic systems is hard to determine, often a combination of both a GDOS and an exponential density of states (expDOS) was suggested.[140,141]

In addition to the GDM, the charge carrier transport in disordered systems can be characterized based on the concept of transport energy. It was developed first for a pure expDOS

$$g_{exp}(E) \propto \exp\left(-\frac{E}{E_A}\right) \quad , \tag{3.10}$$

with the tail slope energy E_A, commonly used to describe localized tail states in inorganic disordered semiconductors.[142] Later, the model was extended to systems with a GDOS (Equation 3.9) with the aim of describing disordered organic materials.[135,143,144] According to Equation 3.7, downhops are more likely than uphops. This implies the thermalization of photogenerated polarons to energetically low, unoccupied states until the density of occupied states (DOOS) reaches a thermal equilibrium value E_{eq} (Figure 3.4a). In the thermalized system, charge carrier transport takes place by hopping at the transport energy E_{tr} where uphops and downhops are balanced. Below E_{tr}, charge carriers are immobile. Thus, the total charge carrier density n can be divided into the density of mobile charges n_c and trapped charges n_t that are captured in the tail of the DOS.[145] The concept is useful to describe transport in organic semiconductors in analogy to band transport. If a charge carrier relaxes below E_{tr}, it has to be thermally activated above E_{tr} in order to contribute to the transport again. The hopping processes above and below E_{tr} resembles multiple trapping and release (MTR) processes as illustrated in Figure 3.4b. It must be emphasized that both the GDM as well as the MTR approach characterize charge carrier transport in single materials. Due to the enhanced spatial disorder introduced by the interpenetrating D-A network and the presence of distinct percolation paths (Section 2.2.2), transport processes in BHJ solar cells are even more complicated to describe.

3.2.2. Nongeminate Recombination

During the transport of photogenerated or injected polarons to the respective electrodes, electrons and holes originating from a different precursor state can meet each other and recombine at the D-A interface in a nongeminate process (Section 2.2.2). The recombination does not take place directly but via the formation of a bound polaron pair as an intermediate step with a certain probability of being dissociated again (Equation 3.4). The dynamics of free charge carriers in a BHJ solar cell can be described by the continuity equation

$$\frac{\mathrm{d}n}{\mathrm{d}t} = -\frac{1}{q}\frac{\mathrm{d}j_n}{\mathrm{d}x} + G - R \quad , \tag{3.11}$$

with the spatial derivative of the current $\mathrm{d}j_n/\mathrm{d}x$, the optical generation rate G of free charge carriers, and the recombination rate R. The latter is commonly expressed as

$$R = k_{rec}\left(np - n_0 p_0\right) \quad , \tag{3.12}$$

with the nongeminate recombination coefficient k_{rec} and the intrinsic density of electrons n_0 and holes p_0. The recombination rate in Equation 3.12 is proportional to the product of the density of free electrons and holes making it a bimolecular process. In contrast to geminate processes (Equation 3.1), this implies an efficient, n-dependent charge carrier lifetime τ_{eff} according to

$$\tau_{eff}(n) = \frac{1}{k_{rec} n} \quad . \tag{3.13}$$

A widely-used model to characterize the recombination of free polarons in BHJ solar cells is Langevin theory.[146] The model was introduced in 1903 and describes the recombination of oppositely charged ions in a homogeneous distributed reservoir. Its application is justified for organic semiconductors due to their low charge carrier mobility below 10^{-4} $\mathrm{m}^2(\mathrm{Vs})^{-1}$.[147] In Langevin theory, the recombination coefficient is typically denoted as γ. It is derived from the assumption that two charge carriers recombine if their thermal energy is less than Coulomb attraction without applying an electric field, i.e., their distance falls below the Onsager radius r_c (Equation 3.3).[15,119] Based on the the rather low ε_r, the condition is highly relevant for organic semiconductors and yields

$$\gamma = \frac{q}{\varepsilon_r \varepsilon_0}(\mu_e + \mu_h) \quad , \tag{3.14}$$

with the sum of electron and hole mobility ($\mu_e + \mu_h$). Thus, Equation 3.14 enters the assumption that the process of finding the respective recombination partner is the rate limiting process and not the recombination process itself. Assuming charge neutrality $n = p$ with $n^2 \gg n_0 p_0$ and balanced electron and hole mobilities $\mu_e = \mu_h$, the Langevin recombination rate is given as

$$R_L = \gamma n^2 = \frac{q}{\varepsilon_r \varepsilon_0}\mu n^2 \quad , \tag{3.15}$$

with the recombination order 2. However, when analyzing the charge carrier decay dynamics in organic BHJ solar cells, deviations from Langevin-type recombination were observed.[148] Complementary charge extraction experiments on annealed P3HT:$PC_{61}BM$ solar cells revealed a recombination rate R which could only partly be explained by Equation 3.15 under the assumption of an additional reduction factor $\zeta = R/R_L$. Instead, best fits of the charge carrier decay dynamics were obtained by the presumption of a third order process $\mathrm{d}n/\mathrm{d}t \propto n^3$.[149,150] This observation established the use of a generalized continuity equation

$$\frac{\mathrm{d}n}{\mathrm{d}t} = -k_\lambda n^{\lambda+1} \quad , \tag{3.16}$$

with the recombination order $\lambda+1$, in order to characterize the recombination dynamics in BHJ solar cells. [151,152] The deviations from Equation 3.15 can be related to the phase separation of D-A blends, since the related spatial separation of charge carriers clearly disagrees the assumptions made in Langevin theory. Though, the origin of a super-second order decay is still highly debated. One famous explanation claims that trapping and release cause a charge carrier dependent mobility $\mu(n)$ that completely accounts for the additional n-dependence of the recombination prefactor in a Langevin-type approach. [153] Alternatively, a recombination limited by the spatial trapping of charge carriers in the presence of phase segregation is suggested. [152] In a recent publication, Rauh et al. showed that the n-dependence of the charge carrier mobility does not solely reproduce the n-dependence of the recombination rate for PTB7:$PC_{71}BM$ and P3HT:$PC_{61}BM$ at and below RT, respectively. Thus, an additional detrapping limited recombination was supposed. However, the result was limited to PTB7 based devices processed by the use of DIO, since a field independent polaron pair dissociation had to be assumed. [92]

Based on the last two sections, it seems reasonable that the generation of photocurrent in a BHJ solar cells, i.e., the photogeneration of free charge carriers as well as their transport and recombination, crucially depends on the D-A intermixing. Thereby, there is still great need for research on a more precise understanding of the connection between the alteration of blend morphology and fundamental processes on the way from light absorption to photocurrent extraction. In the present work, this interrelation is studied for different material systems with the aim of gaining further insights into the complex topic.

4. Experimental

As outlined in Section 2.2, BHJ solar cells are commonly made of either polymers or small molecules as electron donor that are blended with fullerene derivatives as electron acceptor, allowing a wide number of different material combinations. This chapter gives an overview of the D and A constituents used in the present work and summarizes their main properties. In addition, the fabrication of photovoltaic devices is illustrated. The main scope of this work is to study morphological changes of these blends and to understand their effect on device physics. For this purpose, transient charge extraction techniques are applied to working solar cells. The methods are analogue to pump-probe experiments, i.e., an optical excitation is followed by an electronic probe. Particular attention is paid to the technique time delayed collection field (TDCF) in order to probe the electric-field dependence of free charge carrier generation yield as well as open circuit corrected transient charge extraction (OTRACE) yielding information about charge carrier transport and nongeminate recombination dynamics under working conditions of a solar cell. Both methods are described in detail in the following. Furthermore, a brief overview of less frequently used techniques is given.

4.1. Materials

4.1.1. Donor Materials

Starting in the 1920s, polymer science can generally be divided into three time stages giving rise to three generations of polymers. [154] Whereas typical monomer-based donors used in first BHJ solar cells, e.g., MDMO-PPV and P3HT, can be assigned to the second generation of polymers, the development of novel third generation copolymers with a more complex chemical structure was decisive for the significant increase in device efficiency during the last years. Including the thiophene based polymer pBTTT-C_{16} as well as the low-bandgap copolymers PTB7 and PBDTTT-C, this thesis serves both sides of donor materials. In addition, the merocyanine (MC) dye MD376 is used as a member of the class of small molecules. In the following paragraphs, the main structural, electrical and optical properties of the neat materials are characterized.

pBTTT-C_{16}: The repeat unit of poly(2,5-bis(3-alkyl-thiophen-2-yl)-thieno[3,2-b]thiophene) (pBTTT, Figure 4.1a) is formed by two thiophene rings, which are connected by an thieno[3,2-b]thiophene unit. To ensure solubility in organic solvents, a pendant alkane chain, e.g. tetrahexyl ($C_{14}H_{29}$) or hexadecyl ($C_{16}H_{33}$), is attached to each thiophene ring. pBTTT was introduced as promising material for organic electronics due to a high ionization potential and thus

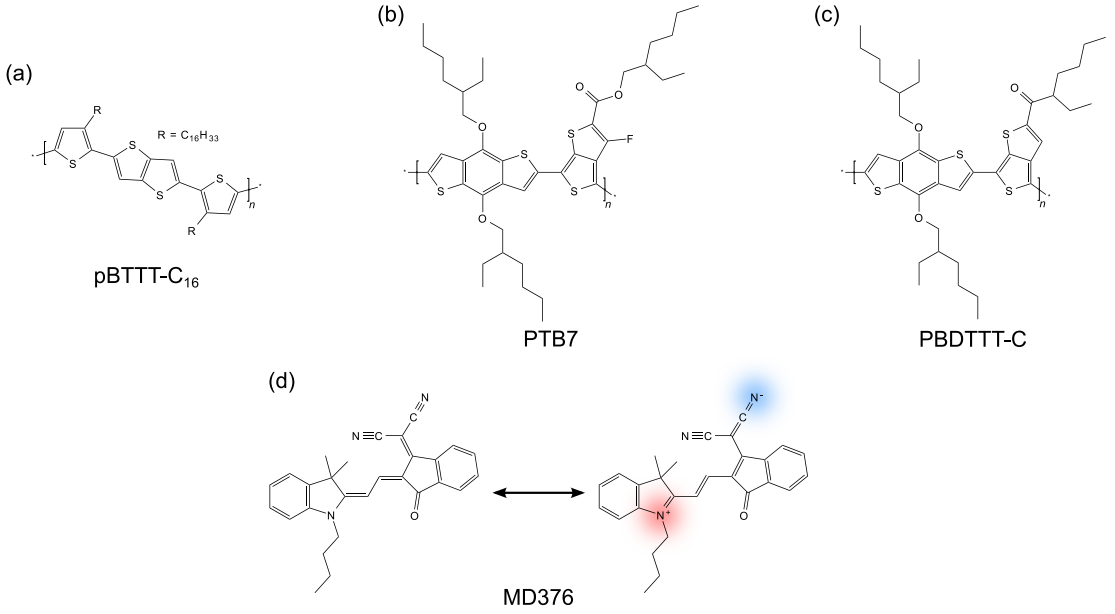

Figure 4.1.: Molecular structure of the polymers **(a)** pBTTT-C_{16}, **(b)** PTB7, **(c)** PBDTTT-C and **(d)** the merocyanine dye MD376, used as electron donating materials in this work. The full chemical names can be found in the main text. In the case of MD376, the polyene-type (left) and zwitterionic (right) resonance structures are shown.

an improved oxidative stability as well as a high field-effect transistor (FET) mobility of up to 0.6 $cm^2/(Vs)$.[155] These superior properties, e.g., as compared to P3HT, are based on the incorporation of the unsubstituted thienothiophene unit into the polymer backbone. This aromatic unit increases the distance of adjacent side chains allowing the interdigitation of polymer chains upon the heat treatment of thin films.[156–160] This self organization of adjacent polymer chains results in the formation of highly ordered and lamellar structured domains (Figure 5.1a) benefitting charge transport. As it will be outlined in more detail in Section 5, the decreased side chain density additionally allows the intercalation of certain acceptor molecules (Figure 5.1b and c). Films of neat pBTTT typically show an absorption in the range of 400 nm to 650 nm. HOMO and LUMO energy levels of -5.1 eV and -3.1 eV, as determined by ultraviolet photoelectron spectroscopy (UPS) and absorption spectra, are reported in literature.[83] In this work, poly(2,5-bis(3-hexyl-thiophen-2-yl)-thieno[3,2-b]thiophene) (pBTTT-C_{16}) is used. The material was synthesized by Martin Heeney's group (Faculty of Natural Sciences, Department of Chemistry, Imperial College London) as described in Reference 156 and showed a molecular weight of M_n = 24,800 g mol^{-1} and M_w = 42,600 g mol^{-1} as measured by gel permeation chromatography (GPC) against polystyrene standards.

Low-bangap copolymers, PTB7 and PBDTTT-C: During the last years, the continuous increase in PCE of state-of-the-art BHJ devices up to peak values beyond 10 %[8] has been mainly driven by the development of novel low-bandgap copolymers, i.e, polymers containing two or more functional repeat units.[161–163] In order to optimize photovoltaic performance, these copolymers are designed to accommodate a variety of requirements. These are: (i) a

wider absorption range realized by a reduced E_g, (ii) HOMO and LUMO levels optimized with respect to the LUMO of the acceptor to increase V_{oc} [164,165] and to achieve a more efficient charge separation, as well as (iii) an extended conjugated system and π-π overlap between polymer backbones facilitating charge transport. [166] A prominent concept to realize this goals are D-A copolymers built up by the combination of an electron rich and an electron deficient building block. It can be assumed that the interaction between these two subunits introduces a local dipole moment causing an intrachain partial charge transfer and reduces CT binding energy in polymer-fullerene mixtures. [167] Apart from fluorine or carbazole based polymers, [168–170] D-A monomers that are built up by the electron rich benzo[1,2-b:4,5-b']dithiophene (BDT) and the electron deficient thieno[3,4-b]thiophene (TT) subunit, form one of the most successful groups of these new materials. It is expected that the use of TT results in a reduced energy gap, whereas the BDT subunit provides a conjugated system and sufficient π-π overlap. [166] As for all D-A copolymers, a further optimization of the interfacial energy level alignment can be realized by the variation of side chains or functional groups, e.g., by fluorination of a subunit. It must be noted that enhancing the absorption range is commonly accompanied with a decrease in the polymer's HOMO-LUMO difference. Therefore, in D-A blends, lowering E_g of the polymer usually reduces both the D-A LUMO offset and the energetic difference between the HOMO level of the donor and the LUMO level of the acceptor diminishing the driving force for efficient exciton dissociation and V_{oc}, respectively. Thus, the development of new donor materials requires a carefully optimized balance between absorption and charge separation. [168]

The copolymer poly[(4,8-bis-(2-ethylhexyloxy)-benzo(1,2-b:4,5-b')dithiophene)-2,6-diyl-alt-(4-(2-ethylhexyl)-3-fluorothieno[3,4-b]thiophene-)-2-carboxylate-2-6-diyl)] (PTB7, Figure 4.1b) was introduced as a member of the systematically synthesized PTB family by Liang et al. [36,171,172] Today it is one of the most successful examples of low-bandgap D-A polymers built up by the combination of BDT and TT subunits. The additional fluorination of the TT building block decreases the HOMO and LUMO levels determined by cyclic voltammetry (CV) to -5.15 eV and -3.31 eV, respectively. PTB7 shows an absorption in the range from 400 nm to 750 nm (Figure 2.4). [36] For this work, the polymer was purchased from 1-material.

The copolymer poly[(4,8-bis-(2-ethylhexyloxy)-benzo(1,2-b:4,5-b')dithiophene)-2,6-diyl-alt-(4-(2-ethylhexanoyl)-thieno[3,4-b]thiophene-)-2-6-diyl)] (PBDTTT-C, Figure 4.1c) was introduced by Chen et al. [173] PBDTTT-C has a molecular structure similar to PTB7 with the difference of a non-fluorinated TT subunit and the 2-ethylhexyl side chain being bound to the TT without bridging oxygen (O) atom. HOMO and LUMO energy levels of -5.12 eV and -3.35 eV are reported in literature. [173] The copolymer shows an absorption similar to that of PTB7. PBDTTT-C used in this work was purchased from Solarmer Materials Inc. having a molecular weight $> 20,000$ g mol^{-1}.

Merocyanine dyes, MD376: Merocyanine (MC) dyes are low-molecular weight colorants which are traditionally used for printing and the coloration of textiles. [174] In recent years, they were successfully introduced for photovoltaic application in both ruthenium-free dye-sensitized solar cells [175] and as donor materials in organic BHJ solar cells. [174,176–178] MC dyes

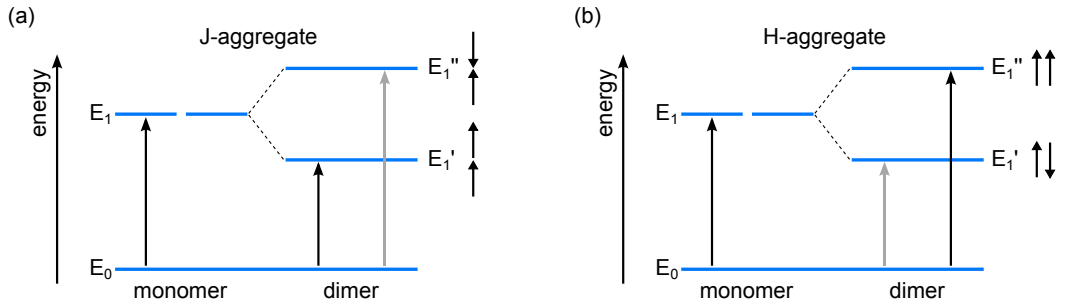

Figure 4.2.: Illustration of the absorption shift due to the interaction of two monomers in dimeric aggregates based on excitonic coupling. The monomeric transition dipoles are represented by small arrows, dipole-allowed and dipole-forbidden transitions by black and grey lines, respectively (modified from Reference 15). **(a)** In J-aggregates, a head-to-tail configuration is energetic favorable as compared to a head-to-head orientation. Since the latter results in a vanishing dimeric dipole moment, the corresponding transition is forbidden causing a red-shifted absorption. **(b)** In the case of H-aggregates, the allowed state corresponds to a parallel alignment of dipoles and is energetically higher, leading to a blue-shifted absorption.

are typically built up by an electron donating and an electron withdrawing moiety, that are connected by a polymethine chain. Depending on the strength of the D and A subunits, an intramolecular CT provokes the presence of a large dipole moment already in the ground state that correlates to an equal contribution of the neutral polyene-type and the so-called zwitterionic resonance structures. Consequently, the large transition moment gives rise to superior absorption coefficients as compared to common polymers and the electronic properties of MC dyes, i.e., the absorption range and HOMO and LUMO levels, can be widely tuned by the variation of the D and A subunits and/or the length of the methine bridge.[179] An increasing acceptor strength is typically related to a shift of the absorption maximum to the NIR region due to a leveling of the C-C bonding lengths, i.e., the π-conjugated system of the polymer approaches the cyanine limit. As a characteristic property of MC dyes, this reduced E_g comes along with low-lying HOMO levels.[176] In the solid film, the bipolarity of MC dyes is partially compensated by a self-assembling of the molecules into physical dimers on the supramolecular level. This formation of molecular aggregates typically involves the change of spectral properties relative to the individual molecule, e.g., the shift of absorption and emission bands or the splitting of spectral lines.[15] It is known in literature that dipolar MC dyes tend to form either so-called J- or H-aggregates in solid films corresponding to either a slipped arrangement or dimeric stacks, both with a parallel arrangement of the dipole moments.[180] Thus, the absorption spectrum is accordingly shifted to longer wavelength (red or bathochromic shift) or to shorter wavelength (blue or hypsochromic shift) relative to the monomer absorption band (Figure 4.2). J- and H-aggregates are additionally characterized by a strong, nearly resonant and an almost vanishing fluorescence, respectively.[181]

The MC dye MD376 is built up from an electron donating indolenine unit with a butyl side chain that is connected by a dimethine chain with a highly electron withdrawing 2-(3-oxo-indan-1-ylidene)-malononitrile acceptor unit. Figure 4.1d shows the polyene-type and the zwitterionic resonance structures of the molecule. HOMO and LUMO energy levels of −5.8 eV

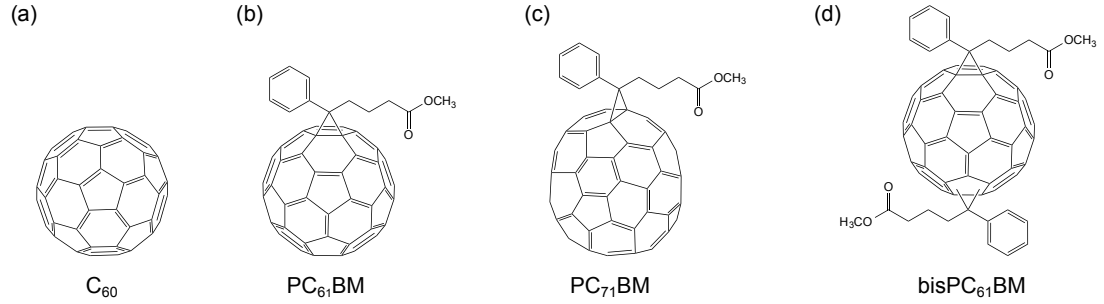

Figure 4.3.: Molecular structure of the electron acceptors **(a)** C_{60}, **(b)** $PC_{61}BM$, **(c)** $PC_{71}BM$, and **(d)** $bisPC_{61}BM$. The full chemical names can be found in the main text.

and −3.7 eV, as derived from CV and absorption spectra, are reported in literature.[174,176] It must be emphasized that the HOMO level is measured for single molecules in solution and might differ from the actual value of solid films due the aforementioned formation of molecular aggregates. MD376 used in this work was synthesized by the group of Prof. Frank Würthner (Organic Materials and Nanosystems Chemistry, University of Würzburg).

4.1.2. Fullerene Acceptors

The discovery of the buckminsterfullerene C_{60} (Figure 4.3a) in 1985 by Kroto and coworkers was honored by the Nobel Price in Chemistry in 1996.[182] Only a few years later, the spherical shaped molecule became widely available for research due to the development of a simplified synthesis process.[183–185] Nowadays, the spherical symmetry, the high electron affinity, and the superior charge carrier mobility make C_{60} and its soluble derivatives the most widely used acceptor material in organic photovoltaics.[52,186–188] Despite an ongoing research on the functionalization of C_{60} as well as on fullerene free acceptors,[188–193] the methanofullerenes $PC_{61}BM$ and $PC_{71}BM$ remain the acceptor molecules of choice for solution based organic solar cells. Their most relevant properties are summarized in the following paragraphs, including the bisadduct $bisPC_{61}BM$.

$PC_{61}BM$: The fullerene derivative [6,6]-phenyl-C_{61}-butyric acid methyl ester (Figure 4.3b) was first synthesized by Hummelen et al. for the use in photodetectors and photodiodes.[194] $PC_{61}BM$ shows a higher solubility in organic, hydrophobic solvents as compared to C_{60} due to the attached substituent. Furthermore, a higher electron mobility of $2{\cdot}10^{-3}$ cm^2 $(Vs)^{-1}$ was derived from SCLC measurements.[195] Reliable HOMO and LUMO energy levels of -5.7 eV and -3.7 eV can be estimated from CV measurements and both the work functions of -6.1 eV and -3.8 eV as well as the optical bandgap of 1.9 eV of C_{60}. Furthermore, it was found that the LUMO level of $PC_{61}BM$ exceeds C_{60} by about 90 meV.[196] The low LUMO energy of $PC_{61}BM$ benefits D-A electron transfer but is associated with an unavoidable energy loss limiting V_{oc} and thus the photovoltaic performance of $PC_{61}BM$ based blends. A further inconvenience arises from the only weak absorption of $PC_{61}BM$ in the solar spectral range based on the high symmetry of the C_{60} cage.

$PC_{71}BM$: In an attempt to increase solar light harvesting, the methanofullerene [6,6]-phenyl-C_{71}-butyric acid methyl ester (Figure 4.3c) was synthesized based on the asymmetric C_{70} buckyball and used by Wienk et al. for the first time.[47] The asymmetry causes the existence of two minor and one major isomers. In combination with the higher molecular weight, it additionally provokes a much stronger absorption in the visible spectral range.[196] $PC_{71}BM$ shows a SCLC electron mobility of $1{\cdot}10^{-3}$ cm^2 $(Vs)^{-1}$ and work functions only marginally changed as compared to $PC_{61}BM$.[188,197] Fullerene synthesis forms a mixture of mostly C_{60}, a small part of C_{70} and smallest shares of higher fullerene compounds. As a result, $PC_{71}BM$ production requires a more difficult purification forcing up prices by a factor of roughly 10 relative to the C_{60} analog.

bis$PC_{61}BM$: As pointed out, a major drawback of PCBM based solar cells is the low LUMO energy level of the fullerene causing an inordinate loss in V_{oc}. However, the synthesis of PCBM also includes fullerene bisadducts, for example bis$PC_{61}BM$ (Figure 4.3d), which can be separated. The second substituent has two significant effects as compared to the respective monoadduct. On the one hand, an increase of about 0.1 eV in the LUMO level can be observed yielding a appropriate increase in V_{oc}.[198] On the other hand, the additional substituent can have a significant effect on the blend microstructure, e.g., as it was deduced from PL and X-ray diffraction (XRD) measurements on P3HT and pBTTT based blends, respectively.[81,199] An non-optimal morphology might also be the origin of a reduced SCLC electron mobility of $7{\cdot}10^{-4}$ cm^2 $(Vs)^{-1}$.[198]

4.2. Device Fabrication

All devices were fabricated in a standard diode architecture as illustrated in Figure 2.2b. A 1.1 mm thick glass substrate was used. It was coated with an about 150 nm thick layer of indium tin oxide (Visiontek Systems Ltd., 15 Ω/sq) as anode. In order to prevent short circuits between both electrodes when contacting the device, the ITO layer was structured in a wet chemical lithography process. The substrates had a size of 12.5 × 12.5 mm^2. Before the actual device fabrication, they were cleaned by consecutive steps using soap water, deionized water and oxygen plasma etching.

In the case of polymer:fullerene blends, a 40 nm thin film of water-based poly(3,4-ethylenedioxythiophene):poly(styrenesulfonate) (PEDOT:PSS, Clevios Al 4083) was spin cast as HTL under ambient conditions. For the following annealing at 130 °C for 10 min and all further steps, the samples were transferred to a nitrogen filled glovebox system. It provided an inert atmosphere with a water and oxygen content below 0.1 ppm. In the case of pBTTT-C_{16} based blends, the active layer was spin cast from 1,2-dichlorobenzene (DCB, Sigma Aldrich Chromasolv®) at 65 °C yielding an active layer thickness d of around 110 nm. The films were annealed at 85 °C for 30 min. PBDTTT-C and PTB7 based blends were spin cast from chlorobenzene (CB, Sigma Aldrich Chromasolv®) at 50 °C resulting in a film thickness in the range of 100 to 120 nm (PBDTTT-C:$PC_{71}BM$) and about 85 nm (PTB7:$PC_{71}BM$). The respective amount of the solvent additive DIO (Sigma Aldrich) was added to the CB solution about 30 min before spin casting.

In the final step, the metal cathode consisting of calcium (Ca) and aluminum (Al) with a layer thickness of about 3 nm and 120 nm was deposited from the gas phase at a base pressure below 10^{-6} mbar and a deposition rate of around 0.2 Ås^{-1} and 2.5 to 6 Ås^{-1}, respectively. The cathode defined an active area of 3 mm^2, unless stated otherwise. This size was chosen in order to minimize resistive-capacitive (RC) limitations in charge extraction measurements (Section 4.3).

Films and devices based on the small molecule MD376 were fabricated by Prof. Klaus Meerholz's group (Organic Nanoelectronics, University of Cologne). A 50 nm layer of molybdenum trioxide (MoO_3) was used as HTL and deposited from the gas phase. MD376:$PC_{61}BM$ blends were spin cast from CB without the use of additives or a subsequent thermal annealing step. In contrast, MD376:C_{60} blends were co-evaporated from the gas phase at a base pressure of about 10^{-8} mbar and a deposition rate of around 0.2 Ås^{-1}. During vacuum deposition, the substrate was kept at room temperature. Both fabrication techniques resulted in a film thickness on the order of 50 nm. In the last step, the metal cathode consisting of Ca and silver (Ag) with a layer thickness of about 3 nm and 100 nm was deposited from the gas phase defining an active area of 3 mm^2.

4.3. Charge Extraction Techniques

4.3.1. Time Delayed Collection Field

As outlined in Section 3.1, the CT dissociation in BHJ solar cells is still not understood in any detail. Thus, a variety of techniques is preferable to gain deep insight into processes arising at the D-A heterointerface. By applying a constant bias voltage to the sample during charge generation, the charge extraction technique time delayed collection field allows to investigate the field dependence of polaron pair dissociation. In addition, by varying the delay time between optical excitation and charge carrier extraction, it is possible to study nongeminate recombination dynamics. TDCF dates back to the work of Mort et al. in 1980, who studied recombination losses in amorphous silicon and chalcogenides.[200–202] Although the method was quickly transferred to phthalocyanine small molecules by Popovic in 1983,[203] first measurements on films of conjugated polymers were performed not until the mid-1990s.[204,205] Today, TDCF is a well established technique in the field of polymer:fullerene BHJ solar cells.[96,112,122,123,206]

Figure 4.4a illustrates the voltage pulse being applied to the sample during a TDCF experiment. Charge carriers are generated by a short laser pulse while a constant pre-bias voltage V_{pre} is applied to the device. After a certain delay time t_d, mobile charge carriers remaining in the device are extracted by a reverse bias rectangular voltage pulse of height V_{col} and length t_{col}. In order to avoid recombination during extraction of photogenerated charge carriers, V_{col} has to be chosen sufficiently high, i.e., in the range of several volts, and t_{col} sufficiently long, in particular in the µs time range at room temperature. TDCF can be used in two different modes. In a pre-bias dependent measurement, V_{pre} is varied from V_{col} to V_{oc} and t_d is kept constant at a small value, typically a few 10 ns. Thus, polaron pair dissociation, i.e., the CTS-CSS transition (Figure 3.2), is more or less forced by the presence of an internal electric field. It can be

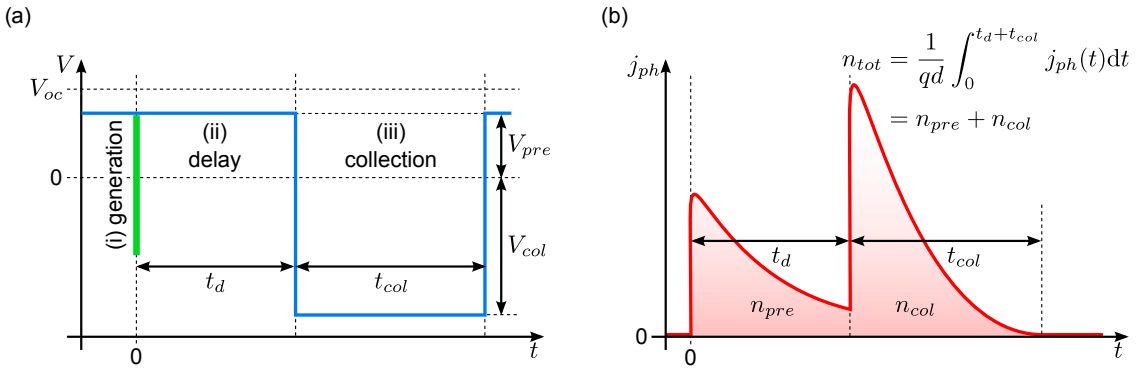

Figure 4.4.: (a) Schematic illustration of the voltage pulse during a TDCF measurement. (i) Charge carriers are generated by a short laser pulse while a constant pre-bias V_{pre} is applied to the device. (ii-iii) After a certain delay time t_d, charge carriers remaining in the device are extracted by a rectangular voltage pulse of the height V_{col} and pulse length t_{col}. **(b)** Schematic illustration of the corresponding photocurrent transient. The total density of extracted charge carriers $n_{tot} = n_{pre} + n_{col}$ is given by adding the integral of the pre-bias peak and the collection peak.

fairly approximated by $F = (V_{bi} - V_{pre})/d$, with the built-in potential V_{bi} and the active layer thickness d. Electron-hole pairs that are not dissociated undergo geminate recombination. If the laser intensity is chosen sufficiently low, nongeminate losses can be ruled out, as it is usually tested in an illumination dependent TDCF measurement prior to the pre-bias dependent study. In the second mode, i.e., delay time dependent measurements, V_{pre} is kept at a constant value, typically close to V_{oc}, in order to approach zero internal electric field and to provide strongest recombination losses. At the same time t_d is varied from the 10 ns to the µs time range. Whereas the amount of extractable charge carriers will be determined only by geminate losses for the shortest delay times, nongeminate recombination will set in with increasing t_d.

TDCF transients $j_{dark}(t)$ recorded without illumination show an initial spike of displacement current starting at t_d due to application of the rectangular collection pulse. This displacement current also overlays the transient $j(t)$ recorded with laser illumination. Thus, in order to obtain the photocurrent transient $j_{ph}(t)$, $j_{dark}(t)$ has to be subtracted from $j(t)$, as it is commonly done in the first step of data evaluation. Figure 4.4b schematically shows $j_{ph}(t)$ that typically consists of two peaks. The first represents the generation of mobile charge carriers on a fast time scale and their extraction by V_{pre}. The second corresponds to charge carriers that survive recombination and are extracted by V_{col}. Conclusions about recombination losses can be drawn by evaluating the integral of $j_{ph}(t)$ observed at a given V_{pre} and t_d:

$$n_{tot} = \frac{1}{qd}\left(\int_0^{t_d} j_{ph}(t)\mathrm{d}t + \int_{t_d}^{t_d+t_p} j_{ph}(t)\mathrm{d}t\right) = n_{pre} + n_{col} \quad . \tag{4.1}$$

The sum of n_{pre} and n_{col} thus equals the total density of photogenerated charge carriers less the ones lost by recombination. [207]

For all TDCF measurements shown in this thesis, the device was mounted under inert atmosphere in a closed cycle optical cryostat (Janis Research). Short laser pulses (< 80 ps) of a neodymium doped yttrium aluminum garnet (Nd:YAG) laser (Ekspla PL2210) with an energy of

2.33 eV and 1.17 eV were used for charge carrier generation. A repetition rate of 5 Hz was chosen to prevent electrical charging of the sample. The laser intensity was varied by a combination of neutral density filters. The TDCF pulse was applied using a arbitrary waveform generator (AWG, Agilent Technologies 81150A). The resulting current transient was measured via the 50 Ω input resistor of a digital storage oscilloscope (Agilent Technologies Infiniium DSO90254A). To circumvent the internal delay of the AWG of around 370 ns, both an electrical output signal of the laser as well as the output of a photodiode were used to trigger the AWG and the oscilloscope, respectively. Limited by the instrumental time constants, a minimum delay time of 10 ns could be realized. For a better signal-to-noise (S/N) ratio, transients were averaged 25 times using the digital storage oscilloscope.

4.3.2. Open Circuit Corrected Transient Charge Extraction

An important figure of merit that characterizes transport and affects recombination in organic solar cells is the charge carrier mobility μ (Section 3.2). Consequently, μ is directly linked to the performance of a photovoltaic device. There are a multitude of techniques to determine μ in organic semiconductors and blend systems under specific measurement conditions, e.g., quantifying μ by a combination of j-V and charge extraction measurements,[117,153] calculating μ from photocurrent transients as measured by time-of-flight (TOF) and TDCF,[96,208,209] or by evaluating space charge limited currents in electron-only and hole-only devices.[210] This work focuses on the determination of the bulk mobility in organic thin film devices based on the charge carrier extraction by linearly increasing voltage (CELIV) technique. CELIV was first introduced by Petravičius et al. in 1975, who studied the drift of holes in crystalline cadmium selenide.[211] In 2000, the technique was used to study transport properties of microcrytalline Si by Juška et al.[212] Since CELIV requires intrinsic charge carriers to be present in the sample, the technique was later refined by generating additional charge carriers using a short laser pulse before extraction (photo-CELIV).[213] Today, photo-CELIV is a widely used technique to study transport and nongeminate recombination in BHJ solar cells.[152,214–218] Although photo-CELIV allows to ascertain μ as well as the charge carrier density n simultaneously, there are major disadvantages, which are being discussed below. In a pioneering work, Baumann et al. recently introduced the novel technique open circuit corrected transient charge extraction[219] that circumvents the drawbacks of CELIV. In the following, both CELIV and OTRACE will be introduced in more detail and methods to determine n and μ from current transients are presented.

The schematic timeline of a photo-CELIV experiment is shown in Figure 4.5a. In a first step, charge carriers are photogenerated by a short laser pulse. To minimize the amount of charge carriers leaving the bulk due to the built-in field V_{bi}, a constant offset voltage V_{off} is applied in forward direction.[215] After a certain delay time t_d, charge carriers remaining in the device are extracted by a reverse bias triangular voltage ramp with the slope $S = V_p / t_p$. With increasing t_d, less charge carriers are extracted due to recombination processes within the active layer.

Figure 4.5b schematically illustrates the electrical response $j(t)$ of the sample to the voltage ramp. It consists of a rectangular current transient due to the capacitive displacement current

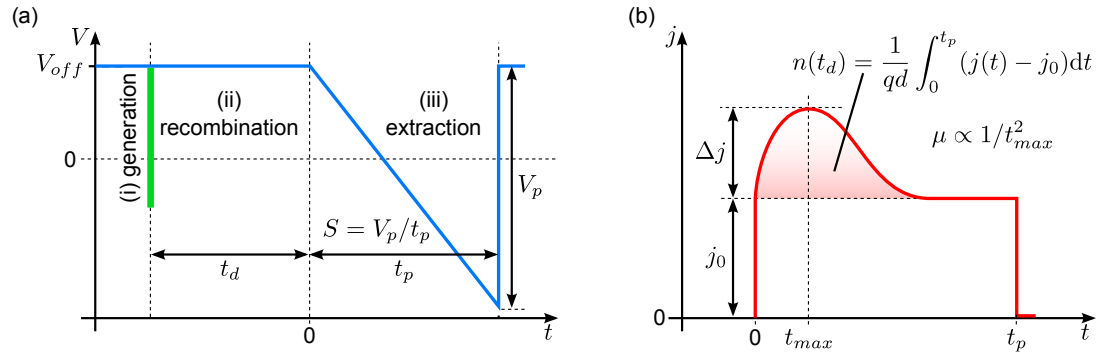

Figure 4.5.: (a) Schematic illustration of the voltage pulse being applied to a solar cell during a photo-CELIV measurement. (i) Charge carriers are generated by a short laser pulse while the device is being kept at a constant bias voltage V_{off}. (ii-iii) After a certain delay time t_d, charge carriers remaining in the device are extracted by a triangular voltage pulse of height V_p and pulse length t_p. **(b)** Schematic illustration of the corresponding current transient. It consists of a rectangular contribution j_0 due to the geometric capacitance of the sample and an extraction peak of the height Δj representing the density of photogenerated charge carriers $n(t_d)$. The square of the maximum peak position t_{max} is inverse proportional to the charge carrier mobility $\mu(t_d)$.

$j_0 = \varepsilon_r \varepsilon_0 S/d$, which is superposed by an extraction peak of height Δj. Since the latter represents photogenerated charge carriers, integrating the photocurrent transient $j(t) - j_0$ yields the charge carriers density n corresponding to a certain t_d:

$$n(t_d) = \frac{1}{dq}\int_0^{t_p}(j(t) - j_0)\mathrm{d}t \quad . \tag{4.2}$$

In contrast to TDCF, it cannot be excluded that charge carriers recombine during their extraction by a linearly increasing voltage ramp. Thus, calculating $n(t_d)$ using Equation 4.2 underestimates n if t_d and t_{max} are in a comparable range, since recombination during extraction is not included.[220] To overcome this issue, n might be evaluated as a function of $(t_d + t_{max})$. However, this approach usually overestimates n. In addition, it is on the expense of temporal resolution.

In order to account for recombination during extraction,[151,221] $n(t_d)$ derived from Equation 4.2 is corrected iteratively in this thesis. For this purpose, the initial charge carrier density $n_{it0}(t_d)$ is calculated by the integral of the OTRACE transients $j_{t_d}(t)$ according to Equation 4.2. Subsequently, regarding the entire range of t_d, the recombination coefficient k_λ, the recombination order $\lambda + 1$, and finally the recombination rate R are calculated from a fit of $n_{it0}(t_d)$ according to the generalized continuity equation (Equation 3.16). Regarding a certain delay time t_d, the number of charge carriers recombining during extraction $n_R(t_d)$ can be derived using $j_{t_d}(t)$ as well as the integral of $\mathrm{d}n/\mathrm{d}t = -k_\lambda n^{\lambda+1}$:

$$n_R(t_d) = \int_0^{t_p} k_\lambda \cdot \left(n_{it0}(t_d) - \frac{1}{q \cdot d}\int_0^t j_{t_d}(t')\,\mathrm{d}t'\right)^{\lambda+1} \mathrm{d}t \quad . \tag{4.3}$$

In the final step, $n_R(t_d)$ and $n_{it0}(t_d)$ are added and the calculation is repeated until convergence is found. Both the charge carrier density n as function of delay time t_d and as function of $t_d + t_{max}$ are compared with the iteratively corrected $n_{corr}(t_d)$ in Figure 6.10b.

The first analytical consideration to obtain the charge carrier mobility μ from (photo-)CELIV transients by evaluating the time t_{max} at which the current transient shows its maximum value was made by Juška et al.[212] Based on an electrostatic approach, the Ricatti-type first order differential equation

$$\frac{\mathrm{d}l(t)}{\mathrm{d}t} + \frac{\sigma}{2\varepsilon_r\varepsilon_0 d} l^2(t) = \frac{\mu S t}{d} \tag{4.4}$$

was found. σ denotes the conductivity of the studied material. Equation 4.4 describes the time dependence of the extraction depth l, yielding an expression of μ for a low and high conductivity approximation that is described by $\Delta j / j_0 \ll 1$ and $\Delta j / j_0 \gg 1$, respectively. For the intermediate case, μ was found to be given by

$$\mu = \frac{2d^2}{3St_{max}^2}\left(1 + 0.36\frac{\Delta j}{j_0}\right) \quad . \tag{4.5}$$

with the numerically estimated correction factor 0.36 accounting for electric field redistribution during extraction.[222] The equation was used in several publications.[213–215,223] Based on a numerical solution of Equation 4.4, Deibel et al. and Bange et al. showed that Equation 4.5 is valid only for small $\Delta j / j_0$ and substantially underestimates μ with an relative deviation increasing with larger $\Delta j / j_0$.[224,225] To get more reliable results, alternative reduction factors were suggested. In 2011, Lorrmann et al. derived a full analytical framework for Equation 4.4 and presented a parametric approach for calculating μ from CELIV transients yielding

$$\mu = \frac{d^2}{2St_{max}^2}\left[\frac{1}{6.2\left(1 + 0.002\frac{\Delta j}{j_0}\right)} + \frac{1}{\left(1 + 0.12\frac{\Delta j}{j_0}\right)}\right]^2 \quad . \tag{4.6}$$

It was shown that Equation 4.6 is valid for all regimes of $\Delta j / j_0$ with a relative error less than 5 %.[226] It must be noted that (photo-)CELIV experiments only provide an effective μ averaged over the mobilities of all extracted charge carriers, mostly determined by the fastest ones.[117] Recently, Hanfland et al. analyzed the reliability of μ as derived from Equation 4.5 by an one-dimensional drift diffusion approach assuming an expDOS (Equation 3.10).[227] It was shown that both an increased trap density and energetic disorder, i.e., an increased tail slope energy E_A, yield a considerable deviation from the average device mobility. In addition, the calculations revealed that the applied increasing voltage itself effects μ due to a field-assisted release of charge carriers from shallow trap states.

As for all transient charge extraction techniques, the time resolution of (photo-)CELIV is limited by the RC delay of the setup, which is primarily given by the geometric capacitance of the device. This RC limitation provokes a shift of t_{max} to longer times yielding an underestimated μ. In photo-CELIV, a constant offset voltage V_{off} is used to prevent photocurrent during and

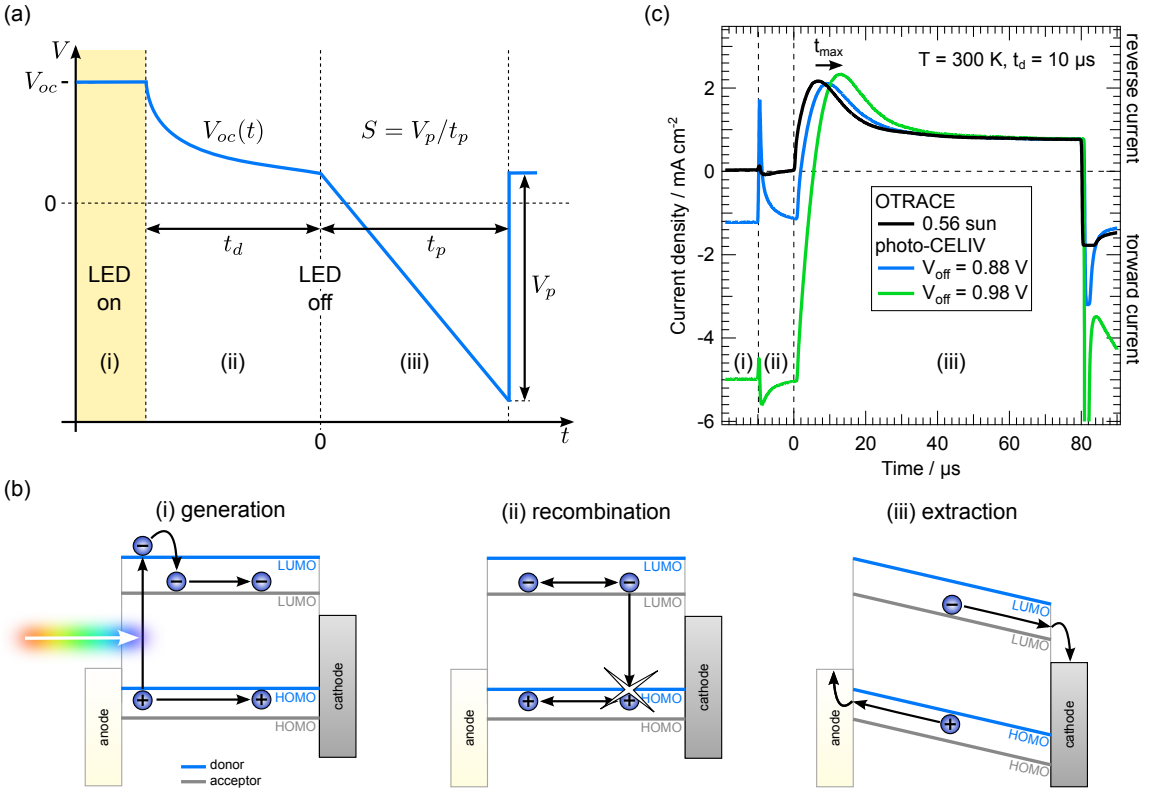

Figure 4.6.: (a) Schematic illustration of the voltage pulse being applied to a solar cell during the OTRACE measurement. (i) In contrast to photo-CELIV, charge carriers are generated by a high power LED. To realize charge carrier generation under steady state conditions, the open circuit voltage V_{oc} corresponding to the respective LED intensity is applied. (ii) After switching off the LED the V_{oc} transient is applied, suppressing any current flow in the external circuit. (iii) After a certain delay time t_d, charge carriers remaining in the device are extracted by a triangular voltage pulse of the slope S, alike in the case of photo-CELIV. **(b)** Energy level diagrams illustrating the charge carrier dynamics during the three time sections of an OTRACE experiment. **(c)** Comparison of the measurement signals derived from photo-CELIV and OTRACE measurements on PCDTBT:$PC_{71}BM$ solar cells (modified from Reference 219). The photo-CELIV signal clearly shows charge carrier injection in forward direction due to the applied bias V_{off} and a shift of the extraction peak t_{max} to longer times.

shortly after the laser pulse. However, a rather high $V_{off} > V_{oc}$ is usually needed for the compensation of the internal field that causes the injection of charge carriers through non-blocking contacts. Consequently, the capacitance of the sample and the RC time are further increased. In addition, injected charge carriers interact with photogenerated ones and disturb their recombination kinetics. In order to overcome these major issues, the novel extraction technique OTRACE accounts for the time dependence of V_{off} after photoexcitaion of charge carriers. Figure 4.6a illustrates the timeline of the OTRACE approach. The major difference as compared to photo-CELIV is that charge carriers are generated under steady state conditions by a white light emitting diode (LED) approaching solar cell operating conditions. In addition, to impede photocurrent during charge carrier generation, the respective V_{oc} is applied to the device. After switching off the LED, the open circuit voltage transient $V_{oc}(t)$ is used as time dependent offset voltage accounting for the open circuit voltage decay (OCVD, Section 4.4) due to recom-

bination.[228] Thus, an effective compensation of photocurrent as well as recombination under zero internal electric field are realized during t_d. Subsequently, charge carriers are extracted by a triangular voltage pulse in accordance to the common CELIV technique. In Figure 4.6b photo-CELIV transients of PCDTBT:$PC_{71}BM$ BHJ solar cells measured at an offset voltage of 0.88 V and 0.98 V are compared with the OTRACE transient obtained under an illumination intensity of 0.56 sun. The photo-CELIV transients clearly show a forward current during t_d due to charge carrier injection. As a consequence, t_{max} is shifted to longer times yielding an underestimated mobility according to Equation 4.6. In contrast, the OTRACE transient is only limited by the intrinsic, geometric capacitance of the device. A more detailed description and comparison of the photo-CELIV and OTRACE techniques can be found in References 147 and 219.

For all OTRACE measurements shown in this thesis, the device was mounted under inert atmosphere in an closed cycle optical cryostat (Janis Research). An array of high power white light emitting diodes (Luxeon Star Rebel LED) was used for illuminating the sample. The LEDs were pulsed at a frequency of 10 Hz for which steady state conditions of an organic solar cell during illumination can be assumed. The illumination intensity was varied between 0.01 and 3.16 sun by the LED current and neutral density filters. In a first step, a 1.5 GΩ input resistance of a voltage amplifier (FEMTO Messtechnik GmbH) was used to record the V_{oc} transient. In a second step, the OTRACE pulse was applied using a arbitrary waveform generator (Agilent Technologies 81150A) allowing a variation of t_d from 100 ns to 10 ms. The resulting current transient was recorded by a digital storage oscilloscope (Agilent Technologies Infiniium DSO90254A) after being amplified by a current-voltage amplifier (FEMTO Messtechnik GmbH DHPCA-100). For a better S/N ratio, transients were averaged 25 times using the digital storage oscilloscope.

4.4. Complementary Methods

In this work, complementary methods for the structural, optical and electrical characterization of organic BHJ thin films and devices were applied in addition to the charge extraction techniques TDCF and OTRACE. Although a detailed description of the individual methods is beyond the scope of this work, the following paragraphs sketch both their basic principle and experimental setup. For the purpose of more detailed informations, the reader is referred to the given references.

X-ray diffraction: XRD is a suitable method to study the molecular structure and crystallinity of neat organic materials or the molecular mixing of polymer:fullerene blends.[229] In an XRD measurement, the sample is irradiated by X-rays with a wavelength λ smaller than the typical length scale of the molecular structure. The observation of diffraction peaks can be intuitively understood from fulfilling the Bragg condition

$$2\delta = n\lambda = 2a\sin(\theta) \quad , \tag{4.7}$$

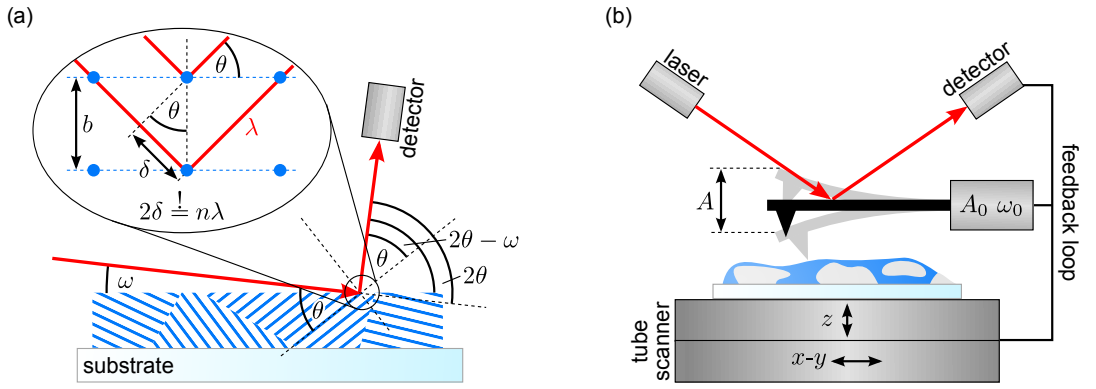

Figure 4.7.: (a) Basic arrangement of a XRD setup in grazing incident mode (modified from Reference 231). The polycrystalline, thin film sample is irradiated by X-rays under the constant angle ω. If the the Bragg condition (Equation 4.7) is fulfilled, a diffraction peak can be observed at an angle $2\theta - \omega$. The inset illustrates the Bragg condition. Rays scattered from adjacent lattice planes will interfere constructively once the angle θ causes a path-length difference which equals an integer multiple of the wavelength λ. **(b)** Schematic illustration of an AFM operating in intermittent contact mode. The cantilever is oscillated with a frequency ω_0 and amplitude A_0. Tapping the surface decreases the the amplitude A of the oscillation down to a setpoint A/A_0. This tip-sample interaction is detected by the reflection of a laser beam and is compensated by adjusting the z-position via a feedback loop.

with the difference δ of the optical path-length, the integer value n, the plane distance a, and the angle of incidence θ. A reflection can be observed once reflected rays from successive lattice planes interfere constructively (Figure 4.7a). Thus, the observed diffraction pattern can be used to reconstruct main features of the molecular structure of the sample. This includes the average size b of crystalline domains. It can be estimated from the line broadening of the diffraction peaks using the Scherrer equation

$$b = \frac{K\lambda}{\Delta_{2\theta}\cos(2\theta/2)} \quad , \tag{4.8}$$

with shape factor K close to unity and the line width $\Delta_{2\theta}$ at half the maximum intensity (full width half maximum, FWHM) after subtracting the instrumental line broadening. For polycrystalline, thin film samples, it is preferable to use a constant grazing angle of incidence in order to illuminate a sufficient and constant volume of the lattice (Figure 4.7a).[230,231]

XRD measurements were performed by Nis Hauke Hansen. Samples were fabricated on glass/ITO/PEDOT substrates as described in Section 4.2 without deposition of the metallic electrodes. The spectra were recorded using copper K_α radiation under grazing incidence in a 3003 T/T XRD setup (General Electric Inspection Technologies).

Atomic force microscopy (AFM): The scanning probe technique AFM can be used in order to gather surface structural information of thin film samples. While raster scanning across the surface of interest, the deflection of a mechanical probe, typically a silicon or silicon nitride cantilever with a sharp tip, is detected by the reflected spot of a laser beam hitting the upper part of the probe (Figure 4.7). In order to prevent collisions of the tip with the surface,

a feedback loop is used keeping the probe sample interaction on a constant level. [232] Nowadays, piezoelectric tube scanners are used, [233] allowing highest resolution on the subnanometer length scale. One of the main AFM operation modes is the so-called intermittent contact (IC) or tapping mode. [234] In IC-AFM the cantilever is oscillated with a frequency ω_0 at or close to its resonance frequency and an amplitude A_0 in the 100 nm range. When the tip is brought into intermittent contact with the sample, tapping the surface decreases the amplitude A of the oscillation. As soon as a predetermined setpoint A/A_0 is reached, the z-position is readjusted to maintain a constant force on the sample. Information about the sample surface are obtained by imaging the z-position as well as the phase of the oscillation relative to the driving signal, both as a function of the tip's lateral position. [235,236]

IC-AFM measurements were performed by the group of Robert Magerle (Chemical Physics, Technical University of Chemnitz). Thin film samples fabricated on glass/ITO/PEDOT substrates without metallic electrodes (Section 4.2) were scanned under ambient conditions using a NanoWizard ll (JPK Instruments AG) and silicon cantilevers (Pointprobe NCH, NanoWorld AG). The typical measurement parameters were a resonance frequency of $\omega_0 \approx 290$ kHz, a free amplitude of $A_0 \approx 60$ nm and an amplitude setpoint of $A/A_0 \approx 0.9$. In order to calculate the root mean square (RMS) roughness of large-area, $10 \times 3.5\ \mu m^2$ height images, JPK Data Processing software (Version 4.3.52) was used.

Photothermal deflection spectroscopy (PDS): PDS is an indirect, high sensitivity pump-probe measurement technique used to determine the optical absorption of a thin film sample. The film is immersed in an inert, non-absorbing deflection medium and gets illuminated by a monochromatic, modulated pump beam. The nonradiative decay of photons absorbed in the film heats up the deflection medium and causes a change of its refractive index that is proportional to the number of absorbed photons. The altered refraction is detected by a second probe beam. [237,238]

PDS measurements were performed by Alberto Salleo's group (Department of Materials Science and Engineering, Stanford University). Thin films of the active polymer:fullerene blends were spin cast on quartz substrates with a film thickness d comparable to working devices (Section 4.2). The samples were immersed in perfluorohexane (C_6F_{14}, 3M Fluorinert FC-72) and illuminated by the focused beam of a monochromated 150 W xenon (Xe) lamp that was mechanically chopped with a frequency of 3.333 Hz. The deflection angle of the probing 1.96 eV helium-neon laser beam was measured using a position-sensitive Si detector in combination with a lock-in amplifier (Stanford Research Systems SR830). PDS was used up to an energy of 1.98 eV. In addition, the absorption coefficient α was determined above an energy of 1.9 eV using an integrating sphere and the approximation

$$\alpha = -\frac{1}{d}\ln\left(\frac{T}{1-R}\right) \quad , \tag{4.9}$$

with the transmission coefficient T and the reflection coefficients R. PDS results were scaled to absolute values by matching the overlapping range between 1.9 eV and 1.98 eV.

Photoluminescence spectroscopy: For PL measurements on polymer:fullerene blends, they were spin cast on glass/PEDOT substrates (Section 4.2). Steady state measurements were performed by Kristofer Tvingstedt. A focused 3.06 eV laser beam was used for excitation. The PL was caught via an edge pass filter (cut-on energy 2.25 eV) and a liquid light guide and spectrally dispersed by a spectrograph (Acton SP2500, Princeton Instruments) fitted with an array of Si detectors. In order to study the decay dynamics of emitting excited states, time-resolved PL (TRPL) spectroscopy was used. The measurements were performed by Björn Gieseking. The output of a frequency doubled titanium-sapphire laser system (Spectra Physics Mai Tai, 100 fs, 1.56 eV) was focused on the sample mounted in a liquid helium cryostat. A fluence of 12 nJ cm^{-2} was used. After spectral dispersion, the PL was detected by a streak camera (Hamamatsu C 5680-22). The setup had a temporal resolution of 18 ps and the detection window was limited to 1.5 ns. A more detailed description of the used TRPL setup can be found in Reference 167.

Transient absorption (TA) spectroscopy: TA spectroscopy is a pump-probe technique to monitor the temporal evolution of non-emitting excitations, for example polarons, in organic semiconductors. A schematic illustration of the interplay of the pump and probe pulse is depicted in Figure 4.8 using the example of a three level system. Since the energy of the probe beam is chosen to be smaller than the energetic difference $E_{|1\rangle-|0\rangle}$ between the levels $|0\rangle$ and $|1\rangle$, no significant absorption is detected without optical excitation of the sample. The additional use of the pump pulse matching $E_{|1\rangle-|0\rangle}$ causes the population of the excited state $|1\rangle$ and thus the partial absorption of the probe pulse, if its energy is chosen to match $E_{|2\rangle-|1\rangle}$. The subsequent relaxation from level $|1\rangle$ to the ground state $|0\rangle$ causes a decrease in the TA signal with increasing delay time t_d between pump and probe pulse. It can be shown that the change in optical density ΔOD of the sample, i.e., the transmitted intensity I as a function of probing wavelength λ and t_d relative to transmitted intensity $I_{ref}(\lambda)$ measured in the absence of the pump pulse, can be written as

$$\Delta OD(\lambda, t_d) = \log_{10}\left(\frac{I_{ref}(\lambda)}{I(\lambda, t_d)}\right) = \frac{\sigma(\lambda)N(t_d)d}{\ln(10)} \quad , \tag{4.10}$$

with the absorption cross section $\sigma(\lambda)$ and the number density of the excited species $N(t_d)$. Therefore, $\Delta OD(\lambda, t_d)$ is directly proportional to the population of level $|1\rangle$ and yields information about the decay dynamics of the probed species. [167]

TA measurements were done by Björn Gieseking. Samples were processed by spin casting polymer:fullerene blends on glass/PEDOT substrates (Section 4.2) and mounted in a liquid helium cryostat. Two optical parametric amplifiers (OPA, Light Conversion TOPAS-C) were pumped by a regenerative amplifier system (Spectra Physics Spitfire Pro, 118 fs, 1 mJ, 1.56 eV). The output of the first OPA was used for pump pulses (110 fs, centered at 2.64 eV) with a fluence of 9.4 μJ cm^{-2}. The output of the second OPA was employed for probing in the infrared (IR) spectral range. The delay time between pump and probe was realized via a motorized linear stage. In order to detect absorption changes only induced by the pump pulse, every second

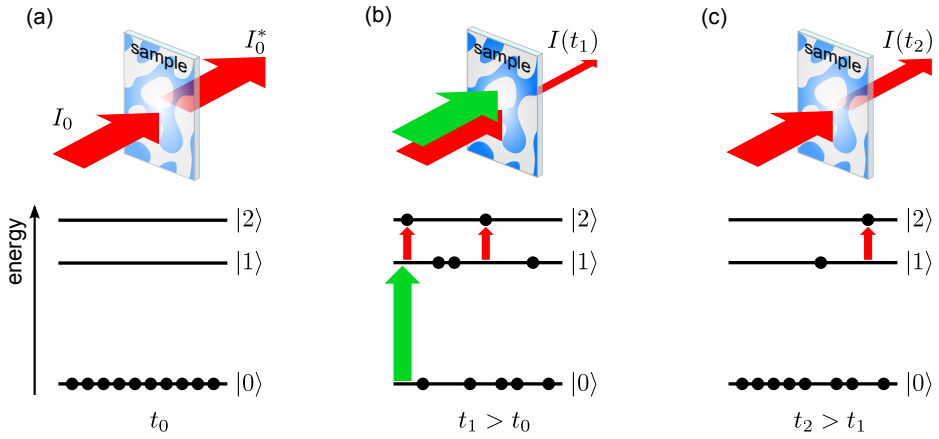

Figure 4.8.: Illustration of the basic principle of TA using the example of a three level system (modified from Reference 167). **(a)** Without optical excitation of the sample, the probe pulse is transmitted with minor absorption losses. **(b)** The excitation of the sample by the pump pulse causes the absorption of the probe beam proportional to the population of the excited state $|1\rangle$. **(c)** The relaxation from $|1\rangle$ to the ground state $|0\rangle$ leads to a weakening of the absorption with the increase in the delay time between pump and probe pulse.

pulse was blocked via an optical chopper. The path of the excitation beam was stabilized by an automated beam alignment system (TEM Messtechnik Aligna). The transmitted intensity of the probe pulses was measured using a nitrogen cooled, pre-amplified photodiode. Before being recorded, the response of the detector for every pulse was integrated using a single channel boxcar. The temporal resolution of the TA setup was in the order of 400 fs as determined by a cross-correlation measurement. A more detailed description of the setup can be found in Reference 167.

Current-voltage characterization: j-V measurements of organic solar cells were conducted under inert atmosphere instantaneously after vacuum deposition of the electrodes. The device was illuminated by an Oriel 1160 AM1.5 G solar simulator with an irradiance calibrated to 100 mW cm^{-2} using a PTB7:$PC_{71}BM$ test device according to Reference 100. A Keithley 237 source measurement unit (SMU) was used for voltage sweeps in forward direction.

Fourier transform photocurrent spectroscopy (FTPS): FTPS allows the fast and highly sensitive measurement of the spectral photocurrent response of a photoconductive sample. The technique was originally introduced for probing subgap absorption phenomena of thin films of hydrogenated microcrystalline silicon.[239] Applied to OPV devices, FTPS has the required sensitivity to probe the low signal photocurrent that arises from the direct excitation of the subgap CT complex.[103,104] The centerpiece of FTPS is a Fourier transform infrared spectrometer (FTIR). It collects actual spectra via the Fourier transform of an interferogram. In particular, it detects the intensity distribution of the light, which is emitted by a NIR source and passed an interferometer, as a function of the variable delay between interfering beams, e.g., in a Michelson interferometer with one movable mirror.[240] In order to obtain the FTPS signal of a photoconductive sample, the device is used as external detector of the FTIR and the obtained

signal is normalized to the response of a second, spectrally independent detector. Compared to dispersive spectrometers using monochromatic light, FTPS has the advantage of a shorter scan time at a higher S/N ratio since all wavelengths are measured simultaneously and the light intensity is not restricted by entrance and exit slits.

In this work, FTPS measurements were performed by the group of Alberto Salleo (Department of Materials Science and Engineering, Stanford University) using the continuous scan (CS) mode.[241] Encapsulated devices were illuminated by via the external light beam output of a FTIR spectrometer (Thermo Electron IS-50R) equipped with a quartz tungsten halogen (QTH) lamp and a quartz beamsplitter. The photocurrent response of the solar cell was amplified by a low noise current pre-amplifier (Stanford Research SR570) and fed back to the external detector port of the FTIR.

Open circuit voltage decay (OCVD): OCVD is a basic approach to study the internal loss mechanisms of a photovoltaic device.[242,243] In an OCVD measurement, the solar cell is connected to the high-impedance input resistance of a voltage amplifier. Charge carriers are generated by pulsed illumination with a repetition rate that has to be set sufficiently low in order to reach steady state conditions. After switching-off illumination, the exclusive pathway for the decay of charge carriers is recombination, since the external current is impeded at all times. This decreasing charge carrier density effects a decay of the open circuit voltage according to

$$V_{oc} = \frac{k_B T}{q} \ln\left(\frac{np}{n_0 p_0}\right) \quad . \tag{4.11}$$

The photovoltage transient can be used to derive a quantity proportional to the recombination coefficient k_{rec} according to the general recombination rate (Equation 3.12). Combining Equation 3.12 and Equation 4.11 results in

$$k_{rec} = -\left(\frac{\mathrm{d}n}{\mathrm{d}t}\right)\left(n^2 - \frac{1}{c}\right)^{-1} \tag{4.12}$$

$$= -c^{1/2}\left[\frac{1}{2V_T}\exp\left(\frac{V_{oc}(t)}{2V_T}\right)\frac{\mathrm{d}}{\mathrm{d}t}V_{oc}(t)\right]\left[\exp\left(\frac{V_{oc}(t)}{V_T}\right) - 1\right]^{-1} \quad , \tag{4.13}$$

with the constant $c = 1/(n_0 p_0)$ and the thermal voltage $V_T = k_B T/q$. It must be emphasized that the time-dependence of V_{oc} implies an n-dependence of k_{rec} and therefore includes a recombination order exceeding two. Recording the voltage transient $V_{oc}(t)$ thus directly yields information about the recombination dynamics of photogenerated charge carriers.

OCVD measurements were performed under inert atmosphere in an closed cycle optical cryostat (Janis Research). For illuminating the sample, an array of high power white light emitting diodes (Luxeon Star Rebel LED) was used allowing to adjust the intensity between 0.01 and 3.16 sun by changing the LED current and using neutral density filters. The LEDs were pulsed at a frequency of 10 Hz. To realize open circuit conditions, a 1.5 GΩ input resistance of a voltage amplifier (FEMTO Messtechnik GmbH) was used. The V_{oc} transient were averaged 25 times and recorded using a digital storage oscilloscope (Agilent Technologies Infiniium DSO90254A).

5. The Effect of Pure Fullerene Domains

Abstract: In order to study the role of intercalated and pure fullerene domains in photogeneration of free charge carriers, TDCF and FTPS are applied on pBTTT-C_{16}:$PC_{61}BM$ solar cells with various blend ratios. The measurements show that the influence of excess energy on photogeneration is subordinate to the influence of an increasing fullerene loading. This causes the formation of pure fullerene domains beyond a blend ratio of 1:1 in addition to an intercalated, bimolecular crystal. The drastically reduced field dependence of photogeneration in a 1:4 pBTTT-C_{16}:$PC_{61}BM$ blend is thus explained by the dissociation of polaron pairs via thermalized charge transfer states favored by an enhanced electron delocalization along spatially extended fullerene domains. Additional TDCF measurements are performed on non-intercalated pBTTT-C_{16}:bis$PC_{61}BM$ devices for a more accurate view of the highly efficient transfer of electrons from the bimolecular crystal into the pure fullerene domains. The measurements reveal a field dependence of free charge carrier generation similar to the 1:4 pBTTT-C_{16}:$PC_{61}BM$ blend. Based on this finding, it is concluded that the presence of pure fullerene domains is the major driving force for an efficient, field independent dissociation of polaron pairs.

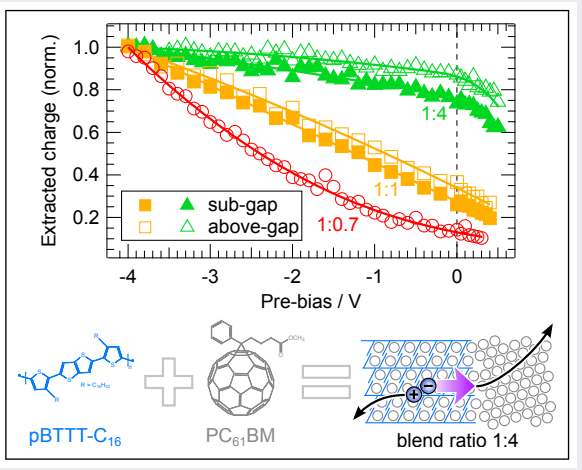

5.1. Introduction

As outlined in Chapter 2 and 3, the precise understanding of the key factors driving an efficient generation of photocurrent in organic BHJ solar cells are still not fully understood. In particular, the influence of excess photon energy on the dissociation of polar pairs, the role of vibrationally and energetically non-relaxed charge transfer states as illustrated in Figure 3.2, and the effect of the active layer morphology are still intensively debated. The aim of the following chapter is to contribute to a clarification of these issues. For this purpose, both field and wavelength dependent TDCF measurements (Section 4.3.1) as well as FTPS using different bias voltages (Section 4.4) were applied to BHJ solar cells based on the polymer pBTTT-C_{16} (Section 4.1). The techniques allow to study the yield of free charge carrier generation in dependence on

the photon energy including the direct excitation into the CTS manifold. Justification for the choice of pBTTT-C_{16} as model system is provided by the easily tunable ratio between mixed and pure phases depending on the acceptor type and fraction (Figure 5.1).[81,84,244] Lamellar structured domains are formed in films of neat pBTTT due to the interdigitation of adjacent side chains. The crystalline phases are characterized by the distance d_{100} between polymer backbones (Figure 5.1a). Blending the polymer with either $PC_{61}BM$ or $PC_{71}BM$ along with one fullerene molecule per pBTTT monomer (50 mol%) results in the intercalation of fullerene molecules in between the polymer side chains and the formation of a so-called bimolecular crystal (BMC),[82] as illustrated in Figure 5.1b. Its structure is stabilized by van der Waals interactions and was recently studied by Miller et al. on a molecular level using XRD, molecular simulations, and spectroscopic methods.[245,246] An increase in PCBM loading beyond 50 mol% provokes the formation of pure fullerene domains adjacent to the BMC, since all sites in between the polymer side chains are occupied. In contrast to PCBM, no BMC but phase segregation of the polymer and the fullerene occurs when choosing the bisadducts bis$PC_{61}BM$ or bis$PC_{71}BM$ (Figure 5.1c). In this case, the formation of pure phases appears not to be affected by the blend ratio. The absence of a BMC in the case of 1:1 pBTTT:bis$PC_{61}BM$ blends causes a superior photovoltaic performance as compared to 1:1 pBTTT:$PC_{61}BM$ blends that is ascribed to reduced recombination losses compensating lower exciton harvesting in segregated phases. The use of a higher fullerene loading in pBTTT-C_{16}:$PC_{61}BM$ blends yields a maximized performance for a mixing ratio of 1:4. It is related to the presence of both an efficient exciton dissociation and an improved transport and spatial separation of charge carriers relative to pBTTT:bis$PC_{61}BM$ and 1:1 pBTTT:$PC_{61}BM$ devices.[81,83,84]

In the present chapter, a systematic tuning of the morphology of pBTTT-C_{16}:$PC_{61}BM$ blends is realized by choosing D-A ratios of 1:0.7, 1:1 and 1:4. These fullerene loadings allow the formation of partially (1:0.7) or almost fully intercalated phases (1:1), the latter with a sufficient linking of BMCs, as well as a morphology displaying the coexistence of both intercalated and pure $PC_{61}BM$ phases (1:4) (Figure 5.1b). Blends using bis$PC_{61}BM$ are processed in the best performing 1:1 mixing ratio (Figure 5.1c). In the following section the structural properties of pBTTT-C_{16} blend films are addressed by using XRD and PDS (Section 4.4). The section is followed by the investigation of the effect of pure fullerene domains on the field dependence of charge carrier generation by TDCF. Finally, the effect of excess photon energy is analyzed by TDCF using sub-gap excitation and complementary FTPS measurements. Both PDS and FTPS measurements and the corresponding data evaluation presented in this section were done by Koen Vandewal (Stanford University). Device preparation and TDCF measurements were done by Benedikt Allendorf. XRD measurements were conducted by Nis Hauke Hansen.

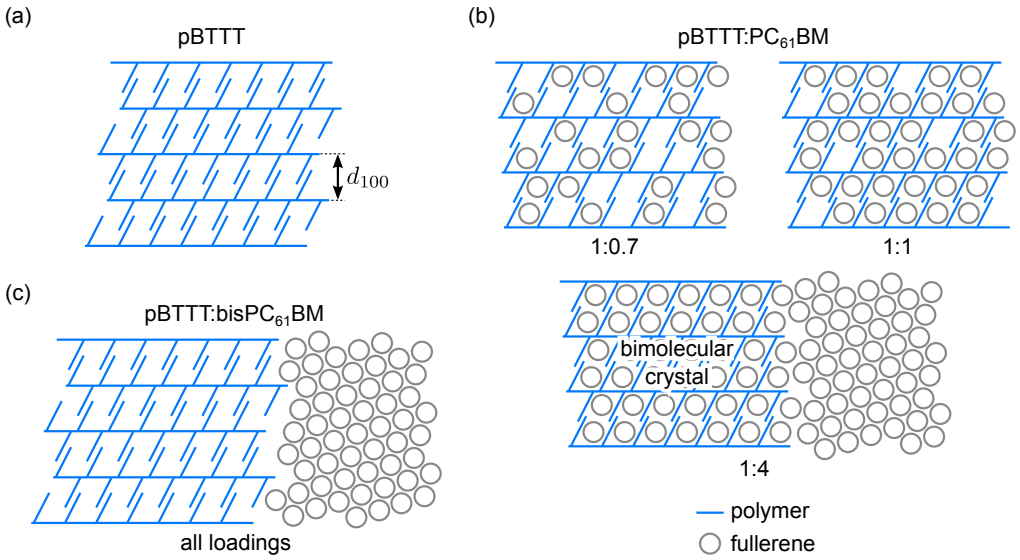

Figure 5.1.: Schematic illustration of the morphologies of pBTTT based blends (modified from Reference 84). **(a)** Throughout a heating and cooling cycle, a lamellar, interdigitated structure of crystalline pBTTT phases is formed. d_{100} denotes the interlamellar spacing between polymer backbones. **(b)** Schematics of the morphology of pBTTT:PC$_{61}$BM blends with varying stoichiometry. Fullerene molecules occupy the sites between adjacent side chains that increase d_{100}. Only partially or almost fully intercalated phases are formed in the case of 1:0.7 and 1:1 blends, respectively. Beyond one PC$_{61}$BM molecule per pBTTT monomer (50 mol%), pure acceptor domains are formed in addition to the bimolecular crystal. **(c)** Using the bisadduct bisPC$_{61}$BM, no intercalation but phase segregation occurs independent of the blend ratio.

5.2. Results

5.2.1. Structural Properties of pBTTT-C$_{16}$ Based Blends

Figure 5.2a shows specular XRD patterns recorded for neat pBTTT-C$_{16}$ films and pBTTT-C$_{16}$ blended with PC$_{61}$BM in a 1:1 and 1:4 ratio. To verify BMC formation, the patterns were fitted by a Gaussian showing a diffraction peak at 0.268 Å^{-1} (neat pBTTT-C$_{16}$) that shifts to about 0.203 Å^{-1} in the 1:1 blend. According to the Bragg condition (Equation 4.7), the diffraction peaks correspond to an increase in the distance between pBTTT-C$_{16}$ chains from d_{100} = 2.34 to 3.10 nm. This expansion of the crystal lattice is in good agreement with d_{100} = 2.35 nm and 3.10 nm for neat pBTTT-C$_{16}$ and pBTTT-C$_{16}$:PC$_{61}$BM, respectively, reported in literature. [81] It demonstrates the intercalation of fullerene molecules in between polymer side chains. The 1:4 blend shows a similar peak shift but a decreased amplitude. The reduced signal height most probably results from the distortion of the BMC domains by the pure fullerene phases. Only a minor shift was found for blends of pBTTT-C$_{16}$:bisPC$_{61}$BM as compared to pBTTT-C$_{16}$:PC$_{61}$BM that is consistent with the segregation of the blend into pure pBTTT-C$_{16}$ and bisPC$_{61}$BM phases. In addition to the interlamellar spacing of the polymer backbones, the evaluation of the FWHM according to the Scherrer equation (Equation 4.8) yields an average size of pure domains and BMC phases of about 20 nm, which is typical for well performing BHJ devices. [5]

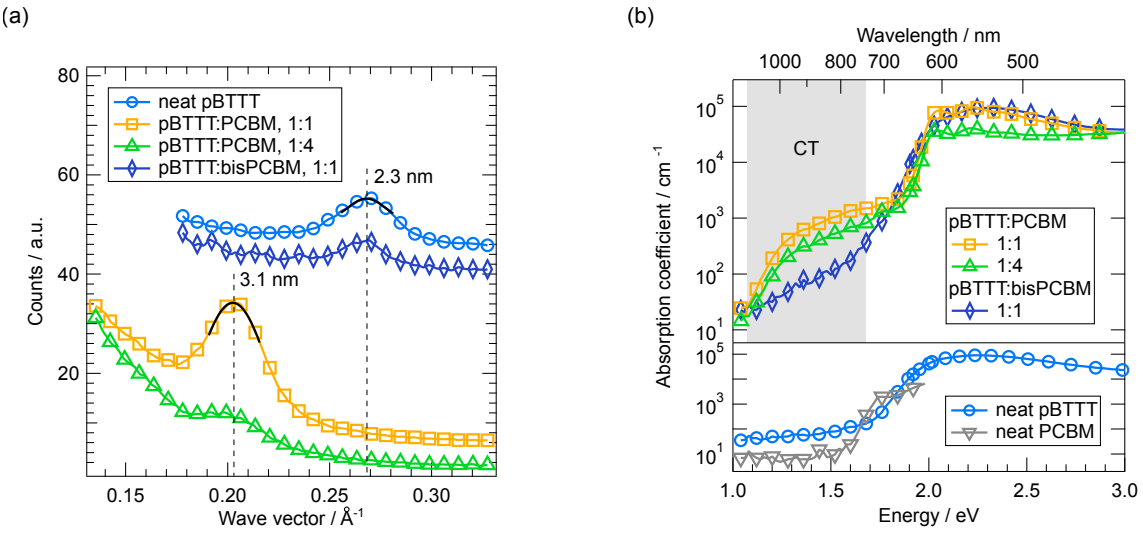

Figure 5.2.: (a) Specular XRD patterns (smoothed) on a neat pBTTT-C_{16} film and on pBTTT-C_{16} based blend films. For the sake of clarity, the curves are vertically offset. The values of the distance d_{100} between polymer chains in the crystal derived from a Gaussian fit (black lines) are assigned to the respective peak positions. **(b)** Absorption coefficient α as measured by PDS of neat pBTTT-C_{16}, neat $PC_{61}BM$, and pBTTT-C_{16}:fullerene films.

Figure 5.2b depicts high sensitivity PDS measurements of the absorption coefficient α as a function of photon energy performed on above films and neat $PC_{61}BM$. The spectra show a pronounced absorption band between 1.1 and 1.9 eV for pBTTT-C_{16}:$PC_{61}BM$. This sub-gap absorption cannot be attributed to the absorption of either of the neat materials and is therefore ascribed to CT complexes formed at the D-A interface in the intercalated phase. [103,107,110] The presence of a BMC is further confirmed by the different strength of the CT absorption regarding both blend ratios. In the 1:4 film, the content of pBTTT-C_{16} is four times lower than in the 1:1 blend. The observation of a weaker CT signature of the 1:4 blend can be explained by the formation of additional $PC_{61}BM$ domains and a decrease in the interfacial area per unit volume. The CT absorption band for pBTTT-C_{16}:bis$PC_{61}BM$ is expected to be strongly reduced in absorption strength, since the interfacial area per unit volume is substantially reduced due to segregated phases relative to intercalated $PC_{61}BM$ based blends. This reduction in density of interfacial polaron pairs perfectly matches with PDS measurements showing that the strength of sub-gap absorption below an energy of 1.65 eV of pBTTT-C_{16}:bis$PC_{61}BM$ is reduced by more than one order of magnitude as compared to pBTTT-C_{16}:$PC_{61}BM$.

5.2.2. Pre-bias Dependent Photogeneration

In order to determine the field dependence of the free charge carrier generation yield, pre-bias dependent TDCF measurements were performed on solar cells made of pBTTT-C_{16}:$PC_{61}BM$ and pBTTT-C_{16}:bis$PC_{61}BM$. Figure 5.3 shows the current-voltage characteristics of the devices, which were chosen as best performing solar cells from a series of several samples each. The j-V curves were measured under a simulated AM1.5 G spectrum and an illumination intensity of 100 mW cm^{-2}. The respective photovoltaic parameters can be found in Table 5.1. A reduced

open circuit voltage of V_{oc} = 335 mV was observed for the 1:0.7 $PC_{61}BM$ device. Furthermore, both the fill factor and the short circuit current density j_{sc} increase with $PC_{61}BM$ content leading to a maximum PCE of 1.8 % of the 1:4 $PC_{61}BM$ device. These results confirm the findings reported in literature.[81,83,84] In order to obtain both an efficient exciton harvesting as well as minor geminate and nongeminate recombination, a significant fraction of pure fullerene phase needs to coexist with the BMC phase. Hence, the bis$PC_{61}BM$ device has its best performance at a lower fullerene loading due to the absence of a BMC. In our case, it reaches a PCE of 0.7 %. Thereby, an increase of about 60 meV in V_{oc} can be ascribed to the higher LUMO level of bis$PC_{61}BM$.[198] The decrease of about a factor of 2.5 in j_{sc}, as compared to the 1:4 $PC_{61}BM$ device and to the value reported in Reference 81, might be ascribed to an incomplete exciton harvesting in a non-ideal microstructure.[199]

	V_{oc} / mV	j_{sc} / mA cm^{-2}	FF / %	PCE / %
pBTTT-C_{16}:$PC_{61}BM$, 1:0.7	335	0.12	27	10^{-3}
pBTTT-C_{16}:$PC_{61}BM$, 1:1	543	1.8	33	0.3
pBTTT-C_{16}:$PC_{61}BM$, 1:4	541	6.6	56	1.8
pBTTT-C_{16}:bis$PC_{61}BM$, 1:1	603	2.3	56	0.7

Table 5.1.: Photovoltaic parameters of pBTTT-C_{16}:$PC_{61}BM$ and pBTTT-C_{16}:bis$PC_{61}BM$ devices obtained from the j-V curves in Figure 5.3.

TDCF measurements were performed on above devices using a pre-bias between -4 V and the respective V_{oc}. Since the laser intensity was adjusted to be in a range showing a linear proportionality between photogeneration and illumination intensity at a pre-bias close to V_{oc} (not shown), nongeminate recombination losses can be excluded. In addition, the intensity was adjusted to reach a similar value of the total extracted charge carrier density n_{tot} at V_{pre} = −4 V for all devices. Both conditions yielded a pulse fluence of 0.1 to 0.4 µJ cm^{-2}. Figure 5.4a shows n_{tot} as a function of V_{pre} derived at a photon energy of 2.33 eV (open symbols), i.e., above the optical gap of the blend components.[83] In order to compare the field dependent photogeneration of the studied devices with each other, n_{tot} was normalized to the maximum value of a polynomial fit (Figure 5.4b). The decrease in n_{tot} with decreasing internal electric field amounts to more than 90 % for the 1:0.7 blend in the studied pre-bias range, implying a strong field dependence of photogeneration that even prevents n_{tot} from reaching a saturation value at -4 V. The pre-bias dependence is slightly weakened to at least 70 % over the same range for the 1:1 blend. Only the presence of pure fullerene domains in the case of the 1:4 blend induces a rather low decrease of 25 % with respect to an apparent saturation level, i.e., relative to the density of initially generated charge carriers. Comparing the field dependence of the two best performing 1:4 pBTTT-C_{16}:$PC_{61}BM$ and 1:1 pBTTT-C_{16}:bis$PC_{61}BM$ blends, a similar behavior for both blends is apparent for a pre-bias in reverse direction. Between 0 V and V_{oc}, the normalized n_{tot} of pBTTT-C_{16}:bis$PC_{61}BM$ exceeds pBTTT-C_{16}:$PC_{61}BM$, which results in an overall field dependence of about 15 % for the bis$PC_{61}BM$ device.

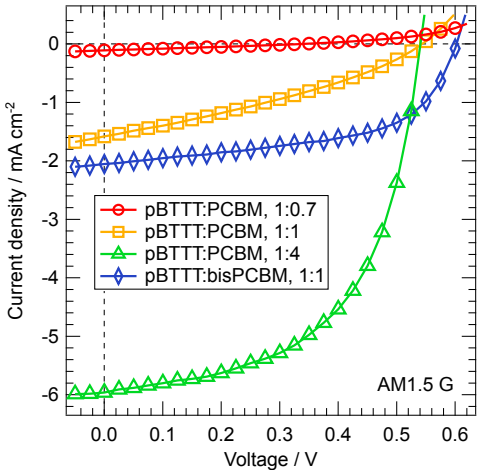

Figure 5.3.: j-V characteristics of pBTTT-C_{16}:$PC_{61}BM$ and pBTTT-C_{16}:bis$PC_{61}BM$ devices obtained under 1 sun illumination intensity and simulated AM1.5 G spectrum. The corresponding photovoltaic parameters can be found in Table 5.1.

The pre-bias dependence of n_{tot} can be ascribed to an increasing dissociation yield at increasing internal fields and thus a field assisted CTS-CSS transition (Figure 3.2).[96,112] Minor differences in the field dependence from -4 to 0 V in the case of the 1:4 pBTTT-C_{16}:$PC_{61}BM$ blend as compared to the pBTTT-C_{16}:bis$PC_{61}BM$ blend (Figure 5.4b, bottom) suggest a polaron pair dissociation only slightly affected by the presence of the intercalated phase. The observation can be understood in terms of an almost complete extraction of electrons out of the BMC into pure fullerene phases. To quantify this finding, the ratio of the two polynomial fits was calculated and denoted as BMC extraction yield (Figure 5.4b, right axis). It can be understood as an upper limit of the extraction efficiency expecting an exclusive CT generation within the BMC without any photogeneration contribution from the boundary in the case of the $PC_{61}BM$ device. The approach is justified due to the fine D-A intermixing within the intercalated phase. At negative pre-bias, the BMC extraction yield is close to unity and decreases to a value of about 83 % close to V_{oc}. This incomplete extraction for $PC_{61}BM$ at vanishing internal fields most probably results from a less efficient polaron pair dissociation due to a hindered delocalization of electrons within the intercalated phase and therefore enhanced recombination losses.[247] Due to the chosen low laser intensity, only geminate processes are expected. However, despite the present losses, the BMC extraction yield demonstrates that the transfer of charge carriers from the BMC into pure domains is still highly efficient close to V_{oc} and that it is only driven to lesser extent by an external voltage. Based on this result, the presence of an intrinsic driving force for charge generation seems reasonable, as discussed below.

It must be emphasized that a better approximation of the extraction efficiency, i.e., taking into account a relative photogeneration contribution δ of the boundary between intermixed and pure $PC_{61}BM$ phases, is given by

$$\text{BMC extraction yield} = \frac{q_{tot}^{norm}(\text{pBTTT:PCBM}) - \delta\, q_{tot}^{norm}(\text{pBTTT:bisPCBM})}{(1-\delta)\, q_{tot}^{norm}(\text{pBTTT:bisPCBM})} \quad , \tag{5.1}$$

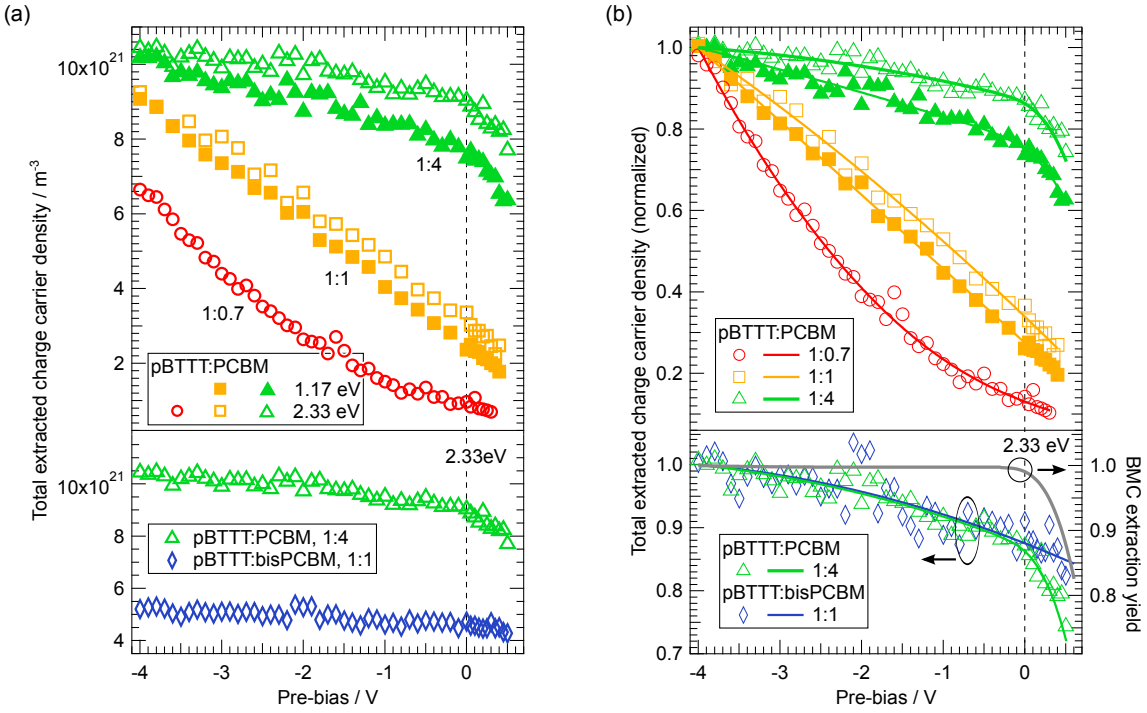

Figure 5.4.: (a) Total extracted charge carrier density n_{tot} as a function of V_{pre} derived from pre-bias dependent TDCF measurements on pBTTT-C_{16}:PC_{61}BM devices with various stoichiometries (top) as well as pBTTT-C_{16}:PC_{61}BM and pBTTT-C_{16}:bisPC_{61}BM devices (bottom). Measurement conditions were t_d = 20 ns, V_{col} = −4 V, and t_{col} = 20 µs. Open (filled) symbols correspond to the data obtained at an excitation energy of 2.33 eV (1.17 eV). **(b)** Extracted charge carrier density n_{tot} (symbols, left axis) normalized to the maximum value of a corresponding polynomial fit (solid lines). The ratio between the 1:4 pBTTT-C_{16}:PC_{61}BM and the pBTTT-C_{16}:bisPC_{61}BM fits is depicted as BMC extraction yield (grey line, right axis).

with the normalized extracted charge carrier density q_{tot}^{norm} of the respective blend. Equation 5.1 was evaluated for δ ranging from 0 to 0.75 in Figure 5.5. Even for an unreasonably high proportion of δ = 0.75, the extraction yield still reaches values close to unity for a pre-bias below 0 V and is strongly reduced only close to V_{oc}. This overall weak dependence of the extraction yield on δ supports the validity of the above assumption.

5.2.3. Wavelength Dependent Photogeneration

To clarify the correlation between fullerene loading and the pre-bias dependence of n_{tot} in pBTTT-C_{16}:PC_{61}BM blends (Figure 5.4, top) and the influence of excess photon energy on the photogeneration, additional TDCF measurements were performed using an excitation energy of 1.17 eV. The energy is about 0.8 eV below the optical gap of pBTTT, allowing the excitation of the CTS manifold as it can be seen from PDS spectra in Figure 5.2b. In analogy to TDCF measurements using an above-gap excitation of 2.33 eV, the laser intensity was chosen in the range of a linearly increasing photocurrent ensuring the absence of nongeminate recombination. In addition, a maximum value of n_{tot} similar to the measurements at 2.33 eV was aspired (Figure 5.4a). Both conditions required an increase in the pulse fluence to about 10 µJ cm^{-2}, which

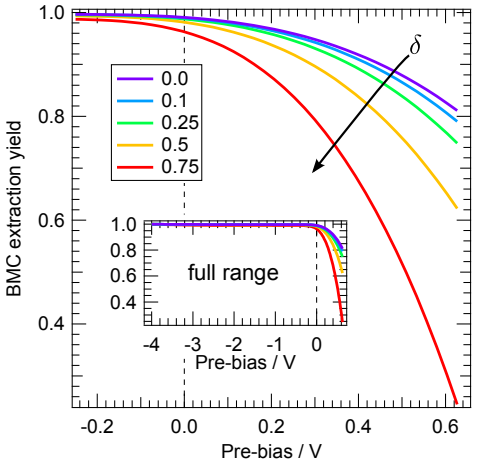

Figure 5.5.: BMC extraction yield according to Equation 5.1 for a relative contribution δ of the boundary ranging from 0 to 0.75. The inset shows the full pre-bias range.

roughly coincides with the ratio of the absorption coefficient α at 1.17 eV and 2.33 eV in Figure 5.2b. The total extracted charge carrier density as well as the normalized n_{tot} obtained for the pBTTT-C_{16}:PC_{61}BM blends are presented in Figure 5.4a and b (filled symbols), respectively. The measurements reveal that the excitation energy, i.e., sub-gap or above-gap excitation, is very weak and subordinate to the variation of the fullerene loading and hence to the alteration of the blend morphology.

In addition to TDCF, high sensitivity measurements of the external quantum efficiency were performed using FTPS at an applied bias voltage between -2.5 and 0.5 V in order to verify the energy independence of the polaron pair dissociation over broad range of excitation energy. In contrast to TDCF, the EQE spectra also involve additional nongeminate losses due to the use of higher light intensities. Figure 5.6a shows the EQE of 1:1 and 1:4 pBTTT-C_{16}:PC_{61}BM devices. To compare both blend ratios, the spectra were normalized to the respective spectrum recorded at -2.5 V (Figure 5.6b). The increase of the bias voltage from -2 to 0.5 V (1:1) and respectively 0.25 V (1:4) results in the decrease in EQE of about two orders of magnitude (1:1) and of only a factor of about 1.5 in the case of the 1:4 blend. At first glance, the EQE spectra normalized to EQE(-2.5 V) appear spectrally flat for all chosen bias voltages. Looking in detail, a slight reduction of the normalized EQE with decreasing photon energy can be found in the CTS absorbing region below 1.5 eV. This reduction is especially pronounced for the 1:4 blend. The insets in Figure 5.6 show the normalized EQE at an energy of 1.17 eV and 2.33 eV as a function of the applied bias voltage. A weaker field dependence was found for the 1:4 blend relative to the 1:1 device. This trend confirms the field dependence visible in TDCF measurements (Figure 5.4b). Comparing TDCF and FTPS results, stronger relative losses with decreasing bias in the case of the EQE spectra most probably result from additional nongeminate recombination.

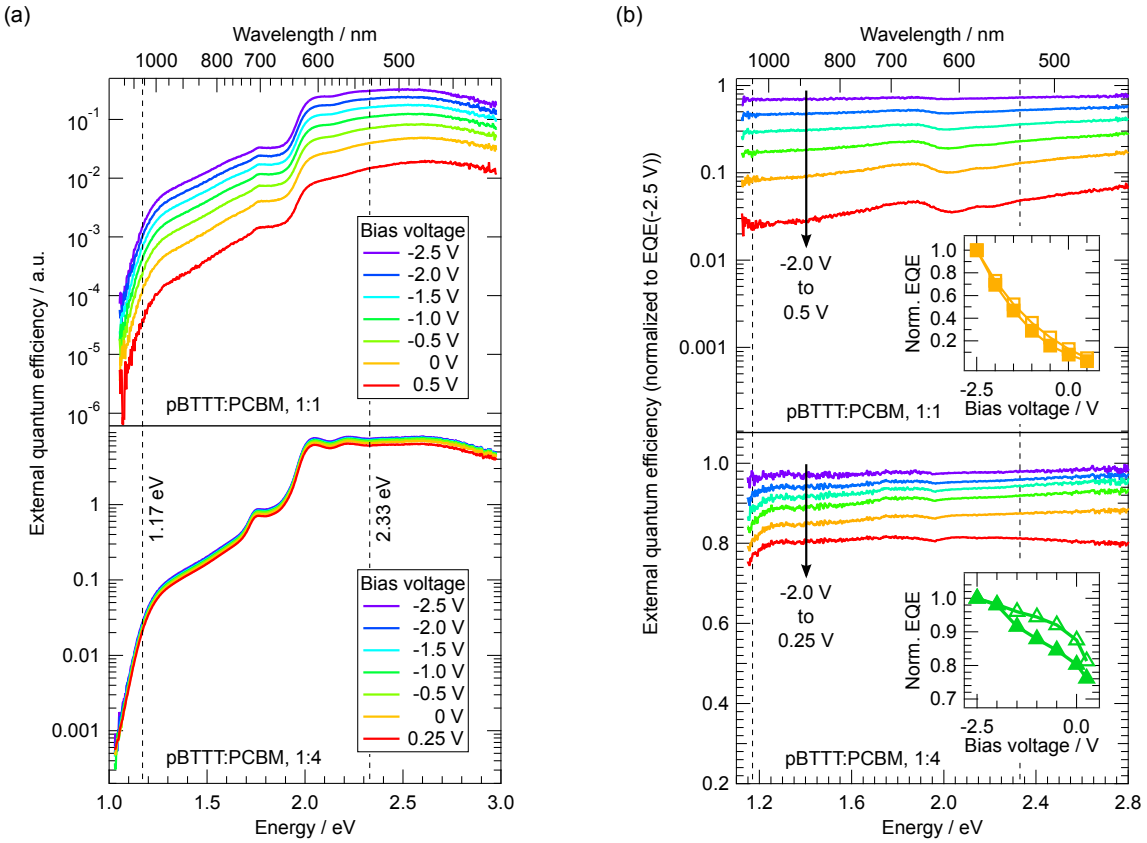

Figure 5.6.: (a) EQE spectra measured by FTPS at bias voltages between -2.5 V and 0.5 V (-2.5 V and 0.25 V) of pBTTT-C_{16}:PC_{61}BM solar cells with a 1:1 (1:4) blend ratio. **(b)** EQE spectra normalized to the spectrum recorded at -2.5 V. The insets show the normalized EQE at an energy of 1.17 eV (filled symbols) and 2.33 eV (open symbols), marked by dashed lines in the main graph.

5.3. Discussion

As it was found in TDCF and FTPS measurements (Figure 5.4b, top and Figure 5.6b, insets), the change of the fullerene loading has a much stronger impact on the field dependence of free charge carrier generation than changing the excitation energy. The observation indicates a dissociation via thermalized CTS, i.e., the relaxation within the CTS manifold is much faster than the separation process (Figure 3.2, green arrow). Similar results were recently reported for P3HT:PC_{61}BM and a variety of other materials. [59–61] However, TDCF and FTPS show a weak energy dependence of a few percent and hence, a slightly more efficient dissociation pathway via higher energy excited CTS cannot be completely excluded. Additionally, there might be other possible explanations for the slight difference in photogeneration, depending on whether an energy of 1.17 eV or 2.33 eV was used for photoexcitation. In this context, it must be mentioned that the increasing deviation between 1.17 eV and 2.33 eV excitation energy with decreasing internal field in Figure 5.4b (top) and Figure 5.6b (insets) is a matter of normalization. First, a diverging local ratio of absorption in donor and acceptor regimes for sub-gap and above-gap excitation might explain the photon energy dependence. The local ratio of absorption is expected to be 1:1 for the direct CT excitation at the D-A interface, whereas the absorption of the

neat materials depends on the excitation energy (c.f. above-gap EQE contributions at 2.33 eV). Second, it is important to point out that Figure 5.6b shows a deviation of the normalized EQE from a constant value below an energy of 1.9 eV where the EQE drops rapidly with energy (Figure 5.6a) and is highly sensitive to any small perturbance. In this energy range, the excitation of deeply trapped charges, which requires an additional field assisted activation to contribute to the photocurrent, seems reasonable. With decreasing photon energy, they form the main part of excited charge carrier distribution that leads to an enhanced field dependence of photogeneration. Moreover, applying an external electric field might cause a shift in absorption (Stark effect). Finally, the variations of free charge carrier generation yield at low photon energies might result from either a change in absorption tail width due to a slight increase in temperature, e.g., caused by carrier injection, [248] or the PEDOT interfacial electrode is becoming partially doped at higher electric fields. The latter is known to affect the absorption mainly at longer wavelengths (electrochromism). Despite such possibilities, it must be emphasized that the influence of excess photon energy on the photogeneration is only minor as compared to a change of the blend morphology. Therefore, the question about the origin of the reduced field dependence for higher fullerene loadings arises (Figure 5.4b), which will be addressed next.

As it can be concluded from PL quenching, [81,83,84] the highly efficient dissociation of photogenerated singlet excitons into polaron pairs takes place already for a small fullerene content due to the formation of intercalated phases of pBTTT-C_{16}:PC_{61}BM. However, a high yield of free charge carrier generation requires the effective spatial separation of polarons. Therefore, it can be assumed that the strong decrease in n_{tot} in the case of the 1:0.7 pBTTT-C_{16}:PC_{61}BM blend results from a poor dissociation due to small delocalization length of electrons confined to fullerene molecules in partially intercalated phases. [64,109,247] This implies both strong geminate and nongeminate recombination losses, which might be the origin of the reduced V_{oc}. The spatial confinement of electrons can be further related to a highly imbalanced, short-range transport due to a dominating hole mobility. This behavior was recently reported by Rance et al., who compared the high frequency mobility $\Sigma\mu$ in neat pBTTT and a 10:1 pBTTT:PC_{61}BM blend. [84]

Increasing the PC_{61}BM loading, i.e., going from a blend ratio of 1:0.7 to 1:1, has no influence on the dissociation of singlet excitons itself, since the D-A interaction is unaffected on a molecular scale. Thus, the reduced field dependence of photogeneration in pBTTT-C_{16}:PC_{61}BM with a mixing ratio of 1:1 most probably results from the formation of an almost complete intercalated polymer crystal and the delocalization of electrons along conducting fullerene channels. However, the formation of small, individual fullerene domains cannot be fully excluded. Therefore, it is more likely to attribute the reduced field dependence to the presence of these domains, as discussed below. Neat PC_{61}BM phases should also yield an increased contribution of the electron mobility that is consistent with the observations reported in the publication by Rance et al. [84] Moreover, recombination losses are reduced increasing both V_{oc} and FF.

In the 1:4 pBTTT-C_{16}:PC_{61}BM blend, large acceptor domains, i.e., pure fullerene phases on the ten nanometers length scale as deduced from XRD measurements, support electron delocalization and maximize the polaron pair dissociation yield. Recently, Jamieson et al. suggested

the presence of an energetic driving force due to an increased electron affinity of $PC_{61}BM$ aggregates with respect to the BMC. The conclusion is based on a significantly slowed-down recombination of mobile charge carriers in a 1:4 blend.[249] The resulting electron transfer from the BMC into pure fullerene phases in pBTTT:$PC_{61}BM$ blends was already mentioned in References 84 and 250 and confirmed for other material systems by Shoaee et al.[130] By comparing TDCF measurements on pBTTT-C_{16}:$PC_{61}BM$ with those on segregated pBTTT-C_{16}:bis$PC_{61}BM$ (Figure 5.4b, bottom), the present study confirms the high BMC extraction yield. Though, minor differences between the field dependence observed for the two different acceptor types indicates that the coexistence of an intercalated phase and pure fullerene domains is not a necessary condition for an efficient dissociation. This observation demonstrates that only the presence of pure $PC_{61}BM$ domains is the main prerequisite for an efficient polaron pair dissociation that is consistent with the theory of an increased delocalization length. Comparative conclusions about the crucial role of fullerene domains were drawn in recent investigations using simulations and ultrafast optical absorption spectroscopy.[131–133] The electron delocalization in fullerene domains can be correlated with an increased local mobility, which is consistent with the considerable contribution of the electron mobility reported in literature.[84] In addition, the formation of an interpenetrating $PC_{61}BM$ network is expected to improve the percolation of free electrons. This conclusion was also drawn in a publication by Baumann et al. by analyzing the temperature dependent charge carrier mobility in 1:1 and 1:4 blends of the similar donor polymer pBTCT-C_{12} and $PC_{61}BM$.[152]

5.4. Conclusions

In summary, the influence of excess energy and morphology on the polaron pair dissociation in pBTTT-C_{16} based BHJ solar cells was analyzed by field and wavelength dependent TDCF measurements and FTPS experiments using different bias voltages. To this purpose, the two acceptor materials $PC_{61}BM$ and bis$PC_{61}BM$ were chosen. pBTTT-C_{16}:$PC_{61}BM$ blends were prepared in three different stoichiometries in order to obtain a blend morphology with partially (1:0.7) and almost complete intercalated phases (1:1) as well as the coexistence of both fully intercalated and pure fullerene domains (1:4). Both TDCF and FTPS revealed an only minor influence of excess photon energy on polaron pair dissociation. In addition, increasing the fullerene loading reduced the field dependence of the free charge carrier generation yield. The observations are attributed to an efficient charge carrier photogeneration via thermally relaxed CTS within the bimolecular crystal. The more efficient dissociation with increasing $PC_{61}BM$ content is assigned to an increased electron delocalization due to the formation of pure acceptor domains. Consequently, geminate recombination within the intercalated phase is minimized that is observed to be quite significant in the 1:0.7 and 1:1 blends. Additional TDCF measurements performed on segregated pBTTT-C_{16}:bis$PC_{61}BM$ blends revealed a weak field dependence almost identical to the 1:4 pBTTT-C_{16}:$PC_{61}BM$ blend. This finding demonstrates the highly efficient transfer of electrons from the BMC into the pure phase and allows the conclusion that not the

presence of both intercalated and pure phases, but the delocalization in pure acceptor domains is the major driving force for efficient, field independent polaron pair dissociation.

6. The Effect of the Solvent Additive Diiodooctane

6.1. Introduction

The active layer morphology of organic BHJ solar cells is critical for both the generation of free charge carriers at the D-A interface and their transport through the interpenetrating D-A network. As outlined in Section 2.2.3, there are different concepts of optimizing the microstructure of state-of-the-art BHJ compounds in order to improve their photovoltaic efficiency. Regarding blends based on low-bandgap copolymers, the most common approach is the use of small quantities of solvent additives in the blend solution that significantly affects the precipitation of one blend component and thus the D-A intermixing.

Using CB as primary solvent and 3 vol% of the additive DIO, the PCE of BHJ solar cells composed of PTB7 (Figure 4.1b) and $PC_{71}BM$ can be increased by more than a factor of two in a conventional device architecture as compared to the DIO-free device.[36] Although it is widely accepted that the use of DIO comes along with a phase separation on a smaller scale and an enhanced D-A intermixing, most probably due to the selective dissolution of PCBM aggregates,[85] the detailed effect of the additive has not been fully clarified yet.[166] Chen et al. claimed that the superior photovoltaic performance of PTB7 based blends can be related to the formation of a hierarchical nanomorphology.[251] This multi-length-scale nanostructure includes D and A nanocrystallites with an average size of several nanometers and nanocrystallite aggregates on the several ten nanometers length scale that are embedded within intermixed D- and A-rich domains of typically hundreds of nanometers. The authors argue that the use of DIO does not influence the average size of individual crystallites, but increases their number. In addition, DIO supposedly improves the D-A intermixing in amorphous domains while preserving their characteristic dimension. Both effects are correlated with a more efficient exciton dissociation and a higher charge carrier mobility. It must be emphasized that the mentioned findings were achieved for PTB7:$PC_{61}BM$ blends showing a rather poor rise of PCE due to DIO as compared to the results reported in Reference 36. In contrast to the hierarchical nanomorphology proposed by Chen et al., only a minor degree of crystallization was found in PTB7:$PC_{71}BM$ blends by Hammond et al.[88] The study additionally showed that the blend nanostructure is rather given by $PC_{71}BM$-rich aggregates surrounded by a PTB7-rich phase. Through the use of DIO, the size of fullerene-rich domains decreases resulting in a more finer dispersion. This finding is supported by the work of Collins et al. reporting on the presence of pure fullerene domains with an average diameter in the 100 nm range that are embedded in

an intermixed, polymer-rich matrix.[91] With only minor changes of domain composition and crystallinity, PTB7:$PC_{71}BM$ processed with DIO reveals a reduced size of acceptor domains. Recently, Hedley et al. suggested that $PC_{71}BM$-rich domains in the non-optimized blend consist of smaller fullerene spheres.[90] In addition, the formation of elongated fiber-like structures in the optimized blend is reported. In analogy to PTB7, solar cells comprising the copolymer PBDTTT-C (Figure 4.1c) in blends with $PC_{71}BM$ yield a PCE up to 6.6 % when processed with 3 % DIO.[173,252] In contrast to PTB7, there are only few publications concerning the effect of DIO on the active layer morphology. Based on the similarity in chemical structure of both polymers, it is commonly assumed that the formation of a rather amorphous morphology as for PTB7 is also true for PBDTTT-C.[253]

With regard to the effect of DIO on device physics, nongeminate recombination is seen as the fundamental loss mechanism for both PTB7:$PC_{71}BM$ solar cells processed without and with DIO. The use of the solvent additive is ascribed to substantially reduce geminate recombination without affecting charge collection.[89,92,93] In this context, the scenario of charge carriers trapped in isolated fullerene domains has to be mentioned. In accordance with PTB7, nongeminate recombination was found as dominant loss mechanism in optimized PBDTTT-C:$PC_{71}BM$ solar cells.[253]

The following chapter comprises two parts. While all studies mentioned above contrast the active layer without DIO and the one with 3 % DIO as the optimum amount of the additive, little is known about the direct correlation between the DIO content and the effect on photocurrent generation. The first part concerns this issue and reports on the use of a systematically increasing amount of 0 %, 0.6 %, 1 %, 3 %, and 10 % DIO in PBDTTT-C:$PC_{71}BM$ devices. As starting point, IC-AFM measurements (Section 4.4) allow first assumptions about the effect of DIO on the surface morphology of the active layers. The study is extended to the bulk morphology by analyzing the dynamics of singlet excitons and bound or free polarons by picosecond TRPL and TA spectroscopy (Section 4.4). The combination of surface imaging and photophysical measurements allows to draft a scenario of the major changes of the active layer morphology as a function of the amount of DIO. Finally, the main objective of this section is to study the effect of these nanostructural changes on the field dependence of free charge carrier formation and nongeminate recombination dynamics by means of TDCF (Section 4.3.1) and OTRACE (Section 4.3.2). IC-AFM measurements and the corresponding data evaluation presented in this section were done by Mario Zerson (Chemnitz University of Technology). Both PL and TA measurements were done by Björn Gieseking. A more detailed analysis of their results can be found in Reference 167.

Despite a multitude of publications, the correlation of the distinctive morphologies of DIO-free and optimized PTB7:$PC_{71}BM$ blends with charge carrier transport and recombination has not yet been clarified in any detail. In order to get insight into this topic, the nongeminate recombination dynamics in PTB7:$PC_{71}BM$ solar cells is analyzed in the second part of the present chapter. Similar to the study on PBDTTT-C:$PC_{71}BM$, the photoluminescence of neat and blend films is studied to verify changes of the nanomorphology due to the use of DIO in a first step. Subsequently, the impact of the altered blend morphology on nongeminate recombination and

charge carrier transport is addressed by means of OTRACE. Combining both elements finally yields information about the origin of the deviation from a pure 2^{nd} order decay in both blends. Photovoltaic devices used in this section were prepared by Markus Glücker. Steady state PL measurements were done by Kristofer Tvingstedt. OTRACE measurements were performed together with Andreas Baumann (Bavarian Center for Applied Energy Research e.V.).

6.2. Photocurrent Generation in PBDTTT-C:$PC_{71}BM$ Blends

Abstract: The effects of a systematically increased amount of the solvent additive DIO on the microstructure of PBDTTT-C:$PC_{71}BM$ blends are correlated with changes in geminate and nongeminate recombination by combining surface imaging, photophysical and charge extraction techniques. Large agglomerates visible in IC-AFM images of the blend processed without DIO are identified as $PC_{71}BM$ domains, which are embedded in an intermixed matrix phase. The associated, rather small D-A interface and missing percolation paths are related to a comparatively poor singlet exciton splitting and predominant geminate recombination losses. A drastic decrease in the size of fullerene domains is observed along with a demixing of the matrix phase in the 0.6 % and 1 % DIO samples. Surprisingly, although the blend processed with the smallest amount of DIO already reveals a highly efficient photogeneration, the maximum PCE is only found for the 3 % DIO device. The finding is related to the formation of interpenetrating polymer and fullerene phases. This fine-tuning of the blend morphology favors the formation of free charge carriers and minimizes nongeminate recombination losses as deduced from charge extraction experiments. In comparison to the 3 % device, the increase in the amount of DIO up to 10 % negatively affects the PCE. The observation is assigned to a lower photogeneration yield and charge carrier trapping in a less interconnected D-A network.

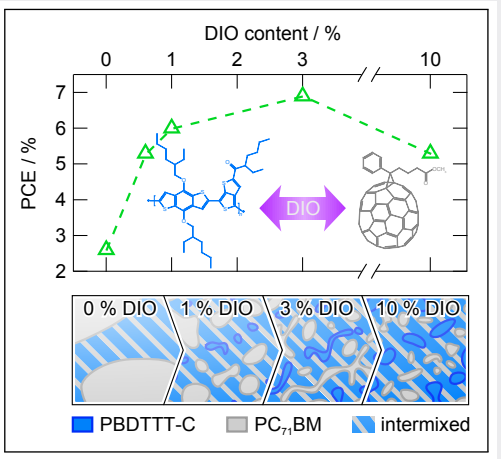

6.2.1. Current-Voltage Characteristics

PBDTTT-C:$PC_{71}BM$ devices were processed using 0 %, 0.6 %, 1 %, 3 %, and 10 % (per volume) of the solvent additive DIO. Figure 6.1 shows the j-V characteristics of the devices selected for the following studies. The corresponding photovoltaic parameters can be found in Table 6.1. The solar cells were chosen with respect to device performance and dark saturation current from a series of more than ten solar cells, each. The standard deviation of the individual parameters was equal to at most 12 % of the mean value. A maximum PCE of 7.1 % was found for the device with 3 % DIO. It results from an increase of about 61 % in j_{sc} and an increase of about 66 % in FF relative to the blend without DIO. The improvement of both parameters overcompensates the slight decrease of about 9 % in V_{oc}. It is striking that the most substantial rise of the PCE already results from the addition of the smallest amounts of DIO, i.e., 0.6 % and 1 % DIO. The photovoltaic performance of the device with 10 % DIO remains at a high level as compared to the best device with 3 % DIO, although j_{sc} is reduced by almost 20 %.

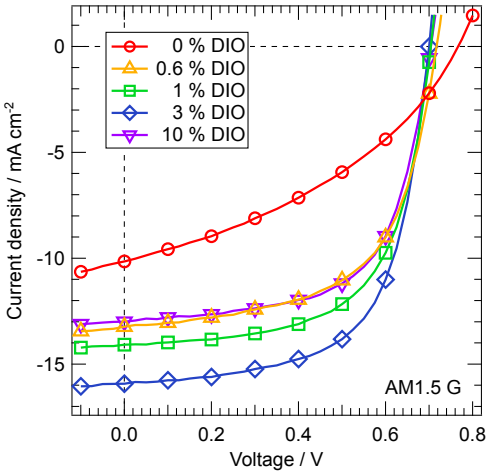

Figure 6.1.: j-V characteristics of PBDTTT-C:$PC_{71}BM$ solar cells with varying DIO content. The illumination intensity was adjusted to 1 sun under a simulated AM1.5 G spectrum.

6.2.2. Surface Morphology

The surface morphology of thin film samples of PBDTTT-C:$PC_{71}BM$ with varying DIO content were studied using IC-AFM. Large scale and high resolution height images are shown in the left and middle column of Figure 6.2, respectively. The surface morphology of the 0 % DIO film is characterized by round agglomerates with an average diameter in the range of 100 to 200 nm embedded in a rather smooth surrounding. The root mean square roughness r_{RMS} amounts to 4.5 nm. With the use of 0.6 % DIO, the surface morphology drastically changes and a more fine-grained surface morphology is formed showing domains with a diameter of less than 50 nm. In addition, about 10 nm deep and 100 nm wide depressions appear close to the bumps, which are identified with collapsed pores of the active layer forming close to the surface during solidification of the film. The surface roughness of the 0.6 % DIO film amounts to 2.9 nm. Adding 3 % DIO results in a further refinement of the surface morphology. Domains and pores appear on the ten nanometers length scale and the surface roughness has a minimum value of 1.7 nm. The use of 10 % DIO inverts this trend and the surface topography is coarsening again. Isolated agglomerates are visible on the hundred nanometers length scale and the surface roughness increases to the maximum value of 8.3 nm. In contrast to the clear

	V_{oc} / mV	j_{sc} / mA cm^{-2}	FF / %	PCE / %
0 % DIO	768	10.1	38.2	3.0
0.6 % DIO	718	13.2	59.5	5.6
1 % DIO	705	14.1	62.6	6.2
3 % DIO	700	15.9	63.4	7.1
10 % DIO	705	13.0	62.4	5.7

Table 6.1.: Photovoltaic parameters of PBDTTT-C:$PC_{71}BM$ solar cells with varying DIO content. Measurements were performed under a simulated AM1.5 G spectrum and an illumination intensity of 1 sun.

variations of the surface morphology visible in IC-AFM height images, the corresponding phase images (Figure 6.2, right column) show a rather fine structure on the nanometer scale with only minor differences in pattern due to the use of DIO.

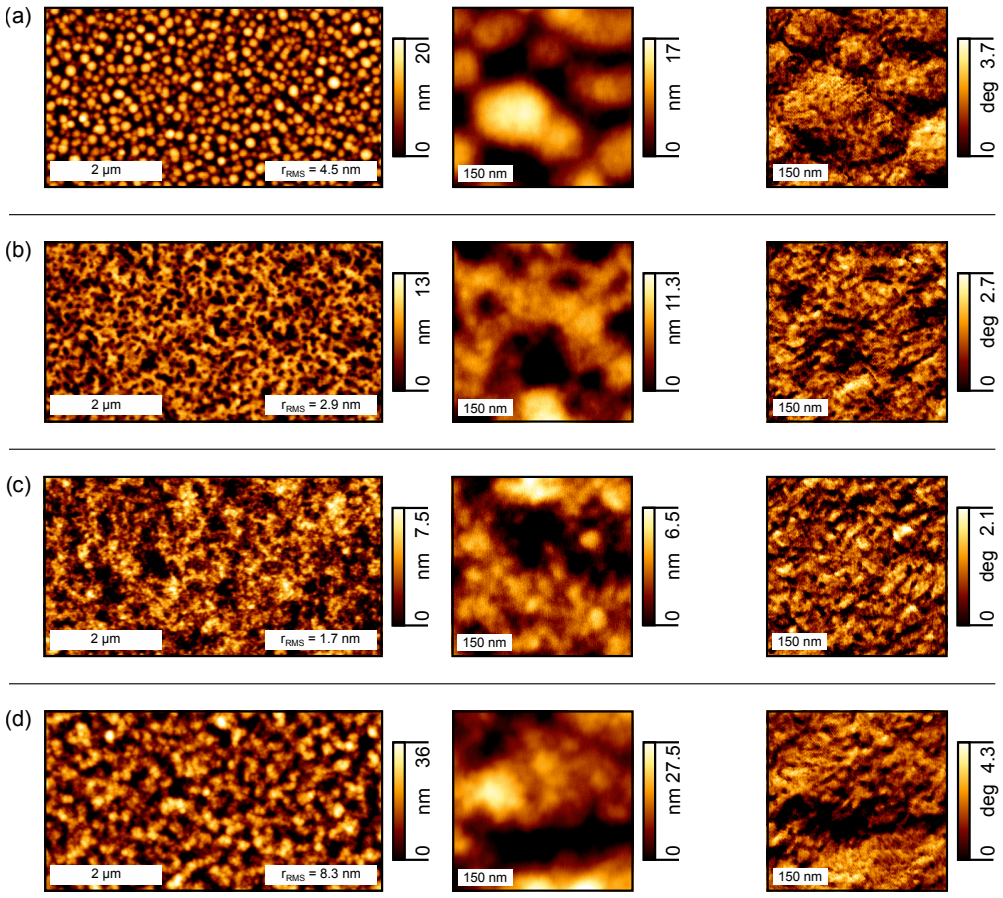

Figure 6.2.: IC-AFM height (left and middle column) and phase images (right column) of thin films of PBDTTT-C:$PC_{71}BM$ prepared with **(a)** 0 %, **(b)** 0.6 %, **(c)** 3 %, and **(d)** 10 % DIO.

The observed changes in surface morphology can be related with the active layer morphology of PTB7:$PC_{71}BM$ blends. Several studies reported the presence of large fullerene domains with an average diameter of 100 to 200 nm embedded in an intermixed matrix phase for blends processed without DIO. [36,88,91,254] Moreover, it is claimed that the addition of 3 % DIO provokes a better dispersion of the $PC_{71}BM$ agglomerates due to the selective dissolving of the fullerene component by the additive. The surface morphology of PBDTTT-C:$PC_{71}BM$ films in Figure 6.2 can be interpreted in a similar way. Based on above studies, it is very likely that the large agglomerates visible in the 0 % DIO film consist of $PC_{71}BM$ and are embedded in an intermixed matrix phase. With the addition of up to 3 % DIO, these domains get smaller, leading to a morphology optimized with regard to free charge carrier generation and collection. The nanoscale structure visible in phase images can be understood in connection with the recent report on the presence of a polymer-rich skin layer of PTB7:$PC_{71}BM$ blend films. [90] IC-AFM phase images in Figure 6.2 suggest that a similar top skin also exist in case PBDTTT-C:$PC_{71}BM$ blends and that its nanoscale, near-surface morphology does not depend on the DIO content. A quite simi-

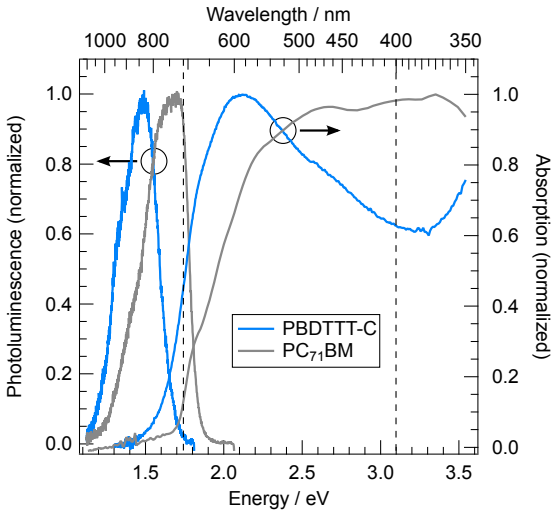

Figure 6.3.: PL spectra (left axis) and absorbance (right axis) of neat films of PBDTTT-C and $PC_{71}BM$. The dashed lines indicate 3.1 eV and 1.74 eV used in TRPL measurements as excitation and probe energy (Figure 6.4).

lar nanostructure is reported for fullerene blends of the PPV derivative poly(2-methoxy-5-3',7'-dimethyloctyloxy-p-phenylene vinylene) (MDMO-PPV).[47,255] With increasing PCBM loading, large fullerene domains are formed that are covered by a polymer-rich matrix phase. It must be emphasized however that AFM merely provides information on the surface morphology and allows only limited conclusions to be drawn about the bulk microstructure.

6.2.3. Nanomorphology and Fast Photogeneration

Figure 6.3 shows the absorbance and photoluminescence of neat PBDTTT-C. Both spectra are strongly overlapping with the respective spectrum of $PC_{71}BM$. As a result, it can be assumed that photoexcitation of PBDTTT-C:$PC_{71}BM$ in the visible spectral range creates singlet excitons in both polymer and fullerene phases. In addition, the blend PL can be expected to be a superposition of donor and acceptor emission.

In order to study the effect of DIO on the singlet exciton dynamics, picosecond time-resolved PL measurements were performed. The time-integrated spectra of PBDTTT-C:$PC_{71}BM$ blends with varying DIO content are shown in Figure 6.4a. The PL spectra can be qualitatively reproduced by a superposition of the individual spectra of the neat materials according to

$$PL_{blend} = A_D PL_D(\Delta T_0) + A_A PL_A(int.) \quad . \tag{6.1}$$

$PL_D(\Delta T_0)$ denotes the initial donor PL (Figure 6.4a, dash-dotted line) and $PL_A(int.)$ the time-integrated acceptor PL (Figure 6.4a, dashed line). $A_{D,A}$ are the corresponding fitting amplitudes, which can be found in Table 6.2. No significant contribution of CT state emission was found within the analyzed spectral range. The correct reproduction of the blend emission by Equation 6.1 requires the use of the separately measured $PL_D(\Delta T_0)$, since the emission of neat PBDTTT-C might be distorted by a dynamic redshift as it was shown for another low-bandgap

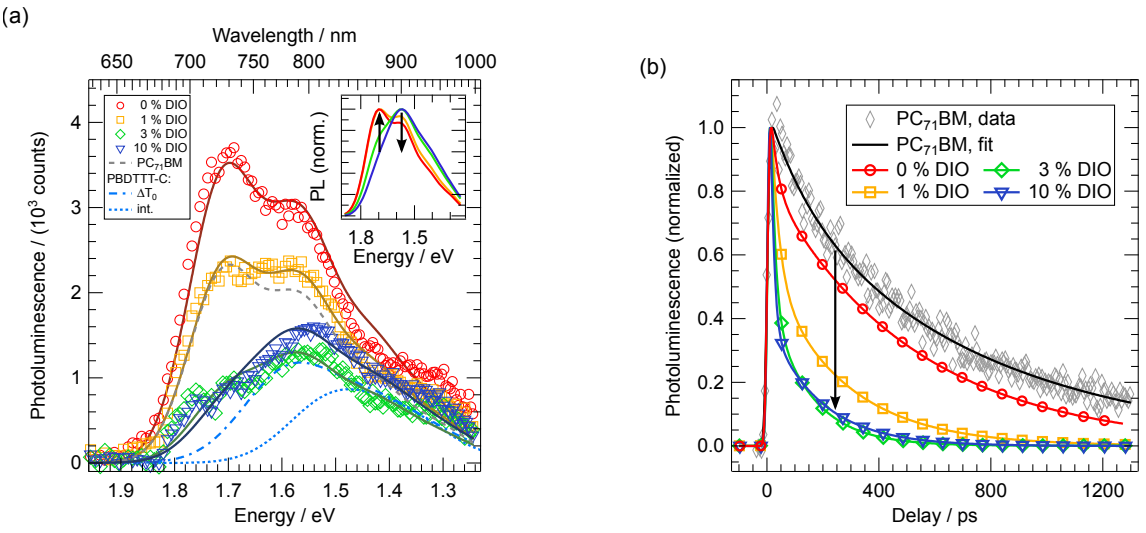

Figure 6.4.: (a) Time-integrated PL spectra of the blend films (symbols) and corresponding fits according to Equation 6.1 (solid lines). Films were excited at 3.1 eV. For comparison also the initial polymer spectrum (dash-dotted line) as well as the time-integrated PL spectra of the fullerene film (dashed line) are shown. Both curves were scaled with the fit amplitudes A_D and A_A of the 10 % and 1 % DIO sample (Table 6.2), respectively. The dotted line corresponds to the integral polymer emission. The inset illustrates the relative spectral change of the fitted spectra. **(b)** Fits of PL transients taken at 1.74 eV reflecting the decay dynamics of excitons generated within $PC_{71}BM$ domains. For comparison also the PL decay of a neat fullerene film is shown.

copolymer.[51] In addition, the donor contribution can only be observed around the initial delay of 30 ps. Both the suppressed redshift as well as the fast quenching of the donor emission in blends with $PC_{71}BM$ indicate a highly efficient exciton dissociation at the D-A interface. Regarding the blend PL, the emission of the 0 % DIO sample is completely reproduced by the PL from $PC_{71}BM$. The addition of 1 % and 3 % DIO goes along with a gradual decrease in PL originating from a reduced contribution of acceptor PL but an increased emission from PBDTTT-C. With the increase in the DIO content up to 10 %, the time-integrated PL slightly increases relative to the 3 % DIO blend that results from the sustained trend of a gradual decreasing $PC_{71}BM$ emission and an increase in the donor PL. This relative spectral change of the fitted blend spectra from being acceptor dominated to being donor dominated is illustrated in the inset in Figure 6.4.

The changes of the absolute PL emission and their spectral composition (Figure 6.4a and Table 6.2) can be related to an altered size of donor and acceptor domains based on the exciton diffusion length d_e of roughly 5 to 10 nm. The suppression of any donor PL in the case of the 0 % DIO blend indicates the presence of acceptor domains that are substantially larger than d_e, since a considerable part of singlet excitons do not reach the D-A interface and decay radiatively. In addition, the absence of donor emission implies the presence of an additional intermixed phase comprising D and A domains with a size on the order of or smaller than d_e. Both conclusions are in accordance with the identification of large domains surrounded by an intermixed phase in the corresponding IC-AFM height image (Figure 6.2a). The altered blend emission upon increasing the fraction of DIO can be related to a reduced size of $PC_{71}BM$ do-

mains as well as the formation of additional pure PBDTTT-C regions within the intermixed phase. In both cases, the resizing is expected to occur on a length scale similar to d_e. On the one hand, an alteration of the domain size on a length scale exceeding d_e would have no effect on PL emission, since excitons may not reach the D-A interface during their lifetime in any case. On the other hand, a highly efficient quenching can be assumed from experience for an intimate mixing of D and A phases that cannot be observed in Figure 6.4a. The assumption of an alteration of the active layer morphology on the ten nanometers length scale is consistent with the observations in IC-AFM height images in Figure 6.2b and c.

In order to verify the interpretation of the effect of DIO on the active layer morphology, PL decay dynamics measured at 1.74 eV are compared for the different PBDTTT-C:$PC_{71}BM$ blends (Figure 6.4b). In addition, also the PL transient for neat $PC_{71}BM$ is shown. The transients were fitted by a biexponential decay. The corresponding time constants and the ratio of the amplitudes are summarized in Table 6.2. The transient of the neat fullerene follows a monoexponential decay with an effective radiative lifetime τ_2 of fullerene singlet excitons of about 700 ps. τ_2 is slightly reduced for the blend without DIO and a second fast channel τ_1 is introduced, which is close to the temporal resolution of the measurement. τ_1 most probably results from the dissociation of excitons at the D-A interface. Thus, the decay dynamics of the 0 % DIO blend can be expected to be mainly determined by the quenching of excitons generated within fullerenes phases. With the addition of up to 3 % DIO, τ_2 is substantially reduced and the relative contribution of the fast decay channel A_1/A_2 increases. The latter continues for the 10 % blend, however, a slight increase in τ_2 as compared to the 3 % blend can be observed. Both the decrease in τ_2 up to 3 % DIO and the gradual increasing contribution of τ_1 can be interpreted in terms of a reduced size of $PC_{71}BM$ domains allowing more excitons to reach the D-A interface during their lifetime. The finding confirms the analysis of time-integrated PL spectra. The increase in τ_2 due to the use of 10 % DIO might be correlated with an enhanced contribution of donor emission due to the presence of PBDTTT-C domains.

The finer dispersion of $PC_{71}BM$ domains with increasing DIO content, as deduced from PL measurements, implies a substantially enhanced interfacial area. Thus, an increased density of initially generated interfacial polaron pairs and free charge carriers can be expected. The

	time-integrated		transient		
	A_D	A_A	τ_1 / ps	τ_2 / ps	A_1/A_2
$PC_{71}BM$	–	–	–	726	–
0 % DIO	–	3530	24	512	0.29
1 % DIO	230	2330	28	264	0.97
3 % DIO	690	700	18	145	1.47
10 % DIO	1180	470	14	186	2.80

Table 6.2.: Donor and acceptor contributions A_D and A_A to the integral blend PL of PBDTTT-C:$PC_{71}BM$ blends derived from a fit according to Equation 6.1 and time constants τ_1 and τ_2 and the corresponding amplitude ratio A_1/A_2 deduced by a biexponential fit of PL transients. For comparison also the decay time for neat $PC_{71}BM$ is shown.

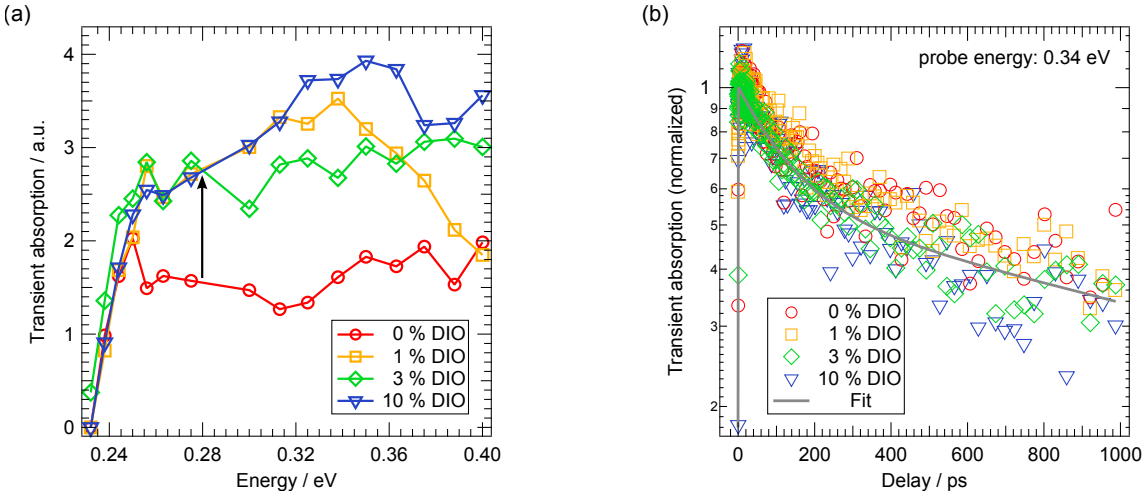

Figure 6.5.: (a) Initial (0.5 ps) TA signal probed in the 0.24 to 0.4 eV region. Already the use of 1 % DIO results in an enhanced initial generation of bound and free charge carriers (arrow) staying on a similarly high level for the 3 % and 10 % film. **(b)** TA transients probed at 0.34 eV for the different blends with varying DIO content. The transients were fitted assuming a biexponential decay, which is shown using the example of 3 % DIO.

change in optical density as studied by TA spectroscopy (Equation 4.10) is directly proportional to the population of both species and thus is an appropriate quantity allowing conclusions to be drawn on the active layer morphology. Figure 6.5a shows the TA spectra of PBDTTT-C:$PC_{71}BM$ films with varying DIO content recorded at 0.5 ps and in the IR region between 0.24 and 0.4 eV. This low energy absorption band is associated with the population of the photogenerated bound polaron pairs or free polarons [58,101,256,257] without spectrally overlapping intrachain excitations. [258] Already the addition of 1 % DIO provokes an increase in the transient absorption by more than a factor of two as compared to the 0 % DIO device (Figure 6.5a, arrow). The further increase in the amount of DIO up to 3 % and 10 % causes only minor changes. The enhanced fast photogeneration for the 1 % DIO blend can be related to a substantial increase in the D-A interface as a consequence of a reduced size of fullerene domains. This observation is in agreement with previous TRPL measurements and with the enhanced PCE of the 1 % DIO device (Table 6.1). However, at first sight, no considerable change of the initial TA signal of the 3 % DIO blend appears to be inconsistent with AFM and PL measurements that indicate further shrinking $PC_{71}BM$ domains and thus a gradual increase in the interfacial area. This contradiction can be clarified taking into account the enhanced donor PL of the 3 % DIO blend (Table 6.2). It indicates the formation of pure PBDTTT-C domains within the intermixed D-A phase compensating decreasing $PC_{71}BM$ phases and their positive effect on the fast photogeneration. The same reasoning holds for the 10 % DIO blend showing both an even more donor dominated PL emission as well as larger agglomerates visible in IC-AFM height images. The reason for a slightly reduced photogeneration of the 3 % DIO blend and an improved photogeneration of 10 % DIO blend, both relative to 1 % DIO, can only be speculated. The trend might result from the competition of shrinking $PC_{71}BM$ domains and the formation of pure PBDTTT-C regions.

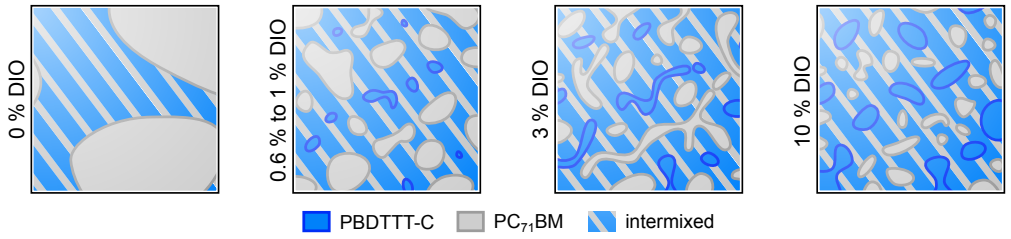

Figure 6.6.: Schematic illustration of the dominant transformations of the morphology of PBDTTT-C:$PC_{71}BM$ blends caused by the use of DIO. Already small amounts of DIO (0.6 % to 1 %) provoke the substantial decrease in the size of pure $PC_{71}BM$ domains surrounded by an intermixed D-A phase. A higher DIO content (3 % and 10 %) results in a fine-tuning of the domain size and linking of pure domains. Their optimum tradeoff, i.e., the most efficient photogeneration and collection of free charge carriers, is achieved by the use 3 % DIO.

Despite a comparable yield of fast photogeneration of the 1 %, 3 % and 10 % DIO blends, the PCE shows a maximum value for 3 % DIO (Table 6.1). To clarify this issue, the decay dynamics probed by TA have to be considered first. Figure 6.4b shows the transients for the different blends. Their decay was found to be independent of the energy of the probe beam and does not change significantly with changing the amount of DIO. Assuming a biexponential decay, a fast and a slow time constant of $\tau_1 = 100$ ps and $\tau_2 = 2$ ns were found with an amplitude ratio A_1/A_2 of about 0.8. These rather short time constants indicate that the decay dynamics are mostly determined by bound polaron pairs.[259] Although, the transients do not cover the nanosecond time regime, which would be characteristic for the dynamics of free charge carriers, it can be speculated that the TA signal of the 1 % and 10 % DIO blend is more dominated by bound polaron pairs than in the case of 3 % DIO. The maximum PCE of the 3 % DIO device thus can be explained rather by a fine-tuning of the active layer morphology than a drastic change in nanostructure as observed for small amounts of DIO, i.e., 0.6 % and 1 % DIO. This fine-tuning is assumed to mainly involve the formation of percolation paths favoring the collection of free charge carriers. The main changes of the active layer morphology are shown in Figure 6.6 as a function of the amount of DIO. The illustration has to be understood as a scenario assumed from combining AFM and photophysical results, but not as a reproduction of the actual blend morphology. It must be emphasized that the precise effect of 10 % DIO is difficult to establish as it will be seen in the context of OTRACE measurements.

6.2.4. Field Dependent Photogeneration and Nongeminate Recombination

In this section, the effect of an altered blend morphology on the photovoltaic performance of PBDTTT-C:$PC_{71}BM$ blends is studied using charge extraction techniques. In contrast to photophysical measurements, the following experiments were performed on operational devices and hence are sensitive to free, extractable charge carriers. In addition, they include larger time scales starting on the ten nanoseconds range. In the first step, pre-bias dependent TDCF was applied using an excitation energy of 2.33 eV. As a basic requirement allowing conclusions to be drawn about the yield of free charge carrier formation, i.e., excluding nongeminate losses during delay and extraction, the laser intensity has to be adjusted to be in a range showing a pho-

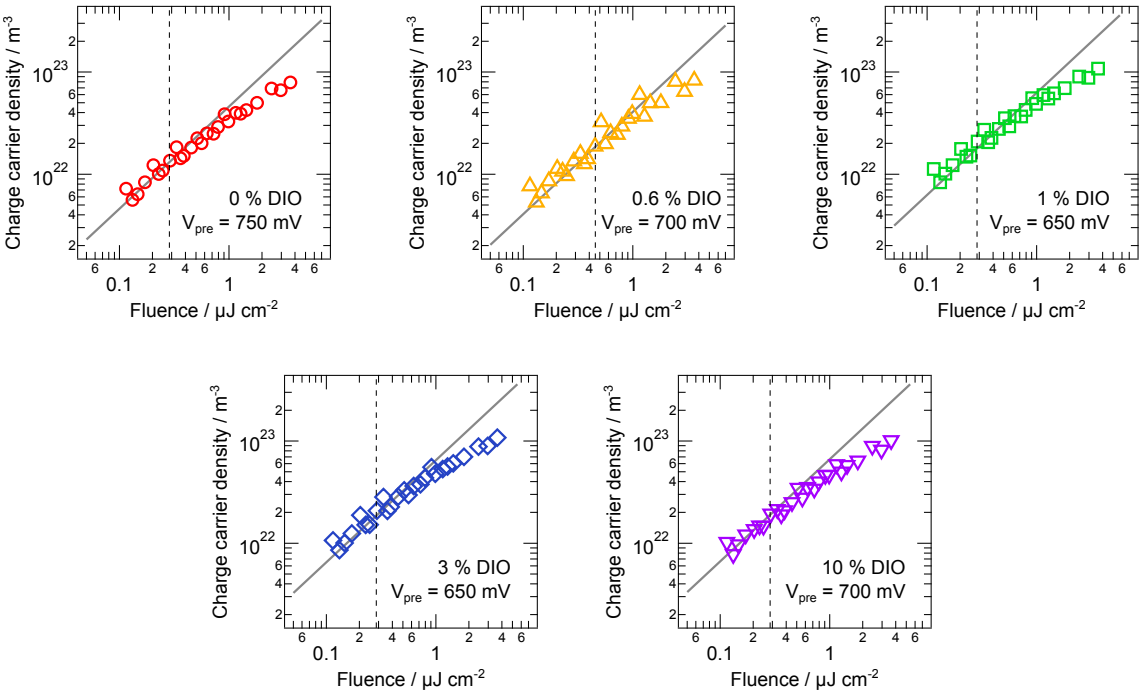

Figure 6.7.: Total extracted charge carrier density n_{tot} as a function of the pulse fluence derived from TDCF measurements on PBDTTT-C:$PC_{71}BM$ solar cells with varying DIO content (t_d = 20 ns, V_{col} = −4 V, t_{col} = 20 µs). The dashed line indicates the pulse fluence which was chosen for the respective pre-bias dependent measurement. Grey lines serve as guides to the eye.

togeneration linearly proportional to the illumination intensity. Figure 6.7 shows the extracted charge carrier density n_{tot} as a function of pulse fluence for the different PBDTTT-C:$PC_{71}BM$ devices. Furthermore, the intensities chosen for the following pre-bias dependent measurements are indicated (dashed lines).

The normalized extracted charge carrier density obtained from pre-bias dependent TDCF measurements is shown in Figure 6.8a. For all devices, n_{tot} is reduced towards lower internal electric fields. This decrease is commonly linked with a field dependent charge carrier photogeneration via bound polaron pairs.[96,112,122] Regarding the 0 % DIO blend, n_{tot} drops to about 65 % of the initial charge carrier density when going from -4 V to V_{oc}, i.e., close to zero internal electric field. The addition of DIO yields a descent to about 80 % (0.6 % DIO) and 85 % (1 % and 3 % DIO) at a pre-bias close to V_{oc} relative to the initial value, respectively, and hence a less field dependent photogeneration and reduced geminate losses. The further increase in the amount of DIO up to 10 % results in the reversed trend and an again increased field dependence with a drop to about 80 % of the saturation value at a pre-bias close to V_{oc}. In addition to local geminate losses explaining the pre-bias dependent decay of n_{tot}, consideration must be given to the extraction of free charge carriers from pure donor and acceptor domains. In a recent publication by Burkard et al., the generation of free charge carriers within large $PC_{71}BM$ domains was demonstrated for excitation energies above 1.85 eV.[46] It is claimed that these charge carriers overcome recombination within the fullerene phases by a hole transfer to the polymer that is favored by an applied external electric field. Due to the presence of large $PC_{71}BM$ agglomer-

ates in the case of the 0 % DIO device, the strong pre-bias dependence of n_{tot} can be partially attributed to this process. Therefore, the weaker field dependence of free charge carrier generation when adding 0.6 % DIO might originate from the decreasing size of fullerene domains and correspondingly a more efficient hole transfer. This finding confirms the observations in the previous sections demonstrating similar profound changes of the active layer morphology for the smallest amount of DIO. At first sight, the weaker field dependence along with a decreasing size of $PC_{71}BM$ domains seems inconsistent with the results presented in Chapter 5 and current publications. Both suggest a more efficient photogeneration with growing fullerene domains.[130–133,249] However, it must be emphasized that in the case of PBDTTT-C:$PC_{71}BM$ the decrease in the size of $PC_{71}BM$ domains starts on a considerably larger length scale of about 100 to 200 nm. The further reduced field dependence of free charge carrier formation due to the use of 1 % and 3 % DIO indicates an optimized phase separation and the formation of percolation pathways between pure domains. Similar results are reported by Albrecht et al. for the copolymer PCPDTBT blended with $PC_{71}BM$ and its fluorinated derivatives.[96,260] In these publications, reduced geminate losses are correlated with the presence of rather pure donor and acceptor domains with an average size of 10 to 20 nm. This range perfectly matches the results of the time-integrated PL study, where similar values are concluded based on the exciton diffusion length. The results shown in Section 6.2.3 also contribute to an understanding of the reversed trend of an increased field dependence in the case of the 10 % DIO blend. It is reasonable to attribute increased geminate losses to both the presence of larger and rather pure donor domains, exceeding their optimum size in the 3 % DIO blend, as well as less interconnected phases. The interpretation of TDCF measurements is therefore consistent with the scenario of a most efficient collection of free charge carriers in the finely-tuned D-A network of the 3 % DIO blend.

The effect of geminate and nongeminate recombination on device performance can be determined by further analyzing the field dependence of free charge carrier generation.[60,61,96,260] For this purpose, n_{tot} is normalized to the current density of the investigated devices at -2.5 V and compared to the j-V characteristics. The difference between n_{tot} and $j(V)$ (Figure 6.8b, shaded area) corresponds to the loss current density due to nongeminate recombination. The field dependence of n_{tot} is largest for the 0 % DIO device. For this additive content $j(V)$ and TDCF agree only in the voltage range below 1 V indicating that the photovoltaic function is affected by both geminate and nongeminate losses. The use of 1 % and 3 % DIO weakens the field dependence of free carrier formation and a discrepancy between $j(V)$ and TDCF can only be found close to V_{oc} in a rather small bias range. The finding demonstrates a high yield of free charge carrier generation and minimized nongeminate losses. This result contradicts a publication by Hawks et al., who claimed nongeminate recombination to be the sole loss mechanism in PBDTTT-C:$PC_{71}BM$ solar cells optimized through the use of 3 % DIO.[253] The conclusion was drawn based on the reconstruction of j-V curves assuming a field independent generation rate. The tested devices resembled the photovoltaic performance of the ones studied in this work. Expanding the scope of the discussion to the closely related copolymer PTB7, it is striking to see that the recombination dynamics in PBDTTT-C:$PC_{71}BM$ clearly differ from PTB7 based

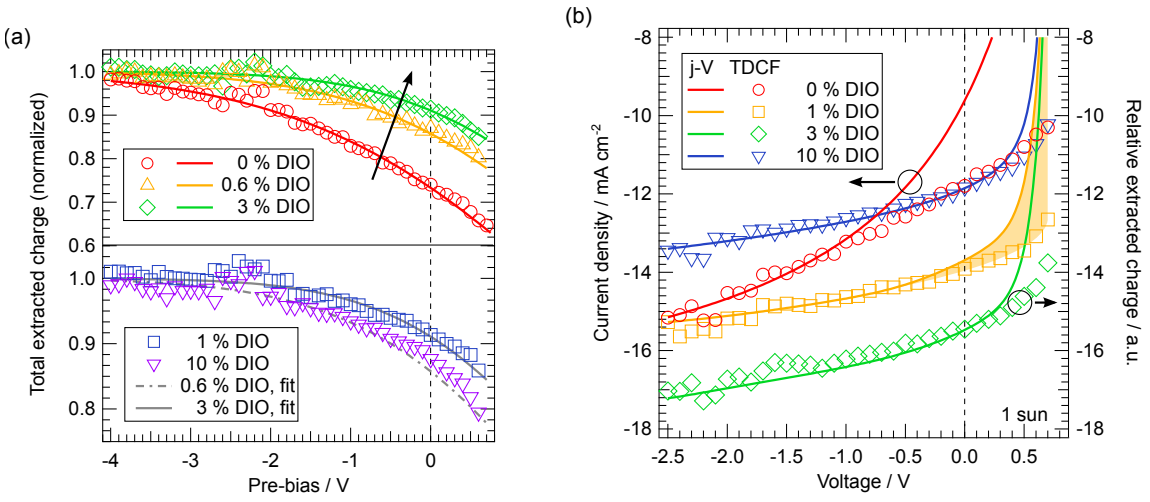

Figure 6.8.: (a) Extracted charge carrier density n_{tot} vs. pre-bias V_{pre} derived from TDCF measurements on PBDTTT-C:$PC_{71}BM$ solar cells (open symbols). Measurement conditions were $t_d = 20$ ns, $V_{col} = -4$ V, and $t_{col} = 20$ µs. n_{tot} was fitted by Gaussian (lines) and normalized to the respective maximum of the fit. The black arrow indicates a decreasing field dependence. Only data for 0 %, 0.6 % and 3 % DIO are shown in the top graph. The normalized n_{tot} obtained on the 1 % and 10 % DIO device roughly coincide with data of the 3 % and 0.6 % DIO device, respectively, as it can be found in the bottom graph. **(b)** Comparison of $j(V)$ (left axis) measured under 1 sun illumination intensity with the relative n_{tot} (right axis). n_{tot} was normalized to the current density at -2.5 V. The difference between $j(V)$ and n_{tot} corresponds to nongeminate recombination losses as indicated by the shaded area using the example of 1 % DIO.

blends. Recently, Foster et al. reported on a similarly reduced geminate recombination but enhanced nongeminate losses, i.e., a reduced charge carrier lifetime, for optimized PTB7:$PC_{61}BM$ solar cells (3 % DIO).[93] A comparable conclusion was drawn by Foertig et al. for PTB7:$PC_{71}BM$ devices.[92]

Regarding the origin of nongeminate losses and charge carrier transport, the charge extraction technique OTRACE was applied. In the first step, the effective charge carrier mobility μ was calculated from the maximum peak position t_{max} of OTRACE transients according to Equation 4.6. Figure 6.9a presents μ as a function of delay time for devices with varying DIO content. Due to RC distortions for $t_d < 10$ µs provoked by the chosen illumination intensity of 1 sun, an average mobility was evaluated for 10 µs $< t_d <$ 1.8 ms (Figure 6.9b). All devices show an average mobility of about $2{\cdot}10^{-8}$ m^2 (Vs)$^{-1}$, which is common for organic solar cells.[219] Surprisingly, OTRACE reveals an increase in μ with the addition of DIO contrary to the findings of Foster et al.[93] They found an almost constant hole mobility, but a decreased electron mobility in optimized devices using the SCLC method. This contradiction can be explained by the fact that μ, as derived from OTRACE transients, provide an estimate of an effective μ including both electron and hole mobility and the influence of trapped charge carriers (Section 4.3.2). Furthermore, OTRACE data reveal the overall highest mobility for the 1 % DIO device. In combination with an even more efficient fast photogeneration (Figure 6.5a) and a similar field dependence (Figure 6.8a) as compared to the 3 % DIO blend, this finding raises the question of the origin of the reduced PCE in the case of the 1 % DIO device. Most probably, the mobility is deter-

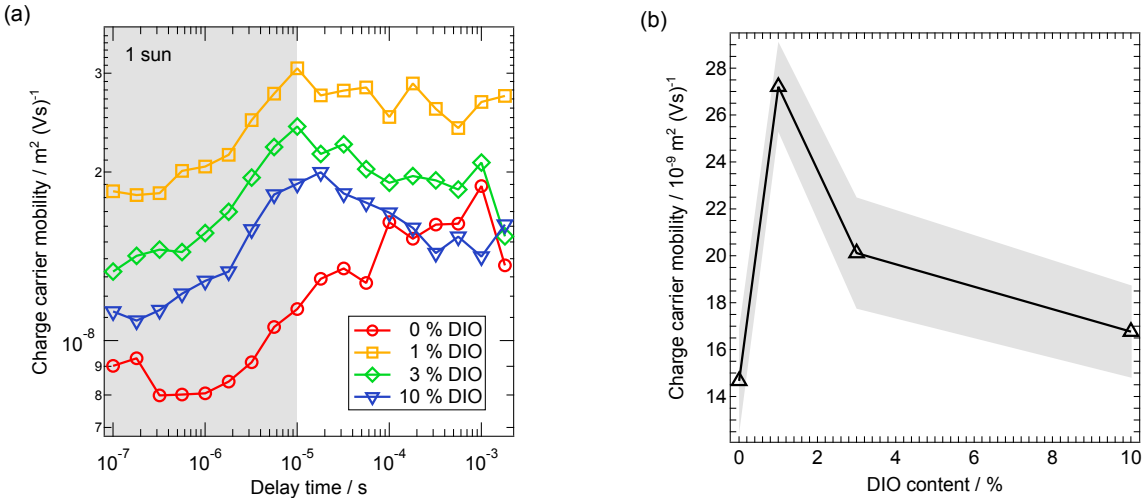

Figure 6.9.: (a) Charge carrier mobility μ vs. delay time t_d derived from the maximum peak position t_{max} of OTRACE transients (S = 90 kV s^{-1}). The increase in μ in the shaded area is attributed to RC distortions.[219] An average value of μ was calculated from the non-shaded time range. **(b)** Average μ derived from the left graph as a function of the DIO content.

mined by charge carriers extracted from well connected regions that form only a small fraction of the 1 % DIO bulk. As already suggested in conjunction with the field dependent photogeneration, remaining and less connected phases provoke an inefficient charge carrier collection that reduces j_{sc}.

In addition to transport properties, OTRACE provides information about the charge carrier density available for extraction under working conditions. Figure 6.10a shows the charge carrier density n as a function of delay time t_d for PBDTTT-C:$PC_{71}BM$ solar cells with 0 %, 1 %, 3 %, and 10 % DIO. The impact of the iterative correction according to Equation 4.3 is visible in Figure 6.10b. This graph compares the corrected charge carrier density $n_{corr}(t_d)$ with n as a function of t_d and as a function of the sum $t_d + t_{max}$. Considering the shortest delay time of 100 ns in Figure 6.10a, $n(t_d)$ increases with the addition of DIO by about 50 % (1 % DIO) and 94 % (3 % DIO) with respect to the device without additive and again decreases by about 20 % (10 % DIO) with respect to 3 % DIO. The trend is in contrast to the fast photogeneration in Figure 6.5a showing a significant increase in transient absorption for 1 % DIO and only minor changes in photogenration efficiency for the 3 % and 10 % DIO blends. In line with the discussion of TA relating to device performance in the previous section, there are two possible explanations for the discrepancy between TA and OTRACE. First, enhanced geminate recombination losses during t_d in the case of the 1 % and 10 % DIO devices (Figure 6.8) might result in a reduced charge carrier density in the OTRACE experiment. Second, an extracted charge carrier density, which is smaller than expected from the yield of fast photogeneration, suggests a less efficient polaron pair dissociation in intermixed D-A phases. Furthermore, an effective extraction requires the adequate collection of charge carriers in interconnected D and A phases. Thus, a fine-tuning of the blend morphology in terms of a demixing of the matrix phases when going from 1 % to 3 % DIO and the formation of percolation pathways seems reasonable. The

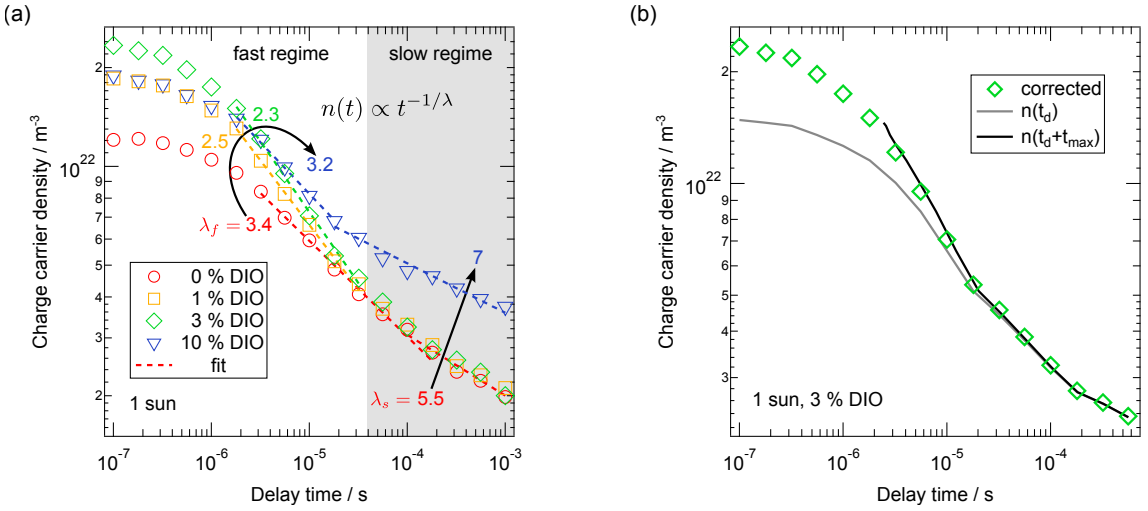

Figure 6.10.: (a) Extracted charge carrier density n vs. t_d of PBDTTT-C:$PC_{71}BM$ devices with varying DIO content derived from OTRACE transients (S = 90 kV s^{-1}). An iterative correction was applied (Equation 4.3). The arrows indicate the trend of the inverse slope λ derived from a power law fit $n(t) \propto t^{-1/\lambda}$ in the fast and slow recombination regime. **(b)** Charge carrier density n as function of delay time t_d and as function of the sum of delay time t_d and the maximum peak position t_{max} compared with the iteratively corrected $n_{corr}(t_d)$ (symbols). Data were derived from OTRACE measurements on PBDTTT-C:$PC_{71}BM$ solar cells processed with 3 % DIO.

reduced initial charge carrier density in the case of the 10 % DIO device similarly supports the assumption of a reduced linking of pure domains and an incomplete extraction under solar cell working conditions.

In addition to the initial charge carrier density, the time dependent decay of n also reflects changes of the active layer morphology induced by DIO. Figure 6.10a shows a fast recombination regime at short times and high n (hereinafter referred to as $f \equiv$ fast) followed by the slow decline of $n(t)$ at long times and small n ($s \equiv$ slow). A similar behavior has already been observed in TA measurements on MDMO-PPV:$PC_{61}BM$ as well as non-annealed and annealed P3HT:$PC_{61}BM$.[261,262] Both regimes follow a power law dependence $n(t) \propto t^{-1/\lambda}$. A corresponding fit yields a substantial decrease in the recombination order given by $\lambda_f = 3.4$ (0 % DIO), 2.5 (1 % DIO), the minimum value of 2.3 (3 % DIO), and the renewed increase to 3.2 (10 % DIO). In contrast, λ_s is about 5.5 and not affected by the additive content up to 3 % DIO. Only the addition of 10 % DIO leads to an increase in λ_s to about 7. The deviation from a pure 2nd order decay, which is characterized by $\lambda + 1 = 2$, suggests a recombination strongly affected by energetically trapped charge carriers.[150,152] Thus, the whole range of t_d is expected to be influenced by both the nongeminate recombination of free polarons as well as the recombination of free and trapped charge carriers. The presence of a fast and slow regime can be understood within the scenario of a recombination dominated by structural properties at short times, i.e., high n, and dominating influence of energetic disorder at long times,. i.e. low n, discussed in detail in Section 6.3. Therefore, the maximum value of λ_f in the case of the 0 % DIO device confirms the scenario for PTB7:$PC_{71}BM$ in the publication by Foertig et al., who suggests the trapping of charge carriers inside isolated fullerene domains.[92] The constant λ_s for 0 %, 1 %

and 3 % DIO can be interpreted as the slope of an exponential distribution of trap states in terms of an Urbach tail energy according to Equation 3.10.[261,263,264] It yields $E_A = \lambda_s kT \approx 140$ meV independent of the blend morphology. The strong decrease in λ_f already for the small amount of 1 % DIO can be seen as a further indication of shrinking acceptor domains that continues up to a DIO content of 3 %. In analogy, the following increase in λ_f for 10 % DIO as compared to 3 % DIO is consistent with the formation of larger polymer phases. However, regarding the substantial increase in λ_s and the fairly large E_A of about 180 meV, a strong influence of the overconcentration of DIO on the energetics of the system, in addition to nanostructural changes, cannot be completely ruled out. In this context, X-ray photoelectron spectroscopy (XPS) revealed a weak signature of the 3d core level of iodine in PTB7:$PC_{71}BM$ films processed with 3 % DIO after drying the active layers under high vacuum conditions.[265] The signature was related to DIO molecules and/or separated iodine atoms remaining in the active layer. They might generate an enhanced trap density or deep tail states in PBDTTT-C:$PC_{71}BM$ films processed with 10 % DIO. It must be emphasized that a possible overestimation of E_A, e.g., as compared to transient photovoltage (TPV) and charge extraction (CE) on PTB7:$PC_{71}BM$ presented by Foertig et al.,[92] is a subject of active study and might result from the OTRACE technique itself. Furthermore, the thickness of the active layer can have an influence on the determination of λ_s.[266]

6.2.5. Conclusions

In this chapter, the effect of a systematically increasing amount of the solvent additive DIO in PBDTTT-C:$PC_{71}BM$ solar cells was studied. The combination of surface imaging, photophysical, and charge extraction techniques revealed a multi-tiered impact of DIO on the active layer morphology and correlated changes in free charge carrier generation and nongeminate recombination dynamics. In analogy to well-studied blends of PTB7:$PC_{71}BM$, the morphology of the blend processed without DIO was found to be dominated by large fullerene domains embedded in a polymer-rich matrix. These agglomerates provoke increased singlet exciton losses due to a rather small D-A interfacial area and give rise to a poor device efficiency of 3.0 %. Already the use of small amounts of DIO (0.6 %) leads to a dramatic decrease in the size of $PC_{71}BM$ domains. The strongly enhanced D-A interface yields a highly efficient exciton dissociation that, however, might be dominated by the generation of bound polaron pairs. In addition, an inefficient collection of free charge carriers in a still finely intermixed D-A matrix without a sufficient number of percolation paths is assumed that would explain the moderate PCE of 5.6 % of the 0.6 % DIO device. The use of up to 3 % DIO shows only a minor impact on the fast photogeneration, which is related to a balanced effect of further decreasing $PC_{71}BM$ domains and the formation of pure PBDTTT-C regions within the intermixed matrix. Both these factors favor free carrier formation and collection. As a result, the 3 % DIO device shows the maximum PCE of 7.1 %. This photovoltaic performance is mostly determined by nongeminate recombination compared to only weak geminate losses. Increasing the DIO content up to 10 % yields a reduced PCE of 5.7 %. Since the measurements revealed a still highly efficient dissociation

of singlet excitons, the reduced photovoltaic performance is related to the photogeneration of predominantly bound polaron pairs and the hindered extraction of free charge carriers in a less interconnected network of pure D and A phases. In the light of the outcomes of Chapter 5, the study demonstrates that the generation of free charge carriers is highly sensitive to the size of both donor and acceptor domains. The findings further highlight the strong impact of blend morphology on the interplay between local photogeneration and charge carrier transport and hence on the photovoltaic performance of BHJ solar cells.

6.3. Nongeminate Recombination in PTB7:$PC_{71}BM$ Blends

Abstract: The effect of an altered blend morphology on charge carrier transport and nongeminate recombination is analyzed by OTRACE measurements on PTB7:$PC_{71}BM$ solar cells processed without and with 3 % of the solvent additive DIO. The study reveals a deviation from a pure bimolecular recombination kinetics in both types of solar cells, that is however stronger affected by charge carrier trapping in the device without DIO. The observation is attributed to the trapping of charge carriers in the interior of large $PC_{71}BM$ domains. As it is known from previous publications and as it is verified by PL measurements within this work, these domains are present in the DIO-free device and their size is significantly reduced through the use of the processing additive. In addition, by relating the charge carrier mobility μ with the generalized recombination rate, it is demonstrated that the carrier density dependence of μ does not account for the super-second order decay in either device. The finding is related to the profound impact of detrapping processes in a partially phase separated blend, slowing-down recombination.

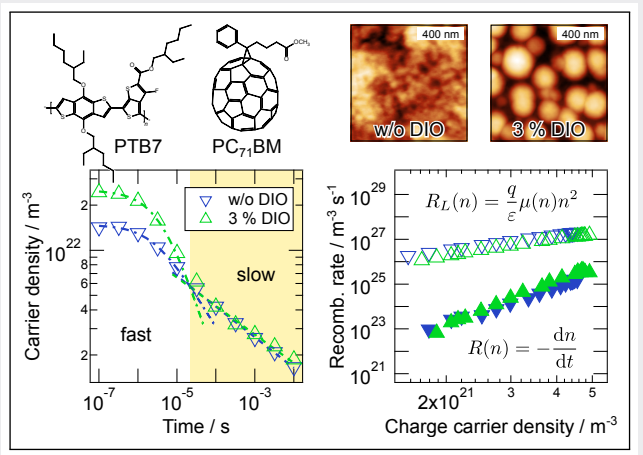

6.3.1. Current-Voltage Characteristics

PTB7:$PC_{71}BM$ devices were fabricated without and with 3 vol% of the processing additive DIO. The j-V characteristics of the solar cells are shown in Figure 6.11. Device parameters can be found in Table 6.3. The measurements were performed under simulated 1 sun conditions. The solar cells had an active area of 9 mm^2. Comparing both devices, the use of DIO results in an almost doubled PCE. This rise in device efficiency is attributed to an increase of 61 % in j_{sc} and of 29 % in FF, compensating the slight decrease of about 6 % in V_{oc}. The result is in accordance with previous publications,[36,91,92] showing a similar effect of DIO on the device parameters of PTB7:$PC_{71}BM$ solar cells spin-cast from chlorobenzene. The increased performance is commonly related to an alteration of the blend morphology mainly characterized by the reduced size of pure fullerene domains that is ascertained in the following using a photophysical approach.

6.3.2. Nanomorphology

Following the reasoning in Section 6.2, the comparison of the spectral shape as well as the absolute value of the photoluminescence of blend films allow conclusions to be drawn about relative changes of the size of neat D and A domains on the ten nanometers length scale and the

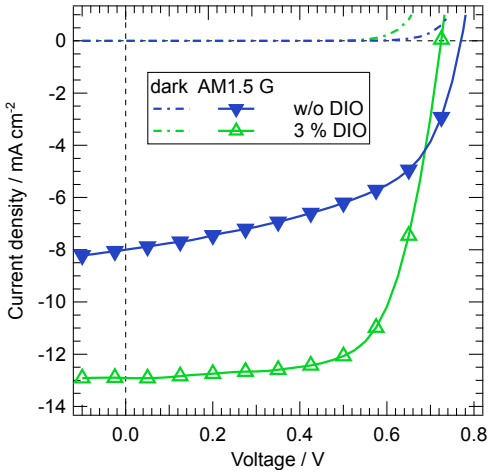

Figure 6.11.: j-V characteristics of PTB7:$PC_{71}BM$ solar cells without and with 3 % DIO. The illumination intensity was adjusted to 1 sun under a simulated AM1.5 G spectrum.

intermixing of the blend constituents. In order to verify the dominant microstructural changes of PTB7:$PC_{71}BM$ blends upon the addition of DIO, steady state PL measurements were performed. Figure 6.12a shows the spectrally corrected, relative photon flux of PTB7:$PC_{71}BM$ films without and with 3 % DIO as well as the normalized photon flux of neat PTB7 and $PC_{71}BM$. An excitation energy of 3.1 eV was used. At this energy, $PC_{71}BM$ shows a much stronger absorbance as compared to PTB7 (Figure 2.4 and 6.3). All films had a thickness that was comparable to the active layer thickness of PTB7:$PC_{71}BM$ devices. Regarding the maximum value of the blend spectra, the PL is reduced by a factor of more than two in the case of the DIO blend. Furthermore, both blend spectra reveal two peaks situated at an energy of 1.57 eV and 1.7 eV with a slightly increased relative contribution of the low energy peak in the case of the DIO blend. By comparison, neat PTB7 reveals a maximum PL emission at around 1.6 eV and neat $PC_{71}BM$ a double peak structure with signatures at about 1.58 eV and 1.75 eV. With regard to the excitation energy and the overlap of donor and acceptor PL, the spectral shape of the blend emission can be correlated with a dominating acceptor PL and an only small proportion of donor PL that is slightly enhanced due to the use of the processing additive. It is important to note that the slight redshift of the blend PL maxima as compared to the neat films might originate from the spectral superposition of the two neat film components.

It is broadly accepted that the morphology of PTB7:$PC_{71}BM$ blends processed without DIO is characterized by the presence of pure fullerene domains with an average diameter in the

	V_{oc} / mV	j_{sc} / mA cm^{-2}	FF / %	PCE / %
w/o DIO	778	8.0	53.8	3.3
3 % DIO	728	12.9	69.4	6.5

Table 6.3.: Photovoltaic parameters of PTB7:$PC_{71}BM$ solar cells without and with 3 % DIO of neat $PC_{71}BM$ and PTB7:$PC_{71}BM$ films. j-V characterization was performed under 1 sun illumination intensity and simulated AM1.5 G conditions.

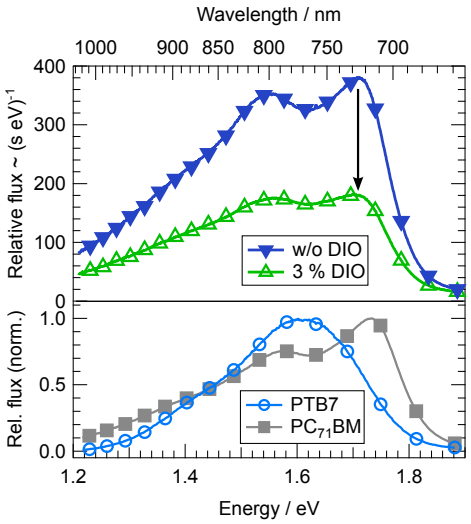

Figure 6.12.: PL spectra of neat PTB7 and $PC_{71}BM$ as well as PTB7:$PC_{71}BM$ blend films without and with 3 % DIO. Films were excited at 3.1 eV. Spectra of neat films were normalized to their maximum value. The arrow indicates the enhanced PL quenching in the blend processed with DIO.

100 nm range that are embedded within a polymer-rich, intermixed matrix phase.[36,85,90,91,93] In addition, based on previous studies, a reduced size of these domains, i.e., a finer D-A intermixing in blends optimized through the use of DIO can be assumed. The spectra shown in Figure 6.12 can be understood on the basis of those findings. Regarding the PL emission of the blend processed without DIO, it is reasonable to assume that the major part of singlet excitons on the acceptor recombine, since the average size of $PC_{71}BM$ domains exceeds the typical exciton diffusion length d_e of 5 to 10 nm.[90] Thus, excitons fail to reach the D-A interface during their lifetime causing a dominating acceptor proportion in the blend PL. A reduced size of $PC_{71}BM$ domains in the blend processed with DIO substantially increases the D-A interfacial area explaining a more efficient quenching of the overall PL emission. In addition, it is more likely that singlet excitons generated within fullerene domains reach the heterojunction, reducing the relative spectral contribution of acceptor PL to the blend emission. In sum, the changing PL emission of PTB7:$PC_{71}BM$ blends without and with DIO supports the assumption of smaller fullerene domains in the case of the DIO blend that is consistent with previous morphological studies.[90,91] This conclusion is further confirmed by a reduced radiative lifetime of fullerene excitons due to the use of DIO. Respective TRPL measurements can be found in Reference 267. Furthermore, AFM height and phase images reveal the presence of a large scale phase separation in DIO-free blends and a smoothing of the surface morphology for blends processed with the solvent additive. Corresponding measurements are shown in Reference 138. It must be emphasized that an apparent proportion of donor emission in the blend spectra indicates the presence of PTB7 domains with a size exceeding d_e within the matrix phase.

6.3.3. Nongeminate Recombination and Charge Carrier Transport

The effect of an altered blend morphology of PTB7:$PC_{71}BM$ solar cells without and with DIO on the nongeminate recombination dynamics and transport properties of photogenerated charge carriers was studied by means of OTRACE. The time dependent decay of the charge carrier density n after photoexcitation at V_{oc} conditions is shown in Figure 6.13a. An illumination intensity of 0.01 sun and 1 sun was chosen. To compensate for recombination during extraction, an iterative correction was applied as described in Section 4.3.2 (Equation 4.3). Both blends reveal a saturation of n at shortest delay times of several 100 ns. With the addition of DIO, the saturation value of $n(t_d)$ increases from $1.5 \cdot 10^{22}$ to $2.5 \cdot 10^{22}$ m^{-3}. This increase in the initial charge carrier density of about 67 % matches the rise of j_{sc} and hence demonstrates the more efficient photocurrent generation of the DIO sample as it was found in j-V characteristics (Figure 6.11). Regarding the decay dynamics of the individual blends, the increased photogeneration realized by a higher illumination intensity provokes a stronger recombination. The finding is a clear evidence for an effective charge carrier lifetime τ_{eff} that depends on the charge carrier density n and hence bimolecular recombination (Section 3.2.2).[219] In addition, a transition from a fast ($f \equiv$ fast) to a slow ($s \equiv$ slow) recombination regime can be found at a delay time of about $4 \cdot 10^{-5}$ s. This observation is in line with the decay dynamics found in solar cells based on the similar copolymer PBDTTT-C in Section 6.2 and with TA studies in literature.[261,262] The presence of two recombination regimes is confirmed by the open circuit voltage decay showed in the inset in Figure 6.13a. According to Equation 4.11, the decay of $V_{oc}(t)$ is consistent with the decrease in n due to charge carrier recombination. Although, OCVD is a straightforward approach to study the recombination dynamics in organic solar cells, e.g., as shown in Chapter 7, the following study focusses on OTRACE measurements, among other reasons, because it allows simultaneous access to n and the charge carrier mobility.

The nongeminate recombination dynamics of the fast and slow regimes are analyzed by the generalized continuity equation (Equation 3.16). Its integration yields

$$n(t) = \left(\lambda k_\lambda t + n_0^{-\lambda}\right)^{-1/\lambda} \quad , \tag{6.2}$$

with the constant of integration n_0. This power law dependence was applied to the fast recombination regime (Figure 6.13b, dash-dotted lines) revealing a change of the recombination order $\lambda + 1$ from $\lambda_{f,w/o} + 1 = 3.3$ (without DIO) to $\lambda_{f,w/} + 1 = 2.2$ (3 % DIO). In the slow regime, i.e, for times $k_\lambda \lambda t \gg n_0^{-\lambda}$, Equation 6.2 simplifies to $n(t) \propto t^{-1/\lambda}$ (dotted lines) yielding comparable values for both devices of $\lambda_{s,w/o} + 1 = 5.9$ and $\lambda_{s,w/} + 1 = 6.3$. The deviation from a pure 2nd order decay ($\lambda + 1 = 2$) indicates a recombination strongly affected by charge carrier trapping over the whole range of t_d.[150,152] In the case of a strong D-A phase separation, the prerequisite for nongeminate recombination is that electrons and holes meet at the D-A interface. This includes the interaction of free polarons as well as the interaction of free and trapped charge carriers. Regarding charge carrier trapping, spatial and energetic traps have to be distinguished. The former describes charge carriers that are locally free but confined in

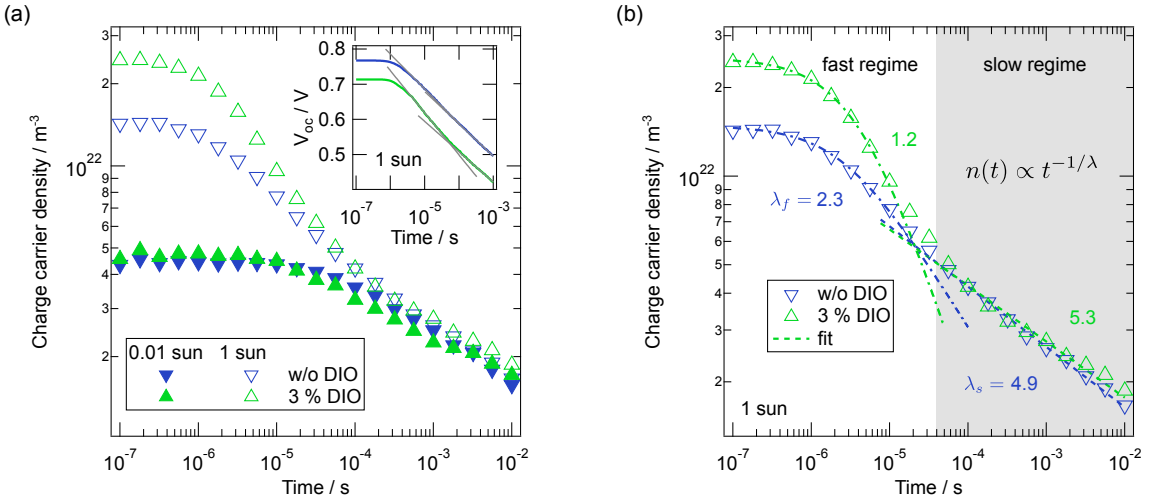

Figure 6.13.: (a) Extracted charge carrier density n vs. t_d of PTB7:$PC_{71}BM$ devices without and with 3 % DIO derived from OTRACE transients (S = 60 kV s^{-1}) recorded under 0.01 and 1 sun illumination intensity. Data were corrected iteratively (Equation 4.3). The inset shows the respective V_{oc} transients (smoothed) recorded under 1 sun illumination intensity. Lines were added as a guide to the eye illustrating two different recombination regimes. **(b)** Identification of the inverse slope λ by power law fits of $n(t)$ in the fast and slow recombination regime.

neat domains due to missing percolation to the electrodes. Hence, spatially trapped charge carriers can interact with free ones but are not extracted in CE experiments. This may lead to an underestimation of the recombination order, i.e., $\lambda + 1 < 2$. Energetic trapping includes charge carriers in the tails of the DOS and may, in contrast, account for $\lambda + 1$ exceeding 2. Energetically trapped charge carriers can participate in a recombination process in two cases. Either they are trapped very close to the heterointerface or, since trapping within neat material phases protects from recombination, they have to be thermally activated,. i.e., released from trap states, making them mobile once again. This crucial impact of localized trap states on the nongeminate recombination dynamics has been reported in several publications.[149,261,262,268] In particular, in References 150 and 152, an increasing deviation from a 2nd order decay with decreasing temperature in P3HT:$PC_{61}BM$ and pBTCT-C_{12}:$PC_{61}BM$, respectively, was explained by the delayed release of charge carriers from energetic traps at low T. A delayed activation due to reduced thermal energy makes recombination less probable since potential recombination partners might already have recombined or are extracted, slowing-down charge carrier decay. Regarding PTB7:$PC_{71}BM$ the super-second order decay can be understood along the same lines, but taking into account the altered nanostructure rather than varying T. The blend morphology of the DIO-free blend is characterized by large, pure fullerene domains. Thus, it seems less likely that charge carriers released from energetic traps in the interior of these domains reach the D-A interface, since re-trapping may occur more frequently as compared to the 3 % DIO device. Furthermore, it seems reasonable to assume that the structural difference between both blends will dominate the decay dynamics at short t_d, i.e., high n, as long as released charge carriers easily find recombination partners. With increasing t_d, i.e., low n, recombination will become less probable since, according to the reasoning above, low-lying trap states contribute

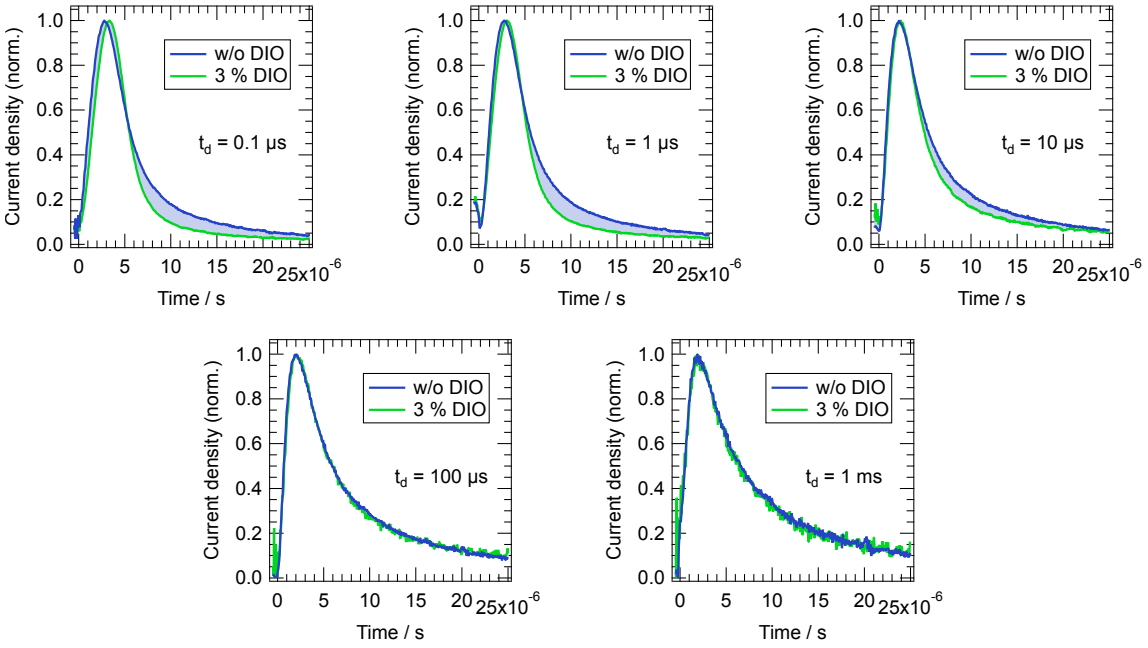

Figure 6.14.: Photocurrent transients $j(t) - j_0$ of PTB7:$PC_{71}BM$ devices without and with 3 % DIO recorded at different delay times t_d. Measurements were performed under 1 sun illumination intensity using a voltage ramp of $S = 60$ kV s^{-1}. All transients were normalized to their maximum value. The shaded areas illustrate an increased contribution of trapped charge carriers at short t_d in the case of the additive-free device.

more and more. Thus, nongeminate recombination will preferentially be affected by thermal activation processes. According to this argumentation, the super-second order decay can be related to energetic trapping. Furthermore, the appearance of a fast and slow recombination regime, as monitored by OTRACE, most probably results from morphological properties and energetic disorder dominating the decay dynamics at high and low n, respectively. Hence, the enhanced $\lambda_{f,w/o}$ of the DIO-free device as compared to $\lambda_{f,w/}$ can be understood in terms of an intensified trapping of charge carriers within neat $PC_{71}BM$ domains, as supposed by Foertig et al.[92] This enhanced contribution of trapped charge carriers is also evident in OTRACE transients. Figure 6.14 shows the normalized photocurrent transients recorded on both devices at different delay times. At 100 ns, 1 µs, and 10 µs, transients of the DIO-free devices show a peak broadening indicating that the extraction of charge carriers requires higher field strength relative to the DIO device, i.e., their release is hindered by trapping. Similar effects were observed recently in PCDTBT:$PC_{61}BM$ solar cells supported by drift-diffusion calculations.[227,269] Regarding the recombination order at long times, λ_s, comparable values between both devices imply an energetic disorder in terms of an exponential distribution of trap states,[261] which is independent of the preparation conditions and hence the blend morphology. This finding might be related to an unchanged D-A matrix phase as supposed by Collins et al.[91] It is important to note that the values of λ_f derived from OTRACE measurements coincide well with TPV and CE results.[92] However, a distinct deviation is found for λ_s. As outlined above, this difference could be induced by the particular experimental conditions.

In order to study the effect of DIO on the transport properties, the effective charge carrier mobility μ was derived from t_{max} of OTRACE transients recorded under 0.01 sun and 1 sun illumination intensity according to Equation 4.6. Typical values of t_{max} were on the order of 10^{-6} s corresponding to electric field strengths of about $1.5 \cdot 10^6$ V m^{-1}. Figure 6.15a depicts μ as a function of delay time. Comparing both light intensities, μ shows a strong initial increase with delay time for 1 sun. This increase demonstrates the striking impact of RC rise on the OTRACE extraction peak, causing a shift of t_{max} towards longer times (Section 4.3.2).[219] This RC limitation extends to longer delay times in the case of the DIO-free device due to delayed bimolecular recombination. In the case of 0.01 sun, no initial increase but a constant value of μ can be found. Although it cannot be fully excluded that data recorded at this low illumination intensity is free of RC distortion, the charge carrier mobility was evaluated using 0.01 sun in the following. A linear fit ranging from 100 ns to 180 µs (without DIO) and to 32 µs (3 % DIO) yields a charge carrier mobility of $\mu_{w/o} = 1.73 \cdot 10^{-8}$ m^2 Vs^{-1} and $\mu_{w/} = 1.15 \cdot 10^{-8}$ m^2 Vs^{-1} for the blend processed without and with DIO, respectively. By using SCLC, Foster et al. found a nearly constant hole mobility of $\mu_h = 1.5 \cdot 10^{-8}$ m^2 Vs^{-1}, but a decrease in the electron mobility from $\mu_e = 4.3 \cdot 10^{-9}$ m^2 Vs^{-1} to $1.4 \cdot 10^{-9}$ m^2 Vs^{-1} in additive-free and optimized PTB7:$PC_{61}BM$ devices. This overall moderate electron transport was related to a close D-A intermixing within the matrix phase, that is further reduced in the optimized blend due to a smaller size of pure fullerene domains. Keeping in mind that OTRACE yields information about an average electron and hole mobility without specifying the contribution of μ_h and μ_e, the trend of charge carrier mobility as observed in this work agrees well with the results published by Foster et al. It is striking that Figure 6.15a reveals a relaxation of μ towards longer times starting at about 200 µs (without DIO) and 50 µs (3 % DIO) that most probably originates from the recombination of the fastest charge carriers first taking place. Since the charge carrier density is simultaneously decreasing with t_d (Figure 6.13), this observation is equivalent with a n-dependent charge carrier mobility. Combining $n(t_d)$ and $\mu(t_d)$, Figure 6.15b shows a slightly stronger carrier density dependence of μ for the DIO device. This apparent n-dependence of μ might also be caused by a time dependence of μ due to charge carrier relaxation into tail states during t_d. In order to ensure a prevalent n-dependence, μ was derived in additional, illumination dependent OTRACE measurements on a second set of PTB7:$PC_{71}BM$ devices without and with 3 % DIO. The samples had an active area of 3 mm^2 and a photovoltaic performance comparable to the ones in Figure 6.3. The inset in Figure 6.15b depicts μ as a function of t_d derived for a constant charge carrier density of $7 \cdot 10^{21}$ m^{-3} and an illumination intensity ranging between 0.01 sun and 1 sun. Although, the measurements reveal slightly different magnitudes of μ as compared to Figure 6.15a, which might be explained by the different experimental conditions, only a minor time dependence is visible. This finding justifies that mobility is relaxed at this timescale making charge charier concentration dependence the dominant factor.

So far, the recombination dynamics in Figure 6.13 was analyzed under the assumption of the generalized continuity equation given in Equation 3.16. Deviations from a pure 2nd order decay were found, which are correlated with a substantial impact of charge carrier trapping in separated phases. Furthermore, Figure 6.15a revealed a charge carrier mobility depending

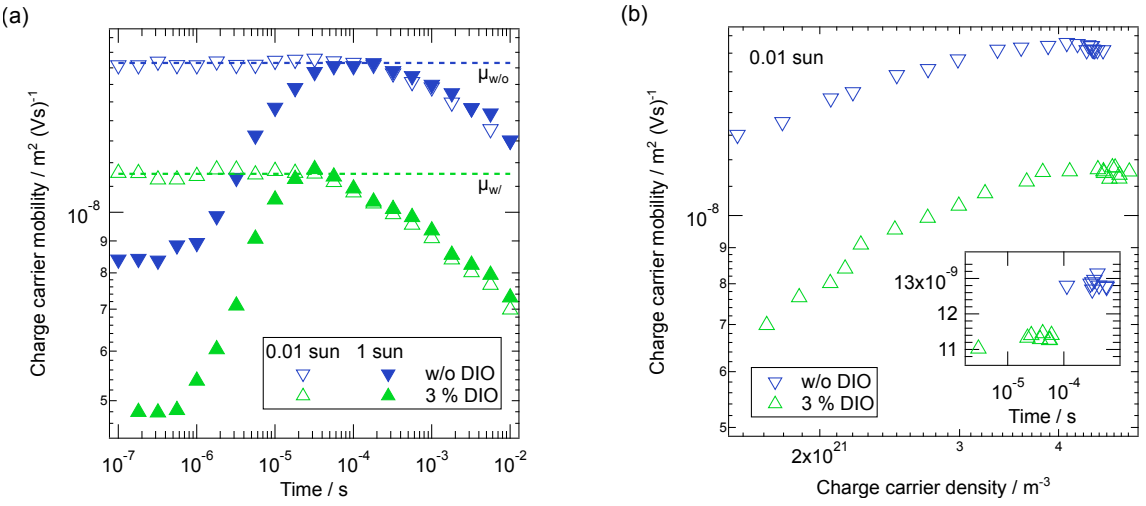

Figure 6.15.: Charge carrier mobility μ vs. **(a)** delay time t_d and **(b)** charge carrier density n of PTB7:$PC_{71}BM$ devices without and with 3 % DIO derived from the maximum peak position t_{max} of OTRACE transients ($S = 60$ kV s^{-1}). The inset shows μ vs. t_d derived from illumination dependent OTRACE transients and a constant n ($S = 75$ kV s^{-1}).

on the charge carrier density n. In this context, a super-second order kinetics was linked with the n-dependent charge carrier mobility in an earlier publication, i.e., it was claimed that $\mu(n)$ completely accounts for an additional n-dependence of the recombination coefficient k_{rec} in a pure bimolecular approach (Section 3.2.2).[153] In contrast, Rauh et al. showed that $\mu(n)$ alone cannot explain a recombination order exceeding two in PTB7:$PC_{71}BM$ solar cells and supposed that a trap-assisted recombination mechanism has to be considered.[270] The statement was justified by the deviating carrier density dependence of $R(n)/n^2$, being proportional to k_{rec}, and $\mu(n)$ derived by relating j-V and CE measurements. However, the approach required the assumption of a field independent polaron pair dissociation and thus was limited to the device processed with 3 % DIO.[92] Furthermore, the charge carrier density was determined by CE at short circuit conditions where corresponding internal electric fields may be too small to extract all charge carriers.[117,123] Bearing in mind the latter, the deviating n-dependence of $R(n)/n^2$ and $\mu(n)$ was most likely overestimated. In the following, the proposition by Rauh et al. is verified for both PTB7:$PC_{71}BM$ devices without and with DIO using $n(t_d)$ and $\mu(n)$ as derived simultaneously by OTRACE measurements. Using n as a function of t_d the recombination rate can be derived according to

$$R(n) = -\frac{\mathrm{d}n}{\mathrm{d}t} \quad . \tag{6.3}$$

By contrast, the Langevin-type recombination rate (Chapter 3.2.2) is given by

$$R_L(n) = \frac{q}{\varepsilon_r \varepsilon_0} \mu(n) n^2 \quad . \tag{6.4}$$

Figure 6.16a shows the general (Equation 6.3) and the Langevin-type (Equation 6.4) recombination rates for an illumination intensity of 0.01 sun. $R_L(n)$ was calculated using both the carrier

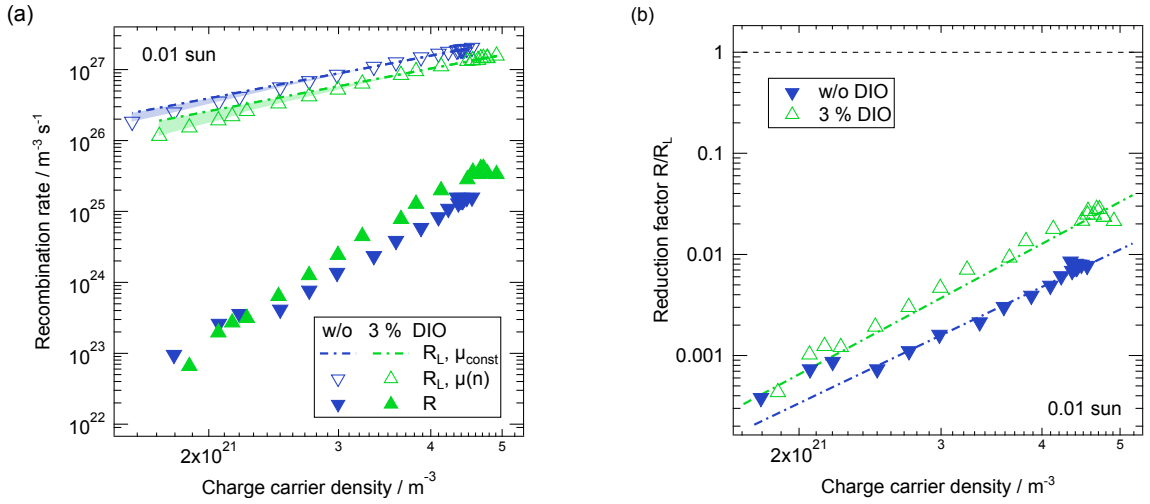

Figure 6.16.: (a) General and Langevin-type recombination rate R and R_L vs. charge carrier density n of PTB7:$PC_{71}BM$ devices without and with 3 % DIO derived from OTRACE measurements under 0.01 sun illumination intensity. **(b)** Reduction factor R/R_L vs. n calculated from the graphs on the left. The dash-dotted lines serve as guides to the eye.

density dependent $\mu(n)$ (Figure 6.15a, open symbols) as well as the constant values $\mu_{w/o}$ and $\mu_{w/}$ (Figure 6.15a, dashed lines). A dielectric constant of $\varepsilon_r = 3.2$, derived from the capacitive response of OTRACE transients, was used. Comparing the Langevin-type recombination rates, a clear impact of the n-dependence of μ on $R_L(n)$ can be seen for small charge carrier densities (shaded areas). However, the effect does not account for the increased slope and the overall decreased value of $R(n)$. Both the different n-dependence of $R(n)$ and $R_L(n)$ as well as the substantially reduced Langevin recombination become clearer by calculating the reduction factor $R(n)/R_L(n)$ (Figure 6.16b). It clearly shows a strong charge carrier dependency and an absolute value less than 1 (dashed line). In addition, smaller values of $R(n)/R_L(n)$ were found for the DIO-free device.

According to Equation 6.3 and 6.4, the reduction factor $R(n)/R_L(n)$ relates the n-dependence of $\mu(n)$ and $R(n)/n^2$. The clear deviation from unity as well as the finite slope of $R(n)/R_L(n)$ in Figure 6.16b identify the diverging carrier density dependence of both quantities. The finding might be related to the different origin of transport and recombination, occurring within neat D and A phases and at the heterointerface, respectively. Thus, different mobile vs. trap populations in the bulk and at the interface would be the consequence. In addition, $R(n)/R_L(n)$ clearly demonstrates that the recombination prefactor is not proportional to $\mu(n)$. Thus, the super-second oder decay cannot be explained by the n-dependence of μ alone. This finding confirms the result of Rauh et al. for optimized PTB7:$PC_{71}BM$ solar cells and, additionally, demonstrates that the conclusion also holds for additive-free devices. Following the reasoning above and in Reference 270, the D-A phase separation has to be considered to account for a recombination order exceeding two. As outlined above, charge carriers in a phase-seperated D-A blend have to be present at the heterointerface in order to recombine. Charge carriers trapped within the bulk of pure domains are unable to undergo recombination and have to be ther-

mally activated to contribute to the species of free ones and to reach the interface. Therefore, two limiting factors exist that lower the nongeminate recombination rate: the trap distribution, i.e., the energetic disorder of the blend, and the extent of phase separation. Since the similar decay of $n(t_d)$ in the slow recombination regime in Figure 6.13 suggest a comparable tail energy of both blends, it is a reasonable assumption—from a qualitative point of view—that the reduced Langevin recombination, i.e., the deviation of the reduction factor from unity, is controlled by structural properties. In this regard, the smaller magnitude of $R(n)/R_L(n)$ in the case of the DIO-free device most likely results from the increased size of fullerene domains. Recently, Gorenflot et al. analyzed the recombination dynamics in P3HT:$PC_{61}BM$ blend films revealing both a super-second order decay and a reduced recombination rate and thus a similar behavior as compared to PTB7:$PC_{71}BM$.[271] The authors ruled out previously proposed models including the two-dimensional transport in crystalline P3HT phases as well as charge carrier density gradients near the electrodes, and discussed several potential explanations for their findings. First, it was found that, even if phase separation yields a reduced recombination rate, the effect is to small to explain experimental observations and does not account for a higher order recombination dynamics. Second, a possible n-dependence of μ, as expected for an exponential DOS, was not completely eliminated but considered unlikely to provoke a super-second order decay, since both P3HT and $PC_{61}BM$ show a behavior consistent with a GDOS. In addition, it was argued that a non-encounter limited recombination, i.e., a rather slow recombination via bound polaron pairs as intermediate step, may account for the reduced recombination rate, but not for $\lambda + 1 > 2$. Finally, the authors showed that the scenario of a mixed interfacial phase between pure D and A domains with an expDOS and a GDOS, respectively, and the recombination via interfacial states reproduces both observations. The conclusions for PTB7:$PC_{71}BM$ in this work are only in part consistent with the findings in Reference 271. Calculating the reduction factor $R(n)/R_L(n)$ from OTRACE data supports that the n-dependence of $\mu(n)$ does not account for the higher order kinetics alone. Furthermore, Gorenflot et al. predicts that R should increase with more interfacial volume fraction, which is in accordance with Figure 6.16 revealing higher recombination rate for the optimized blend and hence smaller domain sizes. However, relating the deviation from a 2^{nd} order decay to the size of fullerene domains clearly contradicts Gorenflot et al. They propose that there is no way of explaining super-second order kinetics with phase separation. The contradiction requires further investigation. Thereby, it must be taken into account that the recombination rate in the case of the 3 % DIO device is close to second-order kinetics and that the morphology of the non-optimized blend, revealing pure fullerene domains of several 100 nm in diameter, differs considerably from conventional polymer:fullerene blends.

6.3.4. Conclusions

PTB7:$PC_{71}BM$ solar cells show a substantial increase in the photovoltaic performance through the use of the processing additive DIO. The improved PCE is commonly related to the decreasing size of pure fullerene domains embedded within an intermixed matrix phase and thus an

enhanced D-A intermixing. [36,85,90,91] In the present chapter, steady state PL spectroscopy was applied to verify the distinct nanostructure of PTB7:PC_{71}BM blends processed without and with 3 % DIO. A pronounced quenching of the blend emission and a decreased relative contribution of the acceptor component to the overall PL is related to a decreased size of PC_{71}BM domains caused by DIO. The effect of the altered blend morphology on the nongeminate recombination dynamics and transport properties was studied using OTRACE. The measurements revealed a super-second order decay and reduced Langevin recombination in both devices. Addressing charge carrier transport, a reduced mobility of the DIO blend was found that is consistent with literature. [93] While both devices showed a slight carrier density dependence of μ, it is demonstrated that $\mu(n)$ is not proportional to the recombination rate in either case. The result gives further evidence that super-second order kinetics in BHJ solar cells cannot be explained by the carrier density dependence of μ alone. In accordance with Rauh et al., [270] the deviation from a pure bimolecular decay is related to charge carriers trapped in separated D-A phases leading to a slowed-down decay of n. A stronger impact of trapping in the case of the DIO-free device is seen as further indication for charge carriers confined in large PC_{71}BM agglomerates, as suggested by Foertig et al. [92] Contrary to the scenario presented in this chapter, Gorenflot et al. recently proposed recombination via interfacial states rather than phase separation as the origin of a super-second order decay. [271]

7. The Effect of Supramolecular Order

Abstract: To understand the outperforming efficiency of vacuum deposited MD376:C_{60} solar cells relative to their solution processed counterpart MD376:$PC_{61}BM$, free charge carrier generation and transport properties of the MC dye based blends are studied. Pre-bias dependent TDCF measurements identify the field dependence of photocurrent generation as the most detrimental factor limiting photovoltaic performance of both devices. The geminate losses appear to be stronger in the case of the solution processed blend. Furthermore, relating illumination dependent j-V characterization and OTRACE measurements, imbalanced transport properties—most likely caused by a reduced hole mobility—are found in MD376:$PC_{61}BM$. Both observations are related to an enhanced charge carrier delocalization due to a higher degree of dimerization in the vacuum deposited blend. The more efficient polaron pair dissociation yield in the case of MD376:C_{60} is additionally associated with a stronger interaction of the donor and acceptor constituents at the heterointerface. The study clearly demonstrates the important influence of supramolecular order on the functionality of organic BHJ solar cells based on MC dyes.

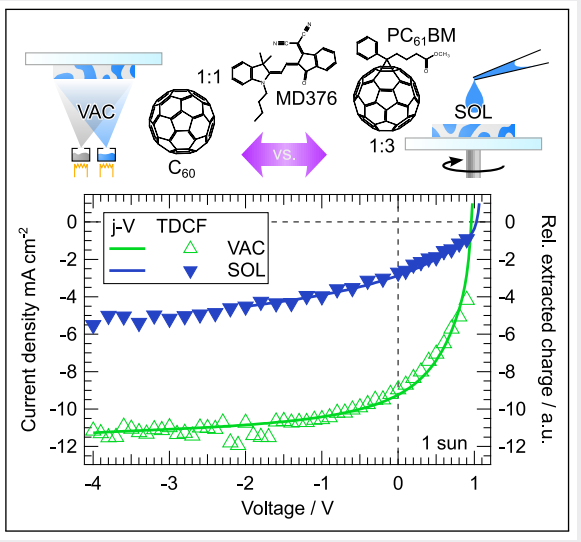

7.1. Introduction

Merocyanine dyes are predestined for the application as donor components in organic BHJ solar cells due to their easy synthesis, their widely tunable electronic properties, and a strong absorption reaching the NIR region.[177] The latter is related to the D-A structure of the small molecules causing an intramolecular CT and a strong permanent ground state dipole moment (Section 4.1.1). Although the bipolarity is expected to cause a high energetic disorder in amorphous solids impeding hopping transport,[272] the chromophores were successfully introduced as electron donor in solution processed blends with $PC_{61}BM$ by Kronenberg et al. in 2008.[174] The PCE could be further increased up to 4.5 % by the optimization of structural and electronic

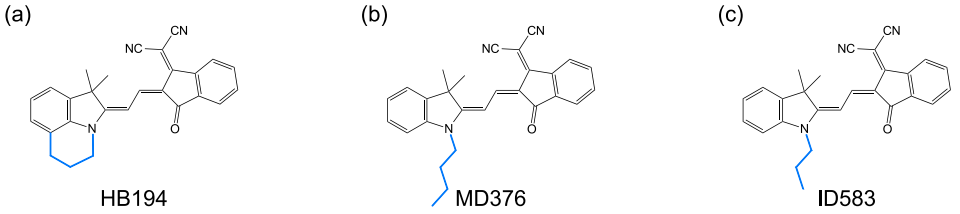

Figure 7.1.: Molecular structure of the MC dyes **(a)** HB194, **(b)** MD376, and **(c)** ID583. The molecules differ by the alkyl substituents attached to donor moiety (blue).

properties as well as an optimized layer stack.[176,177] This rather remarkable photovoltaic performance becomes possible due to a strong dipole-dipole interaction of dye monomers that leads to the formation of close centrosymmetric dimeric aggregates in solid films.[180] The aggregation effectively compensates the bipolarity. Since MC dyes typically show both a high thermal stability and a high solubility, they can be processed by either thermal deposition under high vacuum conditions (VAC) or spin casting from conventional organic solvents (SOL). Using vacuum deposition, the PCE of BHJ solar cells based on MC dyes could be raised up to 6.1 %.[273] For the first time, the effect of the two processing techniques on device efficiency was systematically investigated for the MC dyes MD376 and HB194 blended with either C_{60} (VAC) or $PC_{61}BM$ (SOL).[178] The comparison revealed an increased photovoltaic performance of the VAC devices by a factor of almost two. This superior PCE results from a slightly reduced V_{oc} that is compensated by higher values of j_{sc} and FF. The finding was claimed to be the result of an improved charge carrier generation and reduced recombination losses due to a smaller scale phase separation of the VAC active layer with a typical scale of 10 nm as compared to 20 to 30 nm in the case of the SOL blend. In place of the butyl side chain (MD376), the donor unit of HB194 is bridged by a propylene group (Figure 7.1a and b). This modification of the molecular structure is ascribed a higher rigidity of the donor moiety and an increased molecular interaction in solid films. Indeed, in an earlier publication, an increased PCE of HB194:$PC_{61}BM$ as compared to MD376:$PC_{61}BM$ was found. The finding was explained by superior transport properties due to a more favorable molecular packing of HB194 allowing a higher dye loading in the blend.[176] The previous studies demonstrate that the optimization of the MC dye based BHJ solar cells is decisively driven by the molecular self-assembly and the phase separation of the D and A constituents of the blend and thus occurs on the so-called supramolecular level, i.e., on the ten nanometers length scale.[180] However, despite the key significance of supramolecular order, its effect on the fundamental steps of photocurrent generation has not yet been studied in detail.

The present chapter addresses this issue and presents an analysis of charge carrier transport and recombination in vacuum deposited MD376:C_{60} and solution processed MD376:$PC_{61}BM$ devices. For this purpose, the charge extraction techniques TDCF (Section 4.3.1) and OTRACE (Section 4.3.2) are applied in order to study the field dependence of free charge carrier generation and charge carrier mobility. In addition with OCVD an alternative approach is chosen to elucidate the nongeminate recombination dynamics of both devices. Conclusions about the molecular arrangement are drawn by studying the absorption and photoluminescence of VAC

and SOL films. Their results are finally correlated with the results of the charge extraction measurements. All samples studied in this chapter were processed by Steven Graf and Julian Krumrain (University of Cologne). The external and internal quantum efficiency as well as absorption and PL spectra were measured by Steven Graf. Their more detailed analysis can be found in Reference 274. OTRACE measurements were performed together with Andreas Baumann (Bavarian Center for Applied Energy Research e.V.).

7.2. Results

7.2.1. Photovoltaic Performance

Figure 7.2a shows the j-V characteristics of vacuum deposited MD376:C_{60} and solution processed MD376:$PC_{61}BM$ devices. The corresponding photovoltaic parameters are summarized in Table 7.1. The devices had an active layer thickness of about 55 nm (VAC) and 45 nm (SOL), demonstrating the strong absorption of MC dyes relative to common donor polymers. In addition, the high V_{oc} of both devices can be mainly ascribed to the low-lying HOMO level as the second major benefit of this type of chromophores.[275] It must be noted that the open circuit voltage is additionally increased by the use of MoO_3 as HTL instead of PEDOT:PSS.[273] Since V_{oc} of an organic BHJ solar cell depends on the difference between the HOMO level of the donor and the LUMO level of the acceptor,[164,165] the slightly reduced V_{oc} of the VAC device can be related to the higher LUMO level of $PC_{61}BM$ relative to C_{60} (Section 4.1.2).[178] With regard to device performance, clear differences in regard to the two processing techniques were found despite an almost similar V_{oc}. The PCE of the VAC device exceeds the efficiency of the solution processed sample by almost a factor of 4. This rise of photovoltaic performance results from a substantial increase in j_{sc} and FF compensating the trend in V_{oc}. The finding is in agreement with the performance gain of vacuum deposited HB194 and MD376 devices in a previous publication,[178] although different layer stacks as well as blend ratios of 1:1 for both processing techniques were used in that case. It is important to note that MD376:C_{60} devices showed the highest efficiency for a mixing ratio of 1:1 in contrast to the best performing 1:3 MD376:$PC_{61}BM$ blends. This lower dye loading of the optimized SOL device can be correlated with a reduced absorption and hence accounts to a certain extent for the moderate j_{sc} as it has been concluded in an earlier work.[176] This effect is reinforced by a thinner active layer of the SOL device.

The dark j-V curves are shown on a semilogarithmic scale in Figure 7.2b. It is striking that the SOL device shows a dark saturation current that exceeds the VAC device by more than two orders of magnitude. The impact of parallel resistance is visible up to a voltage of about 0.9 V and therefore, it is more pronounced as compared to the VAC device. This indicates the presence of local shunts that might result from a thinner active layer. The finding is also evident from the dependence of V_{oc} on the illumination intensity (Figure 7.2b, inset). The open circuit voltage shows an almost linear behavior over the hole intensity range in the case of the VAC device, but a strong impact of light intensity in the case of MD376:$PC_{61}BM$. This may explain the non-vanishing V_{oc} of the VAC device in the dark j-V characteristics, which is most prob-

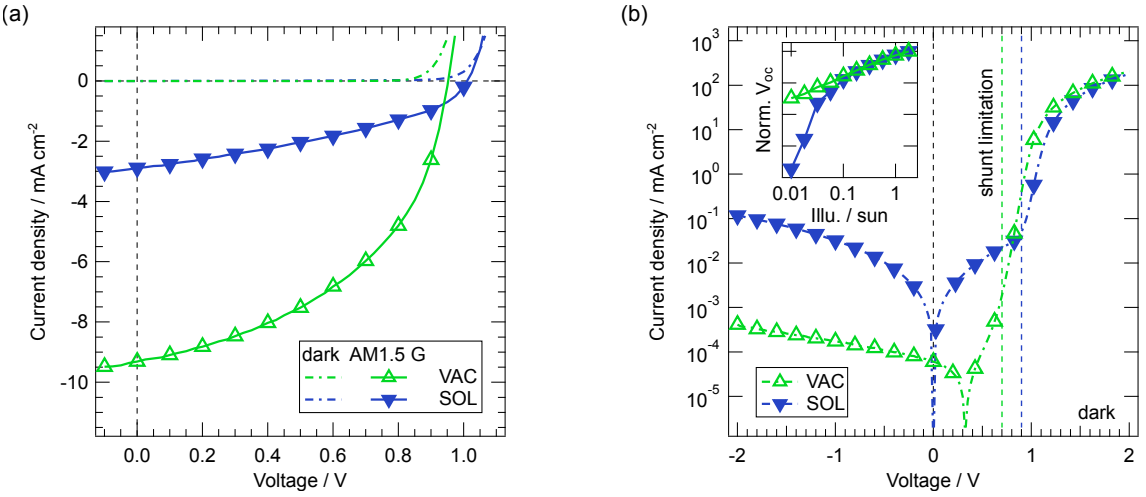

Figure 7.2.: (a) j-V characteristics of vacuum deposited MD376:C_{60} and solution processed MD376:$PC_{61}BM$ solar cells measured in the dark and under a simulated AM1.5 G spectrum with an intensity adjusted to 1 sun. **(b)** Dark j-V characteristics in semilogarithmic representation. The inset shows V_{oc} normalized to its maximum value vs. illumination intensity. The illumination dependent measurements were performed in the optical cryostat using a high power white LED.

ably induced by residual light and thus demonstrates a high sensitivity to lowest illumination intensities.

Reflecting the trend in j-V characteristics, the external quantum efficiency of the VAC device shows a maximum value of 57 % at an energy of about 2 eV, which is reduced to 28 % in the case of the SOL sample (not shown). In order to compare both devices with respect to the different spectral contributions to the photocurrent, the EQE was normalized to the respective maximum value (Figure 7.3a). The graph reveals two striking characteristics. First, MD376:C_{60} shows an enhanced contribution below an energy of 2.0 eV as compared to MD376:$PC_{61}BM$ and hence below the absorption onset of MD376 (shaded area). The observation might be related to an improved D-A interaction in the VAC blend resulting in an increased contribution of interfacial CT complexes to the photocurrent, as discussed below. Additionally, a shift in absorption due to a variation of molecular packing in the solid film on the dye's energy levels seems reasonable. Second, whereas the SOL device shows an only minor contribution to the photocurrent between 2.5 eV and 3.3 eV where MD376 contributes only marginally to the absorption of the blend, the VAC device reveals a substantial increase in the EQE regarding that energy range. The origin of this increased contribution as well as of the outperforming EQE of the VAC device can be partly understood by looking at the internal quantum efficiency (Fig-

	V_{oc} / mV	j_{sc} / mA cm^{-2}	FF / %	PCE / %
MD376:C_{60}, 1:1 (VAC)	952	9.3	47.3	4.2
MD376:$PC_{61}BM$, 1:3 (SOL)	1010	2.9	37.9	1.1

Table 7.1.: Photovoltaic parameters of vacuum deposited MD376:C_{60} and solution processed MD376:$PC_{61}BM$ solar cells measured under 1 sun and simulated AM1.5 G conditions.

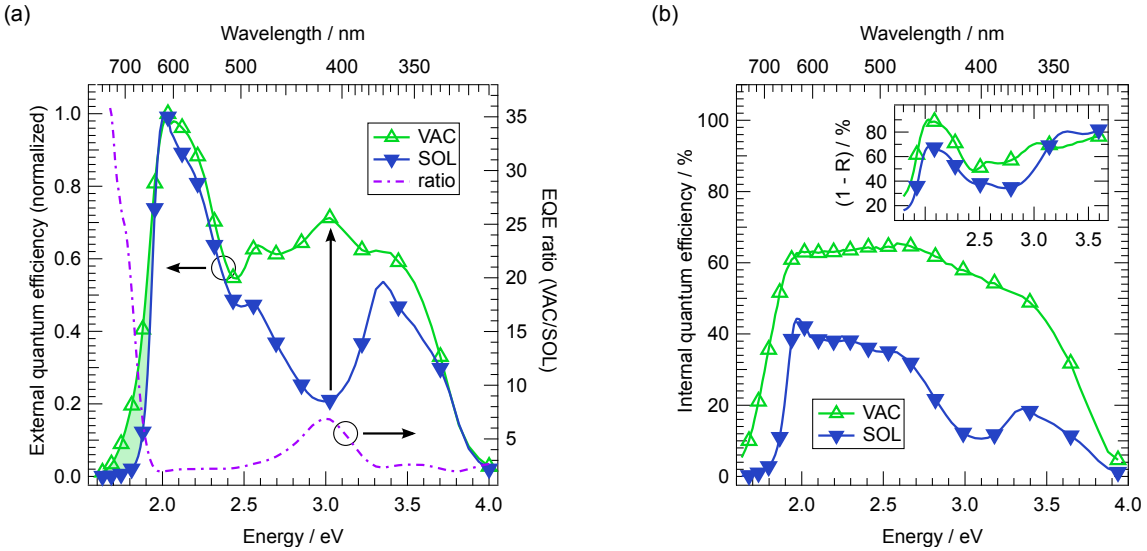

Figure 7.3.: (a) External and **(b)** internal quantum efficiency of MD376:C_{60} (VAC) and MD376:$PC_{61}BM$ (SOL) devices. The EQE was measured without background illumination and normalized to its maximum value. The IQE was derived by the ratio of the EQE and the respective absorbance measured as (1 – reflectance) as shown in the inset.

ure 7.3b), calculated by the ratio of the EQE and the absorbance. The latter was derived from the reflectance of samples comparably stacked as working devices, with the exception of larger metallic electrodes. Whereas the IQE of the VAC device is almost constant in the whole reliable energy range from 2.0 to 3.8 eV, the SOL device shows a pronounced dip between 2.5 eV and 3.5 eV. Since this energy range coincides with the onset of $PC_{61}BM$ absorption (Figure 7.3b, inset), the decrease might be interpreted in terms of a differing fullerene packing in the SOL films used for measuring EQE and reflectance, causing slightly shifted absorption spectra. Albeit the origin of the dip cannot be fully clarified, the rise of the IQE of the VAC device in that energy range is smaller than the increase in EQE that indicates the formation of an additional absorption band. However, regarding the absolute values of the IQE, MD376:C_{60} shows an overall enhanced efficiency. This confirmation of the trend in EQE implies that the difference in j_{sc} is only minor driven by a stronger absorption, but more likely by a highly efficient charge carrier generation and collection in the VAC blend.

7.2.2. Charge Carrier Transport

In order to study the origin of the large difference in fill factor, transport properties of both devices were analyzed. The field dependence of the charge carrier mobility μ was studied by OTRACE measurements. The electric field F was varied by changing the slope of the voltage ramp S. An illumination intensity of 0.1 sun and a constant delay time of 56 µs was chosen. In a prior, intensity and delay time dependent measurement (not shown), both a vanishing distortion by RC effects and no relaxation were found for these settings. The maximum peak position of the OTRACE transients was evaluated according to Equation 4.6. Figure 7.4a shows μ as a function of the square root of the electric field $F^{1/2}$, derived from $F = St_{max}/d$, revealing

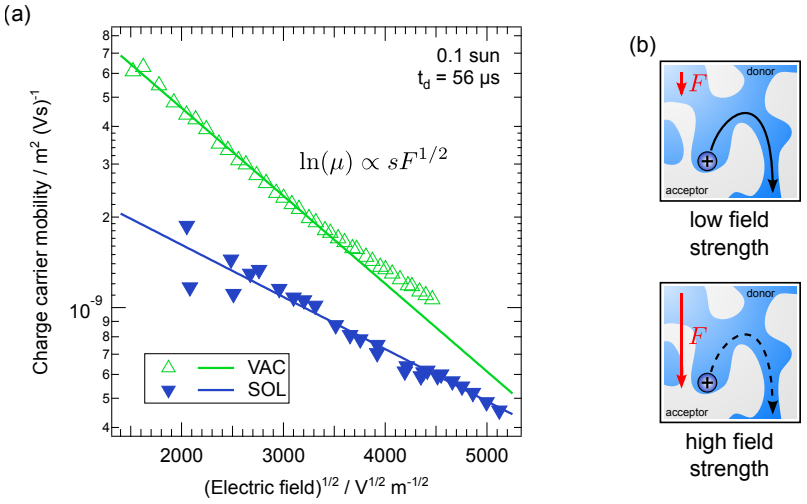

Figure 7.4.: (a) Effective charge carrier mobility μ vs. the square root of the electric field $F^{1/2}$ obtained from field dependent OTRACE transients of MD376:C_{60} (VAC) and MD376:$PC_{61}BM$ (SOL) devices (symbols). The voltage ramp S was varied form 50 to 633 kV m^{-1} (VAC) and 50 to 467 kV m^{-1} (SOL). μ was fitted by an exponential (solid lines). **(b)** Schematic illustration of the negative field dependence of μ using the example of a hole in a D-A network. For high field strengths, the movement against the direction of the electric field becomes less probable.

a two to three times higher mobility of the VAC device. In addition, both blends show a distinct negative dependence of μ on the electric field. Such a negative field dependence has also been reported for other D-A blends, e.g., P3HT:$PC_{61}BM$ and PCPDTBT:$PC_{71}BM$. [96,276] In accordance with the Gaussian disorder model (Section 3.2.1), the finding can be related to a high spatial disorder of the studied blends as illustrated in Figure 7.4b. Especially in the interpenetrating network of D-A blends, direct paths between two sites might be suppressed by dead-ends or in favor of faster detour routes. However, if an electric field is applied, the loop around parts of non-transporting phases might involve hops against the direction of the electric field and hence becomes less probable. This localization of charge carriers induced by the electric field reduces the charge carrier mobility. It was shown that the negative field dependence of μ dominates at low fields, whereas it is overcompensated by a Poole-Frenkel type field effect at high fields, i.e., a positive field dependence. [137]

To quantify the negative field dependence of μ, the slope parameter s was derived by an exponential fit according to $\ln(\mu) \propto sF^{1/2}$. First, it must be noted that $\ln(\mu)$ of the VAC device starts to deviate from a straight line at a field strength of roughly 4000 V$^{1/2}$ m$^{-1/2}$. Second, the VAC sample shows a stronger decrease with increasing electric field (Table 7.2). According

	μ_0 / m^2 (Vs)$^{-1}$	s / V$^{-1/2}$ m$^{1/2}$
MD376:C_{60}, 1:1 (VAC)	1.76(5)·10^{-8}	-6.7(1)·10^{-4}
MD376:$PC_{61}BM$, 1:3 (SOL)	3.6(3)·10^{-9}	-4.0(4)·10^{-4}

Table 7.2.: Parameters μ_0 and s as deduced from an exponential fit of μ vs. $F^{1/2}$ according to the proportionality $\ln(\mu) \propto sF^{1/2}$.

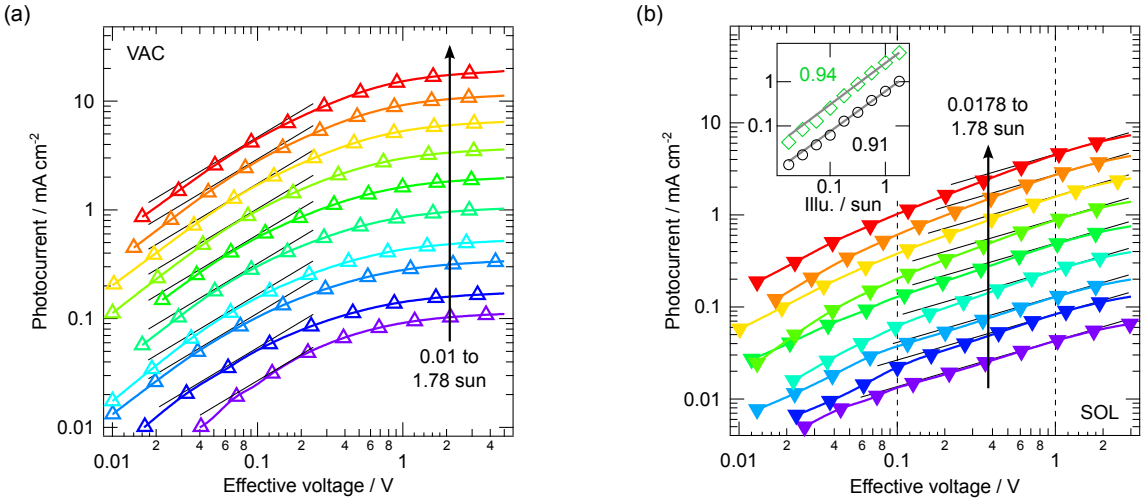

Figure 7.5.: Photocurrent j_{ph} vs. effective voltage of **(a)** MD376:C_{60} (VAC) and **(b)** MD376:$PC_{61}BM$ (SOL) devices derived from illumination dependent j-V characteristics measured in the optical cryostat using a high power white LED. The black line indicates a square-root dependence of j_{ph} on the effective voltage. The inset shows the SOL device j_{ph} vs. illumination intensity at an effective voltage of 0.1 V and 1 V (dashed lines). The written numbers correspond to the slope of a linear fit (grey line).

to the GDM, the slope parameter s is proportional to $(\hat{\sigma}^2 - \Sigma^2)$ and therefore depends on the interplay of energetic and spatial disorder (Equation 3.8). Assuming a comparable energetic disorder in both blends, this would suggest a higher spatial disorder of the VAC blend.

In a previous publication, the overall low FF of solar cells made from MC dyes was presumed to result from a strongly imbalanced charge carrier transport yielding the formation of space charge.[176,273] While OTRACE gives information about the effective value of μ without specifying the contribution of electron and hole mobility, the smaller effective mobility of the SOL device might be related to a reduced mobility of one type of charge carriers, indicating imbalanced transport properties. Mihailetchi et al. showed that in such a case, the photocurrent j_{ph} of a BHJ solar cell is expected to reveal a square-root dependence on voltage that is supplemented by a three-quarter power dependence on illumination intensity only in the space-charge limit.[67] Figure 7.5 shows $j_{ph} = j - j_{dark}$ as a function of the effective voltage $V_0 - V$ of MD376:C_{60} and MD376:$PC_{61}BM$ devices. V_0 denotes the compensation voltage at which the respective j_{ph} vanishes. A square-root dependence is indicated by black lines. The VAC device shows no square-root dependence over the whole range of $V_0 - V$ indicating balanced electron and hole mobilities.[67,277] In contrast, the SOL device suggests a square-root dependence around an effective voltage of 1 V that is slightly more pronounced for lower illumination intensities. However, no three-quarter power dependence of j_{ph} on illumination intensity can be found at an effective voltage of 0.1 V and 1 V (Figure 7.5, inset). The voltage and illumination dependence of j_{ph} of the SOL device indicate that the photocurrent and hence FF might be restricted by an imbalanced transport that, however, is not strong enough to lead to significant build up of space charge.

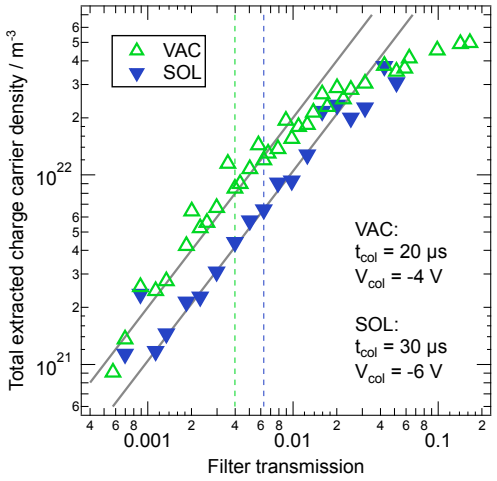

Figure 7.6.: Total extracted charge carrier density n_{tot} vs. filter transmission, i.e., illumination intensity, derived from TDCF measurements on MD376:C_{60} (VAC) and MD376:$PC_{61}BM$ (SOL) devices (V_{pre} = 0.9 V, t_d = 20 ns). The dashed lines indicate the intensity chosen in the linear regime for the respective pre-bias dependent measurement. Grey lines serve as guides to the eye.

7.2.3. Geminate and Nongeminate Recombination

As stated above, the enhanced PCE of MD376:C_{60} relative to MD376:$PC_{61}BM$ can be partly related to superior transport properties, but they fail to account for the overall low FF of both blends as compared to high performance polymer:fullerene systems. Thus, the yield of free charge carrier generation as well as nongeminate losses of charge carriers are assumed as further performance limiting factors and will be studied in the following. First, the field dependence of photogeneration was analyzed by TDCF. Devices were photoexcited using an energy of 2.33 eV, which is dominated by the absorption of the chromophore (Figure 7.9a). Figure 7.6 shows the laser intensity used for pre-bias dependent TDCF measurements. It was chosen in a range characterized by a linear dependence of the total extracted charge carrier density on the illumination intensity in order to exclude nongeminate losses during delay and extraction. The low laser intensity is the major precondition allowing the study of free charge carrier formation. The normalized extracted charge carrier density obtained from pre-bias dependent TDCF measurements on both devices is shown in Figure 7.7a. A saturation of n_{tot} at the most negative pre-bias is followed by a decrease to about 30 % (VAC) and 15 % (SOL) of the initial value when approaching a pre-bias close to V_{oc}, i.e., vanishing internal electric field. This means that the field dependence of n_{tot} and thus geminate losses are stronger in the case of the SOL device as compared to the VAC sample. The observation implies a less efficient dissociation yield, [96,112,122] e.g., caused by stronger bound polaron pairs or a reduced delocalization of charge carriers, as discussed below.

As already emphasized, pre-bias dependent TDCF measurements are not affected by nongeminate losses due to the chosen laser intensity. Thus, further conclusions can be drawn by comparing the normalized n_{tot} with the photocurrent j_{ph} as shown in Figure 7.6b for the two devices. In this graph, j_{ph}, which was recorded under varying illumination intensities, is normalized to the respective short circuit photocurrent under 1 sun conditions. It must be noted

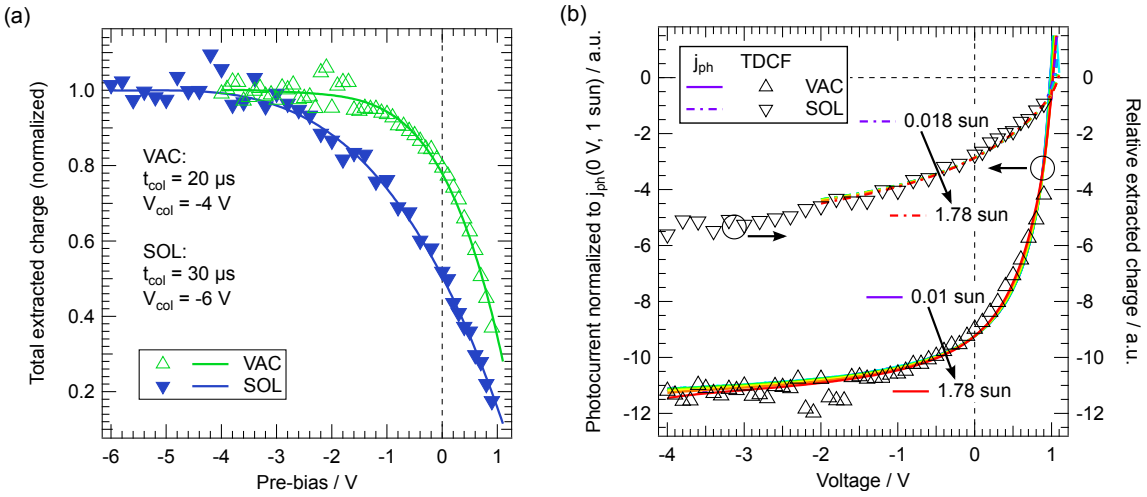

Figure 7.7.: (a) Total extracted charge carrier density n_{tot} vs. pre-bias V_{pre} (symbols) deduced from TDCF measurements on MD376:C_{60} (VAC) and MD376:$PC_{61}BM$ (SOL) devices (t_d = 20 ns). n_{tot} was fitted by a polynomial (lines) and normalized to the respective maximum of the fit. **(b)** Comparison of the relative n_{tot} (right axis) with j_{ph} recorded under varying illumination intensities (left axis). j_{ph} was normalized to j_{ph}(0 V) under 1 sun conditions. n_{tot} was normalized to the current density at -4 V (VAC) and -2 V (SOL).

that $j(V)$ of MD376:$PC_{61}BM$ was measured only down to -2 V due to the high dark saturation current (Figure 7.2b). In both cases, the normalized j_{ph} changes only slightly with illumination intensity indicating 1st order recombination losses (Section 3.1.1). In addition, the shape of the relative n_{tot} perfectly matches j_{ph}. Since a potential mismatch between both quantities arises from an additional loss current density due to nongeminate recombination, [60,61,96,260] this finding demonstrates that the photovoltaic performance of both devices is primarily limited by geminate losses. It can be further concluded that the reduced FF of the SOL device mainly results from a stronger field dependence of free charge carrier generation.

Although nongeminate losses only have minor effect on device performance, the charge carrier decay dynamics are studied. Since OTRACE transients recorded on MD376:C_{60} and MD376:$PC_{61}BM$ devices showed a rather low S/N ratio and might be additionally affected by the presence of local shunts, the OCVD signal was evaluated instead. Figure 7.8a shows the $V_{oc}(t)$ transients measured on the VAC and SOL solar cells using an illumination intensity of 1 sun. The photovoltage transient of the VAC device reveals a distinct single exponential decay in the time range from 10 µs to 1 ms and a subsequent regime with an increased slope starting at an open circuit voltage of about 0.7 V (dashed line). This value approximately correlates with the voltage up to which shunting was observed in the dark j-V characteristics (Figure 7.2b). Hence, the second regime is attributed to an additional recombination current due to local shunts. [243] In contrast, determining a single exponential decay of $V_{oc}(t)$ in the case of the SOL device is rather difficult, since the substantially higher leakage current causes a second, faster decay regime starting already at about 0.9 V.

The observed OCVD behavior can be studied in more detail using Equation 4.11. Assuming charge neutrality $n = p$ and a recombination following the generalized continuity equation

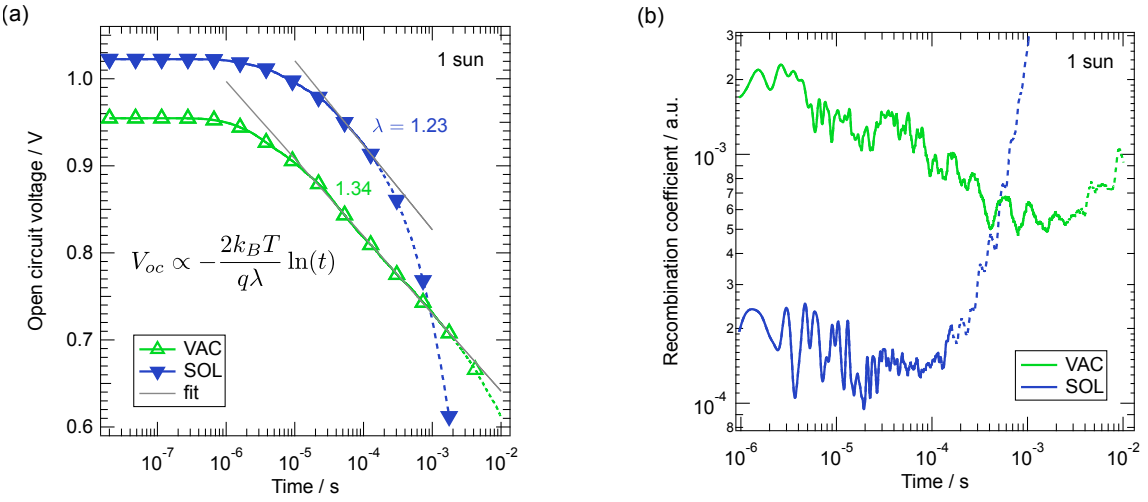

Figure 7.8.: (a) Open circuit voltage transient $V_{oc}(t)$ (smoothed) vs. delay time t_d of MD376:C_{60} (VAC) and MD376:$PC_{61}BM$ (SOL) devices recorded at an illumination intensity of 1 sun. The values of λ were derived from a fit of the single exponential regime of $V_{oc}(t)$ (grey lines). The dashed lines indicate the shunt limited voltage range that was not taken into account. **(b)** Relative recombination coefficient $-c^{-1/2}k_{rec}$ (smoothed) vs. delay time t_d calculated according to Equation 4.13.

(Equation 3.16), i.e., $n(t) \propto t^{-1/\lambda}$ for times $\lambda k_\lambda \gg n_0^{-\lambda}$, the single exponential decrease in $V_{oc}(t)$ can be described by

$$V_{oc}(t) = \frac{k_B T}{q}\left(\ln(c) - \frac{2}{\lambda}\ln(t)\right) \quad , \tag{7.1}$$

with the constant $c = 1/(n_0 p_0)$. This proportionality was applied to extract the slope of $V_{oc}(t)$ in the shunt-free regime, i.e., the recombination order $\lambda + 1$ (Figure 7.8a, grey lines). Similar recombination orders of 2.34 and 2.23 are observed for the VAC and the SOL device, respectively. The photovoltage transient can be further used to calculate a quantity proportional to the recombination coefficient k_{rec} according to Equation 4.13. Figure 7.8b shows $-c^{-1/2}k_{rec}$ as a function of t_d for an illumination intensity of 1 sun. It can be seen that the relative recombination coefficient of the VAC device overshoots the SOL device by about one order of magnitude at short times and slightly decreases with increasing time in both cases. The trend reversed at larger timescales, i.e., 0.1 ms (SOL) and 1 ms (VAC), when the additional shunt-induced loss current sets in (dashed lines). In view of an increased charge carrier mobility of the VAC device (Figure 7.4a), the enhanced recombination coefficient relative to the SOL device seems reasonable, although the discrepancy between both devices is more pronounced as in the case of μ. This difference might be explained by the varying acceptor types C_{60} and $PC_{61}BM$ of both blends. Their different LUMO levels affect the effective bandgap of the D-A blend and hence the intrinsic charge carrier densities n_0 and p_0 that determine the prefactor c.

7.2.4. Photophysical Properties

It seems reasonable to assume that the observed differences in free charge carrier generation and transport between the studied devices are correlated with differences in film formation during vacuum deposition and spin casting. In this regard, first conclusions about the intermolecular interaction on the supramolecular level as well as the interaction of the blend constituents can be drawn from photophysical properties of solid films. Figure 7.9a shows the absorbance of VAC and SOL films of the neat chromophore together with the normalized absorbance of MD376 in CB at a concentration of 10^{-4} mol l^{-1}. The neat films were processed according to the active layer of VAC and SOL devices. The absorption spectrum of the solution shows two clear absorption bands at 2.15 eV and 2.6 eV that can be attributed to the optical excitation of the S_1 state and to the excitation of a singlet state above S_1, respectively. The spectrum is in good agreement with data presented by Peckus et al. [278] Hence, it can be assumed that the solution contains only dissolved monomers at the given concentration. With respect to the absorbance of dissolved MD376, both neat films show a splitting of the main absorption band in terms of a reduced absorption strength at an energy of 2.15 eV and a second, more pronounced peak arising at 2.0 eV. The absorption strength and energetic position of this additional feature seems to be stronger and slightly red shifted for vacuum processing as compared to the spin cast film. In accordance with Reference 278, this double peak structure in the energy range from 1.9 to 2.2 eV can be correlated with an excitonic coupling of neighboring monomers and thus the self-assembly of MD376 into dimeric units. However, since the thin film spectra do not show a distinct red or blue shift, no preferred orientation can be assigned to these aggregates.

In addition to the optical density of neat films, their photoluminescence is compared with the PL of blend films in Figure 7.9b. The vacuum deposited film of neat MD376 shows two main peaks at about 1.7 eV and 1.9 eV that can be attributed to the emission of an intermolecular CT state forming upon the arrangement of chromophores and the PL of the monomer itself, respectively. [278] Both signatures are also visible in the SOL film of neat MD376, although with a substantially reduced emission of the low energy excited state and a more dominant PL of the monomer. This different spectral composition allows the conclusion of a reduced dimerization in the case of the SOL film and thus a less efficient compensation of the bipolarity. As compared to the spectra of neat MD376, both blend films show a highly efficient quenching of the singlet PL and the formation of a new emission band at about 1.5 eV and 1.65 eV in MD376:C_{60} and MD376:$PC_{61}BM$, respectively. This red shifted PL most probably results from a CT state formed at the D-A interface. [278] Regarding the interfacial CT emission, the VAC blend shows an enhanced quenching as compared to the SOL film. Since the PL of both blends was measured under similar experimental conditions, this stronger quenching indicates reduced losses in MD376:C_{60} due to a more favorable D-A interaction at the heterointerface. This interpretation is in agreement with a higher yield of free charge carrier generation as observed in TDCF measurements. It must be emphasized that the different peak positions of the blend PL might result from the LUMO level offset of C_{60} and $PC_{61}BM$.

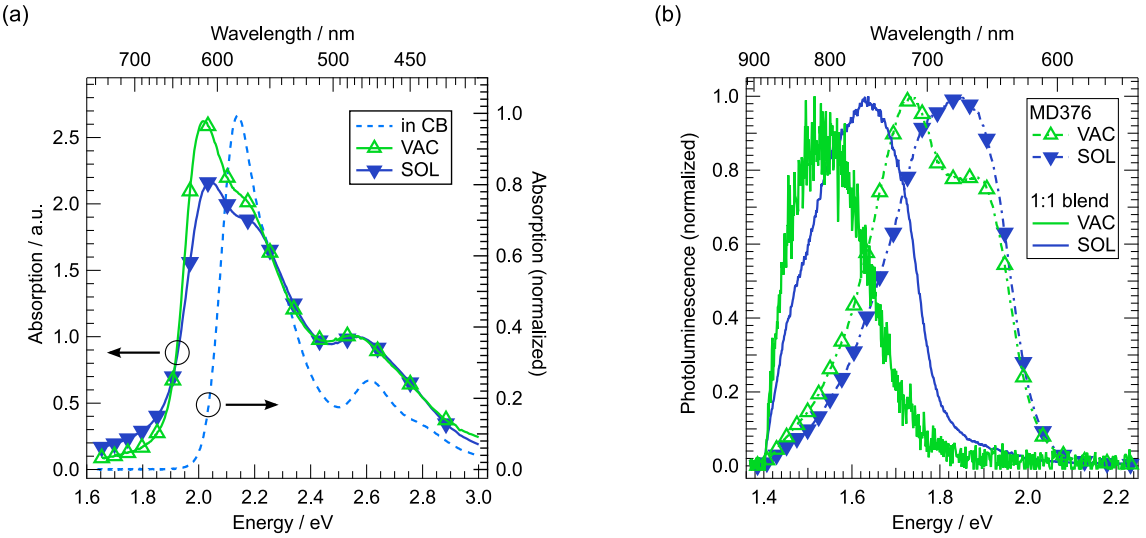

Figure 7.9.: (a) Absorbance of VAC and SOL films of neat MD376 in comparison with the normalized absorbance of MD376 in solution at 10^{-4} mol l^{-1} concentration. **(b)** PL spectra of VAC and SOL films of neat MD376 and the MD376:C_{60} (VAC) and MD376:$PC_{61}BM$ (SOL) blend films with a mixing ratio of 1:1. An excitation energy of 2.58 eV was used. All spectra were normalized to their maximum value.

7.3. Discussion

The arrangement of MC dyes on the supramolecular level plays the key role in their application as donor components in BHJ solar cells. Concerning vacuum deposited and solution processed BHJ films based on MD376, absorption and steady state PL measurements (Figure 7.9) allow the conclusion of both a higher degree of dimerization as well as an enhanced polaron pair dissociation yield at the D-A heterointerface in the case of the VAC blend. A more ordered nanomorphology is further confirmed for the vacuum deposited film by PL lifetime measurements, which are not shown in this thesis but can be found in Reference 274. The stronger intermolecular interaction of the chromophores during vacuum deposition appears conclusive due to a slower film formation and higher processing temperatures, i.e., the thermodynamic equilibrium of the D-A blend can be achieved more easily.[178] The actual packing feature of MC dyes in solid films crucially depends on their rigidity and their planarity, i.e., the torsion angle between the D and A subunits, commonly yielding a longitudinal and traverse displacement of adjacent molecules. The packing motif of MD376 was analyzed by Bürckstümmer et al. using single crystal X-ray analysis.[179] The study revealed a small distortion angle of 5.4° of the chromophore. Furthermore, the close arrangement of the dyes in centrosymmetric dimeric units is reported that are characterized by donor-acceptor π-contact and a small distance of 3.37 Å between parallel planes. Individual π-stacks show a longitudinal shift resulting in a π-contact of acceptor subunits and a distance of 3.55 Å. This antiparallel stacking of monomers result in a dwindling small residual dipole moment on the supramolecular scale without strong interaction of separated dimers. In this context, the pronounced increase in EQE of the VAC device in the region between 2.5 eV and 3.3 eV has to be discussed. A similar observation was

made for VAC and SOL devices based on HB194 and related to a different packing and hence a raised absorption of C_{60} relative to its asymmetric derivative $PC_{61}BM$. Although this cannot be completely ruled out, it seems not very likely because the SOL blend contains a three times higher fullerene loading and the rise of C_{60} absorbance can hardly be so strong. Thus, it seems more reliable to relate this feature to the formation of a blue shifted H-band due to a more pronounced dimerization in the VAC blend. The assumption is supported by the absorbance of blend films, shown in Reference 274. A similar increased contribution of H-aggregated dye manifold to the photocurrent was recently shown for a novel bis(MC) chromophore.[279]

Recent measurements of the FET hole mobility among a series of different MC dyes revealed the highest mobility for spin cast films of the chromophore with the largest molecular dipole moment.[275] The result demonstrates that the bulk mobility is not necessarily reduced by a large bipolarity but crucially depends on the packing fashion of the dyes in solid films. Thus, the increased effective charge carrier mobility of the VAC device as observed in field dependent OTRACE measurements (Figure 7.4) can be related to an improved dimerization provoking a better compensation of the bipolarity. Furthermore, the formation of spatially extended π-stacks providing improved percolation paths in the VAC blend seems reasonable. At first glance, the increased effective mobility of the VAC device is contrary to an increased negative field dependence of μ, since the latter indicates a higher spatial disorder that is commonly linked to a decrease in μ.[280] This increased disorder in the case of the VAC blend might be due to the reduced fullerene loading causing a smaller scale phase separation as observed by TEM measurements on VAC films of HB194.[178] The obvious contradiction is solved assuming a dominant influence of supramolecular order that compensates the negative effect of stronger intermixing on the charge carrier mobility. In addition, the assumption of a similar energetic disorder of both blends entering the interpretation of the slope parameter s has to be seen as a rough approximation, since the elimination of local dipole moments should be taken into account.[272] As already pointed out, the charge extraction technique OTRACE yields informations about an effective blend mobility including contributions of both electrons and holes. However, following the reasoning above, it can be assumed that the reduced mobility of the SOL device is mainly caused by a decreased hole mobility μ_h. This presumption is in line with the limitation of the photocurrent of the SOL device (Figure 7.5) indicating imbalanced transport properties. The assumption of a significantly reduced hole mobility is further supported by FET measurements revealing a rather low μ_h of about 10^{-10} m^2 $(Vs)^{-1}$ in MD376:$PC_{61}BM$ blends as compared to the electron mobility of $2 \cdot 10^{-7}$ m^2 $(Vs)^{-1}$ of the neat fullerene.[176]

The restrictive influence of imbalanced transport might explain the reduced fill factor of the SOL device to some extent, however it does not account for the moderate FF of about 47 % of the VAC device. Incidentally, this value is close to the highest fill factor reported for optimized MC dye based BHJ solar cells up to now.[178,273] As revealed by pre-bias dependent TDCF measurements (Figure 7.7), the voltage dependence of the photocurrent of both devices is essentially limited by the field dependence of charge carrier generation, i.e., geminate recombination. In addition, this field dependence is lower in the case of the VAC device. In this context, the field dependence of charge carrier dissociation in a ID583/C_{60} PHJ solar cells was recently analyzed

by Petersen et al.[281] Except for the propyl side chain of the donor unit, the MC dye ID583 is identical with MD376 (Figure 7.1c). Hence, similar structural and energetic properties can be expected. The PHJ configuration was chosen in order to avoid a field dependent charge carrier collection, i.e., nongeminate recombination of free charge carriers. These losses might superimpose field dependent photogeneration. Petersen et al. demonstrated that the voltage, field and negligible temperature dependence of the photocurrent could only be reproduced under the assumption of a field dependent exciton dissociation tunnel process. This result was interpreted in terms of a charge generation that is not limited by the dissociation of a bound precursor state being energetically lower than the CSS. Although the model can be seen as a possible explanation, it must be emphasized that nongeminate losses are indeed present in a PHJ configuration as shown by Foertig et al.[221] Thus, it seems to be more appropriate to attribute the reduced field dependence in MD376:C_{60} to an enhanced charge carrier delocalization due to a higher degree of dimerization. The importance of delocalization for an efficient polaron pair dissociation has been demonstrated and predominantly associated with crystalline domains in several studies.[55,247,282] This also includes Chapter 5, where a less field dependent photogeneration in 1:4 pBTTT-C_{16}:PC_{61}BM blends was related to the delocalization of electrons in pure fullerene domains. In contrast to this finding, the reduced field dependence of the VAC device indicates that in the present case the major impact stems from delocalization in more ordered donor phases, i.e., the delocalization of CT excitons and/or holes. Otherwise, a positive effect of the higher fullerene loading of the SOL device should be visible. Furthermore, delocalization in well ordered π-aggregates is seen as the major driving force compensating the effect of possibly smaller domains within the VAC blend. Regarding the model proposed by Petersen et al., tunnel processes might be seen as a pre-seperation step, i.e., prior to delocalization. A further explanation of the less field dependent photogeneration is the formation of a more proper interfacial arrangement of the chromophores with respect to the fullerene molecules during vacuum processing. In a recent publication, Ojala et al. showed that the re-arrangement of the dye molecules at the D-A interface significantly increases the CT dissociation efficiency and hence the FF of ID583/C_{60} PHJ solar cells.[283] Although the more favorable orientation of ID583 was achieved by post-annealing or by heating the substrate during vacuum deposition, a similar effect could make the difference between the studied MD376:C_{60} and MD376:PC_{61}BM devices. The interpretation implies a stronger D-A interaction in the case of the VAC blend that would be in agreement with transient PL[274] and the low-energetic tail of the EQE (Figure 7.3).

With regard to the differences in PCE between MD376:C_{60} and MD376:PC_{61}BM devices, different aspects have to be considered. First, it can be assumed that, in addition to the varying LUMO level of the acceptors, the improved dimerization in the VAC blend influences the chromophores' redox potentials and thus contributes to the difference in V_{oc} between both samples.[174] Second, based on the observation that geminate losses are the major factor limiting photovoltaic efficiency, the substantially raised j_{sc} of the VAC device can be related to a more efficient charge carrier generation in addition to a stronger absorption. The enhanced dissociation yield most likely results from more crystalline donor phases and/or and improved arrangement of D and A molecules at the heterointerface. These changes of the blend mor-

phology on the supramolecular level can also be assigned to a reduced field dependence of the photocurrent of the MD376:C_{60} device, although still considerable geminate losses prevent higher values of FF. Regarding MD376:$PC_{61}BM$, the fill factor is further limited by imbalanced electron and hole mobilities.

7.4. Conclusions

In summary, the free charge carrier generation and transport of vacuum deposited MD376:C_{60} and solution processed MD376:$PC_{61}BM$ solar cells were compared in order to understand the pronounced voltage dependence of the photocurrent and the clearly improved power conversion efficiency of the VAC device. Pre-bias dependent TDCF measurements revealed the field dependence of free charge carrier formation as the most detrimental factor limiting the photovoltaic performance of both blends. These geminate losses were found to be significantly enhanced in the case of MD376:$PC_{61}BM$. In addition, the efficiency of the SOL device is further affected by imbalanced transport properties—most probably due to reduced hole mobility—as it was deduced from illumination dependent j-V characterization and the charge extraction technique OTRACE. Based on the absorption and photoluminescence of vacuum deposited and solution processed films of neat MD376 and the blends, the obtained results were associated with an alteration of the blend morphology on the supramolecular level. The slowed down film formation during vacuum deposition suggests a stronger intermolecular interaction that primarily results in a higher degree of dimerization within the MD376:C_{60} blend. Consequently, both the increased effective charge carrier mobility as well as the higher polaron pair dissociation yield can be related to an enhanced delocalization of excitons and/or electrons in spatially extended phases of dimer aggregates. Regarding MD376:C_{60}, reduced geminate losses might be further correlated with a stronger interfacial D-A interaction. The study demonstrates the high sensitivity of the functionality of MC dye based solar cells on the supramolecular packing of the blend constituents. It further contributes to the understanding of the differences in photocurrent generation between vacuum deposited and solvent processed devices.

8. Summary

The present work dealt with the elementary question of how the intermixing of donor and acceptor constituents of an organic BHJ solar cell affects the fundamental steps of photocurrent generation and thus limits device performance. This relationship was investigated using different photovoltaic systems and the charge extraction techniques TDCF and OTRACE. Whereas TDCF allowed conclusions to be drawn about the field dependence of geminate recombination losses, OTRACE yielded information about nongeminate losses and transport properties under realistic operating conditions of a solar cell.

In order to understand the effect of neat fullerene phases on polaron pair dissociation, the field dependent photogeneration in pBTTT-C_{16} based solar cells was studied. The model system allowed a systematically tunable ratio between finely intermixed and segregated domains by varying the acceptor type and loading fraction. It was found that the impact of excess energy on photogeneration is subordinate to the influence of an increase in $PC_{61}BM$. Excess fullerene beyond a blend ratio of 1:1 causes the formation of fullerene domains in addition to intercalated domains. The observation was explained by polaron pair dissociation via fully thermalized CTS in combination with only a minor influence of excited interfacial states. Furthermore, TDCF measurements on fully segregated pBTTT-C_{16}:bis$PC_{61}BM$ blends revealed an almost identical field dependence of photogeneration as compared to 1:4 pBTTT-C_{16}:$PC_{61}BM$. This result showed that the presence of spatially extended, pure fullerene phases is the main prerequisite for an efficient, field independent polaron pair dissociation that can be correlated with the delocalization of electrons along these domains.

By combining TDCF and OTRACE with surface imaging and photophysical techniques, it was possible to monitor the effect of a systematically increased amount of DIO on the bulk morphology of PBDTTT-C:$PC_{71}BM$ blends and to link it with changes in photogeneration and free charge carrier formation. Poor singlet exciton splitting and predominant geminate losses in the DIO-free blend was related to missing percolation paths and the presence of large agglomerates, identified as neat fullerene domains. 0.6 % and 1 % DIO led to a substantial decrease in the size of $PC_{71}BM$ domains, facilitating exciton quenching and provoking a highly efficient local photogeneration. However, the still moderate photovoltaic performance was ascribed to the still finely intermixed D-A phase surrounding fullerene domains. Only the use of 3 % DIO caused a maximum PCE of 7.1 % that was correlated with a highly efficient formation of free charge carriers and minimized nongeminate losses due to the formation of interpenetrating D and A phases. The study convincingly demonstrated that improving the performance of state-of-the-art BHJ devices by the use of solvent additives relies on a crucial balance between local photogeneration and charge carrier extraction.

In the course of optimizing device efficiency through the use of DIO, nongeminate recombination and transport properties were studied in PTB7:$PC_{71}BM$ solar cells without and with 3 % DIO by means of OTRACE. This polymer:fullerene system is known for an active layer morphology that behaves similarly to PBDTTT-C:$PC_{71}BM$ upon processing with DIO. A reduced Langevin-type recombination as well as a deviation from a pure bimolecular decay was found in both the non-optimized and optimized blends. A higher recombination order in the case of the DIO-free blend was explained by charge carrier trapping in the interior of pure $PC_{71}BM$ domains. Regarding transport properties, OTRACE revealed a reduced charge carrier mobility in the 3 % DIO blend that might result from a decreased electron mobility in shrinking $PC_{71}BM$. By relating the nongeminate recombination rate with μ, it was shown that, despite the obvious influence of morphology on charge carrier transport, the charge carrier dependence of μ does not account for the super-second order decay in either device. The observations highlighted the importance of multiple trapping and release processes in the slowing down of recombination in partially phase separated blends.

Apart from varying the composition of the active layer and using processing additives, the film formation of merocyanine dye based blends was manipulated by different film formation methods. Vacuum deposited MD376:C_{60} solar cells exhibited a higher efficiency than the solution processed counterpart MD376:$PC_{61}BM$. Applying pre-bias dependent TDCF, the field dependence of photogeneration was identified as the most detrimental factor limiting photovoltaic performance of both devices, whereas MD376:$PC_{61}BM$ revealed stronger geminate losses. Apart from a contrasting photogeneration, imbalanced transport properties were found in the solution processed blend by illumination dependent j-V characterization and OTRACE measurements. The results were correlated with a higher degree of dimerization of the chromophore molecules and a stronger interfacial interaction of the blend constituents in vacuum deposited MD376:C_{60}. Both morphological factors might provoke an enhanced CT exciton and/or hole delocalization as well as an increased dissociation yield, illustrating the importance of supramolecular order.

To conclude, this work demonstrated the crucial impact of blend morphology on device physics in four comparative studies. Particular importance was attributed to interconnected, neat domains on a length scale similar to the exciton diffusion length and hence on the order of ten nanometers. It was shown that such domains provide both the main driving force for an efficient polaron pair dissociation, mainly due to the delocalization of excitons and/or polarons, as well as percolation paths for an efficient charge carrier extraction. The presented results might serve as a starting point for the advancement and optimization of present D-A systems, allowing a large-scale application of organic photovoltaics in the near future.

Zusammenfassung

Im Bereich der organischen Photovoltaik gilt derzeit die Heterogemisch (*bulk heterojunction*, BHJ)-Solarzelle als eines der vielversprechendsten Konzepte. Der zentrale Aspekt der vorliegenden Arbeit war die Untersuchung des Einflusses der Morphologie auf die Generierung von Photostrom und damit auf die Funktionsfähigkeit eines solchen Bauteils. Als wichtigste Messtechniken kamen die Ladungsextraktionsmethoden *time delayed collection field* (TDCF) und *open circuit corrected transient charge extraction* (OTRACE) zum Einsatz. Während TDCF Informationen über die Feldabhängigkeit der geminalen Rekombination lieferte, wurden unter Verwendung von OTRACE die Transporteigenschaften und nichtgeminale Verluste unter realistischen Arbeitsbedingungen einer Solarzelle analysiert.

Um die Funktion reiner Fullerendomänen bei der Trennung von Polaronpaaren besser zu verstehen, wurde zunächst die feldabhängige Photogenerierung in Bauteilen basierend auf dem Polymer pBTTT-C_{16} mittels TDCF untersucht. Die Wahl fiel auf pBTTT-C_{16}, da das Material in Kombination mit Fullerenderivaten eine systematische Anpassung der Morphologie durch Art und Anteil des Akzeptors erlaubt. Die Messungen zeigten, dass der Einfluss von Überschussenergie auf die Photogenerierung vernachlässigt klein gegenüber dem Einfluss reiner Fullerendomänen ist, die sich zusätzlich zu interkalierten Phasen ab einem Mischungsverhältnis von 1:1 ausbilden. Auf Basis dieser Beobachtung konnte darauf geschlossen werden, dass die Trennung von Polaronpaaren überwiegend über vollständig relaxierte Ladungstransferzustände (*charge transfer states*, CTS) abläuft und nur geringfügig von angeregten CTS beeinflusst wird. Weiterhin zeigten TDCF-Messungen an 1:4 pBTTT-C_{16}:PC_{61}BM und vollständig separierten pBTTT-C_{16}:bisPC_{61}BM Heterogemischen vergleichbar geringe geminale Verluste. Als mögliche Erklärung wurde die verstärkte Delokalisierung von Ladungsträgern in reinen Phasen herangezogen. Das Ergebnis verdeutlicht, dass das Vorhandensein reiner Fullerendomänen die wesentliche Voraussetzung für eine effiziente, feldunabhängige Dissoziation von Polaronpaaren ist.

Durch die Verknüpfung der Ergebnisse von TDCF und OTRACE mit bildgebenden Verfahren und photophysikalischen Methoden war es möglich, den Einfluss eines systematisch erhöhten Anteils des Lösungsmitteladditivs Diiodooktan (DIO) auf die Morphologie und die Generierung freier Ladungsträger in PBDTTT-C:PC_{71}BM zu untersuchen. Ohne die Verwendung von DIO zeigte das Heterogemisch hohe strahlende Verluste und damit eine schlechte Trennung von Exzitonen sowie dominierende geminale Verluste. Die Beobachtungen wurden mit fehlenden Perkolationspfaden und dem Vorhandensein großer Agglomerate, die als von einer durchmischten Matrix umgebene Fullerendomänen identifiziert wurden, in Verbindung gebracht. Bereits die Verwendung von kleinen Mengen des Additivs (0.6 % und 1 % DIO) führte zu einer

deutlichen Verkleinerung der Domänen und hatte eine effiziente lokale Photogenerierung zur Folge. Die trotzdem eher mäßige Effizienz der Bauteile wurde auf Verluste in weiterhin fein durchmischten Bereichen der aktiven Schicht zurückgeführt. Die Erhöhung des DIO Anteils auf 3 % führte zu einer maximalen Bauteileffizienz von 7.1 %. Sie resultierte aus einer hochergiebigen Generierung freier Ladungsträger sowie aus minimierten nichtgeminalen Verlusten. Unter Einbeziehung aller Ergebnisse wurde dies mit der Ausbildung reiner, vernetzter Donator- und Akzeptorphasen erklärt. Die an PBDTTT-C:$PC_{71}BM$ durchgeführte Studie zeigt eindrucksvoll, dass die Optimierung modernster, hocheffizienter Heterogemische auf einem ausgewogenen Verhältnis von lokaler Photogenerierung und der Extraktion von Ladungsträgern beruht.

Im Zuge der Effizienzerhöhung durch den Gebrauch des Additivs DIO wurden nichtgeminale Verluste und der Transport freier Ladungsträgern in PTB7:$PC_{71}BM$ Solarzellen ohne und mit 3 % DIO näher untersucht. Ähnlich wie PBDTTT-C:$PC_{71}BM$ zeigt auch diese Donator-Akzeptor-Kombination eine Morphologie, die durch ausgedehnte Fullerendomänen in Gemischen ohne DIO und deren optimierte Dispersion durch die Verwendung des Additiv geprägt ist. Sowohl für das Bauteil ohne als auch mit 3 % DIO zeigte OTRACE eine reduzierte Langevin-artige Rekombination, die zudem eine deutliche Abweichung von einem bimolekularen Verhalten aufwies. Die dabei auftretende höhere Rekombinationsordnung im Fall der Probe ohne DIO wurde dem Einfangen von Ladungsträgern in Fullerenphasen zugeschrieben. Weiterhin zeigte OTRACE eine reduzierte Ladungsträgermobilität in der mit DIO hergestellten Solarzelle, die wahrscheinlich mit einer verminderten Elektronenmobilität in besser dispergierten Fullerendomänen korreliert. Durch die Verknüpfung der Mobilität mit der nichtgeminalen Rekombinationsrate konnte gezeigt werden, dass trotz des offensichtlichen Einflusses der Morphologie auf Transporteigenschaften die Abweichung von einer reinen bimolekularen Rekombination nicht vollständig über die Ladungsträgerdichtenabhängigkeit der Mobilität erklärt werden kann.

Neben der Änderung der Zusammensetzung von Heterogemischen und der Verwendung von Additiven wurde die Morphologie von Merocyanin-basierten Solarzellen durch verschiedene Herstellungsprozesse beeinflusst. Diese hatten eine deutliche Erhöhung der Effizienz von aufgedampften MD376:C_{60} Zellen im Vergleich zum lösungsprozessierten Donator-Akzeptor-Gemisch MD376:$PC_{61}BM$ zur Folge. Der Unterschied wurde zunächst in einem Vergleich des Photostroms j_{ph} mit der aus TDCF bekannten extrahierten Ladungsträgerdichte untersucht. Die Gegenüberstellung ergab eine maßgebliche Limitierung der Effizienz durch geminale Verluste in beiden Proben, wobei die Photogenerierung in MD376:$PC_{61}BM$ eine stärkere Feldabhängigkeit aufwies. Zudem wurde durch die Verwendung von beleuchtungsabhängigen j-V-Messungen und OTRACE ein unausgeglichener Transport freier Ladungsträger in der lösungsprozessierten Solarzelle festgestellt. Beide Ergebnisse wurden einer verbesserten Dimerisation des Merocyanins MD376 sowie einer stärkeren Donator-Akzeptor-Wechselwirkung und damit einer erhöhten Delokalisierung von CT Exzitonen und/oder Löchern sowie einer effizienteren Polaronpaartrennung im aufgedampften Gemisch zugeordnet.

Zusammenfassend demonstriert die vorliegende Arbeit den entscheidenden Einfluss der Morphologie auf die grundlegenden Prozesse in organischen BHJ-Solarzellen anhand vier ver-

gleichender Studien. Besondere Bedeutung kommt dem Vorhandensein von reinen, untereinander verbundenen Domänen zu, deren Größe etwa der Diffusionslänge von Exzitonen entspricht. Sie liegt damit im Bereich von wenigen 10 nm. Domänen dieser Größe können als treibende Kraft für eine effiziente Trennung von Polaronpaaren und gleichzeitig als Voraussetzung für einen leistungsfähigen Transport gesehen werden. Dabei spielt die erhöhte Delokalisierung von Ladungsträgern in reinen Phasen eine wichtige Rolle. Die vorgestellten Ergebnisse liefern einen Ansatz für die Weiterentwicklung und Optimierung bestehender BHJ-Systeme und können damit die organische Photovoltaik ihrer Anwendung im großen Maßtab näher bringen.

Bibliography

[1] U.S. Energy Information Administration. International Energy Statistics. www.eia.gov (2014).

[2] Renewable Policy Network for the 21st Century. Renewables 2012 – Global Status Report. www.map.ren21.net/gsr/ (2012).

[3] Fricke, J. & Borst, W. L. *Essentials of Energy Technology: Sources, Transport, Storage, Conservation* (Wiley-VCH, Weinheim, 2014), 1st edn.

[4] Schachinger, M. Module Price Index, October 2014. www.pv-magazine.com (2014).

[5] Heeger, A. J. 25th Anniversary Article: Bulk Heterojunction Solar Cells: Understanding the Mechanism of Operation. *Adv. Mater.* **26**, 10–28 (2014).

[6] Deibel, C. & Dyakonov, V. Polymer-Fullerene Bulk Heterojunction Solar Cells. *Rep. Prog. Phys.* **73**, 096401 (2010).

[7] Yu, G., Gao, J., Hummelen, J. C., Wudl, F. & Heeger, A. J. Polymer Photovoltaic Cells: Enhanced Efficiencies via a Network of Internal Donor-Acceptor Heterojunctions. *Science* **270**, 1789–1791 (1995).

[8] Green, M. A., Emery, K., Hishikawa, Y., Warta, W. & Dunlop, E. D. Solar Cell Efficiency Tables (Version 44). *Prog. Photovoltaics Res. Appl.* **22**, 701–710 (2014).

[9] Dennler, G., Scharber, M. C. & Brabec, C. J. Polymer-Fullerene Bulk-Heterojunction Solar Cells. *Adv. Mater.* **21**, 1323–1338 (2009).

[10] Brabec, C. J. *et al.* Polymer–Fullerene Bulk-Heterojunction Solar Cells. *Adv. Mater.* **22**, 3839–3856 (2010).

[11] Brabec, C. J., Heeney, M., McCulloch, I. & Nelson, J. Influence of Blend Microstructure on Bulk Heterojunction Organic Photovoltaic Performance. *Chem. Soc. Rev.* **40**, 1185–1199 (2011).

[12] Yu, P. Y. & Cardona, M. *Fundamentals of Semiconductors - Physics and Materials Properties* (Springer Verlag Berlin Heidelberg, 2010), 4th edn.

[13] Clayden, J., Greeves, N. & Warren, S. *Quantum Theory of Solids* (Oxford University Press, New York, 2012), 2nd edn.

[14] Akamatu, H., Inokuchi, H. & Matsunaga, Y. Electrical Conductivity of the Perylene-Bromine Complex. *Nature* **173**, 168–169 (1954).

[15] Pope, M. & Swenberg, C. E. *Electronic Processes in Organic Crystals and Polymers* (Oxford University Press, New York, 1999), 2nd edn.

[16] Deibel, C., Baumann, A. & Dyakonov, V. Photogeneration and Recombination in Polymer Solar Cells. In Brütting, W. & Adachi, C. (eds.) *Physics of Organic Semiconductors* (Wiley-VCH, Weinheim, 2012), 2nd edn.

[17] Shirakawa, H., Louis, E. J., MacDiarmid, A. G., Chiang, C. K. & Heeger, A. J. Synthesis of Electrically Conducting Organic Polymers: Halogen Derivatives of Polyacetylene, $(CH)_x$. *J. Chem. Soc., Chem. Commun.* 578–580 (1977).

[18] Brütting, W. & Rieß, W. Grundlagen der organischen Halbleiter. *Physik Journal* **7**, 33–38 (2008).

[19] Leo, K. Organic Semiconductor World. www.orgworld.de (2014).

[20] Peierls, R. E. *Electronic Processes in Organic Crystals and Polymers* (Oxford University Press, 1955).

[21] Rehahn, M. Elektrisch leitfähige Kunststoffe: Der Weg zu einer neuen Materialklasse. *Chemie in unserer Zeit* **37**, 18–30 (2003).

[22] Heeger, A. J., Kivelson, S., Schrieffer, J. R. & Su, W. P. Solitons in Conducting Polymers. *Rev. Mod. Phys.* **60**, 781–850 (1988).

[23] Sze, S. M. & Ng, K. K. *Physics of Semiconductor Devices* (John Wiley and Sons, 2006), 3rd edn.

[24] Hertel, D. & Bässler, H. Photoconduction in Amorphous Organic Solids. *ChemPhysChem* **9**, 666–688 (2008).

[25] Chamberlain, G. A. Organic Solar Cells: A Review. *Solar Cells* **8**, 47–83 (1983).

[26] Tang, C. W. Two-Layer Organic Photovoltaic Cell. *Appl. Phys. Lett.* **48**, 183–185 (1986).

[27] Tom J Savenije, T. J., Warman, J. M. & Goossens, A. Visible Light Sensitisation of Titanium Dioxide Using a Phenylene Vinylene Polymer. *Chem. Phys. Lett.* **287**, 148–153 (1998).

[28] Stübinger, T. & Brütting, W. Exciton Diffusion and Optical Interference in Organic Donor-Acceptor Photovoltaic Cells. *J. Appl. Phys.* **90**, 3632–3641 (2001).

[29] Kroeze, J. E., Savenije, T. J., Vermeulen, M. J. W. & Warman, J. M. Contactless Determination of the Photoconductivity Action Spectrum, Exciton Diffusion Length, and Charge Separation Efficiency in Polythiophene-Sensitized TiO_2 Bilayers. *J. Phys. Chem. B* **107**, 7696–7705 (2003).

[30] Lüer, L. *et al.* Oxygen-Induced Quenching of Photoexcited States in Polythiophene Films. *Org. Electron.* **5**, 83–89 (2004).

[31] Markov, D. E., Tanase, C., Blom, P. W. M. & Wildeman, J. Simultaneous Enhancement of Charge Transport and Exciton Diffusion in Poly(*p*-phenylene vinylene) Derivatives. *Phys. Rev. B* **72**, 045217 (2005).

[32] Lewis, A. *et al.* Singlet Exciton Diffusion in MEH-PPV Films Studied by Exciton–Exciton Annihilation. *Org. Electron.* **7**, 452–456 (2006).

[33] Shaw, P. E., Ruseckas, A. & Samuel, I. D. W. Exciton Diffusion Measurements in Poly(3-hexylthiophene). *Adv. Mater.* **20**, 3516–3520 (2008).

[34] Cook, S., Furube, A., Katoh, R. & Han, L. Estimate of Singlet Diffusion Lengths in PCBM Films by Time-Resolved Emission Studies. *Chem. Phys. Lett.* **478**, 33–36 (2009).

[35] Mikhnenko, O. V. *et al.* Exciton Diffusion Length in Narrow Bandgap Polymers. *Energy Environ. Sci.* **5**, 6960–6965 (2012).

[36] Liang, Y. *et al.* For the Bright Future—Bulk Heterojunction Polymer Solar Cells with Power Conversion Efficiency of 7.4%. *Adv. Mater.* **22**, E135–E138 (2010).

[37] He, Z. *et al.* Simultaneous Enhancement of Open-Circuit Voltage, Short-Circuit Current Density, and Fill Factor in Polymer Solar Cells. *Adv. Mater.* **23**, 4636–4643 (2011).

[38] He, Z. *et al.* Enhanced Power-Conversion Efficiency in Polymer Solar Cells Using an Inverted Device Structure. *Nat. Photon.* **6**, 591–595 (2012).

[39] Yoon, S. M. *et al.* Fluorinated Copper Phthalocyanine Nanowires for Enhancing Interfacial Electron Transport in Organic Solar Cells. *Nano Lett.* **12**, 6315–6321 (2012).

[40] Zhou, H. *et al.* High-Efficiency Polymer Solar Cells Enhanced by Solvent Treatment. *Adv. Mater.* **25**, 1646–1652 (2013).

[41] Green, M. A. & Keevers, M. J. Optical Properties of Intrinsic Silicon at 300 K. *Prog. Photovoltaics Res. Appl.* **3**, 189–192 (1995).

[42] Patil, A. O., Heeger, A. J. & Wudl, F. Optical Properties of Conducting Polymers. *Chem. Rev.* **88**, 183–200 (1988).

[43] Mühlbacher, D. *et al.* High Photovoltaic Performance of a Low-Bandgap Polymer. *Adv. Mater.* **18**, 2884–2889 (2006).

[44] Peet, J. *et al.* Efficiency Enhancement in Low-Bandgap Polymer Solar Cells by Processing With Alkane Dithiols. *Nat. Mater.* **6**, 497–500 (2007).

[45] Cook, S., Katoh, R. & Furube, A. Ultrafast Studies of Charge Generation in PCBM:P3HT Blend Films following Excitation of the Fullerene PCBM. *J. Phys. Chem. C* **113**, 2547–2552 (2009).

[46] Burkhard, G. F., Hoke, E. T., Beiley, Z. M. & McGehee, M. D. Free Carrier Generation in Fullerene Acceptors and Its Effect on Polymer Photovoltaics. *J. Phys. Chem. C* **116**, 26674–26678 (2012).

[47] Wienk, M. M. *et al.* Efficient Methano[70]fullerene/MDMO-PPV Bulk Heterojunction Photovoltaic Cells. *Angew. Chem. Int. Ed.* **42**, 3371–3375 (2003).

[48] Shrotriya, V., Ouyang, J., Tseng, R. J., Li, G. & Yang, Y. Absorption Spectra Modification in Poly(3-hexylthiophene):Methanofullerene Blend Thin Films. *Chem. Phys. Lett.* **411**, 138–143 (2005).

[49] Laquai, F., Park, Y.-S., Kim, J.-J. & Basché, T. Excitation Energy Transfer in Organic Materials: From Fundamentals to Optoelectronic Devices. *Macromol. Rapid Commun.* **30**, 1203–1231 (2009).

[50] Howard, I. A., Mauer, R., Meister, M. & Laquai, F. Effect of Morphology on Ultrafast Free Carrier Generation in Polythiophene:Fullerene Organic Solar Cells. *J. Am. Chem. Soc.* **132**, 14866–14876 (2010).

[51] Gieseking, B. *et al.* Excitation Dynamics in Low Band Gap Donor–Acceptor Copolymers and Blends. *Adv. Energy Mater.* **2**, 1477–1482 (2012).

[52] Sariciftci, N. S., Smilowitz, L., Heeger, A. J. & Wudl, F. Photoinduced Electron Transfer from a Conducting Polymer to Buckminsterfullerene. *Science* **258**, 1474–1476 (1992).

[53] Hwang, I.-W. *et al.* Ultrafast Electron Transfer and Decay Dynamics in a Small Band Gap Bulk Heterojunction Material. *Adva. Mater.* **19**, 2307–2312 (2007).

[54] Hwang, I.-W. *et al.* Bulk Heterojunction Materials Composed of Poly(2,5-bis(3-tetradecylthiophen-2-yl)thieno[3,2-b]thiophene): Ultrafast Electron Transfer and Carrier Recombination. *J. Phys. Chem. C* **112**, 7853–7857 (2008).

[55] Guo, J., Ohkita, H., Benten, H. & Ito, S. Charge Generation and Recombination Dynamics in Poly(3-hexylthiophene)/Fullerene Blend Films with Different Regioregularities and Morphologies. *J. Am. Chem. Soc.* **132**, 6154–6164 (2010).

[56] Clarke, T. M., Ballantyne, A. M., Nelson, J., Bradley, D. D. C. & Durrant, J. R. Free Energy Control of Charge Photogeneration in Polythiophene/Fullerene Solar Cells: The Influence of Thermal Annealing on P3HT/PCBM Blends. *Adv. Funct. Mater.* **18**, 4029–4035 (2008).

[57] Lee, J. *et al.* Charge Transfer State Versus Hot Exciton Dissociation in Polymer-Fullerene Blended Solar Cells. *J. Am. Chem. Soc.* **132**, 11878–11880 (2010).

[58] Bakulin, A. A. *et al.* The Role of Driving Energy and Delocalized States for Charge Separation in Organic Semiconductors. *Science* **335**, 1340–1344 (2012).

[59] van der Hofstad, T. G. J., Di Nuzzo, D., van den Berg, M., Janssen, R. A. J. & Meskers, S. C. J. Influence of Photon Excess Energy on Charge Carrier Dynamics in a Polymer-Fullerene Solar Cell. *Adv. Energy Mater.* **2**, 1095–1099 (2012).

[60] Vandewal, K. *et al.* Efficient Charge Generation by Relaxed Charge-Transfer States at Organic Interfaces. *Nat. Mater.* **13**, 63–68 (2014).

[61] Albrecht, S. *et al.* On the Efficiency of Charge Transfer State Splitting in Polymer:Fullerene Solar Cells. *Adv. Mater.* **26**, 2533–2539 (2014).

[62] Hasharoni, K. *et al.* Near IR Photoluminescence in Mixed Films of Conjugated Polymers and Fullerenes. *J. Chem. Phys.* **107**, 2308–2312 (1997).

[63] Benson-Smith, J. J. *et al.* Formation of a Ground-State Charge-Transfer Complex in Polyfluorene//[6,6]-Phenyl-C_{61} Butyric Acid Methyl Ester (PCBM) Blend Films and Its Role in the Function of Polymer/PCBM Solar Cells. *Adv. Funct. Mater.* **17**, 451–457 (2007).

[64] Tvingstedt, K., Vandewal, K., Zhang, F. & Inganäs, O. On the Dissociation Efficiency of Charge Transfer Excitons and Frenkel Excitons in Organic Solar Cells: A Luminescence Quenching Study. *J. Phys. Chem. C* **114**, 21824–21832 (2010).

[65] Kern, J., Schwab, S., Deibel, C. & Dyakonov, V. Binding Energy of Singlet Excitons and Charge Transfer Complexes in MDMO-PPV:PCBM Solar Cells. *Phys. Status Solidi RRL* **5**, 364–366 (2011).

[66] Veldman, D., Meskers, S. C. J. & Janssen, R. A. J. The Energy of Charge-Transfer States in Electron Donor-Acceptor Blends: Insight into the Energy Losses in Organic Solar Cells. *Adv. Funct. Mat.* **19**, 1939–1948 (2009).

[67] Mihailetchi, V. D., Wildeman, J. & Blom, P. W. M. Space-Charge Limited Photocurrent. *Phys. Rev. Lett.* **94**, 126602 (2005).

[68] Lee, C., Tang, J., Zhou, Y. & Lee, S. T. Interface Dipole at Metal-Organic Interfaces: Contribution of Metal Induced Interface States. *Appl. Phys. Lett.* **94**, 113304–113304–3 (2009).

[69] Kumar, A., Sista, S. & Yang, Y. Dipole Induced Anomalous S-Shape I-V Curves in Polymer Solar Cells. *J. Appl. Phys.* **105**, 094512 (2009).

[70] Wagenpfahl, A., Rauh, D., Binder, M., Deibel, C. & Dyakonov, V. S-Shaped Current-Voltage Characteristics of Organic Solar Devices. *Phys. Rev. B* **82**, 115306 (2010).

[71] Wagenpfahl, A., Deibel, C. & Dyakonov, V. Organic Solar Cell Efficiencies Under the Aspect of Reduced Surface Recombination Velocities. *IEEE J. Sel. Top. Quantum Electron.* **16**, 1759–1763 (2010).

[72] Sandberg, O. J., Nyman, M. & Österbacka, R. Effect of Contacts in Organic Bulk Heterojunction Solar Cells. *Phys. Rev. Applied* **1**, 024003 (2014).

[73] Hoppe, H. & Sariciftci, N. S. Morphology of Polymer/Fullerene Bulk Heterojunction Solar Cells. *J. Mater. Chem.* **16**, 45–61 (2006).

[74] Chen, L.-M., Hong, Z., Li, G. & Yang, Y. Recent Progress in Polymer Solar Cells: Manipulation of Polymer:Fullerene Morphology and the Formation of Efficient Inverted Polymer Solar Cells. *Adv. Mater.* **21**, 1434–1449 (2009).

[75] Moulé, A. J. & Meerholz, K. Morphology Control in Solution-Processed Bulk-Heterojunction Solar Cell Mixtures. *Adv. Funct. Mater.* **19**, 3028–3036 (2009).

[76] Padinger, F., Rittberger, R. & Sariciftci, N. Effects of Postproduction Treatment on Plastic Solar Cells. *Adv. Funct. Mater.* **13**, 85–88 (2003).

[77] Chirvase, D., Parisi, J., Hummelen, J. C. & Dyakonov, V. Influence of Nanomorphology on the Photovoltaic Action of Polymer–Fullerene Composites. *Nanotechnology* **15**, 1317 (2004).

[78] Vanlaeke, P. *et al.* P3HT/PCBM Bulk Heterojunction Solar Cells: Relation Between Morphology and Electro-Optical Characteristics. *Sol. Energ. Mat. Sol. Cells* **90**, 2150–2158 (2006).

[79] van Bavel, S. S. v., Sourty, E., With, G. d. & Loos, J. Three-Dimensional Nanoscale Organization of Bulk Heterojunction Polymer Solar Cells. *Nano Lett.* **9**, 507–513 (2009).

[80] van Bavel, S. S., Bärenklau, M., de With, G., Hoppe, H. & Loos, J. P3HT/PCBM Bulk Heterojunction Solar Cells: Impact of Blend Composition and 3D Morphology on Device Performance. *Adv. Funct. Mater.* **20**, 1458–1463 (2010).

[81] Cates, N. C. *et al.* Tuning the Properties of Polymer Bulk Heterojunction Solar Cells by Adjusting Fullerene Size to Control Intercalation. *Nano Lett.* **9**, 4153–4157 (2009).

[82] Mayer, A. C. *et al.* Bimolecular Crystals of Fullerenes in Conjugated Polymers and the Implications of Molecular Mixing for Solar Cells. *Adv. Funct. Mater.* **19**, 1173–1179 (2009).

[83] Parmer, J. E. *et al.* Organic Bulk Heterojunction Solar Cells Using Poly(2,5-bis(3-tetradecyllthiophen-2-yl)thieno[3,2,b]thiophene). *Appl. Phys. Lett.* **92**, 113309 (2008).

[84] Rance, W. L. *et al.* Photoinduced Carrier Generation and Decay Dynamics in Intercalated and Non-intercalated Polymer:Fullerene Bulk Heterojunctions. *ACS Nano* **5**, 5635–5646 (2011).

[85] Lou, S. J. *et al.* Effects of Additives on the Morphology of Solution Phase Aggregates Formed by Active Layer Components of High-Efficiency Organic Solar Cells. *J. Am. Chem. Soc.* **133**, 20661–20663 (2011).

[86] Lee, J. K. *et al.* Processing Additives for Improved Efficiency From Bulk Heterojunction Solar Cells. *J. Am. Chem. Soc.* **130**, 3619–3623 (2008).

[87] Liao, H.-C. *et al.* Additives for Morphology Control in High-Efficiency Organic Solar Cells. *Mater. Today* **16**, 326 – 336 (2013).

[88] Hammond, M. R. *et al.* Molecular Order in High-Efficiency Polymer/Fullerene Bulk Heterojunction Solar Cells. *ACS Nano* **5**, 8248–8257 (2011).

[89] Brenner, T. J. K., Li, Z. & McNeill, C. R. Phase-Dependent Photocurrent Generation in Polymer/Fullerene Bulk Heterojunction Solar Cells. *J. Phys. Chem. C* **115**, 22075–22083 (2011).

[90] Hedley, G. J. *et al.* Determining the Optimum Morphology in High-Performance Polymer-Fullerene Organic Photovoltaic Cells. *Nat. Commun.* **4**, – (2013).

[91] Collins, B. A. *et al.* Absolute Measurement of Domain Composition and Nanoscale Size Distribution Explains Performance in PTB7:$PC_{71}BM$ Solar Cells. *Adv. Energy Mater.* **3**, 65–74 (2013).

[92] Foertig, A. *et al.* Nongeminate and Geminate Recombination in PTB7:PCBM Solar Cells. *Adv. Funct. Mater.* **24**, 1306–1311 (2014).

[93] Foster, S. *et al.* Electron Collection as a Limit to Polymer:PCBM Solar Cell Efficiency: Effect of Blend Microstructure on Carrier Mobility and Device Performance in PTB7:PCBM. *Adv. Energy Mater.* (2014).

[94] Hwang, I.-W. *et al.* Bulk Heterojunction Materials Composed of Poly(2,5-bis(3-tetradecylthiophen-2-yl)thieno[3,2-b]thiophene): Ultrafast Electron Transfer and Carrier Recombination. *J. Phys. Chem. C* **112**, 7853–7857 (2008).

[95] Coates, N. E. *et al.* 1,8-octanedithiol as a Processing Additive for Bulk Heterojunction Materials: Enhanced Photoconductive Response. *Appl. Phys. Lett.* **93**, 072105 (2008).

[96] Albrecht, S. *et al.* On the Field Dependence of Free Charge Carrier Generation and Recombination in Blends of PCPDTBT/$PC_{70}BM$: Influence of Solvent Additives. *J. Phys. Chem. Lett.* **3**, 640–645 (2012).

[97] Scharber, M. C. *et al.* Influence of the Bridging Atom on the Performance of a Low-Bandgap Bulk Heterojunction Solar Cell. *Adv. Mat.* **22**, 367–370 (2010).

[98] Morana, M. *et al.* Nanomorphology and Charge Generation in Bulk Heterojunctions Based on Low-Bandgap Dithiophene Polymers with Different Bridging Atoms. *Adv. Funct. Mat.* **20**, 1180–1188 (2010).

[99] Shockley, W. & Queisser, H. J. Detailed Balance Limit of Efficiency of p-n Junction Solar Cells. *J. Appl. Phys.* **32**, 510–519 (1961).

[100] Shrotriya, V. *et al.* Accurate Measurement and Characterization of Organic Solar Cells. *Adv. Funct. Mater.* **16**, 2016–2023 (2006).

[101] Clarke, T. M. & Durrant, J. R. Charge Photogeneration in Organic Solar Cells. *Chem. Rev.* **110**, 6736–6767 (2010).

[102] Brütting, W. & Adachi, C. Preface. In Brütting, W. & Adachi, C. (eds.) *Physics of Organic Semiconductors* (Wiley-VCH, Weinheim, 2012), 2nd edn.

[103] Vandewal, K. *et al.* The Relation Between Open-Circuit Voltage and the Onset of Photocurrent Generation by Charge-Transfer Absorption in Polymer:Fullerene Bulk Heterojunction Solar Cells. *Adv. Funct. Mater.* **18**, 2064–2070 (2008).

[104] Goris, L. *et al.* Observation of the Subgap Optical Absorption in Polymer-Fullerene Blend Solar Cells. *Appl. Phys. Lett.* **88**, 052113 (2006).

[105] Hallermann, M., Haneder, S. & Da Como, E. Charge-Transfer States in Conjugated Polymer/Fullerene Blends: Below-Gap Weakly Bound Excitons for Polymer Photovoltaics. *Appl. Phjys. Lett.* **93**, 053307 (2008).

[106] Kern, J. *Field Dependence of Charge Carrier Generation in Organic Bulk Heterojunction Solar Cells.* Ph.D. thesis, University of Würzburg (2013).

[107] Deibel, C., Strobel, T. & Dyakonov, V. Role of the Charge Transfer State in Organic Donor-Acceptor Solar Cells. *Adv. Mater.* **22**, 4097–4111 (2010).

[108] De, S. *et al.* Geminate Charge Recombination in Alternating Polyfluorene Copolymer/Fullerene Blends. *J. Am. Chem. Soc.* **129**, 8466–8472 (2007).

[109] Veldman, D. *et al.* Compositional and Electric Field Dependence of the Dissociation of Charge Transfer Excitons in Alternating Polyfluorene Copolymer/Fullerene Blends. *J. Am. Chem. Soc.* **130**, 7721–7735 (2008).

[110] Vandewal, K., Tvingstedt, K., Gadisa, A., Inganäs, O. & Manca, J. V. On the Origin of the Open-Circuit Voltage of Polymer-Fullerene Solar Cells. *Nat. Mater.* **8**, 904–909 (2009).

[111] Hallermann, M. *et al.* Correlation Between Charge Transfer Exciton Recombination and Photocurrent in Polymer/Fullerene Solar Cells. *Appl. Phys. Lett.* **97**, 023301 (2010).

[112] Mingebach, M., Walter, S., Dyakonov, V. & Deibel, C. Direct and Charge Transfer State Mediated Photogeneration in Polymer-Fullerene Bulk Heterojunction Solar Cells. *Appl. Phys. Lett.* **100**, 193302 (2012).

[113] Grancini, G. *et al.* Hot Exciton Dissociation in Polymer Solar Cells. *Nat. Mater.* **12**, 29–33 (2013).

[114] Howard, I. A. & Laquai, F. Optical Probes of Charge Generation and Recombination in Bulk Heterojunction Organic Solar Cells. *Macromol. Chem. Phys.,* **211**, 2063–2070 (2010).

[115] Brédas, J.-L., Norton, J. E., Cornil, J. & Coropceanu, V. Molecular Understanding of Organic Solar Cells: The Challenges. *Acc. Chem. Res.* **42**, 1691–1699 (2009).

[116] Ohkita, H. *et al.* Charge Carrier Formation in Polythiophene/Fullerene Blend Films Studied by Transient Absorption Spectroscopy. *J. Am. Chem. Soc.* **130**, 3030–3042 (2008).

[117] Albrecht, S. *et al.* Quantifying Charge Extraction in Organic Solar Cells: The Case of Fluorinated PCPDTBT. *J. Phys. Chem. Lett.* **5**, 1131–1138 (2014).

[118] Park, S. H. *et al.* Bulk Heterojunction Solar Cells With Internal Quantum Efficiency Approaching 100%. *Nat. Photon.* **3**, 297–302 (2009).

[119] Onsager, L. Initial Recombination of Ions. *Phys. Rev.* **54**, 554–557 (1938).

[120] Braun, C. L. Electric Field Assisted Dissociation of Charge Transfer States as a Mechanism of Photocarrier Production. *J. Chem. Phys.* **80**, 4157–4161 (1984).

[121] Limpinsel, M., Wagenpfahl, A., Mingebach, M., Deibel, C. & Dyakonov, V. Photocurrent in Bulk Heterojunction Solar Cells. *Phys. Rev. B* **81**, 085203 (2010).

[122] Kniepert, J., Schubert, M., Blakesley, J. C. & Neher, D. Photogeneration and Recombination in P3HT/PCBM Solar Cells Probed by Time-Delayed Collection Field Experiments. *J. Phys. Chem. Lett.* **2**, 700–705 (2011).

[123] Kniepert, J., Lange, I., van der Kaap, N. J., Koster, L. J. A. & Neher, D. A Conclusive View on Charge Generation, Recombination, and Extraction in As-Prepared and Annealed P3HT:PCBM Blends: Combined Experimental and Simulation Work. *Adv. Energy Mater.* **4**, 1301401 (2014).

[124] Street, R. A., Cowan, S. & Heeger, A. J. Experimental Test for Geminate Recombination Rpplied to Organic Solar Cells. *Phys. Rev. B* **82**, 121301 (2010).

[125] Arkhipov, V. I., Heremans, P. & Bässler, H. Why is Exciton Dissociation so Efficient at the Interface Between a Conjugated Polymer and an Electron Acceptor? *Appl. Phys. Lett.* **82**, 4605–4607 (2003).

[126] Hoofman, R. J. O. M., de Haas, M. P., Siebbeles, L. D. A. & Warman, J. M. Highly Mobile Electrons and Holes on Isolated Chains of the Semiconducting Polymer Poly(phenylene vinylene). *Nature* **392**, 54–56 (1998).

[127] Savenije, T. J., Kroeze, J. E., Wienk, M. M., Kroon, J. M. & Warman, J. M. Mobility and Decay Kinetics of Charge Carriers in Photoexcited PCBM/PPV Blends. *Phys. Rev. B* **69**, 155205 (2004).

[128] Deibel, C., Wagenpfahl, A. & Dyakonov, V. Origin of Reduced Polaron Recombination in Organic Semiconductor Devices. *Phys. Rev. B* **80**, 075203 (2009).

[129] Kohler, A. *et al.* Charge Separation in Localized and Delocalized Electronic States in Polymeric Semiconductors. *Nature* **392**, 903–906 (1998).

[130] Shoaee, S. *et al.* Charge Photogeneration for a Series of Thiazolo-Thiazole Donor Polymers Blended with the Fullerene Electron Acceptors PCBM and ICBA. *Adv. Funct. Mater.* **23**, 3286–3298 (2013).

[131] Tamura, H. & Burghardt, I. Ultrafast Charge Separation in Organic Photovoltaics Enhanced by Charge Delocalization and Vibronically Hot Exciton Dissociation. *J. Am. Chem. Soc.* **135**, 16364–16367 (2013).

[132] Savoie, B. M. *et al.* Unequal Partnership: Asymmetric Roles of Polymeric Donor and Fullerene Acceptor in Generating Free Charge. *J. Am. Chem. Soc.* **136**, 2876–2884 (2014).

[133] Gélinas, S. *et al.* Ultrafast Long-Range Charge Separation in Organic Semiconductor Photovoltaic Diodes. *Science* **343**, 512–516 (2014).

[134] Anderson, P. W. Absence of Diffusion in Certain Random Lattices. *Phys. Rev.* **109**, 1492–1505 (1958).

[135] Baranovskii, S. D., Cordes, H., Hensel, F. & Leising, G. Charge-Carrier Transport in Disordered Organic Solids. *Phys. Rev. B* **62**, 7934–7938 (2000).

[136] Miller, A. & Abrahams, E. Impurity Conduction at Low Concentrations. *Phys. Rev.* **120**, 745–755 (1960).

[137] Bässler, H. Charge Transport in Disordered Organic Photoconductors a Monte Carlo Simulation Study. *Phys. Stat. Sol. (b)* **175**, 15–56 (1993).

[138] Förtig, A. *Recombination Dynamics in Organic Solar Cells.* Ph.D. thesis, University of Würzburg (2013).

[139] Gill, W. D. Drift Mobilities in Amorphous Charge–Transfer Complexes of Trinitrofluorenone and Poly-*n*-vinylcarbazole. *J. Appl. Phys.* **43**, 5033–5040 (1972).

[140] Tessler, N., Preezant, Y., Rappaport, N. & Roichman, Y. Charge Transport in Disordered Organic Materials and Its Relevance to Thin-Film Devices: A Tutorial Review. *Adv. Mater.* **21**, 2741–2761 (2009).

[141] MacKenzie, R. C. I., Kirchartz, T., Dibb, G. F. A. & Nelson, J. Modeling Nongeminate Recombination in P3HT:PCBM Solar Cells. *J. Phys. Chem. C* **115**, 9806–9813 (2011).

[142] Monroe, D. Hopping in Exponential Band Tails. *Phys. Rev. Lett.* **54**, 146–149 (1985).

[143] Baranovskii, S. D., Faber, T., Hensel, F. & Thomas, P. The Applicability of the Transport-Energy Concept to Various Disordered Materials. *J. Phys.: Condens. Matter* **9**, 2699 (1997).

[144] Arkhipov, V. I., Emelianova, E. V. & Adriaenssens, G. J. Effective Transport Energy Versus the Energy of Most Probable Jumps in Disordered Hopping Systems. *Phys. Rev. B* **64**, 125125 (2001).

[145] Rudenko, A. I. & Arkhipov, V. I. Drift and Diffusion in Materials With Traps. *Philos. Mag. B* **45**, 177–187 (1982).

[146] Langevin, P. Recombinaison et Mobilités des Ions dans les Gaz. *Ann. Chim. Phys.* **28**, 433 (1903).

[147] Baumann, A. *Charge Transport and Recombination Dynamics in Organic Bulk Heterojunction Solar Cells.* Ph.D. thesis, University of Würzburg (2011).

[148] Deibel, C., Baumann, A. & Dyakonov, V. Polaron Recombination in Pristine and Annealed Bulk Heterojunction Solar Cells. *Appl. Phys. Lett.* **93**, 163303 (2008).

[149] Shuttle, C. G. *et al.* Experimental Determination of the Rate Law for Charge Carrier Decay in a Polythiophene: Fullerene Solar Cell. *Appl. Phys. Lett.* **92**, 093311 (2008).

[150] Foertig, A., Baumann, A., Rauh, D., Dyakonov, V. & Deibel, C. Charge Carrier Concentration and Temperature Dependent Recombination in Polymer-Fullerene Solar Cells. *Appl. Phys. Lett.* **95**, 052104 (2009).

[151] Shuttle, C. G. *et al.* Bimolecular Recombination Losses in Polythiophene: Fullerene Solar Cells. *Phys. Rev. B* **78**, 113201 (2008).

[152] Baumann, A. *et al.* Influence of Phase Segregation on Recombination Dynamics in Organic Bulk-Heterojunction Solar Cells. *Adv. Funct. Mater.* **21**, 1687–1692 (2011).

[153] Shuttle, C. G., Hamilton, R., Nelson, J., O'Regan, B. C. & Durrant, J. R. Measurement of Charge-Density Dependence of Carrier Mobility in an Organic Semiconductor Blend. *Adv. Funct. Mater.* **20**, 698–702 (2010).

[154] Gedde, U. W. *Polymer Physics* (John Wiley & Sons, Inc., New York, 2007), 2nd edn.

[155] McCulloch, I. *et al.* Liquid-Crystalline Semiconducting Polymers With High Charge-Carrier Mobility. *Nat. Mater.* **5**, 328–333 (2006).

[156] Kline, R. J. *et al.* Critical Role of Side-Chain Attachment Density on the Order and Device Performance of Polythiophenes. *Macromolecules* **40**, 7960–7965 (2007).

[157] Chabinyc, M. L., Toney, M. F., Kline, R. J., McCulloch, I. & Heeney, M. X-ray Scattering Study of Thin Films of Poly(2,5-bis(3-alkylthiophen-2-yl)thieno[3,2-b]thiophene). *J. Am. Chem. Soc.* **129**, 3226–3237 (2007).

[158] DeLongchamp, D. M. *et al.* High Carrier Mobility Polythiophene Thin Films: Structure Determination by Experiment and Theory. *Adv. Mater.* **19**, 833–837 (2007).

[159] DeLongchamp, D. M. *et al.* Molecular Basis of Mesophase Ordering in a Thiophene-Based Copolymer. *Macromolecules* **41**, 5709–5715 (2008).

[160] Savenije, T. J. *et al.* Photoinduced Charge Carrier Generation in Blends of Poly(Thienothiophene) Derivatives and [6,6]-Phenyl-C_{61}-butyric Acid Methyl Ester: Phase Segregation versus Intercalation. *J. Phys. Chem. C* **114**, 15116–15120 (2010).

[161] Bundgaard, E. & Krebs, F. C. Low Band Gap Polymers for Organic Photovoltaics. *Sol. Energ. Mat. Sol. Cells* **91**, 954–985 (2007).

[162] Heeger, A. J. Semiconducting Polymers: The Third Generation. *Chem. Soc. Rev.* **39**, 2354–2371 (2010).

[163] Dou, L. *et al.* 25th Anniversary Article: A Decade of Organic/Polymeric Photovoltaic Research. *Adv. Mater.* **25**, 6642–6671 (2013).

[164] Scharber, M.-C. *et al.* Design Rules for Donors in Bulk-Heterojunction Solar Cells—Towards 10% Energy-Conversion Efficiency. *Adv. Mater.* **18**, 789–794 (2006).

[165] Koster, L. J. A., Mihailetchi, V. D. & Blom, P. W. M. Ultimate Efficiency of Polymer/Fullerene Bulk Heterojunction Solar Cells. *Appl. Phys. Lett.* **88**, 093511 (2006).

[166] Lu, L. & Yu, L. Understanding Low Bandgap Polymer PTB7 and Optimizing Polymer Solar Cells Based on It. *Adv. Mater.* (2014).

[167] Gieseking, B. *Excitation Dynamics and Charge Carrier Generation in Organic Semiconductors for Photovoltaic Applications.* Ph.D. thesis, University of Würzburg (2013).

[168] Zhang, F. *et al.* Low-Bandgap Alternating Fluorene Copolymer/Methanofullerene Heterojunctions in Efficient Near-Infrared Polymer Solar Cells. *Adv. Mater.* **18**, 2169–2173 (2006).

[169] Blouin, N., Michaud, A. & Leclerc, M. A Low-Bandgap Poly(2,7-Carbazole) Derivative for Use in High-Performance Solar Cells. *Adv. Mater.* **19**, 2295–2300 (2007).

[170] Beaupré, S., Belletête, M., Durocher, G. & Leclerc, M. Rational Design of Poly(2,7-Carbazole) Derivatives for Photovoltaic Applications. *Macromolecular Theory and Simulations* **20**, 13–18 (2011).

[171] Liang, Y. *et al.* Development of New Semiconducting Polymers for High Performance Solar Cells. *J. Am. Chem. Soc.* **131**, 56–57 (2009).

[172] Liang, Y. *et al.* Highly Efficient Solar Cell Polymers Developed via Fine-Tuning of Structural and Electronic Properties. *J. Am. Chem. Soc.* **131**, 7792–7799 (2009).

[173] Chen, H.-Y. *et al.* Polymer Solar Cells with Enhanced Open-Circuit Voltage and Efficiency. *Nat. Photon.* **3**, 649–653 (2009).

[174] Kronenberg, N. M. *et al.* Bulk Heterojunction Organic Solar Cells Based on Merocyanine Colorants. *Chem. Commun.* 6489–6491 (2008).

[175] Mishra, A., Fischer, M. R. & Bäuerle, P. Metal-Free Organic Dyes for Dye-Sensitized Solar Cells: From Structure: Property Relationships to Design Rules. *Angew. Chem. Int. Ed.* **48**, 2474–2499 (2009).

[176] Bürckstümmer, H. *et al.* Tailored Merocyanine Dyes for Solution-Processed BHJ Solar Cells. *J. Mater. Chem.* **20**, 240–243 (2010).

[177] Bürckstümmer, H., Kronenberg, N. M., Meerholz, K. & Würthner, F. Near-Infrared Absorbing Merocyanine Dyes for Bulk Heterojunction Solar Cells. *Org. Lett.* **12**, 3666–3669 (2010).

[178] Kronenberg, N. M. *et al.* Direct Comparison of Highly Efficient Solution- and Vacuum-Processed Organic Solar Cells Based on Merocyanine Dyes. *Adv. Mater.* **22**, 4193–4197 (2010).

[179] Bürckstümmer, H. *Merocyanine Dyes for Solution-Processed Organic Bulk Heterojunction Solar Cells.* Ph.D. thesis, University of Würzburg (2011).

[180] Würthner, F. & Meerholz, K. Systems Chemistry Approach in Organic Photovoltaics. *Chem. Eur. J.* **16**, 9366–9373 (2010).

[181] Würthner, F., Kaiser, T. E. & Saha-Möller, C. R. J-Aggregates: From Serendipitous Discovery to Supramolecular Engineering of Functional Dye Materials. *Angew. Chem. Int. Ed.* **50**, 3376–3410 (2011).

[182] Kroto, H. W., Heath, J. R., O'Brien, S. C., Curl, R. F. & Smalley, R. E. C_{60}: Buckminsterfullerene. *Nature* **318**, 162–163 (1985).

[183] Kratschmer, W., Lamb, L. D., Fostiropoulos, K. & Huffman, D. R. Solid C_{60}: A New Form of Carbon. *Nature* **347**, 354–358 (1990).

[184] Taylor, R., Hare, J. P., Abdul-Sada, A. K. & Kroto, H. W. Isolation, Separation and Characterisation of the Fullerenes C_{60} and C_{70}: The Third Form of Carbon. *J. Chem. Soc. Chem. Commun.* 1423–1425 (1990).

[185] Ajie, H. *et al.* Characterization of the Soluble All-Carbon Molecules C_{60} and C_{70}. *J. Phys. Chem.* **94**, 8630–8633 (1990).

[186] Haufler, R. E. *et al.* Efficient Production of C_{60} (Buckminsterfullerene), $C_{60}H_{36}$, and the Solvated Buckide Ion. *J. Phys. Chem.* **94**, 8634–8636 (1990).

[187] Allemand, P. M. *et al.* Two Different Fullerenes Have the Same Cyclic Voltammetry. *J. Am. Chem. Soc.* **113**, 1050–1051 (1991).

[188] He, Y. & Li, Y. Fullerene Derivative Acceptors for High Performance Polymer Solar Cells. *Phys. Chem. Chem. Phys.* **13**, 1970–1983 (2011).

[189] Riedel, I. *et al.* Diphenylmethanofullerenes: New and Efficient Acceptors in Bulk-Heterojunction Solar Cells. *Adv. Funct. Mater.* **15**, 1979–1987 (2005).

[190] Halls, J. J. M. *et al.* Charge- and Energy-Transfer Processes at Polymer/Polymer Interfaces: A Joint Experimental and Theoretical Study. *Phys. Rev. B* **60**, 5721–5727 (1999).

[191] McNeill, C. R. *et al.* Efficient Polythiophene/Polyfluorene Copolymer Bulk Heterojunction Photovoltaic Devices: Device Physics and Annealing Effects. *Adv. Funct. Mater.* **18**, 2309–2321 (2008).

[192] Zhou, Y. *et al.* Donor–Acceptor Molecule as the Acceptor for Polymer-Based Bulk Heterojunction Solar Cells. *J. Phys. Chem. C* **113**, 7882–7886 (2009).

[193] Cnops, K. *et al.* 8.4% Efficient Fullerene-Free Organic Solar Cells Exploiting Long-Range Exciton Energy Transfer. *Nat. Commun.* **5** (2014).

[194] Hummelen, J. C. *et al.* Preparation and Characterization of Fulleroid and Methanofullerene Derivatives. *J. Org. Chem.* **60**, 532–538 (1995).

[195] Mihailetchi, V. D. *et al.* Electron Transport in a Methanofullerene. *Adv. Funct. Mater.* **13**, 43–46 (2003).

[196] Sieval, B. A. & Hummelen, J. C. Fullerene-Based Acceptor Materials. In Brabec, C., Scherf, U. & Dyakonov, V. (eds.) *Organic Photovoltaics – Materials, Devic Physics, and Manufacturing Technologies* (Wiley-VCH, Weinheim, 2014), 2nd edn.

[197] He, Y. *et al.* High Performance Low Band Gap Polymer Solar Cells With a Non-Conventional Acceptor. *Chem. Commun.* **48**, 7616–7618 (2012).

[198] Lenes, M. *et al.* Fullerene Bisadducts for Enhanced Open-Circuit Voltages and Efficiencies in Polymer Solar Cells. *Adv. Mater.* **20**, 2116–2119 (2008).

[199] Jarzab, D. *et al.* Charge Transfer Dynamics in Polymerâ Fullerene Blends for Efficient Solar Cells. *J. Phys. Chem. B* **113**, 16513–16517 (2009).

[200] Mort, J. *et al.* Nongeminate Recombination of *a*-Si:H. *Phys. Rev. Lett.* **45**, 1348–1351 (1980).

[201] Mort, J. *et al.* Geminate Recombination in *a*-Si:H. *Appl. Phys. Lett.* **38**, 277–279 (1981).

[202] Mort, J., Chen, I., Morgan, M. & Grammatica, S. Geminate and Non-Geminate Recombination in *a*-As_2Se_3. *Solid State Communications* **39**, 1329–1331 (1981).

[203] Popovic, Z. D. A Study of Carrier Generation Mechanism in X-Metal-Free Phthalocyanine. *J. Chem. Phys.* **78**, 1552–1558 (1983).

[204] Esteghamatian, M., Popovic, Z. D. & Xu, G. Carrier Generation Process in Poly(p-phenylene vinylene) by Fluorescent Quenching and Delayed-Collection-Field Techniques. *J. Phys. Chem.* **100**, 13716–13719 (1996).

[205] Hertel, D., Soh, E. V., Bässler, H. & Rothberg, L. J. Electric Field Dependent Generation of Geminate Electron-Hole Pairs in a Ladder-Type π-Conjugated Polymer Probed by Fluorescence Quenching and Delayed Field Collection of Charge Carriers. *Chem. Phys. Lett.* **361**, 99–105 (2002).

[206] Offermans, T., Meskers, S. C. J. & Janssen, R. A. J. Time Delayed Collection Field Experiments on Polymer:Fullerene Bulk-Heterojunction Solar Cells. *J. Appl. Phys.* **100**, 074509 (2006).

[207] Mingebach, M. H. *Photocurrent in Organic Solar Cells.* Ph.D. thesis, University of Würzburg (2012).

[208] Juška, G., Genevičius, K., Arlauskas, K., Österbacka, R. & Stubb, H. Features of Charge Carrier Concentration and Mobility in π-Conjugated Polymers. *Macromol. Symp.* **212**, 209–218 (2004).

[209] Sliaužys, G. *et al.* Recombination of Photogenerated and Injected Charge Carriers in π-Conjugated Polymer/Fullerene Blends. *Thin Solid Films* **511-512**, 224–227 (2006).

[210] Blom, P. W. M., de Jong, M. J. M. & Vleggaar, J. J. M. Electron and Hole Transport in Poly(p-phenylene vinylene) Devices. *Appl. Phys. Lett.* **68**, 3308–3310 (1996).

[211] Petravičius, A. D., Juška, G. B. & Baubinas, R. V. Hole Drift in High-Resistance p-Type CdSe Crystalline Plates. *Sov. Phys. Semicond.* **9**, 1530 (1975).

[212] Juška, G., Arlauskas, K., Viliūnas, M. & Kočka, J. Extraction Current Transients: New Method of Study of Charge Transport in Microcrystalline Silicon. *Phys. Rev. Lett.* **84**, 4946–4949 (2000).

[213] Österbacka, R. *et al.* Mobility and Density Relaxation of Photogenerated Charge Carriers in Organic Materials. *Curr. Appl. Phys.* **4**, 534–538 (2004).

[214] Mozer, A. J. *et al.* Charge Transport and Recombination in Bulk Heterojunction Solar Cells Studied by the Photoinduced Charge Extraction in Linearly Increasing Voltage Technique. *Appl. Phys. Lett.* **86** (2005).

[215] Mozer, A. J. *et al.* Time-Dependent Mobility and Recombination of the Photoinduced Charge Carriers in Conjugated Polymer/Fullerene Bulk Heterojunction Solar Cells. *Phys. Rev. B* **72**, 035217 (2005).

[216] Dennler, G. *et al.* Charge Carrier Mobility and Lifetime Versus Composition of Conjugated Polymer/Fullerene Bulk-Heterojunction Solar Cells. *Org. Electron.* **7**, 229–234 (2006).

[217] Pivrikas, A., Sariciftci, N. S., JuÅąka, G. & Österbacka, R. A Review of Charge Transport and Recombination in Polymer/Fullerene Organic Solar Cells. *Prog. Photovolt. Res. Appl.* **15**, 677–696 (2007).

[218] Juška, G., Genevičius, K., Nekrašas, N., Sliaužys, G. & Dennler, G. Trimolecular Recombination in Polythiophene:Fullerene Bulk Heterojunction Solar Cells. *Appl. Phys. Lett.* **93**, 143303 (2008).

[219] Baumann, A., Lorrmann, J., Rauh, D., Deibel, C. & Dyakonov, V. A New Approach for Probing the Mobility and Lifetime of Photogenerated Charge Carriers in Organic Solar Cells Under Real Operating Conditions. *Adv. Mater.* **24**, 4381–4386 (2012).

[220] Mozer, A. J. *Charge Transport and Recombination in Bulk Heterojunction Plastic Solar Cells*. Ph.D. thesis, Johannes Kepler University of Linz (2005).

[221] Foertig, A. *et al.* Nongeminate Recombination in Planar and Bulk Heterojunction Organic Solar Cells. *Adv. Energy Mater.* **2**, 1483–1489 (2012).

[222] Juška, G. *et al.* Charge Transport in π-Conjugated Polymers From Extraction Current Transients. *Phys. Rev. B* **62**, R16235–R16238 (2000).

[223] Juška, G., Nekrašas, N., Genevičius, K., Stuchlik, J. & Kočka, J. Relaxation of Photoexited Charge Carrier Concentration and Mobility in μc-Si:H. *Thin Solid Films* **451–452**, 290–293 (2004).

[224] Deibel, C. Charge Carrier Dissociation and Recombination in Polymer Solar Cells. *Phys. Stat. Sol. (a)* **206**, 2731–2736 (2009).

[225] Bange, S., Schubert, M. & Neher, D. Charge Mobility Determination by Current Extraction Under Linear Increasing Voltages: Case of Nonequilibrium Charges and Field-Dependent Mobilities. *Phys. Rev. B* **81**, 035209 (2010).

[226] Lorrmann, J., Badada, B. H., Inganäs, O., Dyakonov, V. & Deibel, C. Charge Carrier Extraction by Linearly Increasing Voltage: Analytic Framework and Ambipolar Transients. *J. Appl. Phys.* **108**, 113705–8 (2010).

[227] Hanfland, R., Fischer, M. A., Brütting, W., Würfel, U. & MacKenzie, R. C. I. The Physical Meaning of Charge Extraction by Linearly Increasing Voltage Transients From Organic Solar Cells. *Appl. Phys. Lett.* **103**, 063904 (2013).

[228] Cheyns, D. *et al.* Analytical Model for the Open-Circuit Voltage and Its Associated Resistance in Organic Planar Heterojunction Solar Cells. *Phys. Rev. B* **77**, 165332 (2008).

[229] Cates Miller, N., Hoke, E. T. & McGehee, M. D. Intercalation in Polymer:Fullerene Blends. In Brabec, C., Scherf, U. & Dyakonov, V. (eds.) *Organic Photovoltaics – Materials, Devic Physics, and Manufacturing Technologies* (Wiley-VCH, Weinheim, 2014), 2nd edn.

[230] Ashcroft, N. D. & Mermin, N. W. *Solid State Physics* (Cengage Learning, Boston, Massachusetts, 1976), 1st edn.

[231] Spieß, L., Schwarzer, R., Behnken, H. & Teichert, G. *Moderne Röntgenbeugung – Röntgendiffraktometrie für Materialwissenschaftler, Physiker und Chemiker* (Vieweg+Teubner Verlag, Wiesbaden, 2009), 2nd edn.

[232] Binnig, G., Quate, C. F. & Gerber, C. Atomic Force Microscope. *Phys. Rev. Lett.* **56**, 930–933 (1986).

[233] Binnig, G. & Smith, D. P. E. Single-Tube Three-Dimensional Scanner for Scanning Tunneling Microscopy. *Rev. Sci. Instrum.* **57**, 1688–1689 (1986).

[234] Zhong, Q., Inniss, D., Kjoller, K. & Elings, V. Fractured Polymer/Silica Fiber Surface Studied by Tapping Mode Atomic Force Microscopy. *Surf. Sci. Lett.* **290**, L688–L692 (1993).

[235] Jalili, N. & Laxminarayana, K. A Review of Atomic Force Microscopy Imaging Systems: Application to Molecular Metrology and Biological Sciences. *Mechatronics* **14**, 907–945 (2004).

[236] Geisse, N. A. AFM and combined optical techniques. *Mater. Today* **12**, 40–45 (2009).

[237] Boccara, A. C., Jackson, W., Amer, N. M. & Fournier, D. Sensitive Photothermal Deflection Technique for Measuring Absorption in Optically Thin Media. *Opt. Lett.* **5**, 377–379 (1980).

[238] Jackson, W. B., Amer, N. M., Boccara, A. C. & Fournier, D. Photothermal Deflection Spectroscopy and Detection. *Appl. Opt.* **20**, 1333–1344 (1981).

[239] Vanecek, M. & Poruba, A. Fourier-Transform Photocurrent Spectroscopy of Microcrystalline Silicon for Solar Cells. *Appl. Phys. Lett.* **80**, 719–721 (2002).

[240] Griffiths, P. R. & de Haseth, J. A. *Fourier Transform Infrared Spectrometry* (Chapman & Hall, London, 1995), 1st edn.

[241] Vandewal, K. *et al.* Fourier-Transform Photocurrent Spectroscopy for a Fast and Highly Sensitive Spectral Characterization of Organic and Hybrid Solar Cells. *Thin Solid Films* **516**, 7135–7138 (2008).

[242] Sudheendra Rao, K. & Mohapatra, Y. N. Open Circuit Voltage Decay Transients and Recombination in Bulk-Heterojunction Solar Cells. *Appl. Phys. Lett.* **104** (2014).

[243] Baumann, A. *et al.* Persistent Photovoltage in Methylammonium Lead Iodide Perovskite Solar Cells. *APL Mater.* **2** (2014).

[244] Miller, N. C. *et al.* Molecular Packing and Solar Cell Performance in Blends of Polymers with a Bisadduct Fullerene. *Nano Lett.* **12**, 1566–1570 (2012).

[245] Miller, N. C. *et al.* Use of X-Ray Diffraction, Molecular Simulations, and Spectroscopy to Determine the Molecular Packing in a Polymer-Fullerene Bimolecular Crystal. *Adv. Mater.* **24**, 6071–6079 (2012).

[246] Miller, N. C. *et al.* Factors Governing Intercalation of Fullerenes and Other Small Molecules Between the Side Chains of Semiconducting Polymers Used in Solar Cells. *Adv. Energy Mater.* **2**, 1208–1217 (2012).

[247] Deibel, C., Strobel, T. & Dyakonov, V. Origin of the Efficient Polaron-Pair Dissociation in Polymer-Fullerene Blends. *Phys. Rev. Lett.* **103**, 036402 (2009).

[248] Vandewal, K., Tvingstedt, K., Gadisa, A., Inganäs, O. & Manca, J. V. Relating the Open-Circuit Voltage to Interface Molecular Properties of Donor:Acceptor Bulk Heterojunction Solar Cells. *Phys. Rev. B* **81**, 125204 (2010).

[249] Jamieson, F. C. *et al.* Fullerene Crystallisation as a Key Driver of Charge Separation in Polymer/Fullerene Bulk Heterojunction Solar Cells. *Chem. Sci.* **3**, 485–492 (2012).

[250] Miller, N. C. *et al.* The Phase Behavior of a Polymer-Fullerene Bulk Heterojunction System That Contains Bimolecular Crystals. *J. Polym. Sci., B: Polym. Phys.* **49**, 499–503 (2011).

[251] Chen, W. *et al.* Hierarchical Nanomorphologies Promote Exciton Dissociation in Polymer/Fullerene Bulk Heterojunction Solar Cells. *Nano Lett.* **11**, 3707–3713 (2011).

[252] Huo, L. *et al.* Replacing Alkoxy Groups with Alkylthienyl Groups: A Feasible Approach To Improve the Properties of Photovoltaic Polymers. *Angew. Chem. Int. Ed.* **50**, 9697–9702 (2011).

[253] Hawks, S. A. *et al.* Relating Recombination, Density of States, and Device Performance in an Efficient Polymer:Fullerene Organic Solar Cell Blend. *Adv. Energy Mater.* **3**, 1201–1209 (2013).

[254] Liu, F. *et al.* Understanding the Morphology of PTB7:PCBM Blends in Organic Photovoltaics. *Adv. Energy Mater.* **4** (2014).

[255] Hoppe, H. *et al.* Nanoscale Morphology of Conjugated Polymer/Fullerene-Based Bulk-Heterojunction Solar Cells. *Adv. Funct. Mater.* **14**, 1005–1011 (2004).

[256] Österbacka, R., An, C. P., Jiang, X. M. & Vardeny, Z. V. Two-Dimensional Electronic Excitations in Self-Assembled Conjugated Polymer Nanocrystals. *Science* **287**, 839–842 (2000).

[257] Drori, T. *et al.* Below-Gap Excitation of π-Conjugated Polymer-Fullerene Blends: Implications for Bulk Organic Heterojunction Solar Cells. *Phys. Rev. Lett.* **101**, 037401 (2008).

[258] Carsten, B. *et al.* Examining the Effect of the Dipole Moment on Charge Separation in Donor–Acceptor Polymers for Organic Photovoltaic Applications. *J. Am. Chem. Soc.* **133**, 20468–20475 (2011).

[259] Jarzab, D. *et al.* Low-Temperature Behaviour of Charge Transfer Excitons in Narrow-Bandgap Polymer-Based Bulk Heterojunctions. *Adv. Energy Mater.* **1**, 604–609 (2011).

[260] Albrecht, S. *et al.* Fluorinated Copolymer PCPDTBT with Enhanced Open-Circuit Voltage and Reduced Recombination for Highly Efficient Polymer Solar Cells. *J. Am. Chem. Soc.* **134**, 14932–14944 (2012).

[261] Nelson, J. Diffusion-Limited Recombination in Polymer-Fullerene Blends and Its Influence on Photocurrent Collection. *Phys. Rev. B* **67**, 155209 (2003).

[262] Clarke, T. M., Jamieson, F. C. & Durrant, J. R. Transient Absorption Studies of Bimolecular Recombination Dynamics in Polythiophene/Fullerene Blend Films. *J. Phys. Chem. C* **113**, 20934–20941 (2009).

[263] Kirchartz, T., Pieters, B. E., Kirkpatrick, J., Rau, U. & Nelson, J. Recombination Via Tail States in Polythiophene:Fullerene Solar Cells. *Phys. Rev. B* **83**, 115209 (2011).

[264] Foertig, A., Rauh, J., Dyakonov, V. & Deibel, C. Shockley Equation Parameters of P3HT:PCBM Solar Cells Determined by Transient Techniques. *Phys. Rev. B* **86**, 115302 (2012).

[265] Väth, S. The Role of Processing Additives in Organic Solar Cells After the Preparation Process. DPG Spring Meeting, Dresden (2014).

[266] Kirchartz, T. & Nelson, J. Meaning of Reaction Orders in Polymer:Fullerene Solar Cells. *Phys. Rev. B* **86**, 165201 (2012).

[267] Müller, B. *Einfluss der Morphologie auf Exzitonendynamik und Ladungsträgergeneration in PTB7:PC_{70}BM Blends.* Master's thesis, University of Würzburg (2012).

[268] Faist, M. A. *et al.* Effect of multiple adduct fullerenes on charge generation and transport in photovoltaic blends with poly(3-hexylthiophene-2,5-diyl). *J. Polym. Sci., B: Polym. Phys.* **49**, 45–51 (2011).

[269] Clarke, T. M. *et al.* Charge Carrier Mobility, Bimolecular Recombination and Trapping in Polycarbazole Copolymer:fullerene (PCDTBT:PCBM) Bulk Heterojunction Solar Cells. *Org. Electron.* **13**, 2639–2646 (2012).

[270] Rauh, D., Deibel, C. & Dyakonov, V. Charge Density Dependent Nongeminate Recombination in Organic Bulk Heterojunction Solar Cells. *Adv. Funct. Mater.* **22**, 3371–3377 (2012).

[271] Gorenflot, J. *et al.* Nongeminate Recombination in Neat P3HT and P3HT:PCBM Blend Films. *J. Appl. Phys.* **115**, 144502 (2014).

[272] Dieckmann, A., Bässler, H. & Borsenberger, P. M. An Assessment of the Role of Dipoles on the Density-of-States Function of Disordered Molecular Solids. *J. Chem. Phys.* **99**, 8136–8141 (1993).

[273] Steinmann, V. *et al.* Simple, Highly Efficient Vacuum-Processed Bulk Heterojunction Solar Cells Based on Merocyanine Dyes. *Adv. Energy Mater.* **1**, 888–893 (2011).

[274] Graf, S. *Excited States and Recombination in Organic Bulk Heterojunction Solar Cells Based on Merocyanines.* Ph.D. thesis, University of Cologne (2014).

[275] Bürckstümmer, H. *et al.* Efficient Solution-Processed Bulk Heterojunction Solar Cells by Antiparallel Supramolecular Arrangement of Dipolar Donor–Acceptor Dyes. *Angew. Chem. Int. Ed.* **50**, 11628–11632 (2011).

[276] Mozer, A. J. *et al.* Charge Carrier Mobility in Regioregular Poly(3-hexylthiophene) Probed by Transient Conductivity Techniques: A Comparative Study. *Phys. Rev. B* **71**, 035214 (2005).

[277] Mihailetchi, V. D., Koster, L. J. A., Hummelen, J. C. & Blom, P. W. M. Photocurrent Generation in Polymer-Fullerene Bulk Heterojunctions. *Phys. Rev. Lett.* **93**, 216601 (2004).

[278] Peckus, D. *et al.* Charge Transfer States in Merocyanine Neat Films and Its Blends with [6,6]-Phenyl-C_{61}-butyric Acid Methyl Ester. *J. Phys. Chem. C* **117**, 6039–6048 (2013).

[279] Zitzler-Kunkel, A., Lenze, M. R., Meerholz, K. & Würthner, F. Enhanced Photocurrent Generation by Folding-Driven H-Aggregate Formation. *Chem. Sci.* **4**, 2071–2075 (2013).

[280] Koster, L. J. A. Charge Carrier Mobility in Disordered Organic Blends for Photovoltaics. *Phys. Rev. B* **81**, 205318 (2010).

[281] Petersen, A. *et al.* Field-Dependent Exciton Dissociation in Organic Heterojunction Solar Cells. *Phys. Rev. B* **85**, 245208 (2012).

[282] Tamai, Y., Tsuda, K., Ohkita, H., Benten, H. & Ito, S. Charge-Carrier Generation in Organic Solar Cells Using Crystalline Donor Polymers. *Phys. Chem. Chem. Phys.* **16**, 20338–20346 (2014).

[283] Ojala, A. *et al.* Merocyanine/C_{60} Planar Heterojunction Solar Cells: Effect of Dye Orientation on Exciton Dissociation and Solar Cell Performance. *Adv. Funct. Mater.* **22**, 86–96 (2012).

[284] National Institute of Standards and Technology, Physical Measurement Laboratory. The NIST Reference on Constants, Units, and Uncertainity. physics.nist.gov/cuu/Constants/ (2014).

A. Nomenclature

Abbreviations

A	acceptor
AFM, IC-AFM	(intermittent contact) atomic force microscopy
AM	air mass
AWG	arbitrary waveform generator
BDT	benzo[1,2-b:4,5-b']dithiophene
BHJ	bulk heterojunction
BMC	bimolecular crystal
CB	chlorobenzene
CE	charge extraction
CSS	charge separated state
CT	charge transfer
CTC	charge transfer complex
CTS	charge transfer state
CV	cyclic voltammetry
D	donor
DCB	1,2-dichlorobenzene
DIO	1,8-diiodooctane
DOOS	density of occupied states
DOS	density of states
e-h	electron-hole
EBT	electron back transfer
EQE	external quantum efficiency
expDOS	expontential density of states
FET	field-effect transistor
FF	fill factor
FIR	far-infrared
FTIR	Fourier transform infrared spectrometer
FTPS	Fourier transform photocurrent spectroscopy
FWHM	full width half maximum
GDM	Gaussian disorder model
GDOS	Gaussian density of states
HOMO	highest occupied molecular orbital
HTL	hole transport layer

IQE	internal quantum efficiency
IR	infrared
ISC	intersystem crossing
ITO	indium tin oxide
j-V	current-voltage
LED	light emitting diode
LUMO	lowest unoccupied molecular orbital
MC	merocyanine
MEH-PPV	poly(2-methoxy-5-(2-ethylhexyloxy)-1,4-phenylenevinylene)
MoO_3	molybdenum trioxide
MTR	multiple trapping and release
NIR	near-infrared
Nd:YAG	neodymium doped yttrium aluminum garnet
OCVD	open circuit voltage decay
ODT	1,8-octanedithiol
OPA	optical parametric amplifier
OPV	organic photovoltaic
OTRACE	open circuit corrected transient charge extraction
P3HT	poly(3-hexylthiophene-2,5-diyl)
pBTTT	poly(2,5-bis(3-alkyl-thiophene-2-yl)thieno[3,2-b]thiophene), without further specification of the side chain
pBTTT-C_{16}	poly(2,5-bis(3-hexyl-thiophen-2-yl)-thieno[3,2-b]thiophene)
$PC_{61}BM$	[6,6]-phenyl-C_{61}-butyric acid methyl ester
$PC_{71}BM$	[6,6]-phenyl-C_{71}-butyric acid methyl ester
PCBM	$PC_{61}BM$ and/or $PC_{71}BM$ fullerene derivatives
PCDTBT	poly[[9-(1-octylnonyl)-9H-carbazole-2,7-diyl]-2,5-thiophenediyl-2,1,3-benzothiadiazole-4,7-diyl-2,5-thiophenediyl]
PCE	power conversion efficiency
PCPDTBT	poly[2,6-(4,4-bis-(2-ethylhexyl)-4H-cyclopenta[2,1-b;3,4-b']-dithiophene)-alt-4,7-(2,1,3-benzothiadiazole)]
PDS	photothermal deflection spectroscopy
PEDOT:PSS	poly(3,4-ethylenedioxythiophene):poly(styrenesulfonate)
PHJ	planar heterojunction
PL, TRPL	(time-resolved) photoluminescence
PTB7	poly[(4,8-bis-(2-ethylhexyloxy)-benzo(1,2-b:4,5-b')dithiophene)-2,6-diyl-alt-(4-(2-ethylhexyl)-3-fluorothieno[3,4-b]thiophene-)-2-carboxylate-2-6-diyl)]
PV	photovoltaic
RC	resistive-capacitive
RMS	root mean square
RT	room temperature (T = 300 K)

S/N	signal-to-noise
S_0	singlet exciton ground state
S_1	singlet exciton exited state
SCLC	space-charge limited current
Si-PCPBDTBT	poly[(4,40-bis(2-thylhexyl)dithieno[3,2-b:20,30-d]silole)-2,6-diyl-alt-(4,7-bis(2-thienyl)-2,1,3-benzothiadiazole)-5,50-diyl]
SMU	source measurement unit
SOL	solution processed
SR	spectral response
SRC	standard reporting conditions
T_1	triplet exciton excited state
TA	transient absorption
TCO	transparent conductive oxide
TDCF	time delayed collection field
TEM	transmission electron microscopy
TOF	time-of-flight
TPV	transient photovoltage
TT	thieno[3,4-b]thiophene
UPS	ultraviaolet photoelectron spectroscopy
VAC	vacuum processed
XRD	X-ray diffraction

Important Variables and Constants

All constants are adapted from the set of CODATA internationally recommended values of the fundamental physics constants maintained by the National Institute of Standards and Technology. [284]

a	electron-hole distance (thermalization length), also: plane distance
α	absorption coefficient
$c = 2.998 \cdot 10^8$ m s^{-1}	speed of light in vacuum
d	active layer or film thickness
d_e	exciton diffusion length
E	energy
E_{CT}	CT ground state energy
E_A	activation energy (tail slope energy, Urbach tail energy)
E_b	Coulomb binding energy
E_b^{exc}	exciton binding energy
E_b^{pp}	polaron pair binding energy
E_g	band gap
$\varepsilon_0 = 8.854 \cdot 10^{-12}$ As V^{-1}s^{-1}	vacuum permittivity
ε_r	dielectric constant (relative permittivity)
F	electric field
γ	Langevin recombination coefficient
$h = 6.626 \cdot 10^{-34}$ Js	Planck constant
j	current density
j_{sc}	short circuit current density
k_{CTS}	charge separation rate
k_{EBT}	triplet transfer rate
k_{rec}	nongeminate recombination coefficient
$k_B = 1.380 \cdot 10^{-23}$ J K^{-1}	Boltzmann constant
$k_B T$	thermal energy
$k_d(F)$	field dependent dissociation rate
k_f	recombination rate of the singlet exciton or CTS
k_r	recombination rate of the CSS
λ	recombination order, also: wavelength
μ	mobility
n	charge carrier density, also: electron density, integer value
n_{pp}	polaron pair density
n_{col}	charge carrier density extracted by collection pulse
n_{pre}	charge carrier density extracted by pre-bias voltage
n_{tot}	total extracted charge carrier density

n_0	intrinsic electron density, also: constant of integration
n_c, n_t	density of free (trapped) charge carriers
n_{id}	ideality factor
ν	hopping rate, also: frequency
OD	optical density
OPV	organic photovoltaics
p_0	intrinsic hole density
P_L	total incident irradiance
$P(F)$	escape probability
p	hole density
PL	photoluminescence emission intensity
$q = 1.602 \cdot 10^{-19}$ As	elementary charge
r_{RMS}	root mean square roughness
r_c	Onsager radius (Coulomb capture radius)
R	nongeminate recombination rate, also: reflection coefficient
R_f	geminate recombination rate
R_L	Langevin-type recombination rate
R_s, R_p	series (shunt or parallel) resistance
S	voltage ramp
σ	energetic disorder parameter, also: conductivity, absorption cross section
Σ	spatial disorder parameter
T	temperature
t_d	delay time
t_p	pulse length
τ	lifetime
V	voltage
V_{col}	collection voltage
V_{oc}	open circuit voltage
V_{pre}	pre-bias voltage
V_p	pulse height

B. Publications and Conference Contribution

Full Papers

1. The Crucial Influence of Fullerene Phases on Photogeneration in Organic Bulk Heterojunction Solar Cells. **A. Zusan**,K. Vandewal, B. Allendorf, N. H. Hansen, J. Pflaum, A. Salleo, V. Dyakonov & C. Deibel. *Adv. Energy Mater.* **4** (2014).

2. The Effect of Diiodooctane on the Charge Carrier Generation in Organic Solar Cells Based on the Copolymer PBDTTT-C. **A. Zusan**, B. Gieseking, M. Zerson, V. Dyakonov, R. Magerle & C. Deibel. *Sci. Rep.* **5** (2015).

3. Influence of Structural Changes on the Nongeminate Recombination in PTB7:$PC_{71}BM$ Solar Cells. **A. Zusan**, B. Gieseking, J. Rauh, A. Baumann, K. Tvingstedt, B. Müller, M. Glücker, V. Dyakonov & C. Deibel. *Submitted* (2015).

4. Charge Carrier Transport and Geminate Recombination in Vacuum Deposited and Solution Processed Merocyanine Dye Based Solar Cells. **A. Zusan**, S. Graf, J. Krumrain, K. Meerholz, V. Dyakonov & C. Deibel. *In preparation* (2015).

Contributed Talks

1. The Influence of Fullerene Loading on the Charge Carrier Photogeneration in Intercalated Bulk Heterojunction Solar Cells. **A. Zusan**, K. Vandewal, B. Allendorf, N. H. Hansen, J. Pflaum, A. Salleo, V. Dyakonov & C. Deibel. *European Materials Research Society (E-MRS) Spring Meeting*, Lille (2014).

2. The Influence of Fullerene Loading on the Photogeneration in Intercalated Polymer:Fullerene Bulk Heterojunction Solar Cells. **A. Zusan**, K. Vandewal, B. Allendorf, N. H. Hansen, J. Pflaum, M. Heeney, A. Salleo, V. Dyakonov & C. Deibel. *Deutsche Physikalische Gesellschaft (DPG) Frühjahrstagung*, Dresden (2014).

3. Influence of Nanostructural Changes on the Charge Carrier Dynamics in PTB7 Based Solar Cells. **A. Zusan**, A. Baumann, J. Lorrmann, C. Deibel & V. Dyakonov. *DPG Frühjahrstagung*, Regensburg (2013).

4. Charge Carrier Dynamics in Low-Bandgap Bulk Heterojunction Solar Cells. **A. Zusan**, A. Baumann, J. Lorrmann, C. Deibel & V. Dyakonov. *Deutsche Forschungsgemeinschaft (DFG) Schwerpunktprogramm SPP 1355 Workshop*, Würzburg (2012).

Poster Presentations

1. 3 % DIO—As If That Weren't Enough... Detailed Study of the Effect of Processing Additive on the Photogeneration in PBDTTT-C Based Solar Cells. **A. Zusan**, B. Gieseking, M. Zerson, V. Dyakonov, R. Magerle & C. Deibel. *Bayerisches Staatsministerium für Bildung und Kultus, Wissenschaft und Kunst, Solar Technologies go Hybrid (SolTech) Workshop*, Wildbad Kreuth (2014)

2. Being Trapped on Acceptor Islands—Influence of Structural Changes on the Nongeminate Recombination in PTB7:$PC_{71}BM$ Solar Cells. **A. Zusan**, B. Gieseking, B. Müller, A. Baumann, V. Dyakonov & C. Deibel. *DFG Schwerpunktprogramm SPP 1355 Spring School*, Weinböhla (2013).

3. Charge Transport and Recombination Dynamics in Low-Bandgap Polymer:Fullerene Solar Cells. **A. Zusan**, A. Baumann, C. Deibel & V. Dyakonov. *DPG Frühjahrstagung*, Berlin (2012).

C. Danksagung

An dieser Stelle möchte ich mich bei allen Personen bedanken, die mich in den letzten Jahren bei meiner Arbeit am Lehrstuhl für Experimentelle Physik 6 begleitet und unterstützt haben und ohne die diese Arbeit in der jetzigen Form nicht hätte entstehen können. Insbesondere geht mein Dank an...

... Prof. Vladimir Dyakonov für das Ermöglichen meiner Promotion, die Unterstützung während meiner Zeit an seinem Lehrstuhl sowie die Hilfe und Anmerkungen zu Manuskripten und Konferenzbeiträgen, die stets dabei halfen die eigene Arbeit zu verbessern.

... Prof. Carsten Deibel für die Vergabe des Themas, die Betreuung meiner Promotion, sein stets offenes Ohr bei Fragen und Problemen, die zahlreichen Diskussionsrunden, das detaillierte Korrekturlesen unzähliger Manuskripten und die damit verbundenen, zielführenden Verbesserungsvorschläge in Würzburger wie auch in Chemnitzer Zeiten.

... Priv. Doz. Achim Schöll für das Interesse an dieser Arbeit und deren Begutachtung.

... Andreas Baumann, Mike Heiber und Stefan „Väthi“ Väth für für die Hilfe beim Korrekturlesen dieser Dissertation.

... Andy, Markus Mingebach und Jens Lorrmann für das Einlernen eines fachfremden Kellerkinds und dem geduldigen Beantworten aller meiner Fragen. Zudem ein besonderes Dankeschön für das Bereitstellen aller Makros, die kurzfristige Auswertung vieler Datensätze wenn Python nicht so wollte wie ich und die ständige IT-Unterstützung jeglicher Art.

... die gesamte OPV Gruppe und insbesondere an alle Mistreiter am Transport-Setup. Im Speziellen erwähnt seien Kristofer Tvingstedt, Mike, Alexander Förtig und Stefan Walter für die vielen Diskussionen und die produktive und kurzweilige Zusammenarbeit innerhalb und außerhalb des Labors.

... die nicht-OPV Jungs Björn „Börni“ Gieseking, Andreas „Fritzi“ Fritze und Nis Hauke Hansen für alle ergänzenden Messungen, die Möglichkeit den Todestern zu nutzen, den schonenden Umgang mit einem nicht-Photophysiker und alle „free hugs!“.

... alle Kooperationspartner für die erfolgreiche Zusammenarbeit in unterschiedlichen Projekten. Besonders erwähnt seien Prof. Koen Vandewal, Mario Zerson und Steven Graf.

- ... meine Masteranden Benedikt Allendorf, Philipp Pelchmann und Katrin Anneser. Ein riesen Dankeschön für die Mithilfe, alle Messungen und Auswertungen sowie das klaglose Aufarbeiten des obligatorischen Datenwirrwarrs.
- ... Prof. Jochen Fricke für die Möglichkeit mehrmals seine Vorlesung „Einführung in die Energietechnik“ zu betreuen und die interessanten Einblicke die dabei vermittelt wurden.
- ... alle Bürokollegen der vergangenen Jahre für die ständige Hilfe bei allerlei Fragen sowie die vielen sinnvollen und sinnlosen Diskussionen („Steck ne Banane in dein Ohr...“). Danke an den harten Kern aus E13 Stefan, Julia Kern und unser zeitweises „evergreen“ Jasmin sowie die E04-Crew Julia Rauh, André Thiem-Riebe und Valentin Baianov
- ... unsere IT-Beauftragten Hannes Kraus und Andreas „Hex“ Sperlich für das Lösen aller Soft- und Hardwareprobleme und das Wiederherstellen von wichtigen Dateien, die im Eifer des Gefechts auch mal unwiderruflich gelöscht wurden.
- ... André für seine Hilfe im Labor, die Instandhaltung der Glovebox und dem ganzen Drumherum, das viele Fachsimpeln und alle Tipps und Tricks.
- ... unseren Laserguru Valentin für seine Hilfe beim Justieren des Lasers und das Entwerfen neuer Optiken.
- ... Diep Phan für die Unterstützung bei Reiseanträgen, Abrechnungen, Bestellungen und jeglichen anderen bürokratischen Herausforderungen.
- ... unsere EP6-Mountainbikegruppe um Michel „This boy is insane!“ Auth, Christian Weber, Hannes, Franziska „Franzi“ Fuchs und alle die wir unterwegs aufgegabelt haben. Egal ob Kartoffelturm, A3-Trail, Panoramaweg, Helene-Fischer-Kurve, Steinbachtal, Andy-Schanze, Schwarze Eule, Wurzel-Trail oder M-Weg, für Abwechslung nach Feierabend und an Wochenenden war immer gesorgt.
- ... schlicht und einfach die gesamte Gruppe der EP6 in der ich mich ab dem ersten Tag zuhause gefühlt habe und dank der meine Promotion zu einem unvergesslichen Lebensabschnitt wurde. An der Uni, auf Tagungen und Workshops oder bei diversen Festivitäten, egal wo, wer und wie, es hat mit euch immer riesig Spaß gemacht. Danke für 3 1/2 tolle Jahre!

Fernab vom Arbeitsalltag an der EP6 möchte ich mich bei allen Freunden und meiner Familie bedanken. Mein größtes Dankeschön geht dabei an meine Eltern für die stetige Unterstützung während meines Studiums, meiner Promotion und bei allem was ich sonst so mache sowie, last but not least, an meine Freundin Eva.

D. Curriculum Vitae

E. Eidesstattliche Erklärung

Eidesstattliche Versicherung und Erklärung zur Dissertation gemäß § 5 Abs. 2 und Sätze 2, 3 und 4 der Promotionsordnung vom 22.09.2003 der Fakultät für Physik und Astronomie der Julius-Maximilians-Universität Würzburg.

Hiermit erkläre ich an Eides statt, dass ich die vorliegende Dissertation eigenständig, d. h. insbesondere selbständig und ohne Hilfe einer kommerziellen Promotionsberatung angefertigt und keine anderen als die von mir angegebenen Quellen und Hilfsmittel benutzt habe und dass ich die Gelegenheit zum Promotionsvorhaben nicht kommerziell vermittelt bekommen habe und insbesondere nicht eine Person oder Organisation eingeschaltet habe, die gegen Entgelt Betreuer bzw. Betreuerinnen für die Anfertigung von Dissertationen sucht. Hiermit erkläre ich zudem, dass ich die Regeln der Universität Würzburg über gute wissenschaftliche Praxis eingehalten habe und dass ich die Dissertation in gleicher oder anderer Form nicht bereits in einem anderen Prüfungsfach vorgelegt habe.

Andreas Zusan

Würzburg, den 18. Dezember 2014